On Stability of Falling Films: Numerical and Analytical Investigations

Vom Fachbereich Mathematik
der Technischen Universität Darmstadt
zur Erlangung des Grades eines
Doktors der Naturwissenschaften
(Dr.rer.nat.)
genehmigte Dissertation

von
Dipl.-Math. Christoph Hermann Albert
aus Aschaffenburg

Referenten	Prof. Dr. Dieter Bothe Prof. Dr. Jürgen Saal Prof. Dr. Takaaki Nishida
Tag der Einreichung	24. Juli 2013
Tag der mündlichen Prüfung	14. August 2013

Darmstadt 2013
D 17

Acknowledgment

I would like to thank the numerous people from whom I received support during the completion of this thesis.

First of all, I would like to thank Prof. Dr. Dieter Bothe for introducing me to the fascinating topic of capillary driven flows, and for his invaluable mentoring and support during the last three years. I owe a great deal of gratitude to Prof. Dr. Takaaki Nishida, for introducing me to the analytical approach to film flows, and for his support during my time in Tokyo. I thank Prof. Dr. Yoshiaki Teramoto, who kindly taught me so much about stability of falling films. I am grateful to Prof. Dr. Asei Tezuka, from whom I learned about the numerical approach to stability analysis. I would like to thank Prof. Dr. Jürgen Saal for agreeing to write a report about my thesis.

I thank all the former and present colleagues at *Mathematische Modellierung und Analysis* for many fruitful and interesting discussions, especially the postdocs Dr. Henning Raach, Dr. Holger Marschall and Dr. Matthias Köhne.

I would like to thank the people of the *International Research Training Group 1529* for giving me the opportunity to do a research stay in Tokyo.

Finally, I would like to thank my family for their support.

Deutsche Zusammenfassung

Die vorliegende Arbeit beschäftigt sich mit Fallfilmen: Dünnen Flüssigkeitsfilmen, die unter dem Einfluss der Gravitation vertikale oder geneigte Wände herunterlaufen. Besonderes Augenmerk wird auf die Entstehung von Oberflächenwellen gelegt, sowie auf die Strömungsvorgänge innerhalb dieser Wellen.

Das Einsetzen von Wellen wird durch klassische hydrodynamische Stabilitätstheorie erklärt. Die Grundidee hierbei ist, dass eine Strömung als Überlagerung einer laminaren, stationären Grundströmung und einer kleinen Störung gedacht wird. Findet für große Zeiten eine Dämpfung aller Störungen statt, so bezeichnet man die Grundströmung als stabil, und man erwartet, sie im Experiment zu sehen. Existiert hingegen mindestens eine Störung, die mit der Zeit angefacht wird, so liegt eine instabile Grundströmung vor, die sich im Experiment nicht beobachten lässt. Am Fallfilm ist die Existenz angefachter Störungen anhand der Anwesenheit von Wellen auf der Filmoberfläche leicht sichtbar.

In Kapitel 1 wird das Koordinatensystem festgelegt, und die Gleichungen, die die Strömung beschreiben, werden angegeben. Die Arbeit beruht auf dem kontinuumsmechanischen Modell der Erhaltung von Masse und Impuls, den Navier-Stokes-Gleichungen. Zusätzliche wichtige Effekte ergeben sich durch die freie Oberfläche des Films, die aufgrund von Oberflächenspannungseffekten einen wichtigen Einfluss auf die Entwicklung der Strömung hat. In vielen Situationen ist die Oberflächenspannung nicht an jeder Stelle des Films gleichermaßen stark. Es können sich (erwünschte oder unerwünschte) Verunreinigungen an der Filmoberfläche ansammeln, die die Oberflächenspannung senken. Diese Verunreinigungen werden als *Surfactant* bezeichnet. Die lokale Konzentration dieser Verunreinigungen genügt einer Advektions-Diffusionsgleichung innerhalb der bewegten Filmoberfläche. Dieser Effekt wird in den Kapitel 1 und 2 berücksichtigt. Die laminare Grundströmung, das sogenannte *Nusselt-Profil*, wird angegeben, und es werden dimensionslose Kennzahlen eingeführt.

In Kapitel 2 wird der analytische Zugang zur Stabilität von Fallfilmen verfolgt. Zunächst wird ein Gleichungssystem hergeleitet, das die zeitliche Entwicklung von Störungen der stationären Grundströmung beschreibt. Um das zeitveränderliche Gebiet, auf dem diese Gleichungen definiert sind analytisch behandeln zu können, wird das Gebiet mithilfe der sogenannten Beale-Transformation auf ein zeitunabhängiges Referenzgebiet transformiert, im Anschluss daran linearisiert und als Evolutionsgleichung geschrieben. Der lineare Operator, der in dieser Gleichung vorkommt, wird als linearer Stabilitätsoperator $\boldsymbol{G}$ bezeichnet. Der Rest des Kapitels beschäftigt sich mit dem dazugehörigen Resolventenproblem, und dem Spektrum von $\sigma(\boldsymbol{G})$, das definiert ist als die Menge aller $\lambda \in \mathbb{C}$ sodass $\lambda - \boldsymbol{G}$

nicht bijektiv ist. Das Spektrum bestimmt das asymptotische Verhalten kleiner Störungen in linearer Näherung: Haben alle $\lambda \in \sigma(\boldsymbol{G})$ einen negativen Realteil, so unterliegen alle Störungen für große Zeiten einer exponentiellen Dämpfung. Existiert hingegen mindestens ein $\lambda \in \sigma(\boldsymbol{G})$ mit positivem Realteil $\mathfrak{Re}\lambda$, so existieren angefachte Störungen, und der stationäre Zustand ist instabil. In der vorliegenden Arbeit wird das Resolventenproblem mithilfe der Fourierreihenentwicklung in einem L^2-Setting gelöst. In Kapitel 2.3 wird gezeigt, dass für beliebige dimensionslose Kenngrößen immer ein $\gamma_0 > 0$ existiert, so dass das Resolventenproblem für alle λ mit $\mathfrak{Re}\lambda \geq \gamma_0$ lösbar ist. Da die Gleichungen auf einem beschränkten Gebiet betrachtet werden, impliziert dies, dass die Resolventenoperatoren kompakt sind. Dies erlaubt in Abschnitt 2.4, nähere Angaben zum Spektrum zu machen, indem die Eigenfunktionsgleichung betrachtet wird. Mithilfe von Energiemethoden können Bedingungen an die dimensionslosen Kenngrößen hergeleitet werden, unter denen die Strömung stabil ist. Die Bedingungen sind physikalisch sinnvoll, und es wird eine explizite Spektralschranke von $-\frac{1}{2}$ hergeleitet.

Der Rest der Arbeit befasst sich mit Untersuchungen von Strömungen ohne Surfactant anhand von direkten numerischen Simulationen. Diese werden mithilfe des Volume of Fluid-Solvers FS3D durchgeführt. In Kapitel 3 wird zunächst die verwendete numerische Methode eingeführt, und der Einfluss von verschiedenen Ansätzen zur numerischen Behandlung der Oberflächenspannung auf die Simulationsergebnisse wird untersucht. Es wird gezeigt dass Simulationen mit dem impulserhaltenden *Continuum Surface Stress* (CSS)-Verfahren nicht geeignet sind, die Strömungen im Fallfilm korrekt wiederzugeben. Anhand einer Reihe von Vergleichen mit theoretischen und experimentellen Daten wird gezeigt, dass Simulationen mit einem *balanced Continuum Surface Force* (CSF)-Ansatz die physikalischen Gegebenheiten in guter Näherung abbilden. Der Begriff der *balanced force*-Oberflächenspannung wird erklärt, und es wird ein Grund angegeben, warum bisher keine entsprechende Implementierung für CSS bekannt ist.

In Kapitel 4 wird die lineare Stabilität von Fallfilmen numerisch untersucht. Dazu wird ein neues Verfahren entwickelt, das eng mit dem Algorithmus von Arnoldi zur Bestimmung des Eigensystems großer, dünn besetzter Matrizen verwandt ist. Die Wirkung des Evolutionsoperators $\exp(\boldsymbol{G}T)$ für ein festes $T > 0$ auf Störungen wird mit Hilfe von direkten numerischen Simulationen bestimmt. Aus der Simulation einer Reihe von Störungen wird ein approximatives Eigensystem von $\exp(\boldsymbol{G}T)$ errechnet. Der Spektral-Abbildungssatz für die Matrix-Exponentialfunktion erlaubt schließlich die Bestimmung einer Näherung an das Spektrum von $\boldsymbol{G}$. Um den Algorithmus verwenden zu können muss lineare Algebra auf der Menge der Störungen betrieben werden. Problematisch hierbei ist der freie Rand, der eine einfache Addition von Strömungszuständen zu verschiedenen Zeiten unmöglich macht. Dieses Problem wird durch die Transformation auf ein festes Referenzgebiet mithilfe der Beale-Transformation gelöst. Der Algorithmus wird durch Vergleiche mit numerischen, experimentellen und theoretischen Resultaten validiert. Der Vorteil des Algorithmus gegenüber klassischen Verfahren ist, dass auch nicht-parallele Grundströmungen behandelt werden können. Diese Eigenschaft wird eingesetzt, um den Einfluss des Einströmrandes zu untersuchen.

Kapitel 5 beschäftigt sich mit den Strömungsvorgängen in entwickelten, nichtlinearen Wellen. Es werden Wasserfilme in einer Sauerstoffatmosphäre simuliert, und der Übergang von Sauerstoff in die Flüssigkeit durch die freie Grenzfläche wird untersucht. Besonderes Augenmerk wird auf den Einfluss von Wirbeln auf lokale Stoffübergangsraten gelegt. Es wird beobachtet, dass die Anwesenheit von Wirbeln in den großen Wellen einen qualitativen Einfluss auf die Sauerstoffverteilung im Film und die lokalen Stoffübergangsraten hat. Wirbel in den Wellensenken hingegen zeitigen keinen derartigen Effekt.

Contents

1. Introduction **1**
1.1. Liquid flow down an inclined plane 2
1.2. Differential operators on the interface 5
1.2.1. Definition of differential operators 5
1.2.2. Evaluation of the operators in the considered geometry . . 7
1.3. Governing equations 9
1.3.1. An alternative formulation of the kinematic boundary condition 10
1.3.2. One-phase flow down an inclined plane with a free surface . 10

2. Periodic flow with surfactant **13**
2.1. Introduction 13
2.2. Derivation of the resolvent problem 14
2.2.1. Nondimensionalization 14
2.2.2. Evaluation of the surface differential operators 15
2.2.3. Equations for perturbations to the steady state 16
2.2.4. Transformation to a fixed reference domain and linearization 17
2.2.5. Formulation as an evolution equation 19
2.3. Construction of the resolvent 22
2.3.1. Auxiliary problem A 22
2.3.2. Auxiliary problem B 32
2.3.3. Auxiliary problem C 35
2.3.4. Auxiliary problem D 35
2.3.5. Auxiliary problem E 37
2.3.6. Construction of the resolvent 38
2.4. Stability estimates 41
2.4.1. Inequalities on a periodic slab 41
2.4.2. Derivation of the energy equation 43
2.4.3. Estimates for the perturbation terms 46
2.4.4. Linear stability of the falling film 48
2.5. Conclusion 50

3. Direct numerical simulation **51**
3.1. Introduction 51
3.2. Finite Volume discretization with the Volume of Fluid method . . 52
3.2.1. PLIC advection 54
3.2.2. Timestep constraints 54

3.2.3. Boundary conditions 55
3.2.4. Coupling between velocity and pressure 55
3.3. Numerical treatment of surface tension 56
3.3.1. Numerical implementation of surface tension forces 56
3.3.2. Parasitic currents and balanced force surface tension 57
3.3.3. A necessary condition for the balanced force property . . . 59
3.4. Computational setup 61
3.4.1. Boundary conditions in cross-streamwise direction 61
3.4.2. Inlet boundary conditions 62
3.4.3. Outlet boundary conditions 63
3.4.4. Initial conditions 63
3.4.5. Dimensions of the computational domain 64
3.4.6. Material parameters 64
3.5. Vorticity structure in the wave humps 64
3.6. Validation and surface tension discretization 66
3.6.1. Viscous damping of a capillary wave 66
3.6.2. Comparison to Nosoko's experiments 67
3.6.3. Comparison to Dietze's experiments 68
3.6.4. Grid refinement 68
3.7. Conclusion 72

4. Global linear stability analysis 73
4.1. Introduction 73
4.2. Arnoldi's Algorithm for dynamical systems 74
4.2.1. Formulation 75
4.2.2. A Jacobian free method for stability of dynamical systems . 76
4.3. Arnoldi's Method for two-phase Navier-Stokes 79
4.3.1. Pressure 79
4.3.2. Transformation to a fixed domain 79
4.3.3. Linear algebra on the reference domain 82
4.3.4. Numerical realization 83
4.4. Computational setup 84
4.4.1. Material parameters and resolution 84
4.4.2. Boundary conditions for periodic flow 85
4.5. Validation 85
4.5.1. Neutral stability curve. 85
4.5.2. Most amplified mode 86
4.5.3. Influence of mesh size, T and ϵ 87
4.6. Results with periodic flow 88
4.6.1. Shear modes 88
4.6.2. Surface Modes 89
4.7. Results with Inlet/Outlet 94
4.7.1. Real Modes 94
4.7.2. Influence of domain length 96

4.7.3. Comparison to experiments 99
4.7.4. The convective character of the instability 101
4.7.5. Influence of the outlet boundary condition 101
4.7.6. Influence of the inlet condition 105
4.8. Conclusion 107

5. Vortices and species transfer 111
5.1. Introduction 111
5.2. Governing equations 113
5.3. Material parameters and resolution 114
5.4. Validation 116
5.5. Species transfer into falling film 118
5.5.1. Hydrodynamics 118
5.5.2. Species transfer 125
5.6. Conclusion 133

A. Transformation to the fixed domain 135
A.0.1. Transformation of the differential operators 136
A.0.2. Derivatives of components of the Jacobian 137
A.0.3. Transformation of the velocity components 137

B. Derivation of the Orr-Sommerfeld equation 141

1. Introduction

One of the most prominent questions in hydrodynamics is the question of *stability* of a flow. This question was first raised by Reynolds (1883, 1895). In this famous work, it was observed that flow of water through a pipe can show completely different characteristics. It can either be *laminar*, where water flows in a well-behaved, stationary way along the axis of the pipe, or it can be turbulent, where the onset of eddies introduces a more chaotic, transient behaviour. He noted that the transition from laminar to turbulent behaviour occurs when the quotient of mean flow velocity, pipe diameter and viscosity exceeds a certain value. Nowadays, this dimensionless quotient is known as the *Reynolds number*.

This transition is especially remarkable in view of the fact that there exists a laminar and time-independent solution for the Navier-Stokes equations, which govern the flow of liquid through a pipe. This solution is known as *Hagen–Poiseuille flow*. A simple analytic expression is known, which solves the Navier-Stokes equations for every Reynolds number.

In order to describe this transition to turbulence, hydrodynamic stability theory was developed. At the basis of hydrodynamic stability theory lies the following idea: The complete flow, at a certain moment, is considered to be a superposition of a laminar, time-independent base flow and a perturbation. The notion of *stability* is connected to the question if perturbations to the flow will decay for large times, or if they will grow instead. If every perturbation is damped, we say the basic flow is *stable*, and expect that it can be observed in experimental situations. If, on the other hand, there exists at least one kind of perturbation that is amplified, the flow is *unstable*, and it is expected that the base flow is not seen in experiments. Thorough introductions to hydrodynamic stability theory can be found in Drazin and Reid (2004); Schmid and Henningson (2001).

This work is concerned with *falling films*: Thin films of a viscous, Newtonian liquid, that run down an inclined plane under the action of gravity. Since the pioneering work of Nusselt (1916, 1923), a laminar steady state solution for this flow situation has been known analytically. A falling film is a free surface flow, which means that the domain occupied by the liquid is not constant in time. One consequence of instability on falling films is the onset of surface waves, which are easily visible to the human eye without the need to resort to especially sensitive measurement devices. Surface waves on falling films can be observed in a number of everyday situations, for example when a sloped street or a window shield is covered by water during heavy rainfalls. Many public fountains show the aesthetic interaction of coalescing and bouncing wave fronts on films of falling water. In fact, the famous and important studies by Kapitza and Kapitza (1949) on flow patterns on falling films were performed with tap water in the kitchen of the house in which Pyotr Kapitza and his son were held under arrest by the Soviet Government after refusing to work on the development of nuclear weapons.

Falling films are also important in a variety of apparatus of chemical and mechanical engineering, where they are used in cooling devices, in desalination units, in falling film microreactors, and many other applications where large rates of heat and mass transfer are required. In the context of industrial applications, it was noted that the presence of surface waves has a profound influence on the observed rates of heat and mass transfer, making a thorough understanding of the onset of waves a question of practical interest.

The availability of an explicit steady state solution makes falling films also an attractive field for theoretical studies, especially since many physical effects are of importance. Due to their small thickness, the influence of the wall is important throughout the film, and viscosity cannot be neglected. For the considered flow dimensions, also the effect of surface tension must always be taken into account. The books of Alekseenko et al. (1994), Chang and Demekhin (2002) and Kalliadasis et al. (2012) give a detailed account of the current state of experimental and theoretical understanding of falling liquid films.

The contribution of the presented thesis is the following: In Chapter 2, a new analytical stability criterion for flow down an inclined plane under presence of an insoluble surfactant is derived on the basis of the full Navier-Stokes equations. In Chapter 3, the direct numerical simulation of falling films with a Volume of Fluid-solver is described, and the influence of two different surface tension models on the simulation results is studied. On the basis of this, in Chapter 4, a new algorithm is presented with which the stability of falling films can be investigated in different situations. It is, to the best of our knowledge, the first time that a Jacobian free algorithm for global linear stability analysis of free boundary flows is described. Finally, in Chapter 5, the flow field of saturated, nonlinear surface waves is considered, and the influence of vortices on transport processes is elucidated. It is found that the presence or absence of a vortex inside the nonlinear waves has an important effect on the location of local extrema of mass transfer rate, whereas the occurrence of a localized backflow region does not entail a qualitative difference.

1.1. Liquid flow down an inclined plane

This work is concerned with the flow of a viscous, incompressible, Newtonian liquid down an inclined plane under the action of gravity in an atmosphere of surrounding gas. It is assumed that the wall is completely wetted, and that the liquid flows in the form of a thin, continuous film; see Figure 1.1 for a sketch of the assumed configuration. The domain occupied by the liquid is denoted by $\Omega_L(t)$, the domain occupied by the gas is denoted $\Omega_G(t)$, the interface separating both fluids is denoted by $\Sigma(t)$. The unit normal, pointing from the liquid into the gas, is called $\boldsymbol{n}_\Sigma$. The coordinate system is defined in such a way that the x-axis points in

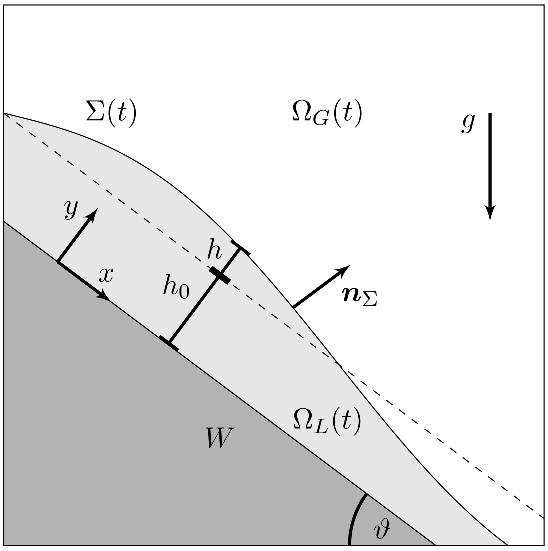

Figure 1.1.: Sketch of the geometrical configuration on a falling film.

streamwise direction, along the wall, and the y-axis in cross-streamwise direction, perpendicular to it. The wall is inclined by an angle ϑ to the direction of gravity.

In the experiment, a certain amount of water per unit time has to enter the flow domain, in order to sustain a continuous, non-rupturing flow. Under the assumption that all the water entering the domain runs down the plane in a laminar, wave free flow, and that the liquid is evenly spread across the wall, the flow rate determines a mean film thickness h_0. In wavy flows, the film is not flat, and we denote deviations from the mean film thickness by $h(t,x)$. With this notation, the interface can be written as

$$\Sigma(t) = \{(x,y) : y = h_0 + h(t,x)\}. \tag{1.1}$$

The bounding wall is denoted by

$$W = \{(x,y) : y = 0\}, \tag{1.2}$$

and the outer normal at a point $(x, h_0 + h(t,x) \in \Sigma$ is given by

$$\boldsymbol{n}_\Sigma = \frac{1}{\sqrt{1+h_x^2}} \begin{pmatrix} -h_x \\ 1 \end{pmatrix}. \tag{1.3}$$

We assume isothermal flow without phase change and take surface tension into account. No slip at the phase boundary is assumed. In this work, only low Mach numbers will be encountered in the gas phase. Therefore, it is justified to model the gas phase as an incompressible fluid.

In the experiment, it often happens that a chemical species is adsorbed at the interface separating liquid and gas. The evolution of the concentration of this

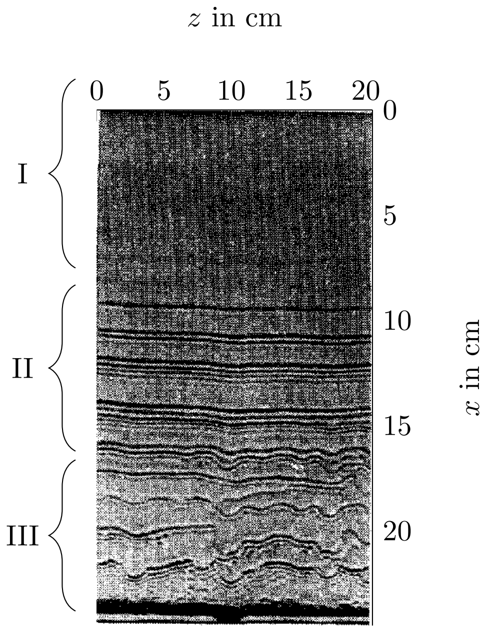

Figure 1.2.: Photographic image of a water film on a vertical plane at 23 °C, Re = 103.5. No controlled disturbances are applied. Reprinted from Nosoko et al. (1996), with permission from Elsevier.

species is governed by an advection-diffusion equation inside the moving interface. Local surface tension is affected by the presence of this chemical species in such a way that a high concentration corresponds to a small surface tension. A gradient in surface tension gives rise to so-called Marangoni stresses, which induce a fluid flow along the interface. The chemical species, therefore, acts as a *surfactant*, short for surface active agent. We will take Marangoni stresses into account, while neglecting the inert mass of the surfactant.

In Figure 1.2, a picture of a falling film is shown. Three different flow regions can be distinguished. In region I, near the inlet, the film is flat and waves are hardly visible. Since the flow field near the inlet is approximately stationary, the development of visible waves from the flat film is accessible to linear stability theory, and Chapters 2 and 4 are concerned with this region. Small perturbations grow exponentially as they are transported downstream.

In region II, the amplitude of the waves has saturated and nonlinear effects have inhibited their growth. It can be clearly observed that the primary instability is two-dimensional, which means that no noteworthy dependence of the nonlinear waves on the spanwise coordinate is apparent. Nonlinear, saturated waves develop into periodic flow patterns, that keep their periodicity and two-dimensionality for a significant downstream distance. The inner flow fields of these waves is considered in Chapters 3 and 5.

Periodic, nonlinear waves are susceptible two perturbations in spanwise direction, and ultimately break up into three-dimensional waves, as can be seen in region III.

These experimental observations may serve as a justification for two simplifications that are often made within this field of study and in the present thesis. On one hand, only the two-dimensional situation is considered. In many flow situations, the Squire Theorem (Squire, 1933) applies, which states that the critical Reynolds number for two-dimensional perturbations of parallel flow between fixed walls is lower than the critical Reynolds number for three-dimensional perturbations. Since this theorem was extended to the case of falling liquid films in Yih (1955), it can serve as another, more theoretical justification for the restriction to two-dimensional flows. Moreover, in Chapter 2 and in parts of Chapter 4, the flow is considered to be periodic in space.

1.2. Differential operators on the interface

In the present situation, the position of the interface is not a simple result of flow processes inside the bulk. Instead, due to capillary effects, the geometrical configuration of the free boundary has an important effect on the flow fields inside the bulk. In this work, a *sharp interface model* is employed, where the interface is regarded as a two-dimensional manifold in three-dimensional space. The first part of this section recalls the definition of some differential operators on hypersurfaces in $\mathbb{R}^3$. For a thorough introduction, see Dierkes et al. (2010), Chapter I, and Prüss and Simonett (2012). For a more concise overview, see the appendix in Bothe et al. (2005) where the proofs of all claims in this section can be found. In the second part, the cited formulas are applied to the considered parametrization of the interface by a height function.

1.2.1. Definition of differential operators

Notation

Let $\Sigma \subset \mathbb{R}^3$ be a two-dimensional, smooth manifold in $\mathbb{R}^3$ such that there is a domain $\Omega \subset \mathbb{R}^2$ and a C^∞-diffeomorphism

$$\boldsymbol{g} : \Omega \to \Sigma. \tag{1.4}$$

We assume that Σ is *regular*, i.e. that the Jacobian $D\boldsymbol{g}(\boldsymbol{x})$ has the maximal rank two for all $\boldsymbol{x} \in \Omega$. Let $\boldsymbol{p} \in \Sigma$. The *tangent space* $T_p\Sigma$ at point $\boldsymbol{p}$ is defined via

$$T_p\Sigma = \{\boldsymbol{\tau} \in \mathbb{R}^3 : \exists C^1 - \text{curve } \boldsymbol{\gamma} : (-\epsilon, \epsilon) \to \Sigma \text{ such that } \boldsymbol{\gamma}(0) = \boldsymbol{p}, \dot{\boldsymbol{\gamma}}(0) = \boldsymbol{\tau}\}. \tag{1.5}$$

With this definition, $T_p\Sigma = \operatorname{span}\{\partial_1\boldsymbol{g}(x), \partial_2\boldsymbol{g}(x))\}$ at $\boldsymbol{x} = \boldsymbol{g}^{-1}(\boldsymbol{p})$.

We define the Gramian Matrix

$$\boldsymbol{G} = \begin{pmatrix} < \partial_1\boldsymbol{g}, \partial_1\boldsymbol{g} > & < \partial_1\boldsymbol{g}, \partial_2\boldsymbol{g} > \\ < \partial_2\boldsymbol{g}, \partial_1\boldsymbol{g} > & < \partial_2\boldsymbol{g}, \partial_2\boldsymbol{g} > \end{pmatrix} =: \begin{pmatrix} g_{11} & g_{12} \\ g_{21} & g_{22} \end{pmatrix}, \tag{1.6}$$

where $< \boldsymbol{a}, \boldsymbol{b} >$ denotes the Euclidian scalar product in $\mathbb{R}^3$. The components of $\boldsymbol{G}^{-1}$ are denoted as

$$\boldsymbol{G}^{-1} = \begin{pmatrix} g^{11} & g^{12} \\ g^{21} & g^{22} \end{pmatrix}. \tag{1.7}$$

Directional derivative and surface gradient

Let $\phi : \Sigma \to \mathbb{R}$ be a scalar field on Σ. We say that $\phi \in C^k(\Sigma)$ if

$$f : \Omega \to \mathbb{R}, x \mapsto \phi(\boldsymbol{g}(x)) \tag{1.8}$$

is in $C^k(\Omega)$. If $\phi \in C^1(\Sigma)$, we define its directional derivative in direction $\boldsymbol{\tau}$ by

$$\frac{\partial \phi}{\partial \boldsymbol{\tau}}(\boldsymbol{p}) := \frac{\mathrm{d}}{\mathrm{d}t}\phi(\boldsymbol{\gamma}(t))|_{t=0} \text{ for a curve } \boldsymbol{\gamma} : (-\epsilon, \epsilon) \to \Sigma \text{ with } \boldsymbol{\gamma}(0) = \boldsymbol{p}, \dot{\boldsymbol{\gamma}}(0) = \boldsymbol{\tau}. \tag{1.9}$$

In order to actually compute a directional derivative, a surface gradient is defined in the following way:

$$\begin{aligned} \nabla_\Sigma \phi &= (g^{11}\partial_1 f + g^{12}\partial_2 f)\partial_1 \boldsymbol{g} + (g^{21}\partial_1 f + g^{22}\partial_2 f)\partial_2 \boldsymbol{g} \\ &=: f^{,1}\partial_1 \boldsymbol{g} + f^{,2}\partial_2 \boldsymbol{g}. \end{aligned} \tag{1.10}$$

It holds that

$$\frac{\partial \phi}{\partial \boldsymbol{\tau}} =< \nabla_\Sigma \phi, \boldsymbol{\tau} > . \tag{1.11}$$

Surface divergence

The surface divergence is defined as an analogue to the usual divergence in $\mathbb{R}^n$. Let $\boldsymbol{\phi} : \Sigma \to \mathbb{R}^3$. We define

$$\nabla_\Sigma \cdot \boldsymbol{\phi}(\boldsymbol{p}) = \sum_{i=1}^{2} < \frac{\partial \boldsymbol{\phi}}{\partial \boldsymbol{\tau}_i}(\boldsymbol{p}), \boldsymbol{\tau}_i(\boldsymbol{p}) > \tag{1.12}$$

where $(\boldsymbol{\tau}_1, \boldsymbol{\tau}_2)$ form an orthonormal basis of $T_p\Sigma$. It can be shown that $\nabla_\Sigma \cdot \boldsymbol{\phi}$ does not depend on the concrete choice of $(\boldsymbol{\tau}_1, \boldsymbol{\tau}_2)$, and even that

$$\nabla_\Sigma \cdot \boldsymbol{\phi}(\boldsymbol{p}) = \sum_{i=1}^{2} < \frac{\partial \boldsymbol{\phi}}{\partial \boldsymbol{\tau}_i}(\boldsymbol{p}), \boldsymbol{\tau}_i^*(\boldsymbol{p}) > \tag{1.13}$$

for any biorthogonal system $(\boldsymbol{\tau}_1, \boldsymbol{\tau}_2, \boldsymbol{\tau}_1^*, \boldsymbol{\tau}_2^*) \subset T_p\Sigma$, i.e. any two bases $\{\boldsymbol{\tau}_i\}, \{\boldsymbol{\tau}_i^*\}$ of $T_p\Sigma$ such that $< \boldsymbol{\tau}_i, \boldsymbol{\tau}_j^* >= \delta_{ij}$. Once a parametrization $\boldsymbol{g}$ of Σ is chosen, the most convenient biorthogonal system is often obtained by setting $\boldsymbol{\tau}_1 = \partial_1 \boldsymbol{g}, \boldsymbol{\tau}_2 = \partial_2 \boldsymbol{g}$. In this case, the dual basis is given as

$$\boldsymbol{\tau}_1^* = g^{11}\boldsymbol{\tau}_1 + g^{21}\boldsymbol{\tau}_2, \boldsymbol{\tau}_2^* = g^{12}\boldsymbol{\tau}_1 + g^{22}\boldsymbol{\tau}_2. \tag{1.14}$$

For concrete computations, we consider

$$\boldsymbol{f} : \Omega \to \mathbb{R}^3, \boldsymbol{x} \mapsto \boldsymbol{\phi}(\boldsymbol{g}(\boldsymbol{x})). \tag{1.15}$$

Computing the directional derivative in direction $\boldsymbol{\tau}_i$ is especially easy, namely

$$\frac{\partial \boldsymbol{\phi}}{\partial \boldsymbol{\tau}_i}(\boldsymbol{p}) = \partial_i \boldsymbol{f}(\boldsymbol{x}), \quad \boldsymbol{x} = \boldsymbol{g}^{-1}(\boldsymbol{p}). \tag{1.16}$$

Using this and inserting (1.14) into (1.13), we obtain

$$\nabla_\Sigma \cdot \boldsymbol{\phi}(\boldsymbol{p}) = \sum_{i,j=1}^{2} g^{ij} < \partial_j \boldsymbol{f}(\boldsymbol{x}), \partial_i \boldsymbol{g}(\boldsymbol{x}) >, \quad \boldsymbol{x} = \boldsymbol{g}^{-1}(\boldsymbol{p}). \tag{1.17}$$

For tangential vector fields, an easier formula for the surface divergence can be obtained:

$$\nabla_\Sigma \cdot \boldsymbol{\phi} = \frac{1}{\sqrt{\det \boldsymbol{G}}} \sum_{i=1}^{2} \partial_i (\sqrt{\det \boldsymbol{G}} f^i). \tag{1.18}$$

Surface Laplacian

Finally, we introduce the surface Laplacian, or Laplace-Beltrami operator, as

$$\Delta_\Sigma \phi := \nabla_\Sigma \cdot \nabla_\Sigma \phi. \tag{1.19}$$

Let $f(\boldsymbol{x}) = \phi(\boldsymbol{g}(\boldsymbol{x}))$. Since $\nabla_\Sigma \phi$ is always a tangential vector field, we can use (1.18) to derive

$$\Delta_\Sigma \phi(\boldsymbol{p}) = \frac{1}{\sqrt{\det G}} \sum_{i,j=1}^{2} \partial_i (\sqrt{\det G} g^{ij} \partial_j f(\boldsymbol{x})), \quad \boldsymbol{x} = \boldsymbol{g}^{-1}(\boldsymbol{p}). \tag{1.20}$$

1.2.2. Evaluation of the operators in the considered geometry

With the chosen coordinate system, the parametrization of the interface is

$$\boldsymbol{g} : x \mapsto \begin{pmatrix} x \\ 1 + h(x) \end{pmatrix}, \tag{1.21}$$

with

$$\partial_x \boldsymbol{g} = \begin{pmatrix} 1 \\ h_x \end{pmatrix}. \tag{1.22}$$

Since we consider the equations in two space dimensions, the Gramian matrix is simply

$$\boldsymbol{G} = g_{11} =< \partial_x \boldsymbol{g}, \partial_x \boldsymbol{g} >= 1 + h_x^2, \tag{1.23}$$

and

$$\boldsymbol{G}^{-1} = g^{11} = \frac{1}{1 + h_x^2}. \tag{1.24}$$

Surface gradient

Let $\phi : \Sigma \to \mathbb{R}$, and let $f : \mathbb{R} \to \mathbb{R}, x \mapsto \phi(\boldsymbol{g}(x))$. Then, by (1.10),

$$\nabla_\Sigma \phi(x,y) = g^{11}(x)\partial_x f(x)\partial_x \boldsymbol{g}(x) = \frac{f_x(x)}{1+h_x^2(x)}\begin{pmatrix}1\\ h_x(x)\end{pmatrix}. \tag{1.25}$$

Surface Laplacian

By (1.20),

$$\Delta_\Sigma \phi(x,y) = \frac{1}{\sqrt{1+h_x^2(x)}}\partial_x \frac{\partial_x f(x)}{\sqrt{1+h_x^2(x)}} = \frac{(1+h_x^2(x))f_{xx}(x) - h_x(x)h_{xx}(x)f_x(x)}{(1+h_x^2(x))^2}. \tag{1.26}$$

Lagrangian derivative

We would also like to evaluate the Langrangian derivative of ϕ in terms of f. Let $\boldsymbol{\psi} = (\psi^x, \psi^y)$ be the solution to the ODE

$$\dot{\boldsymbol{\psi}}(t) = \begin{pmatrix}u(t_0+t, \boldsymbol{\psi}(t_0+t))\\ v(t_0+t, \boldsymbol{\psi}(t_0+t))\end{pmatrix} \tag{1.27}$$

$$\boldsymbol{\psi}(t_0) = \begin{pmatrix}x_0\\ y_0\end{pmatrix}. \tag{1.28}$$

Then:

$$\begin{aligned}\frac{D\phi}{Dt}(t_0,x_0,y_0) &= \frac{\partial}{\partial t}\phi(t_0+t, \psi^x(t_0+t), \psi^y(t_0+t))|_{s=0}\\ &= \frac{\partial}{\partial t} f(t_0+t, \psi^x(t_0+t))|_{t=0}\\ &= \frac{\partial f}{\partial t}(t_0,x_0,y_0) + \frac{\partial f}{\partial x}\frac{\partial \psi^x}{\partial t}(t_0,x_0,y_0)\\ &= (\frac{\partial f}{\partial t} + u\frac{\partial f}{\partial x})(t_0,x_0,y_0).\end{aligned} \tag{1.29}$$

Surface divergence

Similarly, let $\boldsymbol{\phi} : \Sigma \to \mathbb{R}^2$, and let $\boldsymbol{f} = (f^{(1)}, f^{(2)})^\mathsf{T} : \mathbb{R} \to \mathbb{R}^2, x \mapsto \boldsymbol{\phi}(\boldsymbol{g}(x))$. Then, due to (1.17), we have

$$\nabla_\Sigma \cdot \boldsymbol{\phi}(x,y) = g^{11} < \partial_x \boldsymbol{f}(x), \boldsymbol{g}(x) >= \frac{f_x^{(1)}(x) + h_x(x)f_x^{(2)}(x)}{1+h_x^2(x)}. \tag{1.30}$$

1.3. Governing equations

We fix a no-slip boundary condition for the velocity field at the wall. Under these assumptions, conservation of mass and momentum yield the following system of governing equations:

$$\rho\left(\partial_t \boldsymbol{u} + \boldsymbol{u}\cdot\nabla\boldsymbol{u}\right) - \eta\Delta\boldsymbol{u} + \nabla p = \rho g \begin{pmatrix} \sin\vartheta \\ -\cos\vartheta \end{pmatrix}, \qquad y > 0, \boldsymbol{x} \notin \Sigma(t), \tag{1.31}$$

$$\nabla\cdot\boldsymbol{u} = 0, \qquad y > 0, \boldsymbol{x} \notin \Sigma(t), \tag{1.32}$$

$$\boldsymbol{u} = 0, \qquad \boldsymbol{x} \in W, \tag{1.33}$$

$$[\![\boldsymbol{u}]\!] = 0, V_\Sigma = \boldsymbol{u}\cdot\boldsymbol{n}_\Sigma, \qquad \boldsymbol{x} \in \Sigma(t), \tag{1.34}$$

$$[\![p\boldsymbol{I} - \eta(\nabla\boldsymbol{u} + \nabla\boldsymbol{u}^{\mathsf{T}})]\!]\boldsymbol{n}_\Sigma = \nabla_\Sigma\sigma(c) + \sigma(c)\kappa\boldsymbol{n}_\Sigma, \qquad \boldsymbol{x} \in \Sigma(t), \tag{1.35}$$

$$\frac{Dc}{Dt} + c\nabla_\Sigma\cdot\boldsymbol{u} = D\Delta_\Sigma c, \qquad \boldsymbol{x} \in \Sigma(t). \tag{1.36}$$

Here, $\boldsymbol{u}$ denotes the velocity field of the flow, p its pressure, and c the surface concentration of the surfactant. The normal velocity of the interface is denoted by V_Σ. Material parameters of the flow field are the density ρ and the dynamic viscosity η. These are phase dependent, that is $(\rho,\eta) = (\rho_L,\eta_L)$ for $0 < y < h_0 + h(t,x)$, and $(\rho,\eta) = (\rho_G,\eta_G)$ for $y > h_0 + h(t,x)$. The phase indicators L and G stand for "liquid" and "gas", respectively. Moreover, we have a concentration dependent surface tension $\sigma(c)$, and the diffusivity of the chemical species inside the interface is denoted as D.

Above, the notation

$$[\![\Psi]\!](t,\mathbf{x}) := \lim_{h\to 0+}\left(\Psi(t,\mathbf{x}+h\mathbf{n}_\Sigma) - \Psi(t,\mathbf{x}-h\mathbf{n}_\Sigma)\right) \text{ for } \mathbf{x}\in\Sigma(t) \tag{1.37}$$

stands for the jump of a physical quantity Ψ across the interface. The variable κ is defined as

$$\kappa = -\nabla_\Sigma\cdot\boldsymbol{n}_\Sigma. \tag{1.38}$$

It can be shown that this quantity is equal to the sum of the principal curvatures, or twice the mean curvature of differential geometry, see Dierkes et al. (2010), I.2.7.

This system is lacking boundary conditions for the gas phase and boundary conditions in streamwise direction. We will decide on these later. For more information on the equations for conservation of mass and momentum see Slattery (1999); Ishii and Hibiki (2011); for the modeling of the surfactant and the derivation of (1.36), see Bothe et al. (2005).

It will be assumed that there is a characteristic surfactant concentration c_0 and that the surface tension constant is an affine linear function in the surfactant concentration:

$$\sigma(c) = \sigma_0 - \gamma(c - c_0) \tag{1.39}$$

for some $\gamma\in\mathbb{R}$. Here, σ_0 is the characteristic surface tension concentration, which is assumed at the characteristic concentration c_0. Surface tension decreases with a higher surfactant concentration if and only if $\gamma \geq 0$. This condition will be assumed to hold true throughout this theses.

1.3.1. An alternative formulation of the kinematic boundary condition

Since phase change is neglected, a fluid particle that is in the interface at one point in time can never leave it (Wehausen and Laitone, 1960, Chapter B.3). With this, the height function assumption allows the derivation of an alternative formulation of the kinematic boundary condition (1.34). We introduce the scalar field

$$f(t,x,y) = h_0 + h(t,x) - y, \tag{1.40}$$

whose zero level set is, by definition, the interface. Due to (1.34), we then have

$$\frac{Df}{Dt} = 0 \tag{1.41}$$

for points in the interface. Applying the chain rule, we obtain

$$0 = \frac{Df}{Dt} = \partial_t f + \boldsymbol{u} \cdot \nabla f = h_t + u h_x - v. \tag{1.42}$$

1.3.2. One-phase flow down an inclined plane with a free surface

We will be interested in films of water in an atmosphere of air. Since water posseses a density that is about 1000 times and a dynamic viscosity that is about 50 times larger than that of air, it is often justified to consider a simpler model, in which shear stresses at the free boundary are neglected and a constant atmospheric pressure p_A is prescribed in the gas phase. In this case, we consider the one-phase Navier-Stokes equations with a free boundary which, in our setting, read

$$
\begin{aligned}
\rho\left(\partial_t \boldsymbol{u} + \boldsymbol{u}\cdot\nabla\boldsymbol{u}\right) - \eta\Delta\boldsymbol{u} + \nabla p &= \rho\begin{pmatrix}\sin\vartheta \\ -\cos\vartheta\end{pmatrix}, && \boldsymbol{x} \in \Omega(t), && (1.43)\\
\nabla\cdot\boldsymbol{u} &= 0, && \boldsymbol{x} \in \Omega(t), && (1.44)\\
\boldsymbol{u} &= 0, && \boldsymbol{x} \in W, && (1.45)\\
h_t + u h_x &= v, && \boldsymbol{x} \in \Sigma(t), && (1.46)\\
\left(p\boldsymbol{I} - \eta(\nabla\boldsymbol{u} + \nabla\boldsymbol{u}^{\mathsf{T}})\right)\boldsymbol{n}_\Sigma &= p_A\boldsymbol{n}_\Sigma - \nabla_\Sigma\sigma(c) - \sigma(c)\kappa\boldsymbol{n}_\Sigma, && \boldsymbol{x} \in \Sigma(t), && (1.47)\\
\frac{Dc}{Dt} + c\nabla_\Sigma\cdot\boldsymbol{u} &= D\Delta_\Sigma c, && \boldsymbol{x} \in \Sigma(t). && (1.48)
\end{aligned}
$$

Here, $\Omega(t) = \{(x,y) : 0 < y < h_0 + h(t,x)\}$, and $\Sigma(t) = \{(x,y) : y = h_0 + h(t,x)\}$. The material constants ρ and η are those of the liquid.

The Nusselt steady state solution

There is a one-dimensional manifold of steady state solutions to (1.43)-(1.48), which are characterized by a flat interface, a constant concentration of surfactant throughout the interface, a hydrostatic pressure that balances the gravitational force in y-direction, and a semi-parabolic velocity profile that creates so much viscous stress as to balance the gravitational force in x-direction. It reads

$$\begin{aligned}
\boldsymbol{u}_N(y) &= \frac{\rho g \sin\vartheta}{2\eta}\begin{pmatrix}2h_0 y - y^2\\ 0\end{pmatrix}, && (1.49)\\
p_N(y) &= p_A - \rho g (y - h_0)\cos\vartheta, && (1.50)\\
h_N &= 0, && (1.51)\\
c_N &= \text{const.} \ \geq 0, && (1.52)\\
\sigma_N &= \sigma(c_N). && (1.53)
\end{aligned}$$

Here, the mean concentration on the flat film, c_N, is an arbitrary, non-negative constant. We call the velocity field $\boldsymbol{u}_N$ the *Nusselt profile*, after Nusselt (1916).

Dimensionless Numbers

Several dimensionless numbers are used to describe the flow physics of a falling film. The *free surface velocity* of the Nusselt profile

$$u_0 = \frac{g \sin\vartheta h_0^2}{2\nu_L}, \tag{1.54}$$

where $\nu_L = \frac{\eta_L}{\rho_L}$ is the kinematic viscosity of the liquid, is chosen as a characteristic velocity. Choosing the mean film thickness as a characteristic length, we define a Reynolds number

$$\mathrm{Re} = \frac{u_0 h_0}{\nu_L} = \frac{3}{2}\frac{q_0}{\nu_L}, \tag{1.55}$$

where q_0 is the time averaged volume liquid flow rate per unit width at the inlet. The Reynolds number is a dimensionless measure of the relative importance of inertia forces to viscous forces. In many publications, the *mean velocity* of the Nusselt profile,

$$\bar{u} = \frac{1}{h_0}\int_0^{h_0} u_N(y)\mathrm{d}y = \frac{g h_0^2}{3\nu_L} = \frac{2}{3}u_0, \tag{1.56}$$

is chosen as a characteristic velocity instead. We denote the Reynolds number that is defined by choosing $\overline{u}$ as a characteristic velocity by $\overline{\mathrm{Re}}$, and note that $\overline{\mathrm{Re}} = \frac{2}{3}\,\mathrm{Re}$. For a given liquid, there is a one-to-one correspondence between Reynolds number and mean film height:

$$h_0 = \sqrt[3]{\frac{2\nu_L^2\,\mathrm{Re}}{g \sin\vartheta}}. \tag{1.57}$$

The ratio of inertial to gravitational forces is given by the Froude number

$$\mathrm{Fr} = \frac{u_0}{(g h_0)^{1/2}}. \tag{1.58}$$

A dimensionless group consisting only of material parameters is the Kapitza number:

$$\mathrm{Ka} = \frac{\sigma_0}{\rho_L \nu_L^{4/3} g^{1/3}}. \tag{1.59}$$

Alternatively, sometimes the Film number is used:

$$\mathrm{Fi} = \mathrm{Ka}^3\,. \tag{1.60}$$

Finally, the ratio of inertia to surface tension is given by the Weber number

$$\mathrm{We} := \frac{3^{1/3} Ka}{Re^{5/3}}, \tag{1.61}$$

and the ratio of viscous forces to surface tension is given by the capillary number

$$\mathrm{Ca} = \frac{\eta_L u_0}{\sigma_0}. \tag{1.62}$$

Additional characteristic numbers concerning the influence of a surfactant are the Peclet number

$$\mathrm{Pe} = \frac{h_0 u_0}{D} \tag{1.63}$$

and the Marangoni number

$$\mathrm{Ma} = \frac{\gamma c_0}{\sigma_0}. \tag{1.64}$$

2. The resolvent problem for periodic flow down an inclined plane under presence of an insoluble surfactant

2.1. Introduction

A lot of work has been devoted to the analytical study of film flows down an inclined plane. In Teramoto (1985), the Navier-Stokes equations with a free boundary were considered, while surface tension was neglected. Local in time solutions were constructed. In Teramoto (1992), surface tension was taken into account. It was shown that solutions on arbitrarily long time intervals can exist, if the initial perturbation is sufficiently small. The smallness condition on the initial data depends on the desired existence interval. Under the assumption of a small Reynolds number and a small inclination angle, the existence of global in time solutions was shown in Nishida et al. (1993). In Nishida et al. (2005), a Hopf bifurcation theorem was proved. Periodic flow of a certain maximal wavelength was considered, and it was shown that there exists a critical Reynolds number for which a pair of complex conjugated eigenvalues crosses the imaginary axis, implying the existence of time periodic solutions. A nonlinear stability result is achieved in Padula (2012). In the latter result, embedding constants appear whose value is not explicitly given. Finally, in Nishida et al. (2013), the resolvent problem for flow down a vertical plane is considered.

Several publications are concerned with the problem of flow under the presence of a surfactant. In Bothe et al. (2005), the case of a surfactant that is soluble in one phase and can adsorb at the interface is considered. Local in time well-posedness of the system is shown for the model geometry of a deformed half space. In Bothe and Prüss (2010), equilibrium solutions that consist of finitely many droplets or bubbles under the absence of gravity are considered. Linear stability is shown for these equilibria. Local well-posedness of the system of governing equations is proved in Bothe et al. (2012) for more general geometries than a deformed half-space.

The aim of the present chapter is the derivation of a linear stability condition for flow under the presence of an insoluble surfactant down an inclined plane under the action of gravity. In Section 2.2, the system of governing equations is rewritten in dimensionless form, and then linearized around the steady state. The resulting system describes the time evolution of perturbations to the equilibrium solution in linear approximation. Since partial differential equations on non-cylindrical space-time domains are difficult to solve, a transformation due to Bock (1977) is applied, which yields an equivalent system on a reference domain that is not dependent on time. The linearized system is then rewritten as an evolution equation. The operator appearing in this equation is called the *linearized stability operator*.

Assuming periodic flow conditions in space, in Section 2.3, the corresponding resolvent problem is solved by means of a Fourier series approach in an L^2-setting. The proof is based on Nishida et al. (2013), and extends the resolvent construction presented there to account for an insoluble surfactant. It is shown that the linearized stability operator is the generator of an analytic semigroup, and that the resolvent operators are compact.

Based on the compactness of the resolvents, in Section 2.4 a sufficient condition under which the spectrum of the linearized stability operator is entirely contained in the left half plane is derived. The proof is a variation of the free energy method of Padula and Solonnikov (2000). Since this method is applied on a simple, time-independent domain, sharp constants for all inequalities applied in the derivation of the stability condition can be given, yielding a clear condition under which the flow is stable. The stability criterion states that for a given wavelength L, there are sufficiently small Reynolds, Capillary and Péclet numbers such that the flow is stable to perturbations of wavelength $L' \leq L$. No smallness of the inclination angle is required. The only condition on the Marangoni number is that it is positive, which can be assumed to be always true. The condition on Ca is physically reasonable, since a small capillary number corresponds to high surface tension which acts stabilizing on a falling film. For a physical reason why that is the case, see the discussion of local pressure distribution in Section 5.5.1. The condition becomes milder for small L. This is in accordance with the numerical results in Section 4.5.1.

An explicit spectral bound of $-1/2$ is given. Since, for analytic semigroups, the spectral bound of the generator coincides with the growth bounds of the semigroup (Engel and Nagel, 2000, Theorem V.1.10), this implies that, under the stated assumptions, perturbations to the steady state show an asymptotic decay rate of $\exp(-\frac{1}{2}t)$. This result is also new for flows without surfactant, in which case it holds without the assumption on the Péclet number.

2.2. Derivation of the resolvent problem

2.2.1. Nondimensionalization

We want to write the system of governing equations in dimensionless form. In order to do so, we choose characteristic quantities on the basis of the steady state solution. In accordance with Section 1.3.2, we set h_0 as a characteristic length scale, take the free surface velocity u_0 of the Nusselt profile as a characteristic velocity, and choose $t_0 = \frac{h_0}{u_0}$ as a characteristic time. For characteristic pressure, we set

$$p_0 = \frac{\tan\vartheta}{2}(p_N(0) - p_A) = \frac{\rho g h_0 \sin\vartheta}{2} = \frac{\eta u_0}{h_0}. \tag{2.1}$$

We choose the mean concentration on the flat film as a characteristic surfactant concentration, i.e. $c_0 = c_N$, and the characteristic surface tension constant in agreement with that, i.e. $\sigma_0 = \sigma(c_0)$. We introduce dimensionless variables as $\boldsymbol{x} = h_0\tilde{\boldsymbol{x}}, t = t_0\tilde{t}, \boldsymbol{u} = u_0\tilde{\boldsymbol{u}}, p = p_0\tilde{p}, h = h_0\tilde{h}, \sigma = \sigma_0\tilde{\sigma}$, and $c = c_0\tilde{c}$.

Considering equations (1.39) and (1.64), it holds that:

$$\begin{align}
\sigma(c) &= \sigma_0\left(1 - \frac{\gamma c_0}{\sigma_0}(\tilde{c} - 1)\right) \tag{2.2}\\
&= \sigma_0\left(1 - \mathrm{Ma}(\tilde{c} - 1)\right) \tag{2.3}\\
&= \sigma_0\tilde{\sigma}(\tilde{c}). \tag{2.4}
\end{align}$$

Dropping tildes, the system of governing equations can be written as

$$\boldsymbol{u}_t + \boldsymbol{u}\cdot\nabla\boldsymbol{u} - \frac{1}{\mathrm{Re}}\Delta\boldsymbol{u} + \frac{1}{\mathrm{Re}}\nabla p = \frac{1}{\mathrm{Fr}^2}\begin{pmatrix}\sin\vartheta\\ -\cos\vartheta\end{pmatrix}, \qquad \boldsymbol{x} \in \Omega(t), \tag{2.5}$$

$$\nabla\cdot\boldsymbol{u} = 0, \qquad \boldsymbol{x} \in \Omega(t), \tag{2.6}$$

$$\boldsymbol{u} = 0, \qquad \boldsymbol{x} \in W, \tag{2.7}$$

$$h_t + uh_x = v, \qquad \boldsymbol{x} \in \Sigma(t), \tag{2.8}$$

$$\left(p\boldsymbol{I} - (\nabla\boldsymbol{u} + \nabla\boldsymbol{u}^{\mathsf{T}})\right)\boldsymbol{n}_\Sigma = \frac{p_A}{p_0}\boldsymbol{n}_\Sigma + \frac{\mathrm{Ma}}{\mathrm{Ca}}\nabla_\Sigma c - \frac{1}{\mathrm{Ca}}\sigma(c)\kappa\boldsymbol{n}_\Sigma, \quad \boldsymbol{x} \in \Sigma(t), \tag{2.9}$$

$$\frac{Dc}{Dt} + c\nabla_\Sigma\cdot\boldsymbol{u} = \frac{1}{\mathrm{Pe}}\Delta_\Sigma c, \qquad \boldsymbol{x} \in \Sigma(t), \tag{2.10}$$

where – in dimensionless coordinates – $\Omega(t) = \{(x,y) : 0 < y < 1 + h(t,x)\}$, and $\Sigma(t) = \{(x,y) : y = 1 + h(t,x)\}$. In dimensionless variables, the steady state solution reads

$$\begin{align}
\boldsymbol{u}_N(y) &= \begin{pmatrix}2y - y^2\\ 0\end{pmatrix}, \tag{2.11}\\
p_N(y) &= \frac{p_A}{p_0} + 2\cot\vartheta(1 - y), \tag{2.12}\\
h_N &= 0, \tag{2.13}\\
c_N &= 1, \tag{2.14}\\
\sigma_N &= 1. \tag{2.15}
\end{align}$$

2.2.2. Evaluation of the surface differential operators

In order to handle the system of governing equations analytically, we have to explicitly evaluate the surface differential operators in (2.5)-(2.10) in terms of the height function. Applying (1.30) to (1.3), we obtain

$$\kappa(x) = -\nabla_\Sigma \cdot \boldsymbol{n}_\Sigma(x) = \frac{h_{xx}(x)}{(1 + h_x^2(x))^{\frac{3}{2}}}. \tag{2.16}$$

With this, and with (1.25), we can write the stress boundary condition as

$$\begin{aligned} \left(p\boldsymbol{I} - (\nabla \boldsymbol{u} + \nabla \boldsymbol{u}^\mathsf{T})\right) \begin{pmatrix} -h_x \\ 1 \end{pmatrix} =& \frac{p_A}{p_0} \begin{pmatrix} -h_x \\ 1 \end{pmatrix} + \frac{\mathrm{Ma}}{\mathrm{Ca}} \frac{c_x}{\sqrt{1+h_x^2}} \begin{pmatrix} 1 \\ h_x \end{pmatrix} \\ &- \frac{1}{\mathrm{Ca}} \frac{\sigma(c) h_{xx}}{(1+h_x^2)^{\frac{3}{2}}} \begin{pmatrix} -h_x \\ 1 \end{pmatrix}, \boldsymbol{x} \in \Sigma(t). \end{aligned} \tag{2.17}$$

Applying (1.26), (1.29) and (1.30) on the surfactant transport equation, we get

$$c_t + uc_x + c\frac{u_x + h_x v_x}{1 + h_x^2} = \frac{1}{\mathrm{Pe}} \frac{(1 + h_x^2)c_{xx} - h_x h_{xx} c_x}{(1 + h_x^2)^2}, \boldsymbol{x} \in \Sigma(t). \tag{2.18}$$

2.2.3. Equations for perturbations to the steady state

We consider a solution of the system of equations above as the sum of the steady state and a perturbation. We write

$$\boldsymbol{u} = \boldsymbol{u}_N + \boldsymbol{u}', \tag{2.19}$$

$$p = p_N + p', \tag{2.20}$$

$$c = c_N + c' = 1 + c'. \tag{2.21}$$

We insert these into equations (2.5)-(2.10) and drop primes. Moreover, the stress boundary condition is split into its normal and tangential part, by multiplication with $\boldsymbol{n}_\Sigma$ and $\boldsymbol{\tau}_\Sigma$, respectively. Dropping primes, the system of equations governing the evolution of perturbations to the steady state reads

$$\boldsymbol{u}_t + \boldsymbol{u}\cdot\nabla\boldsymbol{u} + \boldsymbol{u}_N\cdot\nabla\boldsymbol{u} + \boldsymbol{u}\cdot\nabla\boldsymbol{u}_N - \frac{1}{\mathrm{Re}}\Delta\boldsymbol{u} + \frac{1}{\mathrm{Re}}\nabla p = 0, \quad \boldsymbol{x}\in\Omega(t), \tag{2.22}$$

$$\nabla\cdot\boldsymbol{u} = 0, \quad \boldsymbol{x}\in\Omega(t), \tag{2.23}$$

$$\boldsymbol{u} = 0, \quad \boldsymbol{x}\in W. \tag{2.24}$$

$$h_t + (u + 1 - h^2)h_x = v, \quad \boldsymbol{x}\in\Sigma(t), \tag{2.25}$$

$$\begin{aligned}(1+h_x^2)(p - 2h\cot\vartheta) - 2v_y - 2h_x(2h - u_y - v_x + h_x u_x)& \\ +\frac{1}{\mathrm{Ca}}\frac{(1-\mathrm{Ma}\,c)h_{xx}}{\sqrt{1+h_x^2}} &= 0,\end{aligned} \quad \boldsymbol{x}\in\Sigma(t) \tag{2.26}$$

$$(1-h_x^2)(-u_y - v_x + 2h) + 2h_x(u_x - v_y) - \frac{\mathrm{Ma}}{\mathrm{Ca}}\sqrt{1+h_x^2}c_x = 0, \quad \boldsymbol{x}\in\Sigma(t) \tag{2.27}$$

$$\begin{aligned}c_t + (u+1-h^2)c_x + (1+c)\frac{u_x + h_x v_x}{1+h_x^2}& \\ -\frac{1}{\mathrm{Pe}}\frac{(1+h_x^2)c_{xx} - h_x h_{xx} c_x}{(1+h_x^2)^2} &= 0.\end{aligned} \quad \boldsymbol{x}\in\Sigma(t) \tag{2.28}$$

We will consider the equations above on a periodic domain $x\in(0,L)$, and only allow perturbations that keep the overall amount of surfactant in the system constant, i.e. $0 = \int_0^L c\sqrt{1+h_x^2}\mathrm{d}x$. Surfactant mass stays conserved, as can be checked by calculating

$$\begin{aligned}\frac{\mathrm{d}}{\mathrm{d}t}\int_0^L c\sqrt{1+h_x^2}\mathrm{d}x &= \int_0^L \Big(c_t\sqrt{1+h_x^2} + \frac{c h_x h_{xt}}{\sqrt{1+h_x^2}}\Big)\mathrm{d}x \\ &= \int_0^L \Big(-u c_x\sqrt{1+h_x^2} - \frac{c u_x + c h_x v_x}{\sqrt{1+h_x^2}} + \frac{c h_x h_{xt}}{\sqrt{1+h_x^2}}\Big)\mathrm{d}x \\ &\quad + \frac{1}{\mathrm{Pe}}\int_0^L \frac{(1+h_x^2)c_{xx} - h_x h_{xx} c_x}{(1+h_x^2)^{\frac{3}{2}}}\mathrm{d}x \\ &= \int_0^L u c\sqrt{1+h_x^2}\mathrm{d}x + \frac{1}{\mathrm{Pe}}\int_0^L \partial_x\Big(\frac{c_x}{\sqrt{1+h_x^2}}\Big)\mathrm{d}x = 0\end{aligned} \tag{2.29}$$

where we have used (2.28) and the time derivative of (2.25).

2.2.4. Transformation to a fixed reference domain and linearization

The above system of governing equations is still defined on a time-dependent domain. In order to efficiently solve this system of equations, we follow Nishida et al. (2005) and transform them to a time-independent reference domain in a way that maintains the divergence condition. In the context of the Navier-Stokes equations, this method has been used for the first time in Bock (1977), and was popularized by Beale (1981, 1984). Details on this transformation are given in Appendix A. The transformation introduces heavy nonlinearities.

From now on, we consider periodic flow. We denote by $\mathbb{T}_L = \mathbb{R}/L\mathbb{Z}$ the torus of length L, and set $\Omega = \mathbb{T}_L \times (0,1)$. The boundaries of Ω are denoted by $W = \partial\Omega \cap \{y = 0\}$ and $\Sigma = \partial\Omega \cap \{y = 1\}$, respectively.

Gathering nonlinear terms on the right hand side, the system of governing equations on the fixed domain can be written as

$$\begin{aligned}
\boldsymbol{u}_t - \frac{1}{\mathrm{Re}}\Delta\boldsymbol{u} + \boldsymbol{u}_N \cdot \nabla\boldsymbol{u} + \boldsymbol{u} \cdot \nabla\boldsymbol{u}_N + \frac{1}{\mathrm{Re}}\nabla p &= \boldsymbol{F}_u, && \boldsymbol{x} \in \Omega, && (2.30)\\
\nabla \cdot \boldsymbol{u} &= 0, && \boldsymbol{x} \in \Omega, && (2.31)\\
\boldsymbol{u} &= 0, && \boldsymbol{x} \in W, && (2.32)\\
h_t + h_x - v &= F_h, && \boldsymbol{x} \in \Sigma, && (2.33)\\
p - 2v_y - 2\cot\vartheta h + \frac{h_{xx}}{\mathrm{Ca}} &= F_n, && \boldsymbol{x} \in \Sigma, && (2.34)\\
u_y + v_x - 2h + \frac{\mathrm{Ma}}{\mathrm{Ca}}c_x &= F_t, && \boldsymbol{x} \in \Sigma, && (2.35)\\
c_t + c_x + u_x - \frac{1}{\mathrm{Pe}}c_{xx} &= F_c, && \boldsymbol{x} \in \Sigma. && (2.36)
\end{aligned}$$

Let $\phi(x) = \sum_{k\in\mathbb{Z}} \phi^{(k)} e^{iklx}$, $l = \frac{2\pi}{L}$ be a function with periodicity L. We define the following Sobolev norm:

$$\|\phi\|^2_{H^s(\mathbb{T}_L)} = \sum_{k\in\mathbb{Z}} |k|^{2s} \left|\phi^{(k)}\right|^2, \quad s \geq 0. \tag{2.37}$$

We define $H^s(\mathbb{T}_L)$ as the space of all functions ϕ for which $\|\phi\|_{H^s(\mathbb{T}_L)} < \infty$. For $s \in \mathbb{N}$, this space coincides with the usual Sobolev space of functions whose distributional derivatives up to order s are L^2-functions. The space of Sobolev functions with vanishing mean value is defined as

$$H^s_0(\mathbb{T}_L) = \left\{\phi \in H^s(\mathbb{T}_L) : \int_{\mathbb{T}_L} \phi(x)\mathrm{d}x = 0\right\}. \tag{2.38}$$

Similarly, let $H^s(\Omega)$ denote the Sobolev space of functions on Ω that are periodic in x with periodicity L. Whenever the domain is clear, the norm on $H^s(\Omega)$ or $H^s(\mathbb{T}_L)$ will be denoted by $\|\cdot\|_s$.

For the treatment of the time-dependent problem, we introduce

$$K^s(\Omega \times \mathbb{R}_+) = H^0(\mathbb{R}_+; H^s(\Omega)) \cap H^{s/2}(\mathbb{R}_+; H^0(\Omega)) \tag{2.39}$$

and

$$K^s_0(\mathbb{T}_L \times \mathbb{R}_+) = H^0(\mathbb{R}_+; H^s_0(\mathbb{T}_L)) \cap H^{s/2}(\mathbb{R}_+; H^0_0(\mathbb{T}_L)). \tag{2.40}$$

The final formulation of the problem under consideration now reads as

$$\begin{aligned}
\boldsymbol{u}_t - \frac{1}{\mathrm{Re}}\Delta\boldsymbol{u} + \boldsymbol{u}_N\cdot\nabla\boldsymbol{u} + \boldsymbol{u}\cdot\nabla\boldsymbol{u}_N + \frac{1}{\mathrm{Re}}\nabla p &= \boldsymbol{b}_u, && \boldsymbol{x}\in\Omega, && (2.41)\\
\nabla\cdot\boldsymbol{u} &= 0, && \boldsymbol{x}\in\Omega, && (2.42)\\
\boldsymbol{u} &= 0, && \boldsymbol{x}\in W, && (2.43)\\
h_t + h_x - v &= b_h, && \boldsymbol{x}\in\Sigma && (2.44)\\
p - 2v_y - 2\cot\vartheta h + \frac{h_{xx}}{\mathrm{Ca}} &= b_n, && \boldsymbol{x}\in\Sigma, && (2.45)\\
u_y + v_x - 2h + \frac{\mathrm{Ma}}{\mathrm{Ca}}c_x &= b_t, && \boldsymbol{x}\in\Sigma, && (2.46)\\
c_t + c_x + u_x - \frac{1}{\mathrm{Pe}}c_{xx} &= b_c, && \boldsymbol{x}\in\Sigma, && (2.47)
\end{aligned}$$

where the right-hand sides are assumed to be given inhomogeneities.

2.2.5. Formulation as an evolution equation

The above system of equations is not in the form of an evolution equation, since there is no time-derivative for the pressure, and inhomogeneities appear in the stress boundary conditions.

The inhomogeneity in the tangential stress boundary condition

In order to write the system of equations (2.41)–(2.47) as an evolution equation in some Banach space, it is first shown how the problem can be reduced to the case $b_t = 0$. In order to do so, the following Lemma is needed:

Lemma 1. *Let* $s \geq 2$, *and let* $b_t \in K_0^{s-3/2}(\mathbb{T}_L\times\mathbb{R}_+)$ *be given. Then there exists a* $\boldsymbol{u}^{(1)} = (u^{(1)}, v^{(1)}) \in K_0^s(\Omega\times\mathbb{R}_+)$ *such that*

$$\begin{aligned}
\boldsymbol{u}^{(1)} &= 0 \text{ on } W,\\
\nabla\cdot\boldsymbol{u}^{(1)} &= 0 \text{ in } \Omega,\\
v^{(1)}|_\Sigma &= 0,\\
u_y^{(1)} + v_x^{(1)} &= b_t \text{ on } \Sigma
\end{aligned}$$

and there is a $C > 0$ *such that*

$$\|\boldsymbol{u}^{(1)}\|_{K_0^s(\Omega\times\mathbb{R}_+)} \leq C\|b_t\|_{K_0^{s-3/2}(\mathbb{T}_L\times\mathbb{R}_+)}.$$

The proof is given in Beale (1984, Page 321). Setting $\boldsymbol{u} = \boldsymbol{u}^{(1)} + \boldsymbol{u}^{(2)}$, the new unknowns $\boldsymbol{u}^{(2)}, p, h, c$ satisfy (2.41)-(2.47) with $b_t = 0$,

The inhomogeneity in the normal stress boundary condition

For the reduction of the inhomogeneity in the normal component of the stress boundary condition, the space

$$G^0(\Omega) = \{\nabla\phi : \phi \in H^1(\Omega), \phi = 0 \text{ on } \Sigma\} \tag{2.48}$$

is introduced, which is a closed subspace of $H^0(\Omega)$ due to the condition $\phi = 0$ on Σ and Poincaré's inequality. We will consider the projection

$$\mathrm{P}^0 : H^0(\Omega) \to (G^0(\Omega))^\perp \tag{2.49}$$

onto the orthogonal complement, i.e.

$$H^0(\Omega) = \mathrm{P}^0\, H^0(\Omega) \oplus G^0(\Omega). \tag{2.50}$$

The following Lemma holds:

Lemma 2. *Let* $s \geq 0$*. Then*

i) $\mathrm{P}^0 : H^s(\Omega) \to H^s(\Omega)$ *is a bounded linear operator.*

ii) Let $\phi \in H^1(\Omega)$*. Then* $\mathrm{P}^0(\nabla\phi) = \nabla\psi$*, where*

$$\begin{aligned} \psi &= \phi \textit{ on } \Sigma, \\ \partial_y \psi &= 0 \textit{ on } W, \\ \Delta\psi &= 0 \textit{ in } \Omega. \end{aligned}$$

iii) Let $\boldsymbol{u} = (u, v) \in \mathrm{P}^0\, H^1(\Omega)$*. Then*

$$\begin{aligned} \nabla \cdot \boldsymbol{u} &= 0 \textit{ in } \Omega, \\ v &= 0 \textit{ on } W. \end{aligned}$$

The proof is given in Beale (1981, Lemma 3.1).

Applying P^0 to equation (2.41) yields

$$\boldsymbol{u}_t - \frac{1}{\mathrm{Re}}\mathrm{P}^0\,\Delta\boldsymbol{u} + \mathrm{P}^0(\boldsymbol{u}_N \cdot \nabla\boldsymbol{u} + \boldsymbol{u} \cdot \nabla\boldsymbol{u}_N) + \frac{1}{\mathrm{Re}}\mathrm{P}^0\,\nabla p = \mathrm{P}^0\,\boldsymbol{b}_u. \tag{2.51}$$

Due to Lemma 2 and equation (2.45), we have

$$\mathrm{P}^0\,\nabla p = \nabla p_1 + \nabla p_2 + \nabla p_3, \tag{2.52}$$

where

$$\Delta p_i = 0 \text{ in } \Omega, \tag{2.53}$$
$$\partial_y p_i = 0 \text{ on } W, \tag{2.54}$$
$$p_1 = 2v_y \text{ on } \Sigma, \tag{2.55}$$
$$p_2 = 2h\cot\vartheta - \frac{1}{\mathrm{Ca}}h_{xx} \text{ on } \Sigma, \tag{2.56}$$
$$p_3 = b_n \text{ on } \Sigma, \tag{2.57}$$

and we can write this as

$$\boldsymbol{u}_t - \frac{1}{\mathrm{Re}} \mathrm{P}^0 \Delta \boldsymbol{u} + \mathrm{P}^0(\boldsymbol{u}_N \cdot \nabla \boldsymbol{u} + \boldsymbol{u} \cdot \nabla \boldsymbol{u}_N) + \frac{1}{\mathrm{Re}} \nabla p_1 + \frac{1}{\mathrm{Re}} \nabla p_2 + \frac{1}{\mathrm{Re}} \nabla p_3 = \mathrm{P}^0 \boldsymbol{b}_u. \tag{2.58}$$

Collecting the terms depending on $\boldsymbol{u}$, we define the operator

$$A\boldsymbol{u} = -\frac{1}{\mathrm{Re}} \mathrm{P}^0 \Delta \boldsymbol{u} + \mathrm{P}^0(\boldsymbol{u}_N \cdot \nabla \boldsymbol{u} + \boldsymbol{u} \cdot \nabla \boldsymbol{u}_N) + \frac{1}{\mathrm{Re}} \nabla p_1. \tag{2.59}$$

We define the operators $Q : \boldsymbol{u} \mapsto u|_\Sigma$ and $R : \boldsymbol{u} \mapsto v|_\Sigma$ as mappings from $\mathrm{P}^0 H^1(\Omega) \to H^0(\mathbb{T}_L)$.

Considering R as a map from $\mathrm{P}^0 H^1(\Omega) \to H^{1/2}(\mathbb{T}_L)$, the adjoint operator R^* is given by the map $R^*\phi = \nabla\psi$, where ψ is the solution of the problem

$$\Delta\psi = 0 \text{ in } \Omega, \tag{2.60}$$

$$\psi = \phi \text{ on } \Sigma, \tag{2.61}$$

$$\partial_y \psi = 0 \text{ on } W. \tag{2.62}$$

This can be seen by calculating

$$\begin{aligned} < \boldsymbol{u}, R^*\phi >_{H^0(\Omega)} &=< \boldsymbol{u}, \nabla\psi >_{H^0(\Omega)} = -\int_\Omega (\nabla \cdot \boldsymbol{u})\psi \mathrm{d}V + \int_\Sigma v\psi \mathrm{d}x + \int_W v\psi \mathrm{d}x \\ &= \int_\Sigma v\phi \mathrm{d}x =< R\boldsymbol{u}, \phi >_{H^0(\Sigma)}, \end{aligned}$$

since $\nabla \cdot \boldsymbol{u} = v|_W = 0$ due to Lemma 2. Conditions (2.60) and (2.62) are necessary since $R^*\phi \in \mathrm{P}^0 H^1(\Omega)$. With these notations, equations (2.41), (2.44) and (2.47) can be written as

$$\partial_t \boldsymbol{u} + A\boldsymbol{u} + \frac{1}{\mathrm{Re}} R^*(2\cot\vartheta - \frac{1}{\mathrm{Ca}}\partial_{xx})h = \mathrm{P}^0 \boldsymbol{b}_u - \frac{1}{\mathrm{Re}} R^* b_n, \tag{2.63}$$

$$\partial_t h + \partial_x h - R\boldsymbol{u} = b_h, \tag{2.64}$$

$$\partial_t c + (\partial_x - \frac{1}{\mathrm{Pe}}\partial_{xx})c + \partial_x Q\boldsymbol{u} = b_c. \tag{2.65}$$

Defining the operator matrix $\boldsymbol{G}$ as

$$\boldsymbol{G}\begin{pmatrix}\boldsymbol{u}\\ h\\ c\end{pmatrix} = \begin{pmatrix} -A & -\frac{1}{\mathrm{Re}}R^*(2\cot\vartheta - \frac{1}{\mathrm{Ca}}\partial_{xx}) & 0 \\ R & -\partial_x & 0 \\ -\partial_x Q & 0 & -\partial_x + \frac{1}{\mathrm{Pe}}\partial_{xx} \end{pmatrix} \begin{pmatrix}\boldsymbol{u}\\ h\\ c\end{pmatrix}, \tag{2.66}$$

this can be written as

$$\frac{\mathrm{d}}{\mathrm{d}t}\begin{pmatrix}\boldsymbol{u}\\ h\\ c\end{pmatrix} - \boldsymbol{G}\begin{pmatrix}\boldsymbol{u}\\ h\\ c\end{pmatrix} = \begin{pmatrix}\mathrm{P}^0 \boldsymbol{b}_u - \frac{1}{\mathrm{Re}}R^* b_n \\ b_h \\ b_c\end{pmatrix}. \tag{2.67}$$

The domain of the operator $\boldsymbol{G}$ is defined as

$$\begin{aligned} \mathcal{D}(\boldsymbol{G}) = \{(\boldsymbol{u}, h, c) \in \mathrm{P}^0 H^0(\Omega) \times H_0^{3/2}(\mathbb{T}_L) \times H_0^0(\mathbb{T}_L) :& \\ \boldsymbol{u} \in H^2(\Omega), \boldsymbol{u} = 0 \text{ on } W, h \in H_0^{5/2}(\mathbb{T}_L), c \in H_0^2(\mathbb{T}_L),& \\ u_y + v_x - 2h - \frac{\mathrm{Ma}}{\mathrm{Ca}}c_x = 0\}.& \end{aligned} \tag{2.68}$$

2.3. Construction of the resolvent

In this section, the construction of resolvent operators for the linearized stability operator $\boldsymbol{G}$ is discussed. Up to Section 2.3.4, the proof follows closely the resolvent construction in Nishida et al. (2013), with the exception that, due to the surfactant, an additional inhomogeneity in the tangential stress boundary condition must be considered.

2.3.1. Auxiliary problem A

In order to construct resolvent operators for $\boldsymbol{G}$, we consider a series of auxiliary problems. We start with the following system of equations:

$$\lambda \boldsymbol{u} - \frac{1}{\mathrm{Re}}\Delta \boldsymbol{u} + \frac{1}{\mathrm{Re}}\nabla p = 0, \qquad \boldsymbol{x} \in \Omega, \tag{2.69}$$

$$\nabla \cdot \boldsymbol{u} = 0, \qquad \boldsymbol{x} \in \Omega, \tag{2.70}$$

$$\boldsymbol{u} = 0, \qquad \boldsymbol{x} \in W, \tag{2.71}$$

$$\lambda h - v = b_h, \qquad \boldsymbol{x} \in \Sigma, \tag{2.72}$$

$$u_y + v_x = b_t, \qquad \boldsymbol{x} \in \Sigma, \tag{2.73}$$

$$p - 2v_y + \frac{1}{\mathrm{Ca}} h_{xx} = b_n, \qquad \boldsymbol{x} \in \Sigma. \tag{2.74}$$

We denote the real part of a complex number λ by $\mathfrak{Re}\lambda$, and its imaginary part by $\mathfrak{Im}\lambda$. The aim of this section is to prove

Proposition 1. *Let $s \geq 2, b_h \in H_0^{s-1/2}(\mathbb{T}_L), b_t \in H_0^{s-3/2}(\mathbb{T}_L), b_n \in H_0^{s-3/2}(\mathbb{T}_L)$. For every $\lambda \in \mathbb{C}$ with $\mathfrak{Re}\lambda \geq 1$, there is a unique solution $(\boldsymbol{u}, p, h)$ of (2.69)-(2.74) such that*

$$\int_0^L p(x,y)\mathrm{d}x = 0 \textit{ for all } 0 \leq y \leq 1, \tag{2.75}$$

$$\int_{\mathbb{T}_L} h(x)\mathrm{d}x = 0, \textit{ and} \tag{2.76}$$

$$\begin{aligned} &\|\boldsymbol{u}\|_{H^s(\Omega)} + |\lambda|^{s/2}\|\boldsymbol{u}\|_{H^0(\Omega)} + \|\nabla p\|_{H^{s-2}(\Omega)} \\ &\quad + |\lambda|^{\frac{s-2}{2}}\|\nabla p\|_{H^0(\Omega)} + \|h\|_{H^{s+1/2}(\mathbb{T}_L)} + |\lambda|^{\frac{s+1/2}{2}}\|h\|_{H^0(\mathbb{T}_L)} \\ &\leq C\Big(\|b_t\|_{H^{s-3/2}(\mathbb{T}_L)} + |\lambda|^{\frac{s-3/2}{2}}\|b_t\|_{H^0(\mathbb{T}_L)} + \|b_n\|_{H^{s-3/2}(\mathbb{T}_L)} \\ &\quad + |\lambda|^{\frac{s-3/2}{2}}\|b_n\|_{H^0(\mathbb{T}_L)} + \|b_h\|_{H^{s-1/2}(\mathbb{T}_L)} + |\lambda|^{\frac{s-1/2}{2}}\|b_h\|_{H^0(\mathbb{T}_L)}\Big). \end{aligned} \tag{2.77}$$

Moreover,

$$\begin{aligned} &\|\boldsymbol{u}\|_{H^2(\Omega)} + |\lambda|\,\|\boldsymbol{u}\|_{H^0(\Omega)} + \|\nabla p\|_{H^0(\Omega)} \\ &\quad \leq C\Big(\|b_n\|_{H^{1/2}(\mathbb{T}_L)} + \|b_t\|_{H^{1/2}(\mathbb{T}_L)} + \|b_h\|_{H^{3/2}(\mathbb{T}_L)}\Big). \end{aligned} \tag{2.78}$$

and

$$\begin{aligned}\|h\|_{H^{5/2}(\mathbb{T}_L)} &+ |\lambda|\,\|h\|_{H^{3/2}(\mathbb{T}_L)} \\ &\leq C\left(\|b_n\|_{H^{1/2}(\mathbb{T}_L)} + \|b_t\|_{H^{1/2}(\mathbb{T}_L)} + \|b_h\|_{H^{3/2}(\mathbb{T}_L)}\right).\end{aligned} \tag{2.79}$$

In order to solve the above system of equations, we expand the unknowns and the given data into Fourier series:

$$\begin{aligned} u(x,y) &= \sum_{k\in\mathbb{Z}} u^{(k)}(y)e^{iklx}, & v(x,y) &= \sum_{k\in\mathbb{Z}} v^{(k)}(y)e^{iklx}, \\ p(x,y) &= \sum_{k\in\mathbb{Z}} p^{(k)}(y)e^{iklx}, & h(x) &= \sum_{k\in\mathbb{Z}} h^{(k)}e^{iklx}, \\ b_h &= \sum_{k\in\mathbb{Z}} b_h^{(k)}e^{iklx}, & b_t &= \sum_{k\in\mathbb{Z}} b_t^{(k)}e^{iklx}, \\ b_n &= \sum_{k\in\mathbb{Z}} b_n^{(k)}e^{iklx}, \end{aligned}$$

where $l = \frac{2\pi}{L}$. Putting these into equations (2.69)-(2.74) leaves us with the following system of ordinary differential equations:

$$\lambda \operatorname{Re} u^{(k)}(y) + k^2l^2u^{(k)}(y) - u^{(k)\prime\prime}(y) + iklp^{(k)}(y) = 0, \qquad 0 \leq y \leq 1, \tag{2.80}$$

$$\lambda \operatorname{Re} v^{(k)}(y) + k^2l^2v^{(k)}(y) - v^{(k)\prime\prime}(y) + p^{(k)\prime}(y) = 0, \qquad 0 \leq y \leq 1, \tag{2.81}$$

$$iklu^{(k)}(y) + v^{(k)\prime}(y) = 0, \qquad 0 \leq y \leq 1, \tag{2.82}$$

$$u^{(k)}(0) = 0, \tag{2.83}$$

$$v^{(k)}(0) = 0, \tag{2.84}$$

$$\lambda h^{(k)} - v^{(k)}(1) = b_h^{(k)}, \tag{2.85}$$

$$u^{(k)\prime}(1) + iklv^{(k)}(1) = b_t^{(k)}, \tag{2.86}$$

$$p^{(k)}(1) - 2v^{(k)\prime}(1) - \frac{1}{\mathrm{Ca}}k^2l^2h^{(k)} = b_n^{(k)}, \tag{2.87}$$

for each $k \in \mathbb{Z}$. Regarding the unique solvability of this system, we have

Lemma 3. *Let* $\mathfrak{Re}\lambda > 0$*, and let the right hand side of (2.80)-(2.87) vanish, i.e.* $b_h^{(k)} = b_t^{(k)} = b_n^{(k)} = 0$*. Then, the unique solution of this system is the trivial one (*$u^{(k)} = v^{(k)} = p^{(k)} = h^{(k)} = 0$*).*

Proof. For a given k, we set $\xi = kl$. Let (u, v, p, h) be a solution of the ODE boundary value problem

$$
\begin{aligned}
\lambda \operatorname{Re} u(y) + |\xi|^2 u(y) - u''(y) + i\xi p(y) &= 0, && 0 \le y \le 1, && (2.88)\\
\lambda \operatorname{Re} v(y) + |\xi|^2 v(y) - v''(y) + p'(y) &= 0, && 0 \le y \le 1, && (2.89)\\
i\xi u(y) + v'(y) &= 0, && 0 \le y \le 1, && (2.90)\\
u(0) &= 0, && && (2.91)\\
v(0) &= 0, && && (2.92)\\
\lambda h - v(1) &= 0, && && (2.93)\\
u'(1) + i\xi v(1) &= 0, && && (2.94)\\
p(1) - 2v'(1) - \frac{|\xi|^2}{\mathrm{Ca}} h &= 0. && && (2.95)
\end{aligned}
$$

We multiply (2.88) with $\overline{u}$, (2.89) with $\overline{v}$, integrate from 0 to 1 and add the equations. Integration by parts in the terms $u''\overline{u}$, $v''\overline{v}$ and $p'\overline{v}$ yields

$$
\begin{aligned}
0 = \int_{[0,1]} \Big((\operatorname{Re}\lambda + |\xi|^2)(|u|^2 + |v|^2) + \left|u'\right|^2 + \left|v'\right|^2 \Big)\,\mathrm{d}y \\
-(u'\overline{u} + v'\overline{v} - p\overline{v})|_1 + \int_{[0,1]} p(i\xi\overline{u} - \overline{v}')\mathrm{d}y
\end{aligned}
\tag{2.96}
$$

where boundary terms at $y = 0$ vanish due to (2.91) and (2.92). The last integral is 0 by (2.90). Adding $0 = (-v'\overline{v} + v'\overline{v})|_1$ and the expression

$$
\begin{aligned}
0 = \int_0^1 \left|i\xi u + v'\right|^2 \mathrm{d}y &= \int_0^1 \Big(|\xi|^2 |u|^2 - i\xi\overline{u}v' + i\xi u\overline{v'} + \left|v'\right|^2 \Big)\,\mathrm{d}y \\
&= \int_0^1 \Big(|\xi|^2 |u|^2 + i\xi\overline{u}'v - i\xi u'\overline{v} + \left|v'\right|^2 \Big)\,\mathrm{d}y - i\xi(\overline{u}v - u\overline{v})|_1 \\
&= \int_0^1 \left|i\xi v + u'\right|^2 \mathrm{d}y - i\xi(\overline{u}v - u\overline{v})|_1
\end{aligned}
\tag{2.97}
$$

to equation (2.96) yields

$$
\begin{aligned}
0 = \int_0^1 \Big(\operatorname{Re}\lambda(|u|^2 + |v|^2) + 2\,|\xi|^2 |u|^2 + 2\left|v'\right|^2 \Big)\,\mathrm{d}y + \int_0^1 \left|i\xi v + u'\right|^2 \mathrm{d}y \\
+ \big(-\overline{u}(u' + i\xi v) + \overline{v}(i\xi u + v') + \overline{v}(p - 2v') \big)\,|_1.
\end{aligned}
\tag{2.98}
$$

The first boundary term vanishes due to (2.94), and the second one vanishes due to (2.90). For the third one, we calculate

$$
\big(\overline{v}(p - 2v')\big)\,|_1 = \overline{v}(1)\frac{|\xi|^2 h}{\mathrm{Ca}} = \frac{|\xi|^2}{\lambda\,\mathrm{Ca}} |v(1)|^2, \tag{2.99}
$$

which leaves us with

$$
\begin{aligned}
0 = \operatorname{Re}\lambda \int_0^1 \Big(|u|^2 + |v|^2 \Big)\,\mathrm{d}y + \int_0^1 \left|i\xi v + u'\right|^2 \mathrm{d}y \\
+2 \int_0^1 \Big(|\xi|^2 |u|^2 + \left|v'\right|^2 \Big)\,\mathrm{d}y + \frac{|\xi|^2}{\lambda\,\mathrm{Ca}} |v(1)|^2 .
\end{aligned}
\tag{2.100}
$$

This implies $u = v = 0$, and by (2.93) and (2.95), $p = h = 0$. $\square$

Since $b_h, b_n, b_t \in H_0^0(\mathbb{T}_L)$, the right-hand side of (2.80)-(2.87) is trivial for $k = 0$. By Lemma 3, we have $u^{(0)} = v^{(0)} = p^{(0)} = h^{(0)} = 0$, and therefore (2.75) and (2.76).

For the rest of this section, we consider this system for $k \neq 0$. We set $\xi = kl$ and $r = \sqrt{\lambda \operatorname{Re} + |\xi|^2}$. If we set $\lambda = \gamma + i\delta$,

$$r = \left((\operatorname{Re}\gamma + |\xi|^2)^2 + (\operatorname{Re}\delta)^2\right)^{1/4} \exp\left(\frac{i\arctan(\frac{\operatorname{Re}\delta}{\operatorname{Re}\gamma + |\xi|^2})}{2}\right). \tag{2.101}$$

Since $|\arctan(x)| < \frac{\pi}{2}$ for all $x \in \mathbb{R}$, $|\arg r| < \frac{\pi}{4}$. The following estimates will be used frequently in this section:

i) $2^{-3/4}(\sqrt{\operatorname{Re}|\lambda|} + |\xi|) \leq |r| \leq \sqrt{\operatorname{Re}|\lambda|} + |\xi|$,

ii) $|\xi|^2 \leq |r|^2 \leq |r + |\xi||^2$,

iii) $|r|\,|\xi| \leq |r + |\xi||^2$.

We write $v^{(k)}$ as a linear combination of fundamental solutions (cf. Solonnikov (1976)):

$$v^{(k)}(y) = Ae^{|\xi|(y-1)} + Be^{r(y-1)} + Ce^{-|\xi|y} + De^{-ry}. \tag{2.102}$$

By the divergence condition (2.82),

$$u^{(k)}(y) = \frac{i}{\xi}(|\xi|\, Ae^{|\xi|(y-1)} + rBe^{r(y-1)} - |\xi|\, Ce^{-|\xi|y} - rDe^{-ry}). \tag{2.103}$$

Substituting $u^{(k)}(y)$ into (2.80) lets us determine $p^{(k)}(y)$ as

$$p^{(k)}(y) = -\frac{\lambda \operatorname{Re}}{|\xi|}(Ae^{|\xi|(y-1)} - Ce^{-|\xi|y}). \tag{2.104}$$

The last unknown $h^{(k)}$ can be determined by substituting (2.102) into (2.85):

$$h^{(k)} = \frac{1}{\lambda}(A + B + Ce^{-|\xi|} + De^{-r}) + \frac{1}{\lambda}b_h^{(k)}. \tag{2.105}$$

With this, $u^{(k)}(y), v^{(k)}(y), p^{(k)}(y)$ and $h^{(k)}$ solve equations (2.80), (2.81), (2.82) and (2.85) for arbitrary $A, B, C, D \in \mathbb{C}$, and we have to determine the coefficients out of the boundary conditions (2.83),(2.84),(2.86) and (2.87).

This leads to the following system of linear equations:

$$\boldsymbol{M}\begin{pmatrix} A \\ B \\ C \\ D \end{pmatrix} = \begin{pmatrix} 0 \\ 0 \\ b_t^{(k)} \\ b_n^{(k)} + \frac{|\xi|^2}{\lambda \operatorname{Ca}} b_h^{(k)} \end{pmatrix} \tag{2.106}$$

where

$$\boldsymbol{M} = \begin{pmatrix} e^{-|\xi|} & e^{-r} & 1 & 1 \\ |\xi|\, e^{-|\xi|} & re^{-r} & -|\xi| & -r \\ 2i\xi & i\frac{r^2+|\xi|^2}{\xi} & 2i\xi e^{-|\xi|} & i\frac{r^2+|\xi|^2}{\xi}e^{-r} \\ -\frac{r^2+|\xi|^2}{\xi} - \frac{|\xi|^2}{\lambda\,\mathrm{Ca}} & -2r - \frac{|\xi|^2}{\lambda\,\mathrm{Ca}} & (\frac{r^2+|\xi|^2}{\xi} - \frac{|\xi|^2}{\lambda\,\mathrm{Ca}})e^{-|\xi|} & (2r - \frac{|\xi|^2}{\lambda\,\mathrm{Ca}})e^{-|\xi|} \end{pmatrix}. \tag{2.107}$$

We have $\det \boldsymbol{M} \neq 0$. Else, there is a $0 \neq (A, B, C, D) \in \ker \boldsymbol{M}$, which implies that there is a non-trivial solution to (2.80)-(2.87) with homogeneous right-hand side. This, however, is a contradiction to Lemma 3.

For $\xi \neq 0$, we use the homogeneity of the first two lines in (2.106) to eliminate C and D:

$$\begin{pmatrix} C \\ D \end{pmatrix} = \frac{1}{r - |\xi|} \begin{pmatrix} -(r + |\xi|)e^{-|\xi|} & -2re^{-r} \\ 2\,|\xi|\, e^{-|\xi|} & (r + |\xi|)e^{-r} \end{pmatrix} \begin{pmatrix} A \\ B \end{pmatrix} =: \boldsymbol{N}_0 \begin{pmatrix} A \\ B \end{pmatrix}. \tag{2.108}$$

Moreover, we set

$$\boldsymbol{M}_0 = \begin{pmatrix} 2i\xi & i\frac{r^2+|\xi|^2}{\xi} \\ -\frac{r^2+|\xi|^2}{\xi} - \frac{|\xi|^2}{\lambda\,\mathrm{Ca}} & -2r - \frac{|\xi|^2}{\lambda\,\mathrm{Ca}} \end{pmatrix} \tag{2.109}$$

and

$$\boldsymbol{M}_1 = \begin{pmatrix} 2i\xi e^{-|\xi|} & i\frac{r^2+|\xi|^2}{\xi}e^{-r} \\ (\frac{r^2+|\xi|^2}{\xi} - \frac{|\xi|^2}{\lambda\,\mathrm{Ca}})e^{-|\xi|} & (2r - \frac{|\xi|^2}{\lambda\,\mathrm{Ca}})e^{-|\xi|} \end{pmatrix}. \tag{2.110}$$

With this, we can write (2.106) as

$$\boldsymbol{M}_0 \begin{pmatrix} A \\ B \end{pmatrix} + \boldsymbol{M}_1 \begin{pmatrix} C \\ D \end{pmatrix} = (\boldsymbol{M}_0 + \boldsymbol{M}_1 \boldsymbol{N}_0) \begin{pmatrix} A \\ B \end{pmatrix} = \begin{pmatrix} b_t^{(k)} \\ b_n^{(k)} + \frac{|\xi|^2}{\lambda\,\mathrm{Ca}} b_h^{(k)} \end{pmatrix}. \tag{2.111}$$

For $\boldsymbol{M}_0$, the following Lemma holds:

Lemma 4. *Let* $\mathfrak{Re}\lambda = \gamma \geq 1$. *Then*

$$\det \boldsymbol{M}_0 = \frac{i}{\xi\,|\xi|} \left((r^2 + |\xi|^2)^2 - 4r\,|\xi|^3 + \frac{\mathrm{Re}}{\mathrm{Ca}}\,|\xi|^3 \right) =: \frac{i}{\xi\,|\xi|} D, \tag{2.112}$$

where

i) $|D| \geq \mathrm{Re}^2$,

ii) $|D| \geq 2\,\mathrm{Re}\,|\lambda|\,|\xi|^2$,

iii) $\frac{\mathrm{Re}}{\mathrm{Ca}}\,|\xi|^3 \leq (\frac{7}{2} + \frac{1}{2\,\mathrm{Ca}}\sqrt{\frac{\mathrm{Re}}{\gamma_0}})\,|D|$,

iv) $(\mathrm{Re}\,|\lambda|)^2 \leq (3 + \frac{1}{2\,\mathrm{Ca}}\sqrt{\frac{\mathrm{Re}}{\gamma_0}})\,|D|$.

This is Lemma 2.5 in Solonnikov (1991).

This allows us to multiply equation (2.111) with

$$\boldsymbol{M}_0^{-1} = \frac{\xi\,|\xi|}{iD} \begin{pmatrix} -2r - \frac{|\xi|^2}{\lambda\,\mathrm{Ca}} & -i\frac{r^2+|\xi|^2}{\xi} \\ \frac{r^2+|\xi|^2}{\xi} + \frac{|\xi|^2}{\lambda\,\mathrm{Ca}} & 2i\xi \end{pmatrix}, \tag{2.113}$$

which yields

$$(\boldsymbol{I} + \boldsymbol{M}_0^{-1}\boldsymbol{M}_1\boldsymbol{N}_0)\begin{pmatrix} A \\ B \end{pmatrix} = \boldsymbol{M}_0^{-1}\begin{pmatrix} b_t^{(k)} \\ b_n^{(k)} + \frac{|\xi|^2}{\lambda\,\mathrm{Ca}} b_h^{(k)} \end{pmatrix}. \tag{2.114}$$

Note that

$$\boldsymbol{M}_0^{-1}\boldsymbol{M}_1\boldsymbol{N}_0 = \frac{1}{r-|\xi|}\begin{pmatrix} -2i\xi(r+|\xi|)e^{-2|\xi|} & 2i\xi\frac{r^2+|\xi|^2}{\xi}e^{-r-|\xi|} \\ -(r+|\xi|)(\frac{r^2+|\xi|^2}{|\xi|} - \frac{|\xi|^2}{\lambda\,\mathrm{Ca}})e^{-2|\xi|} & 2\,|\xi|\,(2r - \frac{|\xi|^2}{\lambda\,\mathrm{Ca}})e^{-|\xi|-r} \end{pmatrix}. \tag{2.115}$$

Due to the exponential factor present in every component of $\boldsymbol{M}_0^{-1}\boldsymbol{M}_1\boldsymbol{N}_0$, for k large enough, the inverse of $(\boldsymbol{I} + \boldsymbol{M}_0^{-1}\boldsymbol{M}_1\boldsymbol{N}_0)$ is given by the Neumann series:

$$(\boldsymbol{I} + \boldsymbol{M}_0^{-1}\boldsymbol{M}_1\boldsymbol{N}_0)^{-1} = \sum_{m\in\mathbb{Z}}(-1)^m(\boldsymbol{M}_0^{-1}\boldsymbol{M}_1\boldsymbol{N}_0)^m. \tag{2.116}$$

Therefore, we can write

$$\begin{pmatrix} A \\ B \end{pmatrix} = (\boldsymbol{I} + e^{-|\xi|}\boldsymbol{L}^{(k)})\boldsymbol{M}_0^{-1}\begin{pmatrix} b_t^{(k)} \\ b_n^{(k)} + \frac{|\xi|^2}{\lambda\,\mathrm{Ca}} b_h^{(k)} \end{pmatrix} \tag{2.117}$$

for every k, where the components of $\boldsymbol{L}^{(k)}$ are uniformly bounded in k. We see that C, D and $e^{-|\xi|}\boldsymbol{L}^{(k)}\boldsymbol{M}_0^{-1}\begin{pmatrix} b_t^{(k)} \\ b_n^{(k)} + \frac{|\xi|^2}{\lambda\,\mathrm{Ca}} b_h^{(k)} \end{pmatrix}$ each contain a factor $e^{-|\xi|}$ or e^{-r}. The estimates in Proposition 1 for terms with these factors are easy to obtain.

Therefore, we concentrate on terms with the critical coefficients

$$\begin{aligned} \begin{pmatrix} \tilde{A} \\ \tilde{B} \end{pmatrix} &= \boldsymbol{M}_0^{-1}\begin{pmatrix} b_t^{(k)} \\ b_n^{(k)} + \frac{|\xi|^2}{\lambda\,\mathrm{Ca}} b_h^{(k)} \end{pmatrix} \\ &= \frac{\xi\,|\xi|}{iD}\begin{pmatrix} (-2r - \frac{|\xi|^2}{\lambda\,\mathrm{Ca}})b_t^{(k)} - i\frac{r^2+|\xi|^2}{\xi}b_n^{(k)} - i\frac{r^2+|\xi|^2}{\xi}\frac{|\xi|^2}{\lambda\,\mathrm{Ca}}b_h^{(k)} \\ (\frac{r^2+|\xi|^2}{|\xi|} + \frac{|\xi|^2}{\lambda\,\mathrm{Ca}})b_t^{(k)} + 2i\xi b_n^{(k)} + 2i\xi\frac{|\xi|^2}{\lambda\,\mathrm{Ca}}b_h^{(k)} \end{pmatrix}. \end{aligned} \tag{2.118}$$

In other words, we will consider

$$
\begin{aligned}
\tilde{v}^{(k)}(y) =& \tilde{A}e^{|\xi|(y-1)} + \tilde{B}e^{r(y-1)} \\
=& -\tilde{A}(e^{r(y-1)} - e^{|\xi|(y-1)}) + (\tilde{A}+\tilde{B})e^{r(y-1)} \\
=& \frac{\xi\,|\xi|}{iD}\left((2r + \frac{|\xi|^2}{\lambda\,\mathrm{Ca}})b_t^{(k)} + i\frac{r^2+|\xi|^2}{\xi}b_n^{(k)} + i\frac{r^2+|\xi|^2}{\xi}\frac{|\xi|^2}{\lambda\,\mathrm{Ca}}b_h^{(k)}\right) \\
& \times (e^{r(y-1)} - e^{|\xi|(y-1)}) \\
& + \frac{\xi\,|\xi|}{iD}\left((\frac{r^2+|\xi|^2}{|\xi|} - 2r)b_t^{(k)} - i\frac{\mathrm{Re}\,\lambda}{\xi}b_n^{(k)} - i\frac{|\xi|^2}{\lambda\,\mathrm{Ca}}\frac{\mathrm{Re}\,\lambda}{\xi}b_h^{(k)}\right)e^{r(y-1)} \\
=& \frac{1}{iD}\left(\xi\,|\xi|\,(2r + \frac{|\xi|^2}{\lambda\,\mathrm{Ca}})b_t^{(k)} + i\,|\xi|\,(r^2+|\xi|^2)b_n^{(k)} + i(r^2+|\xi|^2)\frac{|\xi|^3}{\lambda\,\mathrm{Ca}}b_h^{(k)}\right) \\
& \times (e^{r(y-1)} - e^{|\xi|(y-1)}) \\
& + \frac{1}{iD}\left(\xi(r-|\xi|)^2 b_t^{(k)} - |\xi|\,\mathrm{Re}\,\lambda b_n^{(k)} - i\frac{|\xi|^3}{\mathrm{Ca}}\,\mathrm{Re}\,b_h^{(k)}\right)e^{r(y-1)},
\end{aligned}
\tag{2.119}
$$

$$
\begin{aligned}
\tilde{u}^{(k)}(y) =& \frac{i\,|\xi|}{\xi}\tilde{A}e^{|\xi|(y-1)} + \frac{ir}{\xi}\tilde{B}e^{r(y-1)} \\
=& -\frac{i\,|\xi|}{\xi}\tilde{A}(e^{r(y-1)} - e^{|\xi|(y-1)}) + (\frac{i\,|\xi|}{\xi}\tilde{A} + \frac{ir}{\xi}\tilde{B})e^{r(y-1)},
\end{aligned}
\tag{2.120}
$$

$$
\begin{aligned}
\tilde{p}^{(k)}(y) =& -\frac{\lambda\,\mathrm{Re}}{|\xi|}\tilde{A}e^{|\xi|(y-1)} \\
=& \frac{\xi\,\mathrm{Re}\,\lambda}{iD}\left((2r + \frac{|\xi|^2}{\lambda\,\mathrm{Ca}})b_t^{(k)} + i\frac{r^2+|\xi|^2}{\xi}b_n^{(k)} + i\frac{r^2+|\xi|^2}{\xi}\frac{|\xi|^2}{\lambda\,\mathrm{Ca}}b_h^{(k)}\right)e^{|\xi|(y-1)}
\end{aligned}
\tag{2.121}
$$

and

$$
\begin{aligned}
\tilde{h}^{(k)} =& \frac{1}{\lambda}(\tilde{A}+\tilde{B}) + \frac{1}{\lambda}b_h^{(k)} \\
=& \frac{\xi\,|\xi|}{iD\lambda}(\frac{r^2+|\xi|^2}{|\xi|} - 2r)b_t^{(k)} - \frac{\mathrm{Re}\,|\xi|}{D}b_n^{(k)} + \frac{1}{\lambda}(1 - \frac{\mathrm{Re}}{\mathrm{Ca}}\frac{|\xi|^3}{D})b_h^{(k)} \\
=& -\frac{\mathrm{Re}}{D}\frac{i\xi(r-|\xi|)}{r+|\xi|}b_t^{(k)} - \frac{\mathrm{Re}}{D}\,|\xi|\,b_n^{(k)} + \frac{\mathrm{Re}}{D(r+|\xi|)}\left(r^3 + r^2\,|\xi| + 3r\,|\xi|^2 - |\xi|^3\right)b_h^{(k)}.
\end{aligned}
\tag{2.122}
$$

For the treatment of the y-dependent terms in $\tilde{u}^{(k)}, \tilde{v}^{(k)}$ and $\tilde{p}^{(k)}$, we need

Lemma 5. *Let* $f_1(y) = e^{r(y-1)}$*,* $f_2(y) = \frac{e^{r(y-1)} - e^{|\xi|(y-1)}}{r-|\xi|}$ *and* $f_3(y) = e^{|\xi|(y-1)}$*.*

Then

$$\int_0^1 \left|\frac{\partial^j}{\partial y^j} f_1(y)\right|^2 \mathrm{d}y \leq \frac{1}{\sqrt{2}} \left|r\right|^{2j-1}, j = 0, 1, 2 \ldots, \tag{2.123}$$

$$\int_0^1 \left|f_2(y)\right|^2 \mathrm{d}y \leq \frac{1}{\left|r\right|^2 \left|\xi\right|}, \tag{2.124}$$

$$\int_0^1 \left|\frac{\partial^j}{\partial y^j} f_2(y)\right|^2 \mathrm{d}y \leq C \frac{\left|r\right|^{2j-1} + \left|\xi\right|^{2j-1}}{\left|r\right|^2}, j = 1, 2, 3, \ldots \tag{2.125}$$

$$\int_0^1 \left|\frac{\partial^j}{\partial y^j} f_3(y)\right|^2 \mathrm{d}y \leq \frac{1}{2} \left|\xi\right|^{2j-1}, j = 0, 1, 2 \ldots \tag{2.126}$$

Proof. The estimates for f_1 and f_2 follow from Solonnikov (1991), Lemma 3.1 by the transformation

$$\begin{aligned} \int_0^1 \left|f_1(y)\right|^2 \mathrm{d}y &= \int_0^1 \left|e^{r(y-1)}\right|^2 \mathrm{d}y = \int_{-1}^0 \left|e^{ry}\right|^2 \mathrm{d}y \\ &= \int_0^1 \left|e^{-ry}\right|^2 \mathrm{d}y \leq \int_0^\infty \left|e^{-ry}\right|^2 \mathrm{d}y. \end{aligned} \tag{2.127}$$

The estimate for f_3 can be obtained by direct calculation:

$$\int_0^1 \left|\frac{\partial^j}{\partial y^j} f_3(y)\right|^2 \mathrm{d}y = \frac{1}{2} \left|\xi\right|^{2j-1} (1 - e^{-2|\xi|}) \leq \frac{1}{2} \left|\xi\right|^{2j-1}. \tag{2.128}$$

□

We start by showing the regularity estimates for $\tilde{v}$ in (2.77). For regularity in space, we calculate

$$\begin{aligned} \int_0^L \int_0^1 \left|\partial_x^\alpha \partial_y^\beta \tilde{v}(x, y)\right|^2 \mathrm{d}y\mathrm{d}x &= \int_0^L \int_0^1 \left|\partial_x^\alpha \partial_y^\beta \sum_{k \in \mathbb{Z}} \tilde{v}^{(k)}(y) e^{i\xi x}\right|^2 \mathrm{d}y\mathrm{d}x \\ &= \int_0^L \int_0^1 \left|\sum_{k \in \mathbb{Z}} (\partial_y^\beta \tilde{v}^{(k)}(y)) \xi^\alpha e^{i\xi x}\right|^2 \mathrm{d}y\mathrm{d}x \\ &\leq L \sum_k \left|\xi\right|^{2\alpha} \int_0^1 \left|\partial_y^\beta \tilde{v}^{(k)}(y)\right|^2 \mathrm{d}y \\ &\leq L \sum_k \left|r\right|^{2\alpha} \int_0^1 \left|\partial_y^\beta \tilde{v}^{(k)}(y)\right|^2 \mathrm{d}y. \end{aligned} \tag{2.129}$$

As a first step, we set $\alpha = s, \beta = 0$, and estimate

$$
\begin{aligned}
|r|^{2s}\int_0^1 \left|\tilde{v}^{(k)}(y)\right|^2 \mathrm{d}y \leq{} & C\frac{|r|^{2s}}{|D|^2}\left(|\xi|^4\left|2r+\frac{|\xi|^2}{\lambda\,\mathrm{Ca}}\right|^2\left|b_t^{(k)}\right|^2+|\xi|^2\left|r^2+|\xi|^2\right|^2\left|b_n^{(k)}\right|^2\right.\\
&\left.+\frac{\left|r^2+|\xi|^2\right|^2|\xi|^6}{|\lambda|^2\,\mathrm{Ca}^2}\left|b_h^{(k)}\right|^2\right)\left|r-|\xi|\right|^2\int_0^1\left|\frac{e^{r(y-1)}-e^{|\xi|(y-1)}}{r-|\xi|}\right|^2\mathrm{d}y\\
&+C\frac{|r|^{2s}}{|D|^2}\left(|\xi|^2\left|r-|\xi|\right|^4\left|b_t^{(k)}\right|^2+|\xi|^2\,\mathrm{Re}^2\,|\lambda|^2\left|b_n^{(k)}\right|^2\right.\\
&\left.+\left(\frac{\mathrm{Re}}{\mathrm{Ca}}\right)^2|\xi|^6\left|b_h^{(k)}\right|^2\right)\int_0^1\left|e^{r(y-1)}\right|^2\mathrm{d}y\\
\leq{} & \frac{C}{|D|^2}\left(\left(\frac{\mathrm{Re}^2\,|\lambda|^2\,|r|^2\left|r^2+|\xi|^2\right|^2}{\left|r+|\xi|\right|^2}+|r|^2\,|\xi|^2\,\mathrm{Re}^2\,|\lambda|^2\right)|r|^{2s-3}\left|b_n^{(k)}\right|^2\right.\\
&+\left(\frac{\mathrm{Re}^2\,|\lambda|^2\,|r|^2\,|\xi|^2\left|2r+\frac{|\xi|^2}{\lambda\,\mathrm{Ca}}\right|^2}{\left|r+|\xi|\right|^2}+|r|^2\,|\xi|^2\left|r-|\xi|\right|^4\right)|r|^{2s-3}\left|b_t^{(k)}\right|^2\\
&\left.+\left(\frac{\left|r^2+|\xi|^2\right|^2|\xi|^4\,\mathrm{Re}^2\,|\lambda|^2}{|\lambda|^2\,\mathrm{Ca}^2\left|r+|\xi|\right|^2}+\left(\frac{\mathrm{Re}}{\mathrm{Ca}}\right)^2|\xi|^6\right)\left(|r|^{2s-1}\left|b_h^{(k)}\right|^2\right)\right),
\end{aligned}
\tag{2.130}
$$

where Lemma 5 was employed. We now have to show that the factors in front of the Fourier coefficients of the data are bounded by $\frac{C}{|D|^2}$. We estimate

$$
\begin{aligned}
&\frac{\mathrm{Re}^2\,|\lambda|^2\,|r|^2\left|r^2+|\xi|^2\right|^2}{\left|r+|\xi|\right|^2}+|r|^2\,|\xi|^2\,\mathrm{Re}^2\,|\lambda|^2\\
&\leq C\left(\frac{\mathrm{Re}^4\,|\lambda|^4\,|r|^2}{\left|r+|\xi|\right|^2}+\frac{\mathrm{Re}^2\,|\lambda|^2\,|\xi|^4\,|r|^2}{\left|r+|\xi|\right|^2}+\mathrm{Re}^3\,|\lambda|^3\,|\xi|^2+\mathrm{Re}^2\,|\lambda|^2\,|\xi|^4\right)\\
&\leq C\left(\mathrm{Re}^4\,|\lambda|^4+\mathrm{Re}^2\,|\lambda|^2\,|\xi|^4+\mathrm{Re}^3\,|\lambda|^3\,|\xi|^2+\mathrm{Re}^2\,|\lambda|^2\,|\xi|^4\right),
\end{aligned}
\tag{2.131}
$$

$$\begin{aligned}
&\frac{\mathrm{Re}^2 \left|\lambda\right|^2 \left|r\right|^2 \left|\xi\right|^2 \left|2r + \frac{\left|\xi\right|^2}{\lambda \,\mathrm{Ca}}\right|^2}{\left|r + \left|\xi\right|\right|^2} + \left|r\right|^2 \left|\xi\right|^2 \left|r - \left|\xi\right|\right|^4 \\
&\leq C \left(\frac{\mathrm{Re}^2 \left|\lambda\right|^2 \left|r\right|^4 \left|\xi\right|^2}{\left|r + \left|\xi\right|\right|^2} + \frac{\mathrm{Re}^2 \left|\lambda\right|^2 \left|r\right|^2 \left|\xi\right|^4}{\left|r + \left|\xi\right|\right|^2} + \frac{\mathrm{Re}^2 \left|r\right|^2 \left|\xi\right|^6}{\left|r + \left|\xi\right|\right|^2} + \left|r\right|^2 \left|\xi\right|^2 \left|\frac{\mathrm{Re}\,\lambda}{r + \left|\xi\right|}\right|^4 \right) \\
&\leq C \left(\mathrm{Re}^3 \left|\lambda\right|^3 \left|\xi\right|^2 + \mathrm{Re}^2 \left|\lambda\right|^2 \left|\xi\right|^4 + (\frac{\mathrm{Re}}{\mathrm{Ca}})^2 \left|\xi\right|^6 + \mathrm{Re}^4 \left|\lambda\right|^4 \right),
\end{aligned} \tag{2.132}$$

and

$$\begin{aligned}
&\frac{\left|r^2 + \left|\xi\right|^2\right|^2 \left|\xi\right|^4 \mathrm{Re}^2}{\mathrm{Ca}^2 \left|r + \left|\xi\right|\right|^2} + (\frac{\mathrm{Re}}{\mathrm{Ca}})^2 \left|\xi\right|^6 \\
&\leq C(\frac{\mathrm{Re}}{\mathrm{Ca}})^2 \left(\mathrm{Re}^2 \left|\lambda\right|^2 \left|\xi\right|^4 + \left|\xi\right|^6 \right).
\end{aligned} \tag{2.133}$$

Due to Lemma 4, these can can bounded by $\frac{C}{\left|D\right|^2}$. Using Lemma 5,

$$\left|r\right|^{2(s-\beta)} \int_0^1 \left|\partial_y^\beta \tilde{v}^{(k)}(y)\right|^2 \mathrm{d}y \tag{2.134}$$

can be estimated in exactly the same way for integer β. For non-integer β, the desired estimates follow by interpolation, which proves the stated regularity in space for $\tilde{v}$. As we have $\left|\lambda\right| \leq C \left|r\right|^2 \leq C' \left|\lambda\right|$, regularity in time follows, too. The corresponding estimates for $\tilde{u}$ are very similar.

To show the regularity of p, we calculate

$$\begin{aligned}
\left|r\right|^{2s-2} \int_0^1 \left|\tilde{p}^{(k)}\right|^2 (y)\mathrm{d}y \leq{} & C \frac{\mathrm{Re}^2 \left|r\right|^{2s-2} \left|\xi\right|^2 \left|\lambda\right|^2}{\left|D\right|^2} \left(\left|2r + \frac{\left|\xi\right|^2}{\lambda\,\mathrm{Ca}}\right|^2 \left|b_t^{(k)}\right|^2 + \frac{\left|r^2 + \left|\xi\right|^2\right|^2}{\left|\xi\right|^2} \left|b_n^{(k)}\right|^2 \right. \\
& \left. + \frac{\left|r^2 + \left|\xi\right|^2\right|^2}{\left|\xi\right|^2} \frac{\left|\xi\right|^4}{\lambda^2\,\mathrm{Ca}^2} \left|b_h^{(k)}\right|^2 \right) \int_0^1 \left|e^{\left|\xi\right|(y-1)}\right|^2 \mathrm{d}y \\
\leq{} & \frac{C}{\left|D\right|^2} \left(\mathrm{Re}^2 \left|\lambda\right|^2 \left|r\right| \left|\xi\right| \left(\mathrm{Re} \left|\lambda\right| + \left|\xi\right|^2 + \frac{\left|\xi\right|^4}{\left|\lambda\right|^2 \mathrm{Ca}^2} \right) (\left|r\right|^{2s-3} \left|b_t^{(k)}\right|^2) \right. \\
& + \left|\lambda\right|^2 \left|\xi\right|^2 \frac{\mathrm{Re}^2 \left|\lambda\right|^2 + \left|\xi\right|^4}{\left|\xi\right|^2} (\left|\xi\right|^{2s-3} \left|b_n^{(k)}\right|^2) \\
& \left. + \left|\lambda\right|^2 \frac{\mathrm{Re}^2 \left|\lambda\right|^2 \left|\xi\right|^4 + \left|\xi\right|^8}{\left|\xi\right|^2 \left|\lambda\right|^2 \mathrm{Ca}^2} (\left|\xi\right|^{2s-1} \left|b_h^{(k)}\right|^2) \right).
\end{aligned} \tag{2.135}$$

By using $|r| \leq C(\sqrt{\operatorname{Re}|\lambda|} + |\xi|)$, the factors in front of the data can be bounded by $\frac{C}{|D|^2}$ as above. Considering $\tilde{h}$, we estimate

$$\begin{aligned} |r|^{s+1/2} \left|\tilde{h}^{(k)}\right| &\leq C \left(\left|\frac{\operatorname{Re}}{D}\right| |\xi| \left|\frac{r - |\xi|}{r + |\xi|}\right| |r|^2 \, |r|^{s-3/2} \left|b_t^{(k)}\right| \right. \\ &\quad + \left|\frac{\operatorname{Re}}{D}\right| |\xi| \, |r|^2 \, |r|^{s-3/2} \left|b_n^{(k)}\right| \\ &\quad \left. + \left|\frac{\operatorname{Re}}{D}\right| |r|^3 \left|\frac{r}{r + |\xi|}\right| |r|^{s-1/2} \left|b_h^{(k)}\right| \right) \\ &\leq C \left(\frac{\operatorname{Re}|\xi| \, |r|^2}{|D|} (|r|^{s-3/2} \left|b_t^{(k)}\right| + |r|^{s-3/2} \left|b_t^{(k)}\right|) \right. \\ &\quad \left. + \operatorname{Re} \frac{(\sqrt{\operatorname{Re}|\lambda|} + |\xi|)^3}{|D|} |r|^{s-1/2} \left|b_h^{(k)}\right| \right) \\ &\leq C \left(|r|^{s-3/2} \left|b_t^{(k)}\right| + |r|^{s-3/2} \left|b_n^{(k)}\right| + |r|^{s-1/2} \left|b_h^{(k)}\right| \right), \end{aligned} \tag{2.136}$$

which concludes the proof of (2.77).

In order to show the estimate for $\lambda \|h\|_{H^{3/2}(\mathbb{T}_L)}$ in (2.79), we calculate

$$\begin{aligned} |\lambda| \, |\xi|^{3/2} \left|\tilde{h}^{(k)}\right| &\leq |\lambda| \frac{\operatorname{Re}}{|D|} |\xi|^{5/2} \left|\frac{r - |\xi|}{r + |\xi|}\right| \left|b_t^{(k)}\right| \\ &\quad + |\lambda| \frac{\operatorname{Re}}{|D|} |\xi|^{5/2} \left|b_n^{(k)}\right| \\ &\quad + |\lambda| \, |\xi|^{3/2} \frac{1}{|\lambda|} \left|1 - \frac{\operatorname{Re}|\xi|^3}{\operatorname{Ca} D}\right| \left|b_h^{(k)}\right| \\ &\leq C \left(|\xi|^{1/2} \left|b_t^{(k)}\right| + |\xi|^{1/2} \left|b_n^{(k)}\right| + |\xi|^{3/2} \left|b_h^{(k)}\right| \right). \end{aligned} \tag{2.137}$$

The calculations necessary to show the other parabolic estimates in (2.78) and (2.79) are very similar to those used in the derivation of (2.77) in the case $s = 2$.

2.3.2. Auxiliary problem B

With the aid of auxiliary problem A, we are now in a position to consider the following system of equations, where more coupling terms between velocity and interface are taken into account:

$$\lambda \boldsymbol{u} - \frac{1}{\mathrm{Re}}\Delta \boldsymbol{u} + \frac{1}{\mathrm{Re}}\nabla p = 0, \qquad \boldsymbol{x} \in \Omega, \tag{2.138}$$

$$\nabla \cdot \boldsymbol{u} = 0, \qquad \boldsymbol{x} \in \Omega, \tag{2.139}$$

$$\boldsymbol{u} = 0, \qquad \boldsymbol{x} \in W, \tag{2.140}$$

$$\lambda h - v = b_h, \qquad \boldsymbol{x} \in \Sigma, \tag{2.141}$$

$$u_y + v_x - 2h = b_t, \qquad \boldsymbol{x} \in \Sigma, \tag{2.142}$$

$$p - 2v_y - 2\cot\alpha h + \frac{1}{\mathrm{Ca}} h_{xx} = 0, \qquad \boldsymbol{x} \in \Sigma. \tag{2.143}$$

We prove

Proposition 2. *Let* $s \geq 2, b_h \in H_0^{s-1/2}(\mathbb{T}_L), b_t \in H_0^{s-3/2}(\mathbb{T}_L)$. *There exists a* $\gamma_0 > 0$ *such that for every* $\lambda \in \mathbb{C}$ *with* $\mathfrak{Re}\lambda \geq \gamma_0$, *there is a unique solution* $(\boldsymbol{u}, p, h)$ *of (2.138)-(2.143) such that*

$$\int_{\mathbb{T}_L} p(x,y)\mathrm{d}x = 0 \textit{ for all } 0 \leq y \leq 1, \tag{2.144}$$

$$\int_{\mathbb{T}_L} h(x)\mathrm{d}x = 0, \textit{ and} \tag{2.145}$$

$$\begin{aligned} &\|\boldsymbol{u}\|_{H^s(\Omega)} + |\lambda|^{s/2} \|\boldsymbol{u}\|_{H^0(\Omega)} + \|\nabla p\|_{H^{s-2}(\Omega)} \\ &\quad + |\lambda|^{\frac{s-2}{2}} \|\nabla p\|_{H^0(\Omega)} + \|h\|_{H^{s+1/2}(\mathbb{T}_L)} + |\lambda|^{\frac{s+1/2}{2}} \|h\|_{H^0(\mathbb{T}_L)} \\ &\quad \leq C \Big(\|b_t\|_{H^{s-3/2}(\mathbb{T}_L)} + |\lambda|^{\frac{s-3/2}{2}} \|b_t\|_{H^0(\mathbb{T}_L)} \\ &\quad + \|b_h\|_{H^{s-1/2}(\mathbb{T}_L)} + |\lambda|^{\frac{s-1/2}{2}} \|b_h\|_{H^0(\mathbb{T}_L)} \Big). \end{aligned} \tag{2.146}$$

Moreover,

$$\|h\|_{H^{5/2}(\mathbb{T}_L)} + |\lambda| \|h\|_{H^{3/2}(\mathbb{T}_L)} \leq C \Big(\|b_t\|_{H^{1/2}(\mathbb{T}_L)} + \|b_h\|_{H^{3/2}(\mathbb{T}_L)} \Big) \tag{2.147}$$

and

$$\|\boldsymbol{u}\|_{H^2(\Omega)} + |\lambda| \|\boldsymbol{u}\|_{H^0(\Omega)} + \|\nabla p\|_{H^0(\Omega)} \leq C \Big(\|b_t\|_{H^{1/2}(\mathbb{T}_L)} + \|b_h\|_{H^{3/2}(\mathbb{T}_L)} \Big). \tag{2.148}$$

Proof. Let $\tilde{h} \in H_0^{3/2}(\mathbb{T}_L)$. Then, $\cot\alpha\tilde{h} \in H_0^{1/2}(\mathbb{T}_L)$, $2\tilde{h} + b_t \in H_0^{1/2}(\mathbb{T}_L)$, and according to Proposition 1, there is a unique solution $(\boldsymbol{u}, h, p)$ of

$$\lambda \boldsymbol{u} - \frac{1}{\mathrm{Re}} \Delta \boldsymbol{u} + \frac{1}{\mathrm{Re}} \nabla p = 0 \text{ in } \Omega, \tag{2.149}$$

$$\nabla \cdot \boldsymbol{u} = 0 \text{ in } \Omega, \tag{2.150}$$

$$\boldsymbol{u} = 0 \text{ on } W, \tag{2.151}$$

$$\lambda h - v = b_h \text{ on } \Sigma, \tag{2.152}$$

$$u_y + v_x = 2\tilde{h} + b_t \text{ on } \Sigma, \tag{2.153}$$

$$p - 2v_y + \frac{1}{\mathrm{Ca}} h_{xx} = 2 \cot \alpha \tilde{h} \text{ on } \Sigma, \tag{2.154}$$

with $h \in H_0^{3/2}(\mathbb{T}_L)$. We consider the mapping $H_0^{3/2}(\mathbb{T}_L) \to H_0^{3/2}(\mathbb{T}_L), \tilde{h} \mapsto h$. For given $\tilde{h}_1$ and $\tilde{h}_2$, let $(\boldsymbol{u}_1, h_1, p_1)$ and $(\boldsymbol{u}_2, h_2, p_2)$ be the corresponding solutions of (2.149) - (2.154). The difference $(\boldsymbol{u}_1 - \boldsymbol{u}_2, h_1 - h_2, p_1 - p_2)$ is a solution of the homogeneous system ($b_h = b_t = 0$), and equation (2.79) yields

$$\begin{aligned} |\lambda| \, \|h_1 - h_2\|_{3/2} \leq & C \left(\|2(\tilde{h}_1 - \tilde{h}_2)\|_{1/2} + \|2 \cot \alpha (\tilde{h}_1 - \tilde{h}_2)\|_{1/2} \right) \\ \leq & C(2 + 2\cot\alpha) \|\tilde{h}_1 - \tilde{h}_2\|_{3/2}. \end{aligned} \tag{2.155}$$

For $\mathfrak{Re}\lambda$ large enough, the mapping therefore has a unique fixed point h which - together with the corresponding $\boldsymbol{u}$ and p - solves (2.138)-(2.143).

Due to (2.78) and (2.79), we have

$$\begin{aligned} \|h\|_{H^{5/2}(\mathbb{T}_L)} + & |\lambda| \, \|h\|_{H^{3/2}(\mathbb{T}_L)} + \|\boldsymbol{u}\|_{H^2(\Omega)} + |\lambda| \, \|\boldsymbol{u}\|_{H^0(\Omega)} + \|\nabla p\|_{H^0(\Omega)} \\ & \leq C \left(\|b_t\|_{H^{1/2}(\mathbb{T}_L)} + \|b_h\|_{H^{3/2}(\mathbb{T}_L)} + \|h\|_{H^{1/2}(\mathbb{T}_L)} \right) \\ & \leq C \left(\|b_t\|_{H^{1/2}(\mathbb{T}_L)} + \|b_h\|_{H^{3/2}(\mathbb{T}_L)} + \|h\|_{H^{3/2}(\mathbb{T}_L)} \right). \end{aligned} \tag{2.156}$$

Choosing $\mathfrak{Re}\lambda$ large enough, we can absorb $\|h\|_{H^{3/2}(\mathbb{T}_L)}$ on the left hand side, and derive (2.147) and (2.148). Similarly, we obtain

$$\begin{aligned} |\lambda|^{s/2} \|\boldsymbol{u}\|_{H^0(\Omega)} + |\lambda|^{\frac{s-2}{2}} \|\nabla p\|_{H^0(\Omega)} + |\lambda|^{\frac{s+1/2}{2}} \|h\|_{H^0(\mathbb{T}_L)} \\ \leq C \left(|\lambda|^{\frac{s-3/2}{2}} \|b_t\|_{H^0(\mathbb{T}_L)} + |\lambda|^{\frac{s-1/2}{2}} \|b_h\|_{H^0(\mathbb{T}_L)} \right). \end{aligned} \tag{2.157}$$

Equation (2.147) then implies

$$\begin{aligned} \|\boldsymbol{u}\|_{H^s(\Omega)} + \|\nabla p\|_{H^{s-2}(\Omega)} + \|h\|_{H^{s+1/2}(\mathbb{T}_L)} \\ \leq C \left(\|b_t\|_{H^{s-3/2}(\mathbb{T}_L)} + \|b_h\|_{H^{s-1/2}(\mathbb{T}_L)} \right) \end{aligned} \tag{2.158}$$

for $s \leq 4$, which in turn implies the same statement for $s \leq 6$, and so on. □

2.3.3. Auxiliary problem C

In order to take care of the inhomogeneity in the momentum equations, we consider the following system of equations:

$$\lambda \boldsymbol{u} - \frac{1}{\mathrm{Re}}\Delta \boldsymbol{u} + \frac{1}{\mathrm{Re}}\nabla p = \boldsymbol{b}_u, \qquad \boldsymbol{x} \in \Omega, \tag{2.159}$$

$$\nabla \cdot \boldsymbol{u} = 0, \qquad \boldsymbol{x} \in \Omega, \tag{2.160}$$

$$\boldsymbol{u} = 0, \qquad \boldsymbol{x} \in W, \tag{2.161}$$

$$u_y + v_x = 0, \qquad \boldsymbol{x} \in \Sigma, \tag{2.162}$$

$$p - 2v_y = 0, \qquad \boldsymbol{x} \in \Sigma. \tag{2.163}$$

For this system, we cite Lemma 3.3 in Beale and Nishida (1985):

Proposition 3. *Let* $s \geq 2$, $\lambda \in \mathbb{C}$ *with* $\mathfrak{Re}\lambda > 0$, *and* $\boldsymbol{b}_u \in \mathrm{P}^0\, H^{s-2}(\Omega)$. *Then there exists a unique solution* $(\boldsymbol{u}, p)$ *of (2.159) - (2.163) such that*

$$\|\boldsymbol{u}\|_{H^s(\Omega)} + |\lambda|^{s/2}\,\|\boldsymbol{u}\|_{H^0(\Omega)} \leq C\left(\|\boldsymbol{b}_u\|_{H^{s-2}(\Omega)} + |\lambda|^{\frac{s-2}{2}}\,\|\boldsymbol{b}_u\|_{H^0(\Omega)}\right) \tag{2.164}$$

and

$$\begin{aligned}\|\nabla p\|_{H^{s-2}(\Omega)} + |\lambda|^{\frac{s-2}{2}}\,\|\nabla p\|_{H^0(\Omega)} + \|p|_\Sigma\|_{H^{s-3/2}(\mathbb{T}_L)} + |\lambda|^{\frac{s-3/2}{2}}\,\|p|_\Sigma\|_{H^0(\mathbb{T}_L)} \\ \leq C\left(\|\boldsymbol{b}_u\|_{H^{s-2}(\Omega)} + |\lambda|^{\frac{s-2}{2}}\,\|\boldsymbol{b}_u\|_{H^0(\Omega)}\right).\end{aligned} \tag{2.165}$$

Let $(\boldsymbol{u}, p)$ be a solution to (2.159) - (2.163). Then

$$\begin{aligned}\int_0^L v(x,1)\mathrm{d}x = \int_0^L\int_0^1 \partial_y v(x,y)\mathrm{d}y\mathrm{d}x = -\int_0^L\int_0^1 \partial_x u(x,y)\mathrm{d}y\mathrm{d}x = \\ -\int_0^1\int_0^L \partial_x u(x,y)\mathrm{d}x\mathrm{d}y = 0.\end{aligned} \tag{2.166}$$

2.3.4. Auxiliary problem D

We can now treat the resolvent equations without surfactant transport, and without perturbation terms in the momentum equation:

$$\lambda \boldsymbol{u} - \frac{1}{\mathrm{Re}}\Delta \boldsymbol{u} + \frac{1}{\mathrm{Re}}\nabla p = \boldsymbol{b}_u, \qquad \boldsymbol{x} \in \Omega, \tag{2.167}$$

$$\nabla \cdot \boldsymbol{u} = 0, \qquad \boldsymbol{x} \in \Omega, \tag{2.168}$$

$$\boldsymbol{u} = 0, \qquad \boldsymbol{x} \in W, \tag{2.169}$$

$$\lambda h - v = b_h, \qquad \boldsymbol{x} \in \Sigma, \tag{2.170}$$

$$u_y + v_x - 2h = b_t, \qquad \boldsymbol{x} \in \Sigma, \tag{2.171}$$

$$p - 2v_y - 2\cot\alpha h + \frac{1}{\mathrm{Ca}}h_{xx} = 0, \qquad \boldsymbol{x} \in \Sigma. \tag{2.172}$$

Proposition 4. *Let* $s \geq 2, \boldsymbol{b}_u \in \mathrm{P}^0\, H^{s-2}(\Omega), b_h \in H_0^{s-1/2}(\mathbb{T}_L), b_t \in H_0^{s-3/2}(\mathbb{T}_L)$. *There exists a* $\gamma_0 > 0$ *such that for every* $\lambda \in \mathbb{C}$ *with* $\mathfrak{Re}\lambda \geq \gamma_0$, *there is a unique solution* $(\boldsymbol{u}, p, h)$ *of (2.167)-(2.172) such that*

$$\int_{\mathbb{T}_L} h(x)\mathrm{d}x = 0, \text{ and} \tag{2.173}$$

$$\begin{aligned} &\|\boldsymbol{u}\|_{H^s(\Omega)} + |\lambda|^{s/2} \|\boldsymbol{u}\|_{H^0(\Omega)} + \|\nabla p\|_{H^{s-2}(\Omega)} \\ &\quad + |\lambda|^{\frac{s-2}{2}} \|\nabla p\|_{H^0(\Omega)} + \|h\|_{H^{s+1/2}(\mathbb{T}_L)} + |\lambda|^{\frac{s+1/2}{2}} \|h\|_{H^0(\mathbb{T}_L)} \\ &\quad \leq C \Big(\|b_t\|_{H^{s-3/2}(\mathbb{T}_L)} + |\lambda|^{\frac{s-3/2}{2}} \|b_t\|_{H^0(\mathbb{T}_L)} + \|b_h\|_{H^{s-1/2}(\mathbb{T}_L)} \\ &\quad + |\lambda|^{\frac{s-1/2}{2}} \|b_h\|_{H^0(\mathbb{T}_L)} + \|\boldsymbol{b}_u\|_{H^{s-2}(\Omega)} + |\lambda|^{\frac{s-2}{2}} \|\boldsymbol{b}_u\|_{H^0(\Omega)} \Big). \end{aligned} \tag{2.174}$$

Moreover,

$$\|h\|_{H^{5/2}(\mathbb{T}_L)} + |\lambda| \, \|h\|_{H^{3/2}(\mathbb{T}_L)} \leq C \left(\|b_t\|_{H^{1/2}(\mathbb{T}_L)} + \|b_h\|_{H^{3/2}(\mathbb{T}_L)} + \|\boldsymbol{b}_u\|_{H^0(\Omega)} \right) \tag{2.175}$$

and

$$\|\boldsymbol{u}\|_{H^2(\Omega)} + |\lambda| \, \|\boldsymbol{u}\|_{H^0(\Omega)} + \|\nabla p\|_{H^0(\Omega)} \leq C \left(\|b_t\|_{H^{1/2}(\mathbb{T}_L)} + \|b_h\|_{H^{3/2}(\mathbb{T}_L)} + \|\boldsymbol{b}_u\|_{H^0(\Omega)} \right). \tag{2.176}$$

Proof. Let $(\boldsymbol{u}^{(1)}, p^{(1)})$ be the solution to (2.159) - (2.163) with inhomogeneity $\boldsymbol{b}_u$. Set $(\boldsymbol{u}, p) = (\boldsymbol{u}^{(1)} + \boldsymbol{u}^{(2)}, p^{(1)} + p^{(1)})$ in the above system of equations. This leaves us with the problem

$$\lambda \boldsymbol{u}^{(2)} - \frac{1}{\mathrm{Re}} \Delta \boldsymbol{u}^{(2)} + \frac{1}{\mathrm{Re}} \nabla p^{(2)} = 0 \text{ in } \Omega, \tag{2.177}$$

$$\nabla \cdot \boldsymbol{u}^{(2)} = 0 \text{ in } \Omega, \tag{2.178}$$

$$\boldsymbol{u}^{(2)} = 0 \text{ on } W, \tag{2.179}$$

$$\lambda h - v^{(2)} = b_h + v^{(1)}|_\Sigma \text{ on } \Sigma, \tag{2.180}$$

$$u_y^{(2)} + v_x^{(2)} - 2h = b_t \text{ on } \Sigma, \tag{2.181}$$

$$p^{(2)} - 2v_y^{(2)} - 2\cot\alpha h + \frac{1}{\mathrm{Ca}} h_{xx} = 0 \text{ on } \Sigma. \tag{2.182}$$

Due to (2.166), $b_h + v^{(2)}|_\Sigma \in H_0^{s-1/2}(\mathbb{T}_L)$. By Proposition 2, there is a unique solution $(\boldsymbol{u}^{(2)}, p^{(2)}, h)$ of this system. In order to get the stated estimates, we need the trace theorem and (2.164):

$$\|v^{(1)}|_\Sigma\|_{s-1/2} \leq C \|v^{(1)}\|_s \leq C \left(\|\boldsymbol{b}_u\|_{s-2} + |\lambda|^{\frac{s-2}{2}} \|\boldsymbol{b}_u\|_0 \right). \tag{2.183}$$

By the interpolation inequality for Sobolev spaces (Adams (1975), IV.4.17) and Young's inequality, we calculate

$$\begin{aligned}|\lambda|^{\frac{s-1/2}{2}}\|v^{(1)}|_\Sigma\|_0 &\le C\,|\lambda|^{\frac{s-1/2}{2}}\|v^{(1)}\|_{1/2} \le C\,|\lambda|^{\frac{s-1/2}{2}}\|v^{(1)}\|_s^{\frac{1}{2s}}\|v^{(1)}\|_0^{1-\frac{1}{2s}}\\ &\le C\left(\|v^{(1)}\|_s + |\lambda|^{s/2}\|v^{(1)}\|_0\right) \le C\left(\|\boldsymbol{b}_u\|_{s-2} + |\lambda|^{\frac{s-2}{2}}\|\boldsymbol{b}_u\|_0\right).\end{aligned} \tag{2.184}$$

□

2.3.5. Auxiliary problem E

As a last auxiliary problem, we consider the surfactant transport equation without any coupling to the velocity field.

Proposition 5. *Let $s \ge 2$, $b_c \in H_0^{s-2}(\mathbb{T}_L)$. For every $\lambda \in \mathbb{C}$ with $\mathfrak{Re}\lambda \ge \mathrm{Pe}$, there exists a unique solution of the equation*

$$\lambda c + c_x - \frac{1}{\mathrm{Pe}}c_{xx} = b_c \ \textit{in}\ \mathbb{T}_L \tag{2.185}$$

such that

$$\int_{\mathbb{T}_L} c(x)\mathrm{d}x = 0. \tag{2.186}$$

The following estimates hold:

$$\|c\|_{H^s(\mathbb{T}_L)} \le C\|b_c\|_{H^{s-2}(\mathbb{T}_L)}, \tag{2.187}$$

$$|\lambda|^{s/2}\|c\|_{H^0(\mathbb{T}_L)} \le C\,|\lambda|^{\frac{s-2}{2}}\|b_c\|_{H^0(\mathbb{T}_L)}, \tag{2.188}$$

$$|\lambda|^{1/4}\|c\|_{H^{3/2}(\mathbb{T}_L)} \le C\|b_c\|_{H^0(\mathbb{T}_L)}. \tag{2.189}$$

Proof. We expand c and b_c into a Fourier series, obtaining

$$c = \sum_{\xi\neq 0}\frac{b_c^{(k)}}{\lambda + i\xi + \frac{|\xi|^2}{\mathrm{Pe}}}e^{i\xi x}. \tag{2.190}$$

We estimate

$$\left|\frac{|\xi|^s\, b_c^{(k)}}{\lambda + i\xi + \frac{|\xi|^2}{\mathrm{Pe}}}\right|^2 = \frac{|\xi|^4\,\mathrm{Pe}^2}{\left|\lambda\,\mathrm{Pe} + i\xi\,\mathrm{Pe} + |\xi|^2\right|^2}|\xi|^{2s-4}\left|b_c^{(k)}\right|^2 \le \mathrm{Pe}^2\,|\xi|^{2s-4}\left|b_c^{(k)}\right|^2, \tag{2.191}$$

which yields (2.187). In order to show (2.188), we set $\lambda = \alpha + i\beta, \alpha \ge \mathrm{Pe}$, and calculate

$$\begin{aligned}\left|\lambda\,\mathrm{Pe} + i\xi\,\mathrm{Pe} + |\xi|^2\right|^2 &= \mathrm{Pe}^2(\alpha^2+\beta^2) + 2\,\mathrm{Pe}\,\alpha\,|\xi|^2 + |\xi|^4 + \mathrm{Pe}^2\,|\xi|^2 + 2\beta\,\mathrm{Pe}^2\,\xi\\ &\ge \mathrm{Pe}^2(\alpha^2+\beta^2) + 2\,\mathrm{Pe}\,\alpha\,|\xi|^2 + |\xi|^4 + \mathrm{Pe}^2\,|\xi|^2 - \left|2\beta\,\mathrm{Pe}^2\,\xi\right|.\end{aligned} \tag{2.192}$$

We estimate

$$\left|2\beta \operatorname{Pe}^2 \xi\right| = \left|(\operatorname{Pe}\beta)(2\operatorname{Pe}\xi)\right| \leq \frac{1}{2}\operatorname{Pe}^2\beta^2 + 2\operatorname{Pe}^2|\xi|^2 . \tag{2.193}$$

Putting this into the equation above, we derive

$$\left|\lambda \operatorname{Pe} + i\xi \operatorname{Pe} + |\xi|^2\right|^2 \geq \frac{1}{2}\operatorname{Pe}^2|\lambda|^2 , \tag{2.194}$$

and finally

$$\left|\frac{|\lambda|^{s/2}\, b_c^{(k)}}{\lambda + i\xi + \frac{|\xi|^2}{\operatorname{Pe}}}\right|^2 \leq \frac{|\lambda|^2}{\left|\lambda\operatorname{Pe} + i\xi\operatorname{Pe} + |\xi|^2\right|^2}\operatorname{Pe}^2|\lambda|^{s-2}\left|b_c^{(k)}\right|^2 \leq 2\,|\lambda|^{s-2}\left|b_c^{(k)}\right|^2 . \tag{2.195}$$

Inequality (2.189) follows by interpolation:

$$\|c\|_{3/2} \leq C\|c\|_2^{3/4}\|c\|_0^{1/4} \leq C\,|\lambda|^{-1/4}\,\|b_c\|_0. \tag{2.196}$$

□

2.3.6. Construction of the resolvent

The aim of this section is to prove the following theorem:

Theorem 1. *There is a* $\gamma_0 > 0$ *such that, if* $\mathfrak{Re}\lambda \geq \gamma_0$*, there exists the inverse* $(\lambda - \boldsymbol{G})^{-1}$ *in* X *with* $(\lambda - \boldsymbol{G})^{-1}X = \mathcal{D}(\boldsymbol{G})$ *and its operator norm satisfying*

$$\|(\lambda - \boldsymbol{G})^{-1}\|_{\mathcal{L}(X,X)} \leq \frac{C}{|\lambda|}, \tag{2.197}$$

where

$$X = \mathrm{P}^0\, H^0(\Omega) \times H_0^{3/2}(\mathbb{T}_L) \times H_0^0(\mathbb{T}_L). \tag{2.198}$$

This implies

Corollary 1. *There exists a* $\theta \in (\frac{\pi}{2}, \pi)$*, such that, for* $\lambda \in \mathbb{C}$ *with* $|\arg(\lambda - \gamma_0)| \leq \theta$*,* $(\lambda - \boldsymbol{G})^{-1}$ *exists and satisfies*

$$\|(\lambda - \boldsymbol{G})^{-1}\|_{\mathcal{L}(X,X)} \leq \frac{C}{|\lambda|} \tag{2.199}$$

for some $C > 0$.

Proof. According to Theorem 1, every $\lambda = \gamma_0 + is, s \in \mathbb{R}$ is an element of the resolvent set $\rho(\boldsymbol{G})$. Consider $\mu = \lambda - \alpha$ for $\alpha \geq 0$. We calculate

$$\begin{aligned} \mu - \boldsymbol{G} &= \lambda - \boldsymbol{G} - \alpha \\ &= \left(\boldsymbol{I} - \alpha(\lambda - \boldsymbol{G})^{-1}\right)(\lambda - \boldsymbol{G}). \end{aligned} \tag{2.200}$$

By expansion into a Neumann series, this is invertible if $\|\alpha(\lambda - \boldsymbol{G})^{-1}\| \leq \frac{1}{2}$. Let $\alpha \leq \frac{|s|}{2C}$. Then, using (2.197), we have

$$\|\alpha(\lambda - \boldsymbol{G})^{-1}\| \leq \frac{\alpha C}{|\lambda|} \leq \frac{\alpha C}{|s|} \leq \frac{1}{2}. \tag{2.201}$$

Therefore, all $\mu \in \mathbb{C}$ with $|\arg(\mu - \gamma_0)| \leq \frac{\pi}{2} + \arctan(\frac{1}{2C})$ are in the resolvent set.

Equation (2.199) follows by calculating

$$\begin{aligned} \|(\mu - \boldsymbol{G})^{-1}\| &= \|(\lambda - \boldsymbol{G})^{-1}(\boldsymbol{I} - \alpha(\lambda - \boldsymbol{G})^{-1})^{-1}\| \\ &\leq \frac{C}{|\lambda|}\frac{1}{1 - \|\alpha(\lambda - \boldsymbol{G})^{-1}\|} \\ &\leq 2\frac{C}{|\lambda|}. \end{aligned} \tag{2.202}$$

□

We show the claim of Theorem 1 for the simpler operator $(\lambda - \boldsymbol{G}_0)^{-1}$, where perturbation terms of lower order in the momentum equation and the kinematic boundary condition are omitted. More precisely, we consider

$$\boldsymbol{G}_0 \begin{pmatrix} \boldsymbol{u} \\ h \\ c \end{pmatrix} = \begin{pmatrix} -A_0 & -\frac{1}{\mathrm{Re}} R^*(2\cot\vartheta - \frac{1}{\mathrm{Ca}}\partial_{xx}) & 0 \\ R & 0 & 0 \\ -\partial_x Q & 0 & -\partial_x + \frac{1}{\mathrm{Pe}}\partial_{xx} \end{pmatrix} \begin{pmatrix} \boldsymbol{u} \\ h \\ c \end{pmatrix}, \tag{2.203}$$

where

$$A_0 \boldsymbol{u} = -\frac{1}{\mathrm{Re}}\,\mathrm{P}^0\,\Delta \boldsymbol{u} + \frac{1}{\mathrm{Re}} R^* 2 v_y. \tag{2.204}$$

The claim for the original problem then follows by standard perturbation theory (cf. Pazy (1983, Chapter 3)).

The resolvent problem for $\boldsymbol{G}_0$ is rewritten as

$$\lambda \boldsymbol{u} - \frac{1}{\mathrm{Re}}\Delta \boldsymbol{u} + \frac{1}{\mathrm{Re}}\nabla p = \boldsymbol{b}_u, \qquad \boldsymbol{x} \in \Omega, \tag{2.205}$$

$$\nabla \cdot \boldsymbol{u} = 0, \qquad \boldsymbol{x} \in \Omega, \tag{2.206}$$

$$\boldsymbol{u} = 0, \qquad \boldsymbol{x} \in W, \tag{2.207}$$

$$\lambda h - v = b_h, \qquad \boldsymbol{x} \in \Sigma, \tag{2.208}$$

$$u_y + v_x - 2h - \frac{\mathrm{Ma}}{\mathrm{Ca}} c_x = 0, \qquad \boldsymbol{x} \in \Sigma, \tag{2.209}$$

$$p - 2v_y - 2\cot\alpha h + \frac{1}{\mathrm{Ca}} h_{xx} = 0, \qquad \boldsymbol{x} \in \Sigma, \tag{2.210}$$

$$\lambda c + c_x + u_x - \frac{1}{\mathrm{Pe}} c_{xx} = b_c, \qquad \boldsymbol{x} \in \Sigma. \tag{2.211}$$

We have the following, which implies Theorem 1:

Theorem 2. *Let* $s \geq 2, \boldsymbol{b}_u \in \mathrm{P}^0\, H^{s-2}(\Omega), b_h \in H_0^{s-1/2}(\mathbb{T}_L), b_c \in H_0^{s-2}(\mathbb{T}_L)$*. There exists a* $\gamma_0 > 0$ *such that for every* $\lambda \in \mathbb{C}$ *with* $\mathfrak{Re}\lambda \geq \gamma_0$*, there is a unique solution* $(\boldsymbol{u}, p, h, c)$ *of (2.205)-(2.211) such that*

$$\int_{\mathbb{T}_L} h(x)\mathrm{d}x = 0, \tag{2.212}$$

$$\int_{\mathbb{T}_L} c(x)\mathrm{d}x = 0, \ \textit{and} \tag{2.213}$$

$$\begin{aligned} &\|\boldsymbol{u}\|_{H^s(\Omega)} + |\lambda|^{s/2} \|\boldsymbol{u}\|_{H^0(\Omega)} + \|\nabla p\|_{H^{s-2}(\Omega)} + |\lambda|^{\frac{s-2}{2}} \|\nabla p\|_{H^0(\Omega)} \\ &+\|h\|_{H^{s+1/2}(\mathbb{T}_L)} + |\lambda|^{\frac{s+1/2}{2}} \|h\|_{H^0(\mathbb{T}_L)} + \|c\|_{H^s(\mathbb{T}_L)} + |\lambda|^{s/2} \|c\|_{H^0(\mathbb{T}_L)} \\ &\leq C \Big(\|\boldsymbol{b}_u\|_{H^{s-2}(\Omega)} + |\lambda|^{\frac{s-2}{2}} \|\boldsymbol{b}_u\|_{H^0(\Omega)} + \|b_h\|_{H^{s-1/2}(\mathbb{T}_L)} \\ &+ |\lambda|^{\frac{s-1/2}{2}} \|b_h\|_{H^0(\mathbb{T}_L)} + \|b_c\|_{H^{s-2}(\mathbb{T}_L)} + |\lambda|^{\frac{s-2}{2}} \|b_c\|_{H^0(\mathbb{T}_L)} \Big). \end{aligned} \tag{2.214}$$

Moreover,

$$\begin{aligned} &\|h\|_{H^{5/2}(\mathbb{T}_L)} + |\lambda| \|h\|_{H^{3/2}(\mathbb{T}_L)} + \|\boldsymbol{u}\|_{H^2(\Omega)} + |\lambda| \|\boldsymbol{u}\|_{H^0(\Omega)} \\ &+ \|\nabla p\|_{H^0(\Omega)} + \|c\|_{H^2(\mathbb{T}_L)} + |\lambda| \|c\|_{H^0(\mathbb{T}_L)} \\ &\leq C \Big(\|\boldsymbol{b}_u\|_{H^0(\Omega)} + \|b_h\|_{H^{3/2}(\mathbb{T}_L)} + \|b_c\|_{H^0(\mathbb{T}_L)} \Big). \end{aligned} \tag{2.215}$$

Proof. For a given $\tilde{c} \in H_0^{3/2}(\mathbb{T}_L)$, let $(\boldsymbol{u}, p, h)$ be the solution of (2.167)-(2.172) with the given inhomogeneities $\boldsymbol{b}_u, b_h$, and $b_t = \frac{\mathrm{Ma}}{\mathrm{Ca}}\tilde{c}_x \in H_0^{1/2}(\mathbb{T}_L)$. Then, $u_x|_\Sigma \in H_0^{1/2}(\mathbb{T}_L)$, and we can consider the solution c of (2.185) with right hand side $b_c - u_x|_\Sigma$. For two given $\tilde{c}^{(1)}$ and $\tilde{c}^{(2)}$, the difference $(\boldsymbol{u}^{(1)} - \boldsymbol{u}^{(2)}, p^{(1)} - p^{(2)}, h^{(1)} - h^{(2)})$ is then a solution to (2.167)-(2.172) with $\boldsymbol{b}_u = b_h = 0$, $b_t = \frac{\mathrm{Ma}}{\mathrm{Ca}}(\tilde{c}_x^{(1)} - \tilde{c}_x^{(2)})$, and $c^{(1)} - c^{(2)}$ solves (2.185) with right hand side $u_x^{(2)}|_\Sigma - u_x^{(1)}|_\Sigma$. We can therefore estimate

$$\begin{aligned} \|c^{(1)} - c^{(2)}\|_{H^{3/2}(\mathbb{T}_L)} &\leq C\, |\lambda|^{-1/4} \|\boldsymbol{u}^{(1)}|_\Sigma - \boldsymbol{u}^{(2)}|_\Sigma\|_{H^0(\mathbb{T}_L)} \\ &\leq C\, |\lambda|^{-1/4} \|\boldsymbol{u}^{(1)} - \boldsymbol{u}^{(2)}\|_{H^2(\Omega)} \\ &\leq C\, |\lambda|^{-1/4} \frac{\mathrm{Ma}}{\mathrm{Ca}} \|\tilde{c}_x^{(1)} - \tilde{c}_x^{(2)}\|_{H^{1/2}(\mathbb{T}_L)} \\ &\leq C\, |\lambda|^{-1/4} \frac{\mathrm{Ma}}{\mathrm{Ca}} \|\tilde{c}^{(1)} - \tilde{c}^{(2)}\|_{H^{3/2}(\mathbb{T}_L)}. \end{aligned} \tag{2.216}$$

Therefore, for $\mathfrak{Re}\lambda$ large enough, the mapping

$$H^{3/2}(\mathbb{T}_L) \to H^{3/2}(\mathbb{T}_L) : \tilde{c} \mapsto c \tag{2.217}$$

has a unique fixed point which, together with the corresponding $(\boldsymbol{u}, p, h)$ solves (2.205)-(2.211). The stated estimates follow by combining the estimates in Proposition 4 and 5, and by similar arguments as for Auxiliary Problem B. ☐

2.4. Stability estimates

The aim of this is to give a sufficient criterion for the spectrum to be contained in the left half plane:

Theorem 3. *Let*

$$\mathrm{Re} \leq \frac{4}{54 + \frac{27L^2}{4\pi^2}}, \tag{2.218}$$

$$\mathrm{Ca} \leq \left(2\,\mathrm{Re}(1 + \frac{11L^2}{16\pi^2} + \frac{27L^4}{128\pi^2}) + \frac{2}{\mathrm{Re}}(1 + \frac{11L^2}{8\pi^2} + \frac{9L^4}{4\pi^4})\right)^{-1}, \tag{2.219}$$

and

$$\mathrm{Pe} \leq \frac{4\pi^2}{L^2}. \tag{2.220}$$

Then $\sigma(\boldsymbol{G}) \subset \{\zeta \in \mathbb{C} : \mathfrak{Re}\zeta \leq -\frac{1}{2}\}$.

In this section, $\|\cdot\|_0$ is an abbreviation for the usual L^2-norm.

2.4.1. Inequalities on a periodic slab

We start by giving explicit constants for some frequently used inequalities on a periodic slab.

Lemma 6. *(Poincaré-Friedrichs) Let* $f \in H^1(\Omega)$ *with* $f = 0$ *on* W*. Then*

$$\|f\|^2_{L^2(\Omega)} \leq \|f_y\|^2_{L^2(\Omega)}. \tag{2.221}$$

Proof.

$$\begin{aligned} \|f\|^2_{L^2(\Omega)} &= \int_0^L \int_0^1 \left|\int_0^z \partial_y f(x,y)\mathrm{d}y\right|^2 \mathrm{d}z\mathrm{d}x \\ &\leq \int_0^L \int_0^1 (\int_0^z |1|^2\,\mathrm{d}y)(\int_0^z |\partial_y f(x,y)|^2\,\mathrm{d}y)\mathrm{d}z\mathrm{d}x \\ &\leq \int_0^L \int_0^1 |\partial_y f(x,y)|^2\,\mathrm{d}y\mathrm{d}x = \|f_y\|^2_{L^2(\Omega)}. \end{aligned} \tag{2.222}$$

□

Lemma 7. *(Trace) Let* $f \in H^1(\Omega)$ *with* $f = 0$ *on* W*. Then*

$$\|f\|^2_{L^2(\Sigma)} \leq \|f_y\|^2_{L^2(\Omega)}. \tag{2.223}$$

Proof.

$$\begin{aligned} \|f\|^2_{L^2(\Sigma)} &= \int_0^L |f(x,1)|^2\,\mathrm{d}x \\ &= \int_0^L \left|\int_0^1 f_y \mathrm{d}y\right|^2 \mathrm{d}x \\ &\leq \int_0^L (\int_0^1 |1|^2\,\mathrm{d}y)(\int_0^1 |f_y|^2\,\mathrm{d}y)\mathrm{d}x \leq \|f_y\|^2_{L^2(\Omega)}. \end{aligned} \tag{2.224}$$

□

Lemma 8. *(Korn) Let $\boldsymbol{u} = (u, v) \in H^1(\Omega)$ such that $\nabla \cdot \boldsymbol{u} = 0$ in Ω and $\boldsymbol{u} = 0$ on W. Then*

$$\|\nabla \boldsymbol{u}\|^2_{L^2(\Omega)} \leq 3\left[\boldsymbol{u}, \boldsymbol{u}\right], \tag{2.225}$$

where

$$[\boldsymbol{u}, \boldsymbol{u}] = \int_\Omega (|u_x|^2 + \frac{1}{2}|u_y + v_x|^2 + |v_y|^2) \mathrm{d}\boldsymbol{x}. \tag{2.226}$$

The proof that this constant is optimal is given in Teramoto and Tomoeda (2012).

Lemma 9. *(Poincaré) Let $f \in H^1_0(\Sigma)$. Then*

$$\|f\|^2_{L^2(\Sigma)} \leq \frac{L^2}{4\pi^2}\|f_x\|^2_{L^2(\Sigma)}. \tag{2.227}$$

Proof. Expanding f as a Fourier series, we write

$$f = \sum_{k \neq 0} f^{(k)} e^{iklx}, \tag{2.228}$$

where $f^{(k)}$ is the k-th Fourier coefficient, and $l = \frac{2\pi}{L}$. Then,

$$f_x = \sum_{k \neq 0} ikl f^{(k)} e^{iklx}. \tag{2.229}$$

Direct calculation shows

$$\|f\|^2_{L^2(\Sigma)} = L \sum_{k \neq 0} \left|f^{(k)}\right|^2 \tag{2.230}$$

$$= \frac{L^2}{4\pi^2} \frac{4\pi^2}{L} \sum_{k \neq 0} \left|f^{(k)}\right|^2 \tag{2.231}$$

$$\leq \frac{L^2}{4\pi^2} \frac{4\pi^2}{L} \sum_{k \neq 0} k^2 \left|f^{(k)}\right|^2 \tag{2.232}$$

$$= \frac{L^2}{4\pi^2}\|f_x\|^2_{L^2(\Sigma)}. \tag{2.233}$$

□

Since the constant in Poincaré's inequality will be frequently used in the following, we set

$$c_P = \frac{L^2}{4\pi^2}. \tag{2.234}$$

2.4.2. Derivation of the energy equation

Since the resolvents of $\boldsymbol{G}$ are compact, the spectrum of $\boldsymbol{G}$ consists of a point spectrum only. This allows us to consider eigenfunctions of the operator $\boldsymbol{G}$, i.e. functions $(\boldsymbol{u}, p, h)$ such that

$$\lambda \boldsymbol{u} + \boldsymbol{u}_N \cdot \nabla \boldsymbol{u} + \boldsymbol{u} \cdot \nabla \boldsymbol{u}_N - \frac{1}{\mathrm{Re}} \Delta \boldsymbol{u} + \frac{1}{\mathrm{Re}} \nabla p = 0, \qquad \boldsymbol{x} \in \Omega, \tag{2.235}$$

$$\nabla \cdot \boldsymbol{u} = 0, \qquad \boldsymbol{x} \in \Omega, \tag{2.236}$$

$$\boldsymbol{u} = 0, \qquad y = 0, \tag{2.237}$$

$$\lambda h + h_x - v = 0, \qquad \boldsymbol{x} \in \Sigma, \tag{2.238}$$

$$\lambda c + c_x + u_x - \frac{1}{\mathrm{Pe}} c_{xx} = 0, \qquad \boldsymbol{x} \in \Sigma, \tag{2.239}$$

$$p - 2 \cot \vartheta h - 2 v_y + \frac{1}{\mathrm{Ca}} h_{xx} = 0, \qquad \boldsymbol{x} \in \Sigma, \tag{2.240}$$

$$u_y + v_x - 2h + \frac{\mathrm{Ma}}{\mathrm{Ca}} c_x = 0, \qquad \boldsymbol{x} \in \Sigma. \tag{2.241}$$

for some $\lambda = r + is \in \mathbb{C}$.

We multiply equation (2.235) with $\overline{\boldsymbol{u}}$, integrate over Ω, and take real parts. For the terms with the stress tensor, we use integration by parts and the boundary conditions in the following way:

$$\begin{aligned}
\int_\Omega (\nabla p - \Delta \boldsymbol{u}) \cdot \overline{\boldsymbol{u}} \mathrm{d}\boldsymbol{x} &= \int_\Omega (\nabla \cdot [p\boldsymbol{I} - (\nabla \boldsymbol{u} + \nabla \boldsymbol{u}^{\mathsf{T}})]) \cdot \overline{\boldsymbol{u}} \mathrm{d}\boldsymbol{x} \\
&= \int_\Omega (\nabla \cdot \begin{bmatrix} p - 2u_x & -u_y - v_x \\ -u_y - v_x & p - 2v_y \end{bmatrix}) \cdot \begin{pmatrix} \overline{u} \\ \overline{v} \end{pmatrix} \mathrm{d}\boldsymbol{x} \\
&= - \int_\Omega (\begin{pmatrix} p - 2u_x \\ -u_y - v_x \end{pmatrix} \cdot \begin{pmatrix} \overline{u}_x \\ \overline{u}_y \end{pmatrix} + \begin{pmatrix} -u_y - v_x \\ p - 2v_y \end{pmatrix} \cdot \begin{pmatrix} \overline{v}_x \\ \overline{v}_y \end{pmatrix}) \mathrm{d}\boldsymbol{x} \\
&\quad + \int_\Sigma ((-u_y - v_x)\overline{u} + (p - 2v_y)\overline{v}) \, \mathrm{d}x \\
&= - \int_\Omega (p(\overline{u}_x + \overline{v}_y) - 2\left|u_x\right|^2 - \left|u_y\right|^2 - v_x \overline{u}_y - u_y \overline{v}_x - \left|v_x\right|^2 - 2\left|v_y\right|^2) \mathrm{d}\boldsymbol{x} \\
&\quad + \int_\Sigma \left((\frac{\mathrm{Ma}}{\mathrm{Ca}} c_x - 2h)\overline{u} + (2 \cot \vartheta h - \frac{1}{\mathrm{Ca}} h_{xx})(\overline{\lambda h} + \overline{h}_x) \right) \mathrm{d}x \\
&= \int_\Omega 2\left|u_x\right|^2 + 2\left|v_y\right|^2 + \left|u_y + v_x\right|^2 \mathrm{d}\boldsymbol{x} \\
&\quad + \frac{\mathrm{Ma}}{\mathrm{Ca}} \int_\Sigma c_x \overline{u} \mathrm{d}x - 2 \int_\Sigma h \overline{u} \mathrm{d}x + 2\overline{\lambda} \cot \vartheta \int_\Sigma \left|h\right|^2 \mathrm{d}x \\
&\quad + 2 \cot \vartheta \int_\Sigma h \overline{h}_x \mathrm{d}x + \frac{\overline{\lambda}}{\mathrm{Ca}} \int_\Sigma \left|h_x\right|^2 \mathrm{d}x - \frac{1}{\mathrm{Ca}} \int_\Sigma h_{xx} \overline{h}_x \mathrm{d}x.
\end{aligned} \tag{2.242}$$

The term with p in the bulk vanishes as $\boldsymbol{u}$ is divergence free. Integration by parts shows

$$\mathfrak{Re}\int_\Sigma h\overline{h}_x \mathrm{d}x = \mathfrak{Re}\int_\Sigma h_{xx}\overline{h}_x \mathrm{d}x = 0. \tag{2.243}$$

For the perturbation terms, we calculate

$$\mathfrak{Re}\int_\Omega (\boldsymbol{u}_N \cdot \nabla \boldsymbol{u}) \cdot \overline{\boldsymbol{u}} \mathrm{d}\boldsymbol{x} = \mathfrak{Re}\int_\Omega (2y - y^2)(u_x\overline{u} + v_x\overline{v})\mathrm{d}\boldsymbol{x} = 0, \tag{2.244}$$

and

$$\int_\Omega (\boldsymbol{u} \cdot \nabla \boldsymbol{u}_N) \cdot \overline{\boldsymbol{u}} \mathrm{d}\boldsymbol{x} = \int_\Omega (2 - 2y)\overline{u}v\mathrm{d}\boldsymbol{x}. \tag{2.245}$$

Altogether, we get

$$\begin{aligned} r(\|\boldsymbol{u}\|_0^2 + \frac{2\cot\vartheta}{\mathrm{Re}}\|h\|_0^2 + \frac{1}{\mathrm{Re\,Ca}}\|h_x\|_0^2) + \frac{1}{\mathrm{Re}}\int_\Omega (2\,|u_x|^2 + 2\,|v_y|^2 + |u_y + v_x|^2)\mathrm{d}\boldsymbol{x} \\ + \mathfrak{Re}\left(\frac{\mathrm{Ma}}{\mathrm{Re\,Ca}}\int_\Sigma c_x\overline{u}\mathrm{d}x - \frac{2}{\mathrm{Re}}\int_\Sigma h\overline{u}\mathrm{d}x + \int_\Omega (2-2y)\overline{u}v\mathrm{d}\boldsymbol{x}\right) = 0. \end{aligned} \tag{2.246}$$

Similarly, testing (2.239) with c, taking real parts and multiplying the equation with $\frac{\mathrm{Ma}}{\mathrm{Re\,Ca}}$ yields

$$r\frac{\mathrm{Ma}}{\mathrm{Re\,Ca}}\|c\|_0^2 - \frac{\mathrm{Ma}}{\mathrm{Re\,Ca}}\mathfrak{Re}\int_\Sigma \overline{c}_x u\mathrm{d}x + \frac{\mathrm{Ma}}{\mathrm{Re\,Ca\,Pe}}\|c_x\|_0^2 = 0. \tag{2.247}$$

The perturbation term $\int_\Sigma h\overline{u}\mathrm{d}x$ is problematic, since up to now, we do not have any control over h. In order to obtain a dissipative term with h, we employ a variant of the free work method due to Padula and Solonnikov (2000) and construct an auxiliary vector field $\boldsymbol{w}_h$ in the following way:

Given a function $h \in H_0^1(\Sigma)$, we set

$$\boldsymbol{w}_h(x,y) = \begin{pmatrix} w^{(1)} \\ w^{(2)} \end{pmatrix}(x,y) = \begin{pmatrix} \phi(x)\partial_y\psi(y) \\ -\partial_x\phi(x)\psi(y) \end{pmatrix} \tag{2.248}$$

with $\psi(y) = -2y^3 + 3y^2$, and $\phi(x)$ the unique solution in $H_0^2(\Sigma)$ of the problem

$$-\partial_x\phi(x) = h(x), x \in \Sigma. \tag{2.249}$$

With Lemma 9, we have

$$\|\phi\|_0^2 \le \frac{L^2}{4\pi^2}\|h\|_0^2. \tag{2.250}$$

The maximum norms of ψ and its derivatives on the interval $[0,1]$ can be readily obtained and are

$$\|\psi\|_\infty = 1, \|\psi_y\|_\infty = \frac{3}{2}, \|\psi_{yy}\|_\infty = 6. \tag{2.251}$$

By construction, we have

$$\lambda \boldsymbol{w}_h = \boldsymbol{w}_{\lambda h} \tag{2.252}$$

for all $\lambda \in \mathbb{C}$.

Since $\psi(0) = \psi_y(0) = \psi_y(1) = 0$ and $\psi(1) = 1$, the following properties hold:

$$\begin{aligned} \nabla \cdot \boldsymbol{w}_h &= 0 \text{ in } \Omega, & (2.253)\\ \boldsymbol{w}_h &= 0 \text{ on } W, & (2.254)\\ \boldsymbol{w}_h &= (0, h) \text{ on } \Sigma. & (2.255) \end{aligned}$$

Testing (2.235) with $\boldsymbol{w}_h$, performing the same steps as in (2.242) and taking real parts, we derive the equation

$$\begin{aligned} \frac{2\cot\vartheta}{\mathrm{Re}}\|h\|_0^2 + \frac{1}{\mathrm{Re}\,\mathrm{Ca}}\|h_x\|_0^2 + \mathfrak{Re}\left(\lambda \int_\Omega \boldsymbol{u} \cdot \overline{\boldsymbol{w}_h}\mathrm{d}\boldsymbol{x} + \int_\Omega (\boldsymbol{u}_N \cdot \nabla \boldsymbol{u} + \boldsymbol{u} \cdot \nabla \boldsymbol{u}_N) \cdot \overline{\boldsymbol{w}_h}\mathrm{d}\boldsymbol{x}\right.\\ \left. + \frac{1}{\mathrm{Re}} \int_\Omega (2u_x\overline{w_x^{(1)}} + 2v_y\overline{w_y^{(2)}} + (u_y + v_x)(\overline{w_y^{(1)}} + \overline{w_x^{(2)}}))\mathrm{d}\boldsymbol{x}\right) = 0. \end{aligned} \tag{2.256}$$

We add equations (2.246), (2.247) and (2.256). Noting that

$$\mathfrak{Re}\left(\int_\Sigma (c_x\overline{u} - \overline{c}_x u)\mathrm{d}x\right) = 0, \tag{2.257}$$

this yields the equation

$$rA + D + P = 0. \tag{2.258}$$

We have grouped the terms in the following way:

$$A = \|\boldsymbol{u}\|_0^2 + \frac{2\cot\vartheta}{\mathrm{Re}}\|h\|_0^2 + \frac{1}{\mathrm{Re}\,\mathrm{Ca}}\|h_x\|_0^2 + \frac{\mathrm{Ma}}{\mathrm{Re}\,\mathrm{Ca}}\|c\|_0^2. \tag{2.259}$$

For every non-trivial eigenfunction, $A > 0$. Moreover, we have dissipative terms

$$\begin{aligned} D =& \frac{1}{\mathrm{Re}} \int_\Omega (2\,|u_x|^2 + 2\,|v_y|^2 + |u_y + v_x|^2)\mathrm{d}\boldsymbol{x}\\ &+ \frac{2\cot\vartheta}{\mathrm{Re}}\|h\|_0^2 + \frac{1}{\mathrm{Re}\,\mathrm{Ca}}\|h_x\|_0^2 + \frac{\mathrm{Ma}}{\mathrm{Re}\,\mathrm{Ca}\,\mathrm{Pe}}\|c_x\|_0^2\\ =& \frac{2}{\mathrm{Re}}\,[\boldsymbol{u}, \boldsymbol{u}] + \frac{2\cot\vartheta}{\mathrm{Re}}\|h\|_0^2 + \frac{1}{\mathrm{Re}\,\mathrm{Ca}}\|h_x\|_0^2 + \frac{\mathrm{Ma}}{\mathrm{Re}\,\mathrm{Ca}\,\mathrm{Pe}}\|c_x\|_0^2 \end{aligned} \tag{2.260}$$

and perturbation terms

$$\begin{aligned} P = \mathfrak{Re}\left(\int_\Omega (2 - 2y)\overline{u}v\mathrm{d}\boldsymbol{x} - \frac{2}{\mathrm{Re}}\int_\Sigma h\overline{u}\mathrm{d}x + \lambda \int_\Omega u \cdot \overline{\boldsymbol{w}_h}\mathrm{d}\boldsymbol{x}\right.\\ + \int_\Omega (\boldsymbol{u}_N \cdot \nabla \boldsymbol{u} + \boldsymbol{u} \cdot \nabla \boldsymbol{u}_N) \cdot \overline{\boldsymbol{w}_h}\mathrm{d}\boldsymbol{x}\\ \left. + \frac{1}{\mathrm{Re}} \int_\Omega (2u_x\overline{w_x^{(1)}} + 2v_y\overline{w_y^{(2)}} + (u_y + v_x)(\overline{w_y^{(1)}} + \overline{w_x^{(2)}}))\mathrm{d}\boldsymbol{x}\right). \end{aligned} \tag{2.261}$$

2.4.3. Estimates for the perturbation terms

We derive an estimate for the absolute value of P. We start with

$$\begin{aligned} |P_1| := \left|\int_\Omega (2-2y)\overline{u}v\mathrm{d}\boldsymbol{x}\right| &\leq \int_\Omega (|u|^2 + |v|^2)\mathrm{d}\boldsymbol{x} \\ &\leq \int_\Omega (|u_y|^2 + |v_y|^2)\mathrm{d}\boldsymbol{x} \\ &= \|u_y\|_0^2 + \|v_y\|_0^2. \end{aligned} \tag{2.262}$$

We have used $\|y \mapsto 2-2y\|_\infty \leq 2$ and Young's inequality in the first step, and Poincaré-Friedrichs' inequality in the second step.

Further, we calculate

$$\begin{aligned} |P_2| := \left|\frac{2}{\mathrm{Re}}\int_0^L h\overline{u}\mathrm{d}x\right| &\leq \frac{1}{\mathrm{Re}^2}\int_\Sigma |h|^2\,\mathrm{d}x + \int_\Sigma |u|^2\,\mathrm{d}x \\ &\leq \frac{c_P}{\mathrm{Re}^2}\|h_x\|_0^2 + \|u_y\|_0^2. \end{aligned} \tag{2.263}$$

In the last step, we have used the Poincaré- and trace inequalities.

The next term is

$$\begin{aligned} |P_3| :=& \left|\frac{1}{\mathrm{Re}}\int_\Omega (2u_x\overline{w_x^{(1)}} + 2v_y\overline{w_y^{(2)}} + (u_y+v_x)(\overline{w_y^{(1)}} + \overline{w_x^{(2)}}))\mathrm{d}\boldsymbol{x}\right| \\ \leq& \int_\Omega (|u_x|^2 + |v_y|^2 + \frac{1}{2}|u_y+v_x|^2)\mathrm{d}\boldsymbol{x} \\ &+ \frac{1}{\mathrm{Re}^2}\int_\Omega (\left|w_x^{(1)}\right|^2 + \left|w_y^{(2)}\right|^2 + \frac{1}{2}\left|w_y^{(1)} + w_x^{(2)}\right|^2)\mathrm{d}\boldsymbol{x} \end{aligned} \tag{2.264}$$

We estimate the terms with $\boldsymbol{w}_h$ in the following way:

$$\begin{aligned} \int_\Omega \left|w_x^{(1)}\right|^2\mathrm{d}\boldsymbol{x} &= \int_0^L\int_0^1 |\phi_x\psi_y|^2\,\mathrm{d}y\mathrm{d}x \\ &\leq \frac{9}{4}\|h\|_0^2 \\ &\leq \frac{9}{4}c_P\|h_x\|_0^2, \end{aligned} \tag{2.265}$$

$$\begin{aligned} \int_\Omega \left|w_y^{(2)}\right|^2\mathrm{d}\boldsymbol{x} &= \int_0^L\int_0^1 |\phi_x\psi_y|^2\,\mathrm{d}\mathrm{d}x \\ &\leq \frac{9}{4}\|h\|_0^2 \\ &\leq \frac{9}{4}c_P\|h_x\|_0^2, \end{aligned} \tag{2.266}$$

$$\begin{aligned}\int_\Omega \left|w_y^{(1)}\right|^2 \mathrm{d}\boldsymbol{x} &= \int_0^L \int_0^1 |\phi\psi_{yy}|^2 \,\mathrm{d}y\mathrm{d}x \\ &\le 36 \int_0^L |\phi|^2 \,\mathrm{d}x \\ &\le 36c_P\|h\|_0^2 \\ &\le 36c_P^2\|h_x\|_0^2,\end{aligned} \tag{2.267}$$

$$\begin{aligned}\int_\Omega \left|w_x^{(2)}\right|^2 \mathrm{d}\boldsymbol{x} &= \int_0^L \int_0^1 |\phi_{xx}\psi|^2 \,\mathrm{d}y\mathrm{d}x \\ &\le \|h_x\|_0^2.\end{aligned} \tag{2.268}$$

Together, we have

$$|P_3| \le \|u_x\|_0^2 + \|v_y\|_0^2 + \|u_y\|_0^2 + \|v_x\|_0^2 + \frac{1}{\mathrm{Re}^2}\left(1 + \frac{9}{2}c_P + 36c_P^2\right)\|h_x\|_0^2. \tag{2.269}$$

We go on with

$$\begin{aligned}|P_4| :&= \left|\int_\Omega (\boldsymbol{u}_N \cdot \nabla\boldsymbol{u}) \cdot \overline{\boldsymbol{w}_h}\mathrm{d}\boldsymbol{x}\right| \\ &= \left|\int_\Omega (2y - y^2)(u_x\overline{w^{(1)}} + v_x\overline{w^{(2)}})\mathrm{d}\boldsymbol{x}\right| \\ &\le \frac{1}{2}\int_\Omega (|u_x|^2 + |v_x|^2)\mathrm{d}\boldsymbol{x} + \frac{1}{2}\int_\Omega (\left|w^{(1)}\right|^2 + \left|w^{(2)}\right|^2)\mathrm{d}\boldsymbol{x}.\end{aligned} \tag{2.270}$$

The terms with $\boldsymbol{w}_h$ are estimated as

$$\begin{aligned}\int_\Omega \left|w^{(1)}\right|^2 \mathrm{d}\boldsymbol{x} &= \int_0^L \int_0^1 |\phi\psi_y|^2 \,\mathrm{d}y\mathrm{d}x \\ &\le \frac{9}{4}c_P^2\|h_x\|_0^2\end{aligned} \tag{2.271}$$

and

$$\begin{aligned}\int_\Omega \left|w^{(2)}\right|^2 \mathrm{d}\boldsymbol{x} &= \int_0^L \int_0^1 |\phi_x\psi|^2 \,\mathrm{d}y\mathrm{d}x \\ &\le c_P\|h_x\|_0^2.\end{aligned} \tag{2.272}$$

Together, we have

$$|P_4| \le \frac{1}{2}\|u_x\|_0^2 + \frac{1}{2}\|v_x\|_0^2 + (\frac{1}{2}c_P + \frac{9}{8}c_P^2)\|h_x\|_0^2. \tag{2.273}$$

The next term is

$$\begin{aligned}|P_5| :&= \left|\int_\Omega (\boldsymbol{u} \cdot \nabla\boldsymbol{u}_N) \cdot \overline{\boldsymbol{w}_h}\mathrm{d}\boldsymbol{x}\right| \\ &= \left|\int_\Omega (2 - 2y)v\overline{w_h^{(1)}}\mathrm{d}\boldsymbol{x}\right| \\ &\le \|v_y\|_0^2 + \frac{9}{4}c_P^2\|h_x\|_0^2.\end{aligned} \tag{2.274}$$

In order to estimate the last term we need equation (2.252). We calculate

$$\begin{aligned}|P_6| :=&\left|\lambda \int_\Omega \boldsymbol{u} \cdot \overline{\boldsymbol{w}_h} \mathrm{d}\boldsymbol{x}\right| = \left|\overline{\lambda} \int_\Omega \boldsymbol{u} \cdot \overline{\boldsymbol{w}_h} \mathrm{d}\boldsymbol{x}\right| = \left|\int_\Omega \boldsymbol{u} \cdot \overline{\boldsymbol{w}_{\lambda h}} \mathrm{d}\boldsymbol{x}\right| \\ \leq&\frac{1}{2}\int_\Omega (|u_y|^2 + |v_y|^2)\mathrm{d}\boldsymbol{x} + \frac{1}{2}\int_\Omega (\left|w^{(1)}_{\lambda h}\right|^2 + \left|w^{(2)}_{\lambda h}\right|^2)\mathrm{d}\boldsymbol{x}.\end{aligned} \tag{2.275}$$

Taking into account (2.238), $\boldsymbol{w}_{\lambda h} = \boldsymbol{w}_{(v-h_x)}$, which lets us estimate

$$\begin{aligned}\int_\Omega \left|w^{(1)}_{(v-h_x)}\right|^2 \mathrm{d}\boldsymbol{x} &= \int_0^L \int_0^1 \left|\psi_y \phi_{(v-h_x)}\right|^2 \mathrm{d}y\mathrm{d}x \\ &\leq \frac{9}{4} c_P \|v - h_x\|^2_{H^0(\Sigma)} \\ &\leq \frac{9}{2} c_P (\|v\|^2_{H^0(\Sigma)} + \|h_x\|^2_{H^0(\Sigma)}) \\ &\leq \frac{9}{2} c_P (\|v_y\|^2_{H^0(\Omega)} + \|h_x\|^2_{H^0(\Sigma)}),\end{aligned} \tag{2.276}$$

and

$$\begin{aligned}\int_\Omega \left|w^{(2)}_{(v-h_x)}\right|^2 \mathrm{d}\boldsymbol{x} &= \int_0^L \int_0^1 \left|\psi \partial_x \phi_{(v-h_x)}\right|^2 \mathrm{d}y\mathrm{d}x \\ &\leq \int_0^L |v(x,1) - h_x(x)|^2 \mathrm{d}x \\ &\leq 2\|v_y\|^2_{H^0(\Omega)} + 2\|h_x\|^2_{H^0(\Sigma)}.\end{aligned} \tag{2.277}$$

Together, we have

$$|P_6| \leq \frac{1}{2}\|u_y\|_0^2 + (\frac{3}{2} + \frac{9}{4}c_P)\|v_y\|_0^2 + (1 + \frac{9}{4}c_P)\|h_x\|_0^2. \tag{2.278}$$

Summing up, we can estimate

$$\begin{aligned}|P| =& |\mathfrak{Re}(P_1 + P_2 + P_3 + P_4 + P_5 + P_6)| \\ \leq& \frac{7}{2}\|u_y\|_0^2 + \frac{3}{2}\|u_x\|_0^2 + (\frac{9}{2} + \frac{9}{4}c_P)\|v_y\|_0^2 + \frac{3}{2}\|v_x\|_0^2 \\ &+ \left(1 + \frac{11}{4}c_P + \frac{27}{8}c_P^2 + \frac{1}{\mathrm{Re}^2}(1 + \frac{11}{2}c_P + 36c_P^2)\right)\|h_x\|_0^2 \\ \leq& (\frac{9}{2} + \frac{9}{4}c_P)\|\nabla \boldsymbol{u}\|_0^2 \\ &+ \left(1 + \frac{11}{4}c_P + \frac{27}{8}c_P^2 + \frac{1}{\mathrm{Re}^2}(1 + \frac{11}{2}c_P + 36c_P^2)\right)\|h_x\|_0^2.\end{aligned} \tag{2.279}$$

2.4.4. Linear stability of the falling film

We write (2.258) in the following way:

$$r = -\frac{D/2}{A} - \frac{D/2 + P}{A}. \tag{2.280}$$

We calculate

$$\begin{aligned}\frac{1}{2}D+P \geq& \frac{1}{2}D-|P|\\ \geq& \frac{1}{\mathrm{Re}}\,[\boldsymbol{u},\boldsymbol{u}]-(\frac{9}{2}+\frac{9}{4}c_P)\|\nabla\boldsymbol{u}\|_0^2\\ &+\frac{1}{2\,\mathrm{Re}\,\mathrm{Ca}}\|h_x\|_0^2\\ &-\left(1+\frac{11}{4}c_P+\frac{27}{8}c_P^2+\frac{1}{\mathrm{Re}^2}(1+\frac{11}{2}c_P+36c_P^2)\right)\|h_x\|_0^2\\ \geq& \frac{1}{\mathrm{Re}}\,[\boldsymbol{u},\boldsymbol{u}]-3(\frac{9}{2}+\frac{9}{4}c_P)\,[\boldsymbol{u},\boldsymbol{u}]\\ &+\frac{1}{2\,\mathrm{Re}\,\mathrm{Ca}}\|h_x\|_0^2\\ &-\left(1+\frac{11}{4}c_P+\frac{27}{8}c_P^2+\frac{1}{\mathrm{Re}^2}(1+\frac{11}{2}c_P+36c_P^2)\right)\|h_x\|_0^2.\end{aligned} \tag{2.281}$$

Under the conditions

$$\mathrm{Re}\leq\frac{4}{54+27c_P}=\frac{4}{54+\frac{27L^2}{4\pi^2}} \tag{2.282}$$

and

$$\begin{aligned}\mathrm{Ca}&\leq\left(2\,\mathrm{Re}(1+\frac{11}{4}c_P+\frac{27}{8}c_P^2)+\frac{2}{\mathrm{Re}}(1+\frac{11}{2}c_P+36c_P^2)\right)^{-1}\\ &=\left(2\,\mathrm{Re}(1+\frac{11L^2}{16\pi^2}+\frac{27L^4}{128\pi^2})+\frac{2}{\mathrm{Re}}(1+\frac{11L^2}{8\pi^2}+\frac{9L^4}{4\pi^4})\right)^{-1},\end{aligned} \tag{2.283}$$

it holds that $\frac{1}{2}D+P\geq 0$. Note that condition (2.282) implies $\mathrm{Re}<\frac{2}{27}$. Assuming the stated conditions on Re and Ca, we estimate

$$\begin{aligned}r=&-\frac{D/2}{A}-\frac{D/2+P}{A}\\ \leq&-\frac{D/2}{A}\\ =&-\frac{\frac{1}{\mathrm{Re}}\,[\boldsymbol{u},\boldsymbol{u}]+\frac{\cot\vartheta}{\mathrm{Re}}\|h\|_0^2+\frac{1}{2\,\mathrm{Re}\,\mathrm{Ca}}\|h_x\|_0^2+\frac{\mathrm{Ma}}{2\,\mathrm{Re}\,\mathrm{Ca}\,\mathrm{Pe}}\|c_x\|_0^2}{\|\boldsymbol{u}\|_0^2+\frac{2\cot\vartheta}{\mathrm{Re}}\|h\|_0^2+\frac{1}{\mathrm{Re}\,\mathrm{Ca}}\|h_x\|_0^2+\frac{\mathrm{Ma}}{\mathrm{Re}\,\mathrm{Ca}}\|c\|_0^2}\\ \leq&-\frac{1}{2}\frac{\frac{2}{\mathrm{Re}}\,[\boldsymbol{u},\boldsymbol{u}]+\frac{2\cot\vartheta}{\mathrm{Re}}\|h\|_0^2+\frac{1}{\mathrm{Re}\,\mathrm{Ca}}\|h_x\|_0^2+\frac{\mathrm{Ma}}{\mathrm{Re}\,\mathrm{Ca}\,\mathrm{Pe}}\|c_x\|_0^2}{3\,[\boldsymbol{u},\boldsymbol{u}]+\frac{2\cot\vartheta}{\mathrm{Re}}\|h\|_0^2+\frac{1}{\mathrm{Re}\,\mathrm{Ca}}\|h_x\|_0^2+c_P\frac{\mathrm{Ma}}{\mathrm{Re}\,\mathrm{Ca}}\|c_x\|_0^2}\\ \leq&-\frac{1}{2}.\end{aligned} \tag{2.284}$$

The last inequality holds under the assumptions $\mathrm{Re}\leq\frac{2}{3}$, which is already fulfilled due to (2.282), and

$$\mathrm{Pe}\leq\frac{4\pi^2}{L^2}. \tag{2.285}$$

The only condition on the Marangoni number employed here is

$$\mathrm{Ma} \geq 0, \tag{2.286}$$

which as always fulfilled due to the assumption $\gamma \geq 0$ in (1.39).

2.5. Conclusion

In this chapter, periodic flow down an inclined plane under presence of an insoluble surfactant was considered. A system of equations governing the linear evolution of perturbations to the steady state was derived, the system was written as an evolution equation, and the associated resolvent problem was studied in an L^2-setting.

By a series of auxiliary problems, it was shown that for every inclination angle $0 < \vartheta \leq \frac{\pi}{2}$ and for every choice of dimensionless numbers, the linearized stability operator $\boldsymbol{G}$ is the generator of an analytic semigroup. Finally, the spectrum of $\boldsymbol{G}$ was studied. A sufficient condition on Re, Ca and Pe was derived under which a flow with maximal wavelength L is stable. The condition is physically reasonable, and an explicit spectral bound of $-\frac{1}{2}$ was derived.

3. Direct numerical simulation

3.1. Introduction

From this point onward, only flows with constant surface tension on vertical planes are considered. Therefore, for the rest of this thesis, the system of governing equations reads

$$\begin{aligned}
\rho\left(\partial_t \boldsymbol{u} + \boldsymbol{u}\cdot\nabla\boldsymbol{u}\right) - \eta\Delta\boldsymbol{u} + \nabla p &= \begin{pmatrix}\rho g\\ 0\end{pmatrix}, && y>0, \boldsymbol{x}\notin\Sigma(t), && (3.1)\\
\nabla\cdot\boldsymbol{u} &= 0, && y>0, \boldsymbol{x}\notin\Sigma(t), && (3.2)\\
\boldsymbol{u} &= 0, && \boldsymbol{x}\in W, && (3.3)\\
[\![\boldsymbol{u}]\!] = 0, V_\Sigma &= \boldsymbol{u}\cdot\boldsymbol{n}_\Sigma, && \boldsymbol{x}\in\Sigma(t), && (3.4)\\
[\![p\boldsymbol{I} - \eta(\nabla\boldsymbol{u} + \nabla\boldsymbol{u}^\mathsf{T})]\!]\boldsymbol{n}_\Sigma &= \sigma\kappa\boldsymbol{n}_\Sigma, && \boldsymbol{x}\in\Sigma(t), && (3.5)
\end{aligned}$$

where $\sigma > 0$ is a constant.

Chapters 4 and 5 of this work rely on direct numerical simulations of falling films, which are performed with the two-phase Navier-Stokes solver FS3D (*Free Surface 3D*). This solver was originally developed by Rieber and Frohn (1999); Rieber (2004) at the *Fachgebiet für Thermodynamik der Luft- und Raumfahrt*, Universität Stuttgart, and has been continuously expanded at the ITLR and the *Institut für Mathematische Modellierung and Analysis*, Technische Universität Darmstadt. It is especially well-suited for the investigation of viscous two-phase flows with a free boundary, and has been employed and validated for a number of surface tension driven flows. Examples are rising bubbles in water and water-glycerol mixture (Koebe et al., 2003; Bothe et al., 2006), thermocapillary flows (Ma and Bothe, 2011), and binary droplet collisions (Focke and Bothe, 2012).

The aim of Section 3.2 is to give a general overview of the numerical approach. For details, cf. Rieber (2004). FS3D supports two different implementations for surface tension: CSF and CSS, where, in former works, CSS has been shown to deliver good and reliable results in a number of different flow situations. Since the accurate discretization of surface tension is of paramount importance for the simulation of falling films, Section 3.3 gives details of the respective implementation. The CSF surface tension model is available in a so called balanced force implementation. A necessary condition for a surface tension discretization to be balanced is derived, and it is argued that an analogous implementation for CSS is not possible. In Section 3.4, initial and boundary conditions are discussed. In Section 3.5, it is demonstrated that simulations with CSS yield internal flow fields that are different

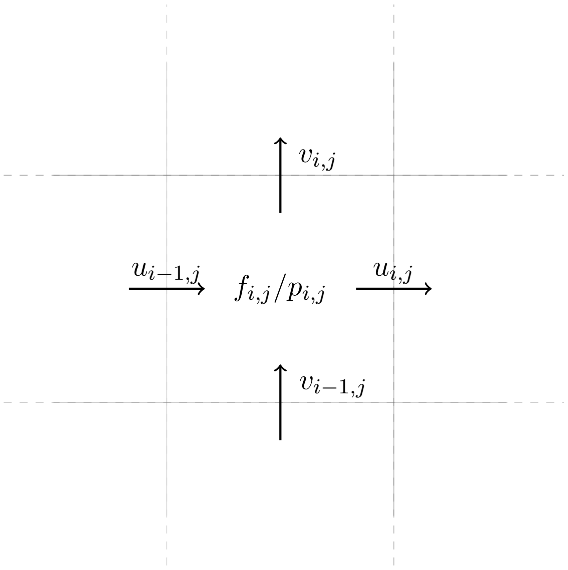

Figure 3.1.: Staggered grid arrangement in FS3D.

from those achieved with CSF. In Chapter 5, however, we will see that the internal flow structure of surface waves is intimately connected to transfer processes of a chemical species from the gas into the liquid. Therefore, it is very important to reach a conclusion on which surface tension model yields correct results. In Section 3.6, simulations with CSF and CSS are compared to a number of analytical and experimental results. CSF is found to deliver better results in every benchmark. The conclusion is drawn that the results of CSF are closer to reality, and all other simulations in this work are performed with CSF. Parts of this chapter are based on Albert et al. (2012).

3.2. Finite Volume discretization with the Volume of Fluid method

FS3D is a finite volume code, which means that the numerical domain is subdivided into control volumes of finite extent, in which the amount of extensive quantities like momentum is stored.

The variables are arranged on a staggered grid according to Harlow and Welch (1965), see Figure 3.1. If a control volume in 2D is indexed by (i, j), the pressure is stored at the center of the cell, whereas the velocity components in x/y-direction are stored at the x/y-face of the control volume. An arrangement like this avoids the decoupling of velocity and pressure fields into checkerboard patterns without the need for artificial damping of velocity fluctuations; cf. Versteeg and Malalasekera (2007), Chapter 6.

A major challenge in the numerical treatment of two-phase flows is the reliable

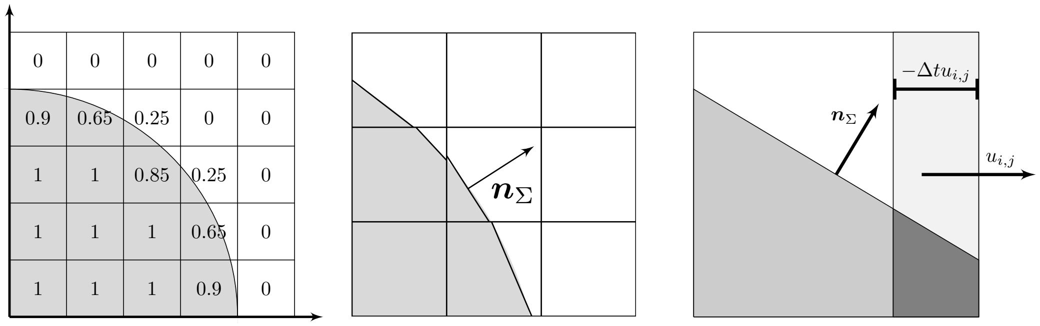

Figure 3.2.: Left: Interface capturing by the Volume of Fluid method. Middle: Piecewise linear interface reconstruction. Right: Computation of advective fluxes of volume fraction. Advected volume fraction is marked dark gray.

capturing of the free boundary. FS3D relies on the *Volume of Fluid (VOF)*-method, developed by DeBar (1974) and Hirt and Nichols (1981). In addition to velocity and pressure, a third variable, the *volume fraction field* f is introduced, which stores an approximation to the characteristic function of one phase. In this work, f is defined as the characteristic function of the domain occupied by the liquid. The volume fraction field is stored cell centered. Accordingly, a cell (i, j) such that $f_{i,j} = 1$ is interpreted as being filled with water, and cells with $f_{i,j} = 0$ as filled with gas. Cells with f-values between 0 and 1 are interpreted as interface cells, see Figure 3.2, left picture.

With the aid of the VOF method, due to the assumed continuity of velocities at the interface, it is possible to give a so called one-phase formulation of the two-phase Navier-Stokes equations, which reads as

$$\frac{\partial(\rho \boldsymbol{u})}{\partial t} + \nabla \cdot (\rho \boldsymbol{u} \otimes \boldsymbol{u}) = -\nabla p + \nabla \cdot \Big(\eta(\nabla \boldsymbol{u} + \nabla \boldsymbol{u}^{\mathsf{T}})\Big) + \rho \boldsymbol{g} + \boldsymbol{f}_\Sigma, \quad \boldsymbol{x} \in \Omega \quad (3.6)$$

$$\nabla \cdot \boldsymbol{u} = 0, \quad \boldsymbol{x} \in \Omega \quad (3.7)$$

$$\frac{\partial f}{\partial t} + \boldsymbol{u} \cdot \nabla f = 0, \quad \boldsymbol{x} \in \Omega. \quad (3.8)$$

For details on this, see Tryggvason et al. (2011, Chapter 2.5). The material parameters are now phase dependent, and assume a weighted average according to the f-value in the cell. Capillary effects are approximated by a body force density term $\boldsymbol{f}_\Sigma$ located around the interface, see Section 3.3. Equation (3.8) governs the advection of the f-field.

The basic idea of the finite volume method is to integrate the governing equations over each computational cell, apply the divergence theorem, and interpret the resulting boundary terms as fluxes from one control volume to the neighbouring one. These fluxes are then used to update the values stored in each cell.

FS3D uses an operator splitting approach, where the individual terms in the system of governing equations are treated consecutively. The nonlinear convective term $\nabla \cdot (\rho \boldsymbol{u} \otimes \boldsymbol{u})$ is discretized by the Godunov method, combined with a van Leer flux limiter (Bell et al., 1989). Viscous fluxes due to the term $\nabla \cdot \big(\eta(\nabla \boldsymbol{u} + \nabla \boldsymbol{u}^{\mathsf{T}})\big)$ are computed by a straight-forward discretization of the Laplacian by central differences.

3.2.1. PLIC advection

If classical numerical methods for hyperbolic conservation laws, as described in LeVeque (2002), are applied to solve equation (3.8), they lead to a numerical smearing of the interface. After a few time steps, several layers of cells with $0 < f < 1$ can exist. Since this behavior is undesirable in sharp interface simulations, a geometrical advection algorithm due to Rider and Kothe (1998), called *piecewise linear interface calculation* (PLIC)-method, is employed.

Based on the f-values, an approximation to the interface normal is computed as

$$\boldsymbol{n}_\Sigma = \frac{\nabla f}{\|\nabla f\|}. \tag{3.9}$$

Now, a linear surface element is constructed in each cell such that it is perpendicular to $\boldsymbol{n}_\Sigma$, and such that the volume enclosed by the PLIC surface and the boundary of the control volume equals the volume fraction value in this cell, cf. Figure 3.2, second picture.

During one time step of size Δt, a volume element of length $u_{i,j}\Delta t$ is advected over the right cell face. The amount of fluid inside this volume element is determined geometrically; see the dark gray area in the right picture of Figure 3.2. The transport is performed for every space direction, employing a direction splitting approach, where the three dimensional advection equation is replaced by three one dimensional equations, whose implementation is markedly simpler. Due to the directional splitting, the volume of the fluid will change slightly, even for an exactly divergence free velocity field. However, the relative volume error is very small, and can be neglected for simulations of falling films.

3.2.2. Timestep constraints

Time discretization is done by the forward (explicit) Euler method. In order to ensure numerical stability of the scheme, various time step constraints, as obtained by a von-Neumann stability analysis (cf. Isaacson (1994)), have to be respected. The relevant constraints are the classical Courant-Friedrichs-Lewy condition

$$\Delta t \leq \frac{\Delta x}{\|\boldsymbol{u}\|_\infty}, \tag{3.10}$$

where Δx denotes the grid width, and the time step constraint for a *forward-time centered space* discretization of viscous momentum transport

$$\Delta t \leq \frac{(\Delta x)^2}{2\max(\nu_L, \nu_G)}. \tag{3.11}$$

Finally, another time step constraint applies, which accounts for the characteristic propagation velocity of capillary waves:

$$\Delta t \leq \sqrt{\frac{(\rho_L + \rho_G)(\Delta x)^3}{4\pi\sigma}}. \tag{3.12}$$

Since $\|\boldsymbol{u}\|_\infty$ can change in the course of a simulation run, the time step is adaptively adjusted to ensure that the CFL condition is never violated.

3.2.3. Boundary conditions

Boundary conditions in FS3D are realized by so-called *dummy cells*, which are two additional layers of computational cells that surround the grid. The computational quantities are continued onto the boundary cells in such a way that the boundary conditions are fulfilled. By this, difference stencils at the boundary can be discretized in the same way as in the interior of the computational domain; see Blazek (2001) for more details.

3.2.4. Coupling between velocity and pressure

Pressure and velocity are coupled by the projection method of Chorin (1968). The velocity field of the old time step $\boldsymbol{u}^n$ is updated by convective and viscous momentum fluxes, and with accelerations due to surface tension. This yields an intermediate velocity field $\boldsymbol{u}^{n,++}$, which is not divergence free anymore. Pressure is then determined as a solution of the Poisson equation

$$\nabla \cdot \left[\frac{\nabla p^{n+1}}{\rho}\right] = \frac{\nabla \cdot \boldsymbol{u}^{n,++}}{\Delta t}. \tag{3.13}$$

The new, divergence free velocity field is then computed as

$$\boldsymbol{u}^{n+1} = \boldsymbol{u}^{n,++} - \frac{\Delta t}{\rho}\nabla p^{n+1}. \tag{3.14}$$

Accelerations due to pressure are computed by central differences of second order at the cell faces, where velocities are stored. Since pressure is obtained as the solution of an elliptic equation of second-order, appropriate boundary conditions must be provided. It is important to note that there is a small, but systematic difference between the physical pressure and the numerical quantity p that is considered here. In fact, the numerical pressure correction step is closely related to the projection operator P^0, which was introduced in Section 2.2.5 to remove pressure from the phase space. For a detailed discussion on this, see Temam (1991). This distinction is especially important when it comes to boundary conditions for equation (3.13). The correct pressure boundary conditions for FS3D are

$$\frac{\partial p}{\partial \boldsymbol{n}_\Omega} = 0, \quad \boldsymbol{x} \in \partial\Omega, \tag{3.15}$$

whenever a (homogeneous or non-homogeneous) Dirichlet boundary condition for the velocity field is applied, and

$$p = 0, \quad \boldsymbol{x} \in \partial\Omega, \tag{3.16}$$

whenever a Neumann condition for the velocity is used. Here, $\boldsymbol{n}_\Omega$ denotes the outer normal on the domain boundary. For a detailed discussion of pressure boundary conditions, see Rempfer (2006).

3.3. Numerical treatment of surface tension

Surface waves on liquid films exhibit regions of high curvature. Due to the small mean film thicknesses considered in this work, capillary effects play a crucial role in the evolution of the flow field, and their discretization is of paramount importance to achieve accurate simulation results.

Two widely spread approaches to incorporate surface tension in VOF simulations are the *Continuum Surface Stress* (CSS)-model due to Lafaurie et al. (1994), and the *Continuum Surface Force* (CSF)-model due to Brackbill et al. (1992). In both cases, surface tension is modeled as a volumetric force density, localized around the interface. The respective expressions for the force densities are

$$\boldsymbol{f}_{CSS} = -\sigma\nabla \cdot [(\boldsymbol{I} - \boldsymbol{n}_\Sigma \otimes \boldsymbol{n}_\Sigma)(\nabla f \cdot \boldsymbol{n}_\Sigma)] \tag{3.17}$$

for the CSS model, and

$$\boldsymbol{f}_{CSF} = \sigma\kappa\nabla f \tag{3.18}$$

for CSF. As the f-field is an approximation to the characteristic function of Ω_L, these expressions have to be understood in the sense of distributions, and they are equivalent as such.

As opposed to $\boldsymbol{f}_{CSF}$, the expression for $\boldsymbol{f}_{CSS}$ is in divergence form, which has the advantage that its numerical realization is momentum conservative. The expression for the CSF-model, on the other hand, is very similar to the pressure gradient ∇p, and it was noted in Renardy and Renardy (2002) that a so-called *balanced force* implementation is possible; see Section 3.3.2 for more information.

In this section, the numerical implementation of both models is described. Afterwards, an exact definition of “balanced forces” is given, and it is explained why it is possible to implement CSF in such a way. Finally, an argumentation is included why it would be difficult to achieve an equivalent implementation for CSS.

3.3.1. Numerical implementation of surface tension forces

CSS

In the implementation of CSS in FS3D, all geometric quantities are computed as finite differences of the f-field, by the observation $\boldsymbol{n}_\Sigma = \frac{\nabla f}{\|\nabla f\|}$ and, accordingly,

$\nabla f \cdot \boldsymbol{n}_\Sigma = \|\nabla f\|$. Due to the PLIC advection algorithm, the interface stays sharp, and there is only one layer of interface cells. In order to avoid the steep gradients associated with this, in a first step, the f-field is convoluted with a B-spline of degree 2, which yields a smoothed field $\tilde{f}$. The gradient of $\tilde{f}$ is then computed at the corners of each control volume by averaging central finite differences; $\nabla\tilde{f}$ at the corners is the result of an 8-point stencil. The four corner gradients at each face are then averaged onto the face centers; altogether these gradients are then the result of an 18-point stencil. The quantity $(\boldsymbol{I} - \boldsymbol{n}_\Sigma \otimes \boldsymbol{n}_\Sigma)\|\nabla f\|$ can then be computed on the face centers, and central differences yield its divergence in the cell center. The resulting body force is evenly distributed to the 6 velocities adjacent to the cell.

CSF

In modern implementations of CSF, curvature is determined by a rather elaborate local reconstruction of the interface out of volume fraction data. In Renardy and Renardy (2002), this is accomplished by fitting a paraboloid to the f-field. Since this procedure is numerically quite expensive, in Francois et al. (2006) an algorithm with a fixed-stencil was proposed, which reconstructs the interface locally as a height function. But even for slightly underresolved parts of the interface, it is not possible to reconstruct a height function in any space direction. Therefore, FS3D uses a more complex algorithm, proposed and described in detail in Popinet (2009). Here, a stencil of variable width is employed to guarantee that a height function is reconstructed whenever it is possible. If this does not work due to insufficient resolution, a two-stage fallback strategy is performed. In a first step, the algorithm tries to fit a paraboloid to all interface points found by height functions in different directions. If not enough interface points are found, a paraboloid is fitted to the barycenters of the PLIC surfaces. The curvature is calculated in the cell centers, from where they are interpolated onto the cell faces, where the velocities are stored. The components of ∇f are, like pressure gradients, computed by central differences; see also section 3.3.3. No smoothing of the f-field is employed.

3.3.2. Parasitic currents and balanced force surface tension

A well-known problem of VOF simulations are *parasitic currents*: spurious, unphysical oscillations of the velocity field around the interface. A striking example is the “static droplet” test case. Let $\Omega = \Omega_L \cup \Omega_G \cup \Sigma$ be a domain, and let $\Omega_L = B_R(\boldsymbol{x})$ s.t. $\operatorname{dist}(\boldsymbol{x}, \partial\Omega) > R$, i.e. let the fluid occupy a sphere of radius R that is located in Ω such that the interface does not touch the domain boundary. In a situation without gravity, the following is a steady state solution of the two-phase Navier-Stokes equations with homogeneous Neumann or Dirichlet boundary conditions at $\partial\Omega$:

$$\boldsymbol{u}_G = 0, \tag{3.19}$$

$$\boldsymbol{u}_L = 0, \tag{3.20}$$

$$p_G = p_A, \tag{3.21}$$

$$p_L = p_A + \frac{2\sigma}{R}. \tag{3.22}$$

Here, p_A is an arbitrary atmospheric pressure, and the surface tension forces due to the curvature of the sphere are balanced by an increase in pressure according to the Young-Laplace law.

If we initialize a two-phase Navier-Stokes solver with a sphere in a gas atmosphere and zero velocities, we cannot expect that the curvature algorithm immediately returns a constant curvature, which corresponds to a sphere. Due to this, some potential energy is initially available in the simulation, and we would expect that, after a transition period, where this initial interface energy is dissipated, a reasonable approximation to this steady state is reached. So far, however, there is no VOF solver that can achieve this for a three-dimensional droplet. What happens instead is that parasitic currents introduce an unphysical amount of kinetic energy into the flow field, which accelerates the droplet until it hits the domain boundary. (On the other hand, a correct behaviour can be achieved in 2D, if the computation is performed with two symmetry planes, see Popinet (2009)).

It is know from experience that parasitic currents are less problematic if the pressure and surface tension terms are discretized in such a way that they can, at least in principle, balance each other. For implementations of the CSF model, this can be checked in the following way:

We override the curvature computation algorithm, and artificially set the curvature to a constant value. If we then initialize the solver with a sphere, an exact balance between pressure and surface tension is achieved, without any parasitic currents up to numerical accuracy[1]. Implementations of the CSF model with this property are called *balanced force* implementations (Renardy and Renardy, 2002; Francois et al., 2006). The implementation of CSF in FS3D has this property; see Boger et al. (2010) for a detailed discussion. Since it is shown in sections 3.5 and 3.6 that simulations of falling films with the CSS model do not reliably reproduce the flow physics of falling films, the question arises if a similar property can be defined for CSS. In the following, a necessary condition for a balanced force implementations is derived, and it is argued that it is difficult to implement CSS accordingly.

---

[1] It should be noted that this behaviour does not depend on the actual initialization of the f-field. In fact, once the curvature is set to a constant value, pressure will balance surface tension for *any* f-field, in accordance with (3.26).

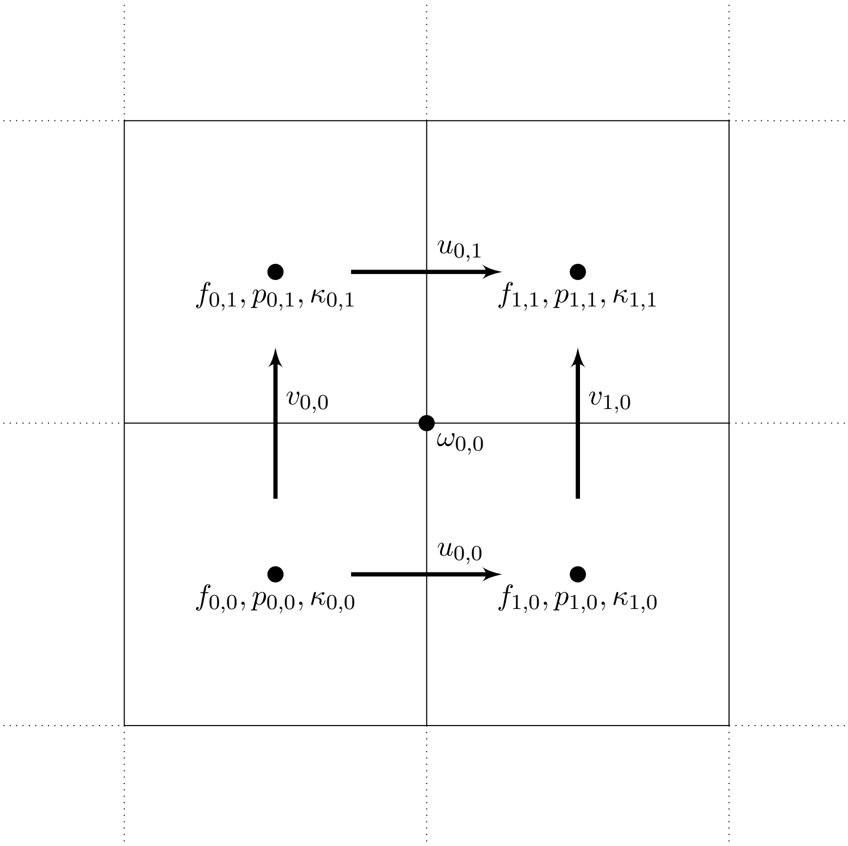

Figure 3.3.: Definition of numerical vorticity

3.3.3. A necessary condition for the balanced force property

For ease of notation, we consider a situation where both fluids have matched material properties, which we set to 1 for convenience: $\rho_L = \rho_G = \eta_L = \eta_G = \sigma = 1$. Moreover, we assume that we have a mesh such that $\Delta x = \Delta t = 1$, that there is no gravity, and that the solver is initialized with zero velocities $\boldsymbol{u}^0$ and homogeneous boundary conditions. By induction, it is then sufficient to consider the first time step: If the velocities are still zero after the first time step, they will stay so, and the steady state solution can be kept indefinitely.

After initialization, the numerical procedure will first accelerate the velocity field with viscous and convective forces, computing an intermediate velocity field $\boldsymbol{u}^{0,+}$. Since $\boldsymbol{u}^0 = 0$, these forces vanish: $\boldsymbol{u}^0 \cdot \nabla \boldsymbol{u}^0 - \eta \Delta \boldsymbol{u}^0 = 0$. Accordingly $\boldsymbol{u}^{0,+} = 0$. Now, accelerations due to surface tension will be computed, yielding a velocity field $\boldsymbol{u}^{0,++} \neq 0$, which is not divergence free. In a final step, p will be computed in such a way that accelerations due to pressure forces will yield a divergence free velocity field $\boldsymbol{u}^1 = \boldsymbol{u}^{0,++} - \frac{\Delta t}{\rho} \nabla p$ for the new time step.

Since pressure forces are represented by the gradient of a scalar field, it is reasonable to expect that they do not introduce vorticity into the flow field. Vorticity in 2D is defined as $\omega = \partial_x v - \partial_y u$. In a staggered grid scheme, it is therefore natural to define a numerical curl at the vertices of the control volumes as

$$\omega_{i,j} = \frac{v_{i+1,j} - v_{i,j}}{\Delta x} - \frac{u_{i,j+1} - u_{i,j}}{\Delta y}, \tag{3.23}$$

see Figure 3.3. If we assume for the moment that the velocities in Figure 3.3 are the sole result of pressure accelerations, it is easy to check that they are curl free[2] (note that all material and numerical parameters were set to 1):

$$\begin{aligned}\omega_{0,0,p} =& v_{1,0} - v_{0,0} - u_{0,1} + u_{0,0} \\ =& (p_{1,1} - p_{1,0}) - (p_{0,1} - p_{0,0}) \\ & - (p_{1,1} - p_{0,1}) + (p_{1,0} - p_{0,0}) \\ =& 0.\end{aligned} \tag{3.24}$$

Therefore, pressure cannot change the curl of the velocity field, and $\boldsymbol{u}^{0,++} - \frac{\Delta t}{\rho} \nabla p = 0$ can only hold if $\boldsymbol{u}^{0,++}$ itself is curl free.

Assume now that the velocities in Figure 3.3 are the sole result of accelerations due to capillary forces by the CSF model with $\kappa = \text{const}$. In that case, we have

$$\begin{aligned}\omega_{0,0,\mathrm{CSF}} =& v_{1,0} - v_{0,0} - u_{0,1} + u_{0,0} \\ =& \frac{\kappa_{1,1} + \kappa_{1,0}}{2}(f_{1,1} - f_{1,0}) - \frac{\kappa_{0,1} + \kappa_{0,0}}{2}(f_{0,1} - f_{0,0}) \\ & - \frac{\kappa_{1,1} + \kappa_{0,1}}{2}(f_{1,1} - f_{0,1}) + \frac{\kappa_{1,0} + \kappa_{0,0}}{2}(f_{1,0} - f_{0,0}) \\ =& \kappa\left((f_{1,1} - f_{1,0}) - (f_{0,1} - f_{0,0}) - (f_{1,1} - f_{0,1}) + (f_{1,0} - f_{0,0})\right) \\ =& 0.\end{aligned} \tag{3.25}$$

It is not very surprising that an implementation of CSF can be numerically curl free for constant curvatures since, on a continuous level,

$$\nabla \times \boldsymbol{f}_{CSF} = \nabla \times (\sigma\kappa\nabla f) = \sigma\kappa\nabla \times \nabla(f) = 0 \tag{3.26}$$

for an *arbitrary* smooth field f.

The CSS model requires different geometrical information from VOF-data. Instead of curvature, it needs information about the normal field. The outer normal field of a sphere centered at $\boldsymbol{x}_0$ is given by

$$\boldsymbol{n}_\Sigma = \nabla\|\boldsymbol{x} - \boldsymbol{x}_0\|. \tag{3.27}$$

However, for general, smooth f,

$$\nabla \times \boldsymbol{f}_{CSS} = \nabla \times (\sigma\nabla \cdot [(\boldsymbol{I} - \nabla\|\boldsymbol{x}\| \otimes \nabla\|\boldsymbol{x}\|)(\nabla f \cdot \nabla\|\boldsymbol{x}\|)]) \neq 0, \tag{3.28}$$

---

[2] Note, however, that for $\rho_L \neq \rho_G$, pressure can indeed generate a non-zero curl at the interface.

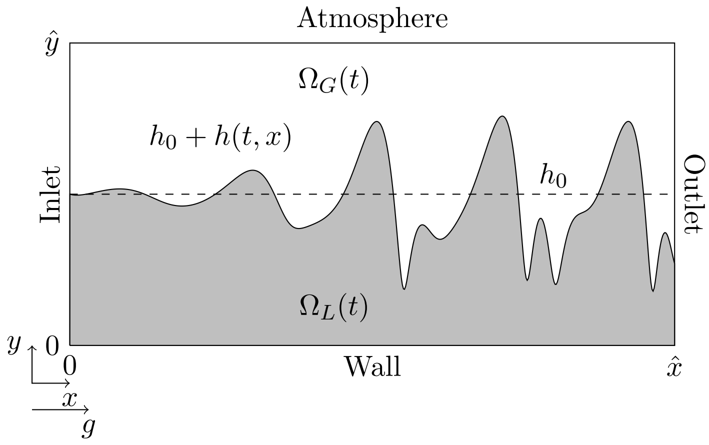

Figure 3.4.: Sketch of the computational setup

as the simple counter example $f(x, y) = x + y$ shows. For a rotationally symmetric $f = f(\|\boldsymbol{x} - \boldsymbol{x}_0\|)$, however, $\nabla \times \boldsymbol{f}_{CSS}$ vanishes, but that property is difficult to reproduce on a Cartesian grid. One might argue that a truly vanishing curl is a numerical curiosity, which can never be achieved in real VOF simulations, and that it would be much more important to find a CSS-implementation whose numerical curl converges to zero after grid refinement. However, no discretization with this property is known, either.

3.4. Computational setup

3.4.1. Boundary conditions in cross-streamwise direction

A sketch of the computational domain is shown in Figure 3.4. All simulations in this work were performed on vertical walls ($\vartheta = \frac{\pi}{2}$). The computational domain is rectangular with size $[0, \hat{x}] \times [0, \hat{y}]$. At the bounding wall, the no-slip boundary condition applies. As we are mainly interested in the flow field of the fluid, and since the density of the gas is typically 3 orders of magnitude lower than that of the fluid, the condition at the upper domain boundary $y = \hat{y}$ is not of paramount importance. Nevertheless, in order to avoid problems with gas flow into the computational domain, we prescribe an *atmospheric boundary condition*, modeling a semi-permeable boundary. Let $u_{i,n_j}, v_{i,n_j}, 1 \leq i \leq n_i$ denote the uppermost level of computational cells, and u_{i,n_j+1}, v_{i,n_j+1} denote the first layer of dummy cells in positive y-direction. The number of control volumes in x- and y-direction are n_i and n_j, respectively. Then, the velocities at the upper boundary are set as

$$u_{i,n_j+1} = u_{i,n_j}, \qquad 1 \leq i \leq n_i, \tag{3.29}$$

$$v_{i,n_j+1} = \max(v_{i,n_j}, 0), \qquad 1 \leq i \leq n_i. \tag{3.30}$$

3.4.2. Inlet boundary conditions

With the exception of the periodic flow in Chapter 4 (cf. Section 4.4.2), most simulations in this work are performed with inflow and outflow boundary conditions. The inlet is realized as a non-homogeneous Dirichlet boundary condition. If not mentioned otherwise, a Nusselt profile is prescribed at the inlet. Due to the presence of the gas phase, the steady state solution differs slightly from the classical Nusselt profile. With the present set of cross-streamwise boundary conditions, it reads

$$\begin{aligned} u_N(y) &= \frac{\rho_L g}{2\mu_L}(2h_0 y - y^2) + \frac{\rho_G g}{\eta_L}(\hat{y} - h_0)y \text{ for } 0 \leq y \leq h_0, \\ u_N(y) &= \frac{\rho_G g}{2\eta_G}(2\hat{y}y - y^2), \\ &\quad + h_0^2 g \left(\frac{\rho_L}{2\eta_L} + \rho_G(\frac{1}{2\eta_G} - \frac{1}{\eta_L}) \right) + g h_0 \hat{y}(\frac{\rho_G}{\eta_L} - \frac{\rho_G}{\eta_G}) \text{ for } h_0 \leq y \leq \hat{y}, \\ v_N &= 0, \\ p_N &= \text{const.} \end{aligned} \tag{3.31}$$

Other choices, which will be considered in Chapter 4, are

$$u_{\text{pipe}}(y)|_{x=0} = \frac{2g}{\nu_L}(h_0 - y)y, \qquad y \leq h_0 \tag{3.32}$$

$$u_{\text{pipe}}(y)|_{x=0} = 0, \qquad y > h_0 \tag{3.33}$$

which models fluid entering the film through a small orifice with no-slip boundaries on two sides, for example a slot. This condition is called *pipe flow*. Finally, *plug flow* can be described at the inlet:

$$u_{\text{plug}}(y)|_{x=0} = \frac{g h_0^2}{3\nu_L}. \tag{3.34}$$

For a given h_0, the volumetric liquid flow rate, which determines the Reynolds number, is identical in all three cases.

It has been customary since the experiments of Kapitza and Kapitza (1949) to apply a periodic perturbation to the flow field at the inlet. This has the advantage that a certain control over the observed surface waves is gained, and that experimental and computational results can be compared. For simulations, another advantage of applying a perturbation at the inlet is that the inlet length of forced waves is significantly shorter than that of naturally excited waves.

This is modeled by prescribing a periodically perturbed version of the steady state velocity at the inlet:

$$u(t, y)|_{x=0} = (1 + A\sin(2\pi\omega t))u_N(y), \tag{3.35}$$

$$v(t, y)|_{x=0} = 0, \tag{3.36}$$

where ω is the frequency of the excitation, and A its amplitude. For every choice of ω, and for every $0 \leq A < 1$, the time averaged flow rate of liquid into the domain, which determines the Reynolds number, is kept constant. As was discussed in Gao et al. (2003), the observed hydrodynamics is virtually independent of the choice of A. In this thesis, all simulations of excited films were performed with a Nusselt profile at the inlet and an excitation amplitude of $A = 0.05$.

3.4.3. Outlet boundary conditions

In a numerical simulation, the domain must be truncated at some point, creating an artificial outflow boundary. The most widely employed boundary at the outlet is the "developed flow" condition, which assumes that at the outlet, no significant change of the velocity field takes place. It reads

$$\frac{\partial \boldsymbol{u}}{\partial x} = 0, \quad x = \hat{x}. \tag{3.37}$$

In Chapter 4, only small perturbations from the developed, parallel flow are considered and this condition is employed; cf., however, Section 4.7.5.

In the present chapter, as well as in Chapter 5, we will consider large, nonlinear waves. As we will see in more detail in Section 5.8, the strong interfacial curvatures observed in the wave troughs can lead to negative velocities in x-direction. In this case, condition (3.37) is not able to suitably handle this phenomenon: If negative u-values occur at this boundary, large amounts of fluid enter the domain, leading to unphysical distortions of the flow, and eventually to the break down of the simulations.

Two possible methods were proposed to deal with this kind of situation. The first one is the introduction of a damping zone in the vicinity of the outlet, where perturbations to the developed, time-independent flow are exponentially damped, see Rieber et al. (2000). This approach guarantees that the flow field at the outlet is always the steady state solution, and can prevent the described problems.

The disadvantage of the damping zone, however, is that a comparatively large portion of the computational domain is occupied by an unphysical flow field. An alternative approach, that was also used in Dietze et al. (2008), is the application of an atmospheric boundary condition at the outlet:

$$u_{n_i+1,j} = \max(u_{n_i,j}, 0), \qquad 1 \leq j \leq n_j, \tag{3.38}$$

$$v_{n_i+1,j} = v_{n_i,j}, \qquad 1 \leq j \leq n_j. \tag{3.39}$$

Since this method minimizes the unphysical impact of the outlet on the inner flow field, the simulations in Chapters 3 and 5 were performed with this approach.

3.4.4. Initial conditions

The computational domain is initialized with a flat film of height h_0, and a velocity profile that is identical to the velocity profile at the inlet. In the case that an excitation frequency is applied, the initial velocity is the one for $\omega = 0\,\mathrm{Hz}$, corresponding to the time averaged inlet velocity.

Parameter	Symbol	Value	Unit
Density liquid	ρ_L	9.98744×10^{-1}	$\mathrm{g\,cm^{-3}}$
Viscosity liquid	η_L	1.068×10^{-2}	$\mathrm{g\,s^{-1}\,cm^{-1}}$
Density gas	ρ_G	1.3138×10^{-3}	$\mathrm{g\,cm^{-3}}$
Viscosity gas	η_G	2.0274×10^{-4}	$\mathrm{g\,s^{-1}\,cm^{-1}}$
Surface tension	σ	7.3638×10^{1}	$\mathrm{g\,s^{-2}}$
Gravitational acceleration	g	9.81×10^{2}	$\mathrm{cm\,s^{-2}}$

Table 3.1.: Material parameters for the water/air system in this chapter.

Parameter	Symbol	Value	Unit
Density liquid	ρ_L	1.0983	$\mathrm{g\,cm^{-3}}$
Viscosity liquid	η_L	3.13×10^{-2}	$\mathrm{g\,s^{-1}\,cm^{-1}}$
Surface tension	σ	4.84×10^{1}	$\mathrm{g\,s^{-2}}$

Table 3.2.: Material parameters for DMSO/water mixture.

3.4.5. Dimensions of the computational domain

All simulations of nonlinear waves in Chapters 3 and 5 were done on a domain of length $\hat{x} = 512h_0$ and height $\hat{y} = 4h_0$. In the linear setting of Chapter 4, only small perturbations of the interface height are considered, and a height of $\hat{y} = 2h_0$ is sufficient. In Chapter 4, the influence of the domain length is investigated. There, the employed domain lengths $\hat{x}$ are described at the appropriate places.

3.4.6. Material parameters

Most calculations in the present chapter were performed for a two-phase system consisting of water at 18 °C in an air atmosphere. The used material parameters are listed in Table 3.1. The simulations for a comparison with experiments by Dietze (Section 3.2) were performed for a mixture of DMSO and water, see Table 3.2. For the material parameters used in Chapter 4 see Section 4.4.1; for those used in Chapter 5, see Section 5.3.

3.5. Vorticity structure in the wave humps

Simulation results achieved with the different surface tension models show qualitative differences. In Chapter 5, the transport of a scalar quantity in falling films is investigated, and it is found that the presence of vortices in the flow field has a large impact on the observed transfer rates. Therefore, it is of paramount importance to correctly capture the vortex structure inside the waves.

In Figure 3.5, velocity streamlines in the coordinate system of the wave are

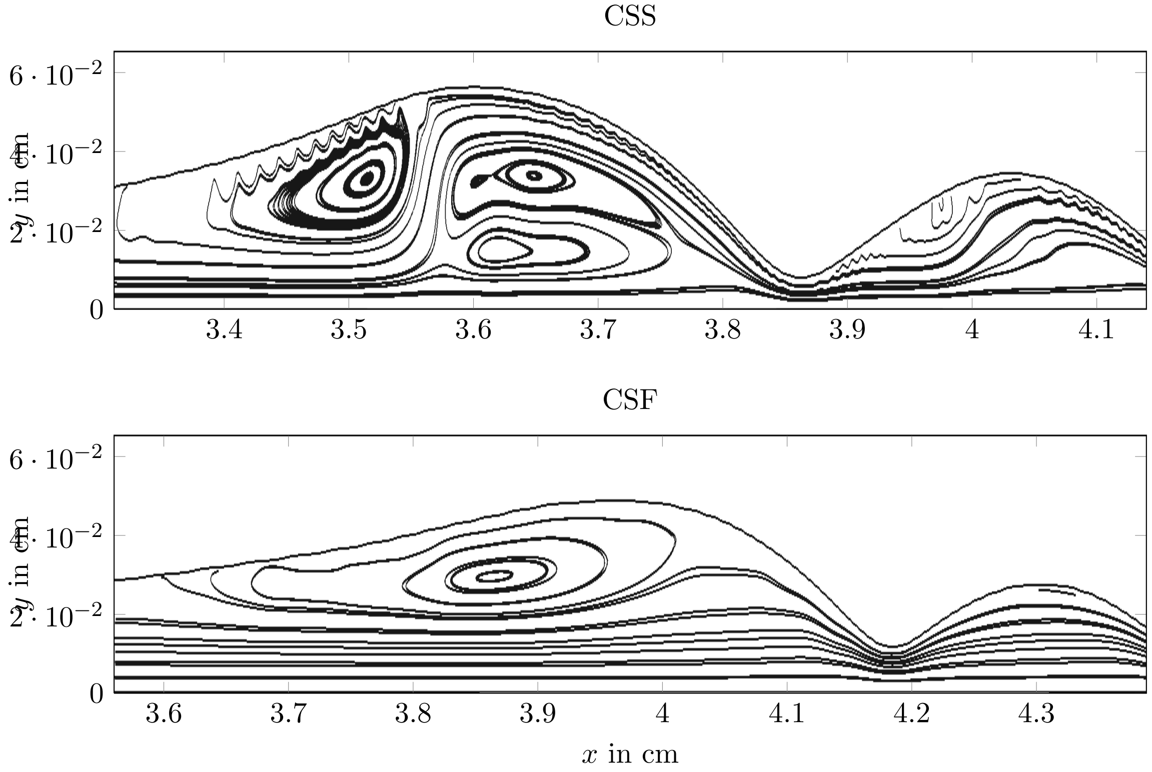

Figure 3.5.: Comparisons of vortices in the large wave between CSS (upper picture) and CSF (lower picture).

shown for simulations with CSS and CSF. The simulations were performed for a water/air system at $\mathrm{Re} = 90, \omega = 20\,\mathrm{Hz}$. Cell size was set to $h_0/16$, and results are shown at $t = 0.22\,\mathrm{s}$. There is a distinct phase shift between both simulations, which makes it inappropriate to show identical details of the film. Since the waves in both pictures are developed, and nonlinear waves are transported downstream without a significant change of their form, however, a comparison between slightly different downstream locations is feasible.

The velocity field of CSS has a very complex vorticity structure, with three clearly visible vortices in the large wave hump, and many smaller ones near the interface. Simulations with CSF, however, show a much smoother velocity field, with only one clearly visible vortex. Naturally, the question arises which surface tension model is to be preferred. In Malamataris and Balakotaiah (2008), the flow structure of waves on falling films was investigated by means of a finite element code. Only one vortex in the large wave humps is found. Direct experimental evidence for the vorticity structure is given in Alekseenko et al. (2007). They do not examine flow down a plane, but flow on the outside of a cylinder that is inclined by an angle $\vartheta > \frac{\pi}{2}$; however, the overall flow situation is comparable, and it is assumed that these measurements can be transferred to the flow down a vertical plane. Their PIV measurements of the flow field show only one vortex. In the next section, we compare results achieved with both surface tension models to a variety of experimental and analytical data, in order to assess which surface tension model yields the correct results.

3.6. Validation and surface tension discretization

The aim of this section is to show, on the basis of a variety of test cases, that the hydrodynamics of falling films in the laminar wavy regime can be accurately captured if the simulations are performed with the CSF model. The CSS model, however, is not suited for this task.

3.6.1. Viscous damping of a capillary wave

In Prosperetti (1981), an analytical solution for the amplitude of a capillary wave, damped by viscous dissipation, between two superposed fluids with non-matched material properties is given. The solution is given in the frequency space, and the inverse Laplace transform is performed with a Matlab tool (Hollenbeck, 1998).

A water/air system is simulated on a quadratic computational domain of edge length 0.28 cm, in which the lower part is filled with water, and the upper part is filled with air. The equilibrium is characterized by a flat interface. In order to see a time evolution, a sinusoidal perturbation of the interface with amplitude 5.0×10^{-3} cm and the maximal wave length is chosen as initial condition. These are typical dimensions of waves on falling films.

In lateral direction, periodic boundary conditions are chosen, whereas a slip boundary is set on the other boundaries. Computations with 32^2, 64^2 and 128^2

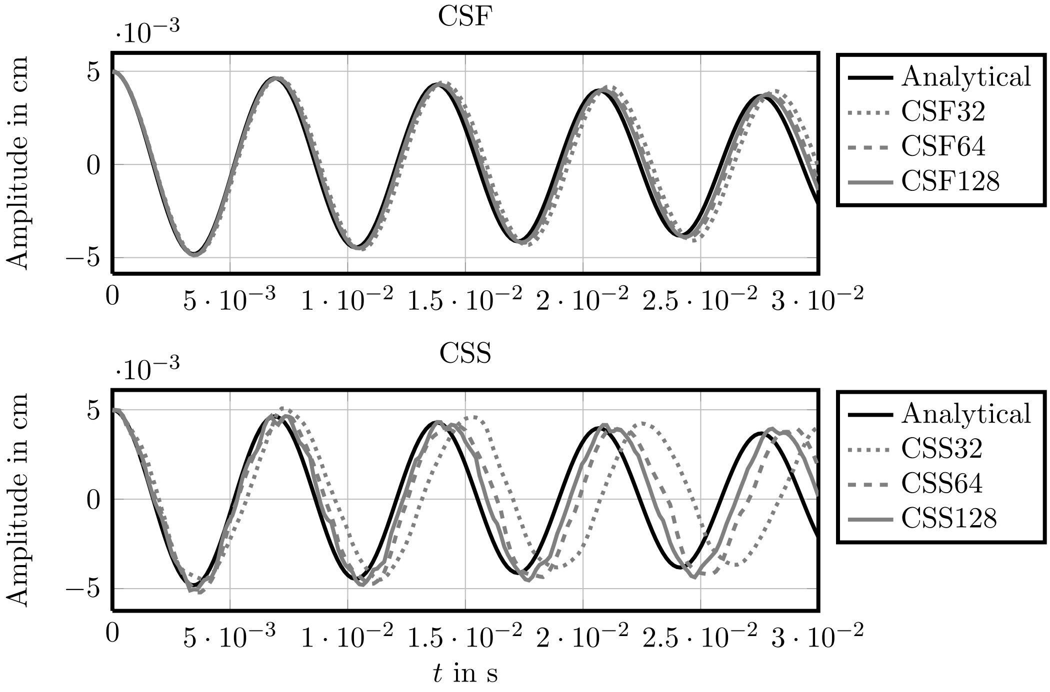

Figure 3.6.: Simulations of a viscously damped capillary wave with CSF and CSS.

quadratic computational cells were performed. See Figure 3.6 for results with both surface tension models. It can be observed that, with CSS, grid refinement leads to the development of unphysical behaviour near the wave peak, which is not the case with CSF. For all considered resolutions, the error with CSF is much smaller, see Table 3.3.

3.6.2. Comparison to Nosoko's experiments

In Nosoko et al. (1996), an experimentally determined dependence of wave peak height and wave velocity on the Reynolds number, wave separation, and material properties of the working fluid of an excited falling film is given. These relations are

$$u_{\mathrm{Nos}} = 1.13 g^{131/300} \nu_L^{19/150} \, \mathrm{Fi}^{-0.02} \, \overline{\mathrm{Re}}^{0.37} \lambda^{0.31}, \tag{3.40}$$

$$h_{\mathrm{Nos}} = 0.49 g^{-61/300} \nu_L^{61/150} \, \mathrm{Fi}^{-0.044} \, \overline{\mathrm{Re}}^{0.46} \lambda^{0.39}, \tag{3.41}$$

where u_{Nos} is the phase velocity, h_{Nos} the peak height, and λ the wave separation.

In order to asses the quality of the numerical simulation by these equations, numerical experiments with water/air films and a cell size of $h_0/16 \times h_0/16$ were performed. Films at $\mathrm{Re} = 37.5/\omega = 45\,\mathrm{Hz}$, $\mathrm{Re} = 75/\omega = 15\,\mathrm{Hz}$, and $\mathrm{Re} = 112.5/\omega = 30\,\mathrm{Hz}$ were simulated.

Surface tension model	32^2	64^2	128^2
L^1-error, CSF	4.1686×10^{-4}	2.4085×10^{-4}	1.5550×10^{-4}
L^2-error, CSF	3.7955×10^{-5}	2.2555×10^{-5}	1.4468×10^{-5}
L^∞-error, CSF	2.1796×10^{-3}	1.3371×10^{-3}	9.0401×10^{-4}
L^1-error, CSS	1.5064×10^{-3}	8.2719×10^{-4}	4.9533×10^{-4}
L^2-error, CSS	1.3113×10^{-4}	7.4080×10^{-5}	4.4641×10^{-5}
L^∞-error, CSS	6.4119×10^{-3}	4.0127×10^{-3}	2.5731×10^{-3}

Table 3.3.: Error norms for the viscous wave test case. L^1- and L^2-erros in cm s, L^∞-error in cm.

The values of the simulated wave distance (λ), wave velocity (u_{Sim}) and peak height (h_{Sim}) were determined by comparing the peaks in the developed wave regime between simulation times 0.435 s and 0.44 s. The relative difference between numerically determined values for phase velocity and peak height, compared to values determined by equations (3.40) and (3.41), are shown in Figure 3.7. It is seen that CSS systematically overestimates the peak height, and underestimates the phase velocity of the waves, whereas the simulations with CSF are quite close to the results of Nosoko.

3.6.3. Comparison to Dietze's experiments

In Dietze et al. (2009), highly accurate film thickness measurements were performed with the *Confocal Chromatic Imaging* technique. *Laser Doppler Velocimetry* was employed to measure the streamwise component of velocity at the interface.

Simulations for comparisons to these experiments were performed. The working fluid in his experiments was not water, but a water/dimethylsulfoxide-mixture, see Table 3.2 for material parameters. The Reynolds number of the film in the experiment was 12.9, and it was excited with a frequency of 16 Hz. The simulations were performed with quadratic cells of length $h_0/16$.

Film thickness and streamwise velocity were evaluated at position $x = 56\,\text{mm}$ over a time span of 0.25 s. As was already seen in the comparisons to Nosoko et al. (1996), the wave peaks obtained with CSS are much higher than in the experiment, whereas the minima in the wave troughs are too small, see Figure 3.8. Results obtained with CSF are much closer to the experiment. The streamwise velocity component at the interface, shown in Figure 3.9, gives a similar picture: CSS overshoots in both directions, while CSF is more reliable.

3.6.4. Grid refinement

In order to assess how the simulations behave after grid refinement, a water/air film at $\text{Re} = 90, \omega = 20\,\text{Hz}$ was simulated with cells of size $h_0/8, h_0/16$ and $h_0/32$

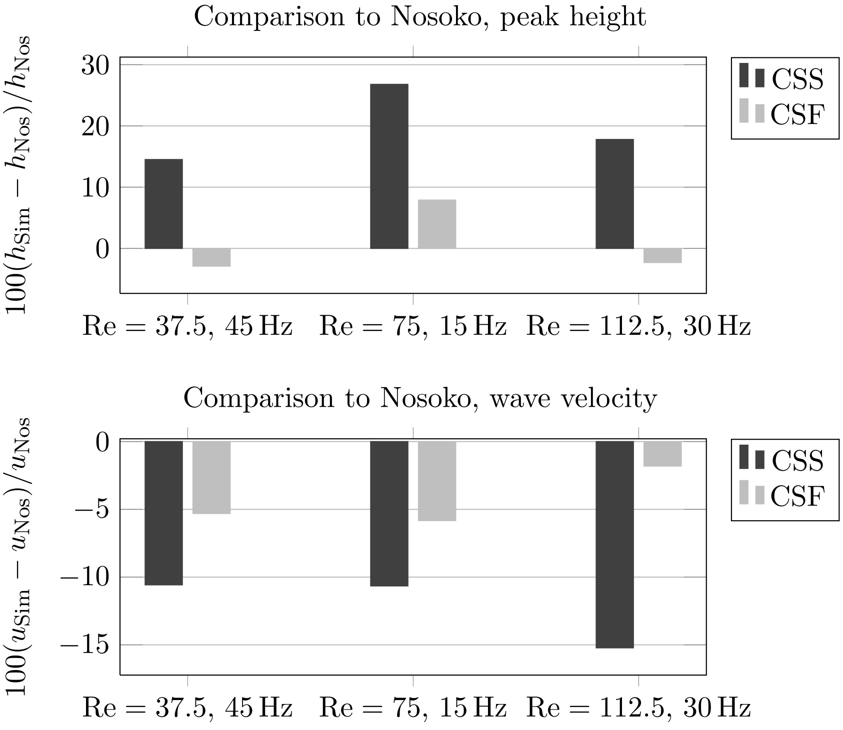

Figure 3.7.: Comparison of wave peak height and wave velocity to Nosoko et al. (1996).

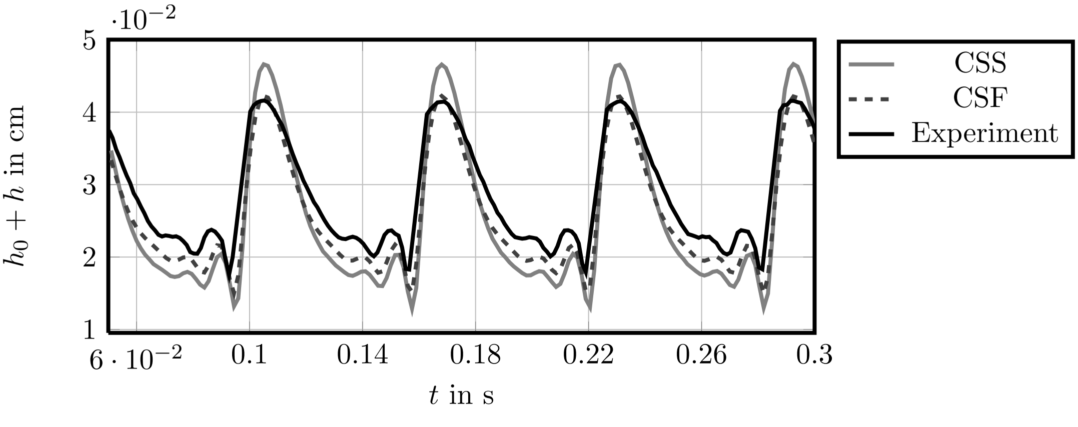

Figure 3.8.: Comparison of local film thickness to CCI measurements in Dietze et al. (2009).

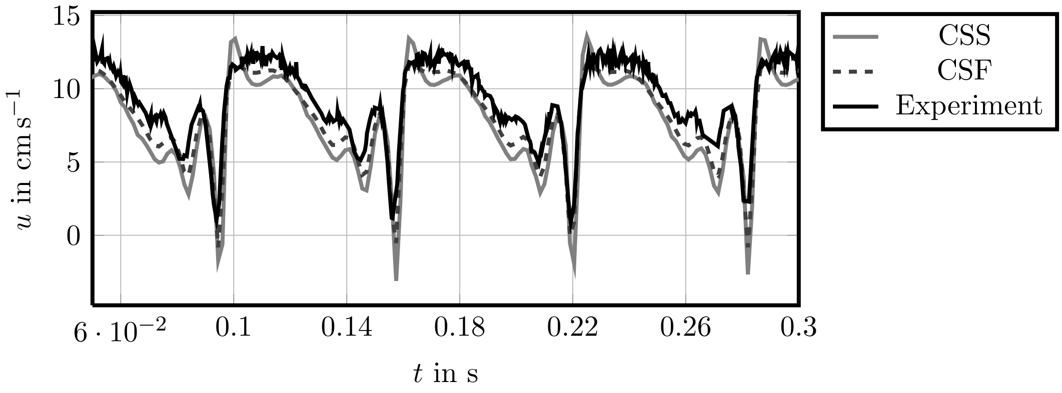

Figure 3.9.: Comparison of streamwise velocity at the interface to LDV measurements in Dietze et al. (2009).

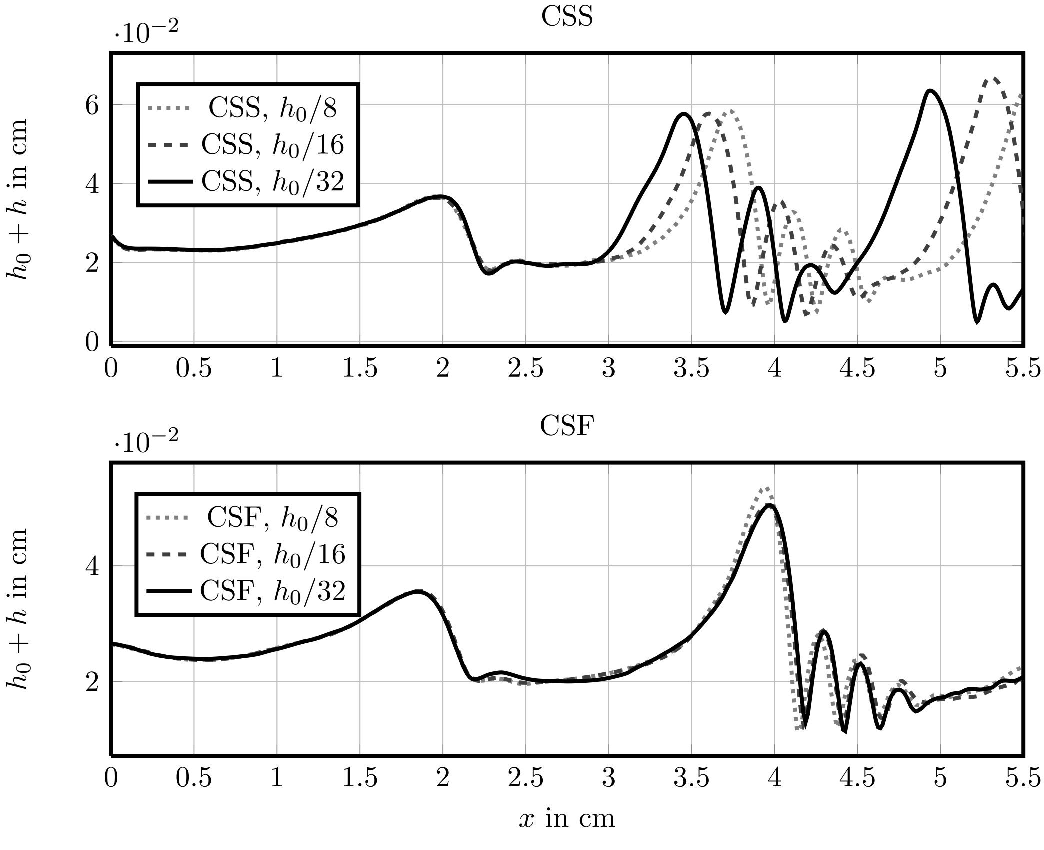

Figure 3.10.: Film thickness after grid refinement.

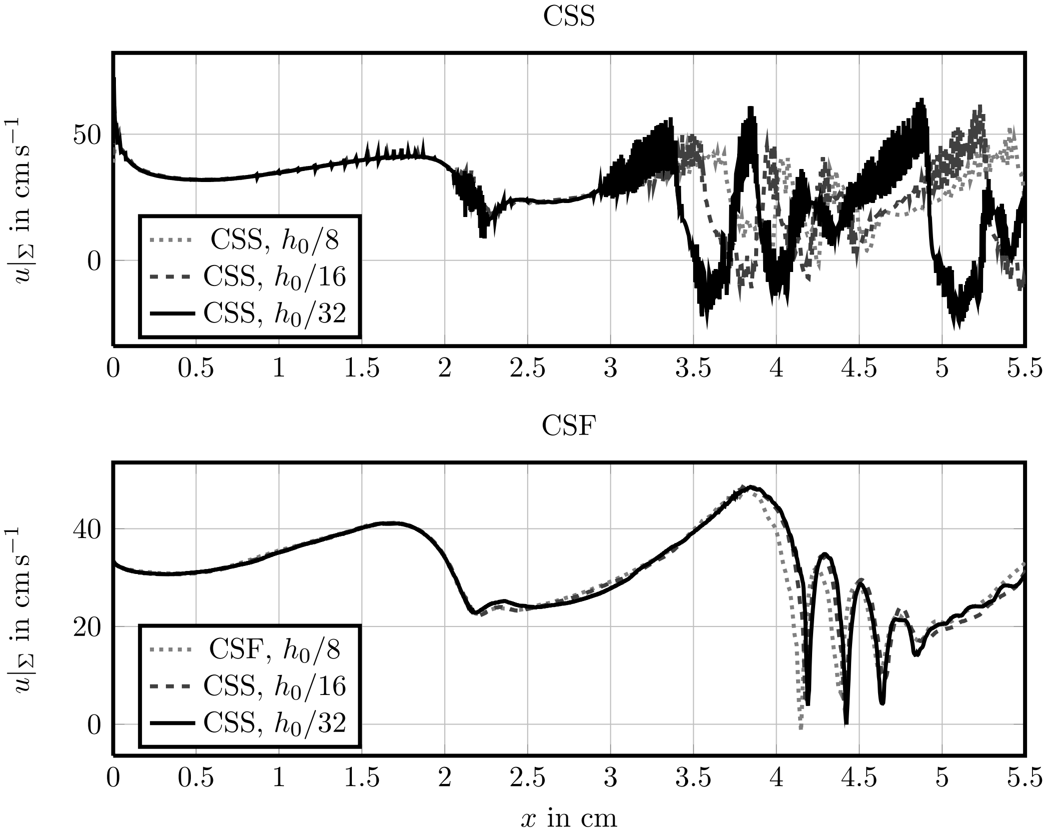

Figure 3.11.: Streamwise velocity at the interface after grid refinement.

on a domain of length $256h_0$. See Figure 3.10 for film height, and Figure 3.11 for streamwise velocity at the interface at $t = 0.22\,\mathrm{s}$.

Simulations with CSS do not converge after grid refinement. Instead, the onset of heavy velocity oscillations is observed. In Section 3.5, a high number of small vortices were noticed in vicinity to the interface. The number of these vortices increased after grid refinement, clearly indicating that those are numerical artifacts.

On the other hand, the convergence of simulations with CSF is satisfactory, when one takes into account that a transient problem was simulated over a comparatively long time. It is concluded that with a resolution of $h_0/16$, the hydrodynamics of falling films in the considered regime is sufficiently resolved. Accordingly, if not mentioned otherwise, all computations are performed with this resolution.

3.7. Conclusion

In this Chapter, the numerical method for direct numerical simulations in this thesis was introduced. The boundary and initial conditions applied for simulations of falling films were described.

The employed numerical solver provides two different methods for the discretization of surface tension, CSS and CSF. It was observed that the velocity fields of simulations with CSS differ from those with CSF. In a number of test cases, results with both surface tension models were compared to experimental and analytical results. It was observed that CSF yields, in every case, results that are closer to the literature.

Despite of that, CSS has the advantage that it can be discretized in a momentum conservative way. An argumentation was provided why CSS cannot be easily discretized in a way that is competitive to CSF.

4. Global linear stability analysis

4.1. Introduction

In Chapter 2, a sufficient condition for stability of the flow field was derived. This condition, however, is an overestimation. If precise stability results are desired, one has to resort to numerical methods.

Much work in this direction has been devoted to the Orr-Sommerfeld approach to linear stability of falling films. Here, two separate points of view have to be distinguished. Starting with the pioneering works of Benjamin (1957) and Yih (1963), the majority of work has been devoted to the temporal formulation of the Orr-Sommerfeld equation, where wave velocity and temporal amplification factor for a perturbation with a prescribed wavelength are searched for. A comprehensive introduction to these equations and alternative approaches can be found in Schmid and Henningson (2001). An overview of methods and known results in the context of falling films is given in Chapter 2 of Chang and Demekhin (2002). For reference, we provide a derivation of the temporal Orr-Sommerfeld equation in Section B.

On the other hand, in Krantz and Owens (1973) a spatial formulation is given, where the wavelength and spatial amplification factor for a perturbation of prescribed frequency is sought. The spatial formulation is in accordance with the physical observation that the amplitude of the waves grows in downstream direction, at least until they become so large that nonlinear effects inhibit their growth.

The Orr-Sommerfeld approach to hydrodynamic stability relies on the assumption that the velocity of the basic flow is homogeneous in two space directions. Effectively, the basic flow may depend on only one space variable, namely the one in cross-streamwise direction, perpendicular to the wall (denoted by y in this work). Since the knowledge of the flow field at a single downstream position is sufficient for this type of analysis, it also called *local stability analysis*.

A real falling film, however, has an inlet, where the liquid enters the wall. This inlet is often designed as a small slit, and the velocities at the inlet are in general different from the one of a developed flow. The inlet introduces an inhomogeneity, and the flow field has to develop over a certain distance until the developed flow is reached, introducing a dependence of the basic flow on x.

At the same time, it is known that the primary instability of a falling film is convective, as has been shown experimentally in Liu et al. (1993) and theoretically in Brevdo et al. (1999). This means that localized perturbations get advected away from their source, leaving the film in an unperturbed state after a finite time. Convectively unstable flows, however, are *noise amplifiers* in the sense of Huerre and Monkewitz (1990), meaning that they are especially susceptible to external noise. The question arises if the inhomogeneity at the inlet has a significant influence on the stability of the film.

In this chapter, this question is studied by means of a *global linear stability analysis*, which is able to take non-homogeneous flow fields into account. The approach is based on an application of Arnoldi iteration (Arnoldi, 1951) to the evolution operator $\exp(\boldsymbol{G}T), T > 0$, where $\boldsymbol{G}$ is the linearized stability operator. For a a single-phase flow with fixed boundaries, this method has been used to identify numerical modes of a solver for the incompressible Euler equations in Eriksson and Rizzi (1985). Later, this approach was employed to find physical modes for a Navier-Stokes flow in Chiba (1998), and for the global linear stability analysis of fully three-dimensional, non-parallel flows in Tezuka and Suzuki (2006). FS3D is used to simulate the response $\exp(\boldsymbol{G}T)\boldsymbol{\zeta}$ to a number of carefully calculated perturbations $\boldsymbol{\zeta}$. In order to calculate these perturbations, one has to perform linear algebra on the phase space, which is problematic due to the free surface. The same transformation that was used in Section 2.2 is employed to define a substitute phase space that is actually a vector space, and on which perturbations can be scaled and added. In the context of free surface flows, Arnoldi's method was used in Christodoulou and Scriven (1988) to investigate the stability of coating flows. Their method relies on the eigensystem analysis of the stiffness matrix inside a finite element solver. In contrast to this, in our approach, an explicit representation of the linearized stability operator $\boldsymbol{G}$ is not needed, it is *Jacobian free*. See Theofilis (2003, 2011) for an overview of different approaches to global linear stability analysis of flows with a fixed boundary. Variants of the presented approach should be applicable to more general stability problems for free boundary flows.

This chapter is structured as follows: In Section 4.2, it is described how Arnoldi's algorithm can be used to analyze the stability of general dynamical system. The algorithm is generalized to the Navier-Stokes equations with a free boundary in Section 4.3. Details on the computational setup used in this chapter can be found in 4.4. In Section 4.5, the Algorithm is validated by comparison to results achieved by the temporal formulation of the Orr-Sommerfeld equation. Results of the stability analysis for periodic flows are shown in Section 4.6, and those on domains with an inlet and an outlet in Section 4.7.

This chapter is based on Albert et al. (2013b).

4.2. Arnoldi's Algorithm for dynamical systems

We start by fixing some notation regarding the stability of stationary solutions of dynamical systems. Then we introduce the general idea of the algorithm, as it has been used to investigate steady states of fixed boundary problems.

4.2.1. Formulation

We consider a general dynamical system, given by the evolution equation

$$\frac{\mathrm{d}\boldsymbol{x}}{\mathrm{d}t} = \boldsymbol{f}(\boldsymbol{x}), \quad \boldsymbol{x}(0) = \boldsymbol{x}_{\mathrm{ini}}. \tag{4.1}$$

Here, $\boldsymbol{x} \in X$, where X is an appropriate phase space. This means that $\boldsymbol{x}$ contains the complete information about the physical state of the system at a given time. When the Navier-Stokes equations are considered as the system of governing equations, $\boldsymbol{x}$ is typically a divergence free velocity field. The phase space X, on the other hand, is the set of all possible configurations (note that the meaning of "phase" in this context is different from when it is used in the sense of "liquid phase"). For mathematical convenience, it is often desirable to have a phase space that is a linear or affine linear space, even if this implies that it contains states that are physically unreasonable. For example, a phase space can be defined as the set of all vector fields on some domain that are divergence free and have finite energy.

In Chapter 2, X was an infinite dimensional function space, defined in (2.198). Since the algorithm considered here is numerical, however, we assume in the following that X is finite dimensional, with $\dim X = N$. The phase space is defined by the discretization of the governing equations within FS3D. Now, X as well as its dimension depend on the resolution. The map

$$\boldsymbol{f} : X \to X \tag{4.2}$$

represents the (typically nonlinear) vector field of phase velocity. In our discrete setting, (4.1) is a system of coupled ODEs, cf. Section 3.2.

Let $\boldsymbol{x}_0$ be a stationary solution of (4.1), i.e. $\boldsymbol{f}(\boldsymbol{x}_0) = 0$. We apply a Taylor series expansion around $\boldsymbol{x}_0$:

$$\boldsymbol{f}(\boldsymbol{x}_0 + \boldsymbol{\zeta}) = \boldsymbol{f}(\boldsymbol{x}_0) + \frac{\partial \boldsymbol{f}(\boldsymbol{x}_0)}{\partial \boldsymbol{x}}\boldsymbol{\zeta} + O(\boldsymbol{\zeta}^2), \tag{4.3}$$

where $\boldsymbol{\zeta}$ is a small disturbance. Considering that the second- or higher-order terms with respect to $\|\boldsymbol{\zeta}\|$ are negligibly small, the linearized stability equations are given by

$$\frac{\mathrm{d}\boldsymbol{\zeta}(t)}{\mathrm{d}t} = \boldsymbol{G}\boldsymbol{\zeta}(t), \quad \boldsymbol{\zeta}(0) = \boldsymbol{\zeta}_0, \tag{4.4}$$

where $\boldsymbol{G} = \frac{\partial \boldsymbol{f}(\boldsymbol{x}_0)}{\partial \boldsymbol{x}}$ is the Jacobian of $\boldsymbol{f}$.

We denote by $\boldsymbol{\varphi}_i$ the eigenmodes of $\boldsymbol{G}$, and by λ_i the corresponding eigenvalues. The solution of (4.4) is given by

$$\boldsymbol{\zeta}(t) = \exp(\boldsymbol{G}t)\boldsymbol{\zeta}_0, \tag{4.5}$$

and as can be seen by considering the Jordan normal form of $\boldsymbol{G}$, the stability behaviour of the steady state is determined by the real parts of the eigenvalues. If they are all negative, the steady state is asymptotically stable; if there is at least one eigenvalue with a positive real part, it is unstable. If there are eigenvalues with a zero real part, and the real parts of all other eigenvalues are negative, we call the steady state neutrally stable. Since we are restricted to a finite dimensional setting, only discrete spectra can occur.

Even a real $\boldsymbol{G}$ will in general have a complex eigensystem. The physical meaning of this is the following: Let $\boldsymbol{\varphi} = \boldsymbol{a} + i\boldsymbol{b}$ be an eigenmode to the eigenvalue $\lambda = \alpha + i\beta$. Then, the function

$$\boldsymbol{\zeta}(t) = \exp(\alpha t)\left(\cos(\beta t)\boldsymbol{a} - \sin(\beta t)\boldsymbol{b}\right) = \mathfrak{Re}\left(\exp(\lambda t)\boldsymbol{\varphi}\right), \tag{4.6}$$

is a solution to the linearized stability equations (4.4) to the initial value $\boldsymbol{\zeta}_0 = \boldsymbol{a} = \mathfrak{Re}\boldsymbol{\varphi}$. At the same time, the function

$$\boldsymbol{\zeta}(t) = \exp(\alpha t)\left(\sin(\beta t)\boldsymbol{a} + \cos(\beta t)\boldsymbol{b}\right) = \mathfrak{Im}\left(\exp(\lambda t)\boldsymbol{\varphi}\right) \tag{4.7}$$

solves (4.4) with initial value $\boldsymbol{\zeta}_0 = \boldsymbol{b} = \mathfrak{Im}\boldsymbol{\varphi}$.

4.2.2. A Jacobian free method for stability of dynamical systems

In principle, it is possible to compute the whole matrix $\boldsymbol{G}$, and to calculate its eigensystem. However, since its dimension N might be extremely large, this is impractical. We use the method of Chiba (1998) to compute an approximate eigensystem on a much smaller vector space of dimension $M \ll N$. Based on Arnoldi iteration, it is an iterative algorithm that uses linear filtering by the evolution operator to determine those parts of the spectrum that are decisive for the asymptotic stability; see Figure 4.1 for a flowchart.

The algorithm is based on the assumption that a numerical solver exists for equation (4.1). In our case, this is FS3D. In the first step, a steady state solution $\boldsymbol{x}_0 \in X$, which is a converged solution for the solver, is computed. Note that $\boldsymbol{x}_0$ is an N-dimensional vector of real numbers. Now, a random initial perturbation $\boldsymbol{\zeta}_1 \in X$, $\|\boldsymbol{\zeta}_1\| = 1$, is determined by computing N random numbers and normalizing. Now simulations with two different initial values, $\boldsymbol{x}_{1+}^{\mathrm{ini}} = \boldsymbol{x}_0 + \epsilon\boldsymbol{\zeta}_1$ and $\boldsymbol{x}_{1-}^{\mathrm{ini}} = \boldsymbol{x}_0 - \epsilon\boldsymbol{\zeta}_1$, for some small $\epsilon > 0$ are started, and the simulation is run for a fixed time $T > 0$. The outcome of these simulation runs is denoted by $\boldsymbol{x}_{1+}$ and $\boldsymbol{x}_{1-}$, respectively. The vector $\boldsymbol{B}\boldsymbol{\zeta}_1 = \exp(\boldsymbol{G}T)\boldsymbol{\zeta}_1$ is calculated from the following equation:

$$\boldsymbol{B}\boldsymbol{\zeta}_1 = (\boldsymbol{x}_{1+} - \boldsymbol{x}_{1-})/2\epsilon. \tag{4.8}$$

The vector $\boldsymbol{B}\boldsymbol{\zeta}_1$ is the state of our perturbation at time T, in other words the solution of equation (4.4) to the initial value $\boldsymbol{\zeta}_1$ at time T.

At this stage, the action of $\boldsymbol{B}$ on the one-dimensional subspace $\mathrm{span}\{\boldsymbol{\zeta}_1\}$ is known. This subspace is extended by computing a new basis vector $\boldsymbol{\zeta}_2$ via the Gram-Schmidt orthogonalization procedure:

$$\boldsymbol{B}\boldsymbol{\zeta}_1 = c_{1,1}\boldsymbol{\zeta}_1 + c_{2,1}\boldsymbol{\zeta}_2, \tag{4.9}$$

$$< \boldsymbol{\zeta}_i, \boldsymbol{\zeta}_j > = \delta_{i,j}. \tag{4.10}$$

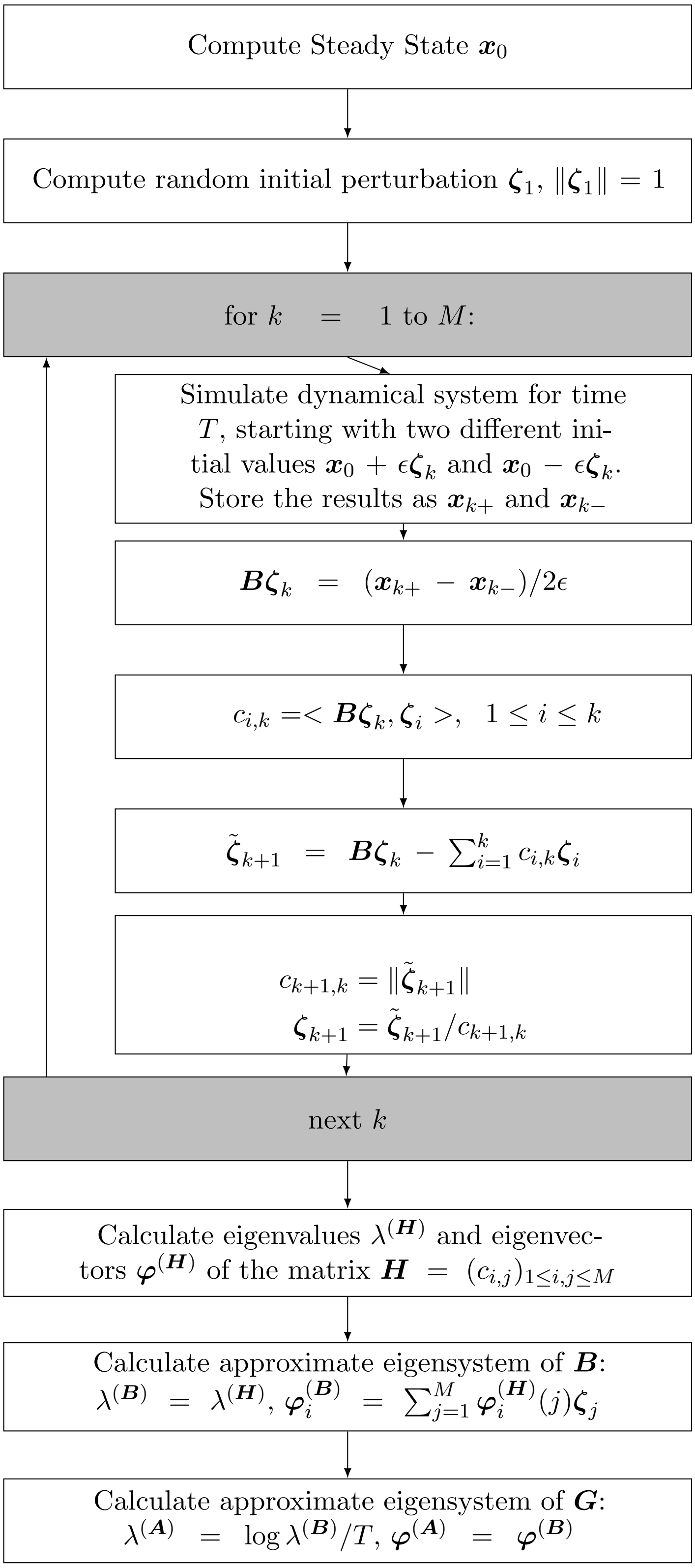

Figure 4.1.: Flowchart of Arnoldi's algorithm for general dynamical systems.

Then the procedure is iterated. Note that - in exact arithmetics - the construction of a new basis vector cannot be performed if and only if $\mathrm{span}\{\boldsymbol{\zeta}_1, \ldots, \boldsymbol{\zeta}_k\}$ is a $\boldsymbol{B}$-invariant subspace of X for some k. This is in general very unlikely, but will happen at the latest after N iterations. In this case, $\boldsymbol{B}$ would be known completely.

Usually, however, the procedure is iterated M times only, until the identity

$$\boldsymbol{B}\boldsymbol{\zeta}_M = c_{1,M}\boldsymbol{\zeta}_1 + \ldots + c_{M,M}\boldsymbol{\zeta}_M + c_{M+1,M}\boldsymbol{\zeta}_{M+1} \tag{4.11}$$

is reached. If $|c_{M+1,M}|$ is sufficiently small, we conclude that the most amplified modes - those responsible for the asymptotic stability behavior - can be well represented in the basis $\{\boldsymbol{\zeta}_1, \ldots, \boldsymbol{\zeta}_M\}$, and we approximate the above expression as

$$\boldsymbol{B}\boldsymbol{\zeta}_M = c_{1,M}\boldsymbol{\zeta}_1 + \ldots + c_{M,M}\boldsymbol{\zeta}_M. \tag{4.12}$$

With this approximation, the action of $\boldsymbol{B}$ is known on the M-dimensional subspace $\mathrm{span}\{\boldsymbol{\zeta}_1, \ldots, \boldsymbol{\zeta}_M\}$:

$$\boldsymbol{B}\{\boldsymbol{\zeta}_1, \ldots, \boldsymbol{\zeta}_M\} = \{\boldsymbol{\zeta}_1, \ldots, \boldsymbol{\zeta}_M\} \underbrace{\begin{bmatrix} c_{1,1} & \cdots & \cdots & c_{1,M-1} & c_{1,M} \\ c_{2,1} & \cdots & \cdots & c_{2,M-1} & c_{2,M} \\ 0 & \ddots & & \vdots & \vdots \\ \vdots & \ddots & \ddots & \vdots & \vdots \\ 0 & \ldots & 0 & c_{M,M-1} & c_{M,M} \end{bmatrix}}_{\boldsymbol{H}}. \tag{4.13}$$

Since this is a square matrix, its eigenvalues $\lambda^{\boldsymbol{H}}$ and $\boldsymbol{\varphi}^{\boldsymbol{H}}$ can be determined. Computing the eigensystem of $\boldsymbol{B}$ amounts to a simple basis change: $\lambda^{\boldsymbol{B}} = \lambda^{\boldsymbol{H}}$, and

$$\boldsymbol{\varphi}_i^{(\boldsymbol{B})} = \sum_{j=1}^{M} \boldsymbol{\varphi}_i^{(\boldsymbol{H})}(j)\boldsymbol{\zeta}_j, \tag{4.14}$$

where $\boldsymbol{\varphi}_i^{(\boldsymbol{H})}(j)$ is the j-th component of the i-th eigenvector of $\boldsymbol{H}$.

Now, the spectral mapping theorem for the matrix exponential allows to determine the eigensystem of $\boldsymbol{G}$. The eigenvectors stay the same, i.e.

$$\boldsymbol{\varphi}^{(\boldsymbol{G})} = \boldsymbol{\varphi}^{(\boldsymbol{B})}, \tag{4.15}$$

and the eigenvalues are obtained by the relation

$$\lambda^{(\boldsymbol{B})} = \exp(\lambda^{(\boldsymbol{G})}T). \tag{4.16}$$

In practice, M is not chosen a priori, but the iteration is repeated until the leading eigenmodes have converged to the desired accuracy.

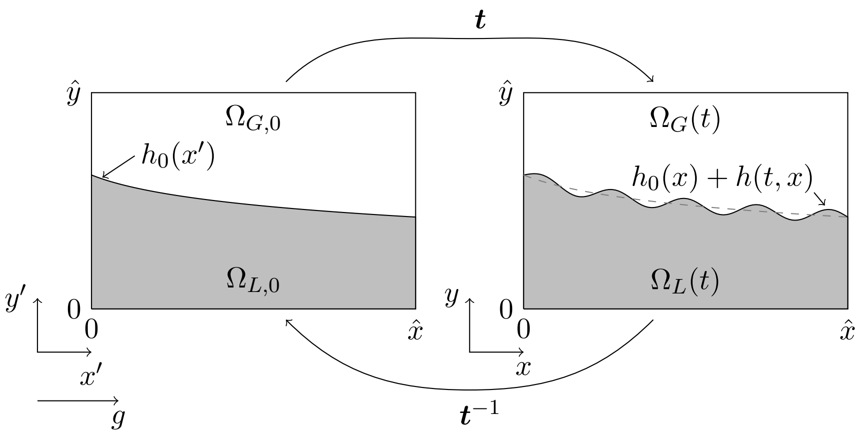

Figure 4.2.: Sketch of the reference and time-dependent domain.

4.3. Arnoldi's Method for two-phase Navier-Stokes

4.3.1. Pressure

There are two problems in applying the above method to the two-phase Navier-Stokes equations. The first one is that the Navier-Stokes equations are not in the form of an evolution equation, since there is no time derivative for the pressure. In Section 2.2.5, this problem was addresses by the introduction of a suitable projection onto a space of solenoidal vector fields. It was noted in Section 3.2.4 that the numerical treatment of the divergence condition within FS3D is closely related to projection methods of this kind. Here, we exploit this property. Since the pressure can always be recovered from the velocity field, a perturbation of the steady state is defined to consist of a perturbation of the interface, and a divergence free perturbation of the velocity field, and only these variables are stored in the vector $\boldsymbol{\zeta}$, which describes a perturbation.

4.3.2. Transformation to a fixed domain

The second problem is that, due to the free interface, the physical phase space is not a vector space. Different initial perturbations yield different configurations of the interface at the end of a simulation run. In fact, a velocity at a certain point (x, y) could either belong to the liquid phase or the gas phase, and a direct summation or subtraction of that velocity component is not a meaningful operation.

Therefore, as in Section 2.2, we employ a transformation of the velocity field between the time-dependent domain and a fixed reference domain which is defined by the steady state, compare Figure 4.2. Sums and differences of velocity fields on the reference domain can be safely performed, since after transformation, only velocities in the liquid are compared to liquid velocities, and vice versa.

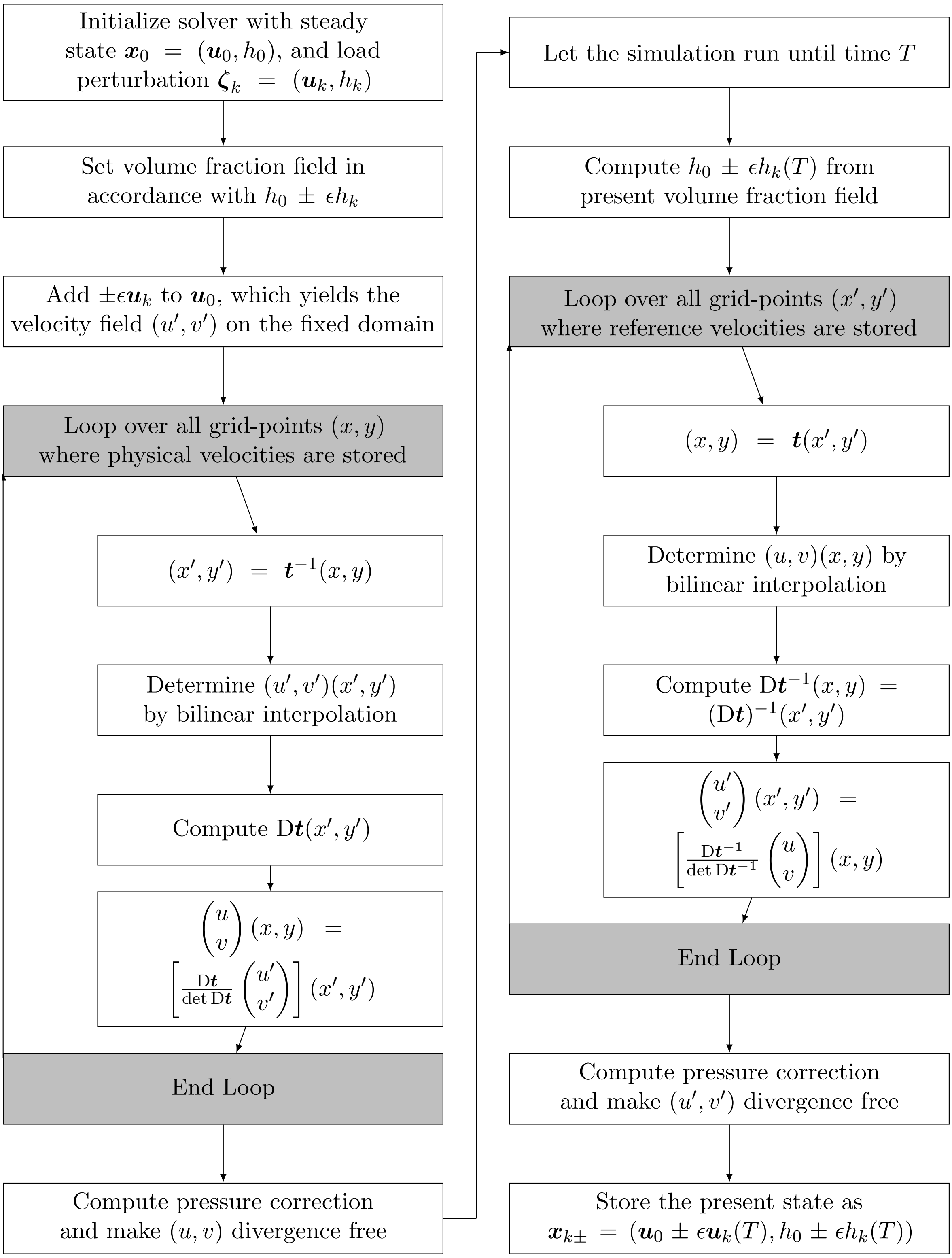

Figure 4.3.: Computing $\boldsymbol{x}_{k\pm}$ out of $\boldsymbol{\zeta}_k$ for free boundary problems.

We call the coordinates in the reference domain x' and y', and the coordinates in the time-dependent domain x and y. Different conditions at the inlet can provoke a non-constant height of the steady state. Therefore, the situation where h_0 is a function of x' is considered. Note that the evolution of the flow field will still take place on the time-dependent, physical domain, and that it is therefore not necessary to transform the complete system of governing equations as it was done in Appendix A.

In order to perform this transformation, a smooth, bijective and invertible mapping between both domains is necessary. The easiest way to do so is to use a map which is piecewise linear in y' for a fixed x'. To assess the feasibility of this, it is important to note that a smooth solution to the governing equations (1.31) - (1.36) is in general not differentiable across the interface and, in fact, neither the steady state nor the found eigenmodes have this property. For conservation of mass in volume of fluid simulations, however, it is essential that the condition on zero divergence (4.34) is maintained in interface cells, and a piecewise linear transformation would violate that. Therefore, we choose a smooth transformation $\boldsymbol{t}(t) : \Omega \to \Omega$, which is defined in the following way:

$$\boldsymbol{t}(t, x', y') = \begin{pmatrix} T^x \\ T^y \end{pmatrix} = \begin{pmatrix} x' \\ \frac{h(t,x')}{h_0(x')^2 - \hat{y} h_0(x')} y'^2 + \frac{h_0(x')^2 - \hat{y} h_0(x') - \hat{y} h(t,x')}{h_0(x')^2 - \hat{y} h_0(x')} y' \end{pmatrix} = \begin{pmatrix} x \\ y \end{pmatrix}. \tag{4.17}$$

For a fixed x', T^y is parabolic in y', and for an arbitrary h it holds that

$$T^y(x', 0) = 0, \tag{4.18}$$

$$T^y(x', h_0(x')) = h_0(x') + h(x'), \tag{4.19}$$

$$T^y(x', \hat{y}) = \hat{y}. \tag{4.20}$$

The crucial property

$$\boldsymbol{t}(t, \Omega_{L,0}) = \Omega_L(t), \tag{4.21}$$

$$\boldsymbol{t}(t, \Omega_{G,0}) = \Omega_G(t), \tag{4.22}$$

$$\boldsymbol{t}(t, \Sigma_0) = \Sigma(t), \tag{4.23}$$

however, holds only if T^y is also monotonously increasing in y'. The derivative

$$\frac{\partial T^y}{\partial y'} = \frac{2h}{h_0^2 - \hat{y} h_0} y' + \frac{h_0^2 - \hat{y} h_0 - \hat{y} h}{h_0^2 - \hat{y} h_0} \tag{4.24}$$

has, for $h \neq 0$, a unique intersection y'_0 with the x-axis. If $h(x') < 0$, then $\frac{\partial T^y}{\partial y'}(x', y')$ is increasing in y', and $y'_0 \leq 0$ must hold. If $h(x') > 0$, then $\frac{\partial T^y}{\partial y'}(x', y')$ is decreasing, and $y'_0 \geq \hat{y}$ must hold. It is easy to see that both conditions are fulfilled if and only if

$$|h(t, x)| < h_0(x) - \frac{h_0(x)^2}{\hat{y}} \text{ for all } t, x'. \tag{4.25}$$

Given a velocity field $(u', v')(x', y')$ on the reference domain, the velocity field on the time-dependent domain is again obtained by Beale's transformation:

$$\begin{pmatrix} u \\ v \end{pmatrix} (x, y) = \left[\frac{1}{\det \mathrm{D}\boldsymbol{t}} \mathrm{D}\boldsymbol{t} \begin{pmatrix} u' \\ v' \end{pmatrix} \right] (x', y') \text{ where } \boldsymbol{t}(x', y') = (x, y). \tag{4.26}$$

Here, $\mathrm{D}\boldsymbol{t}$ denotes the Jacobian of $\boldsymbol{t}$. The transformed velocity field (u, v) is divergence free if and only if (u', v') is divergence free, see Bock (1977) for a proof.

The explicit expressions for the Jacobian and the determinant are

$$\mathrm{D}\boldsymbol{t}(t, x', y') = \begin{pmatrix} 1 & 0 \\ y'(y' - \hat{y}) \left[\frac{\partial_x h}{h_0(h_0 - \hat{y})} + \frac{h \partial_x h_0 (\hat{y} - 2h_0)}{h_0^2 (h_0 - \hat{y})^2} \right] & 1 + \frac{2hy' - \hat{y}h}{h_0(h_0 - \hat{y})} \end{pmatrix}, \tag{4.27}$$

$$\det \mathrm{D}\boldsymbol{t} = 1 + \frac{2hy' - \hat{y}h}{h_0(h_0 - \hat{y})}. \tag{4.28}$$

In order to transform a velocity field from the physical domain to the reference domain, $\boldsymbol{t}^{-1}$ is also needed. Although it would be possible to write down an explicit expression, we prefer to determine the inverse transform by Newton iteration, in order to have good control over floating point errors. The Jacobian of $\boldsymbol{t}^{-1}$ is calculated by the inverse function theorem:

$$\mathrm{D}\boldsymbol{t}^{-1}(x, y) = (\mathrm{D}\boldsymbol{t})^{-1} (x', y') \text{ where } (x', y') = \boldsymbol{t}^{-1}(x, y). \tag{4.29}$$

4.3.3. Linear algebra on the reference domain

Definition of the sum and scaling of perturbations

For every interfacial configuration and every velocity field, we can now compute a corresponding velocity field on the reference domain, which allows us to do linear algebra by the two operations

$$(\boldsymbol{u}_\alpha, h_\alpha) + (\boldsymbol{u}_\beta, h_\beta) = (\boldsymbol{u}_\alpha + \boldsymbol{u}_\beta, h_\alpha + h_\beta), \tag{4.30}$$

$$\gamma(\boldsymbol{u}, h) = (\gamma \boldsymbol{u}, \gamma h), \gamma \in \mathbb{C}. \tag{4.31}$$

Here, $\boldsymbol{u}$ denotes the velocity field of a perturbation, transformed to the reference domain, and h denotes the corresponding interfacial perturbation. The boundary conditions for the velocity perturbations are the same as for the whole velocity field, with the exception of the nonhomogeneous Dirichlet-condition in the inflow/outflow case. Since the steady state already fulfills this condition, the perturbation has to satisfy a homogeneous Dirichlet condition at the inlet.

Definition of the scalar product

To perform the Gram-Schmidt algorithm, a scalar product on the phase space is needed. Note that a norm is not required to define an eigenvector, and the outcome of the stability analysis does not depend on the used scalar product. Nevertheless, we prefer to use a physically meaningful scalar product, which is defined as follows:

$$<(\boldsymbol{u}_\alpha, h_\alpha), (\boldsymbol{u}_\beta, h_\beta)>= \frac{1}{2}\int_0^{\hat{x}}\int_0^{\hat{y}} \rho(x,y)\boldsymbol{u}_\alpha \overline{\boldsymbol{u}_\beta} \mathrm{d}x\mathrm{d}y + \frac{1}{2}\int_0^{\hat{x}} \sigma(\partial_x h_\alpha)\overline{(\partial_x h_\beta)}\mathrm{d}x. \tag{4.32}$$

In the periodic case, we have the condition $\int_0^{\hat{x}} h(x)\mathrm{d}x = 0$, and in the inflow/outflow case, we have $h(0) = 0$. In both cases, due to Poincare's inequality, the scalar product is positive definite. With this scalar product, $\|\boldsymbol{x}\|^2 =< \boldsymbol{x}, \boldsymbol{x} >$ is an approximation to the sum of kinetic energy plus interfacial energy of that state. The expression for the interface energy is derived from the exact expression for the total surface energy

$$\sigma \int_0^{\hat{x}} \sqrt{1 + (\partial_x h(x))^2}\mathrm{d}x \tag{4.33}$$

by Taylor expansion and subtraction of the surface energy of the steady state.

Especially on long domains, the calculation of the scalar product and the construction of new perturbations can be problematic due to accumulating floating point errors. In order to alleviate these problems, we employ the modified Gram-Schmidt algorithm, and calculate the scalar products by Kahan summation (see Kahan, 1965).

4.3.4. Numerical realization

With this, the algorithm can be applied to free boundary problems in the following way, compare Figure (4.3) : In the first step, the steady state $\boldsymbol{x}_0 = (\boldsymbol{u}_0, h_0)$ is calculated by a standard CFD run.

Given a normed perturbation $\boldsymbol{\zeta}_k = (\boldsymbol{u}_k, h_k)$, we can compute $\boldsymbol{B}\boldsymbol{\zeta}_k$ as follows: The VOF-solver FS3D is initialized with $\boldsymbol{x}_0 = (\boldsymbol{u}_0, h_0)$, and the volume of fluid field is adjusted in such a way that it conforms with $h_0 + \epsilon h_k$. Then, $\epsilon \boldsymbol{u}_k$ is added to $\boldsymbol{u}_0$, the result of which is still divergence free. The velocity field $\boldsymbol{u}_0 + \epsilon \boldsymbol{u}_k$ is defined on the reference domain, and $\boldsymbol{t}$ must be applied to transform it to the physical domain.

This is done by looping over all grid points (x, y), where velocities are stored. The physical velocity component at (x, y) is computed out of the velocities at $(x', y') = \boldsymbol{t}^{-1}(x, y)$ on the reference domain. In general, (x', y') will not be a grid point, and the needed velocity components are determined by bilinear interpolation. The derivatives of the height functions in (4.26) are evaluated by central differences.

Since the height functions are closely related to the volume fraction field, their values are stored cell centered. For the transformation of u-velocities, height information is needed on the cell faces, which is computed by simple averaging of the two adjacent height values.

Inside FS3D, divergence is defined where pressure information is stored, compare

Figure (3.1), and a velocity field is considered divergence free if

$$\frac{u_{i,j} - u_{i-1,j}}{\Delta x} + \frac{v_{i,j} - v_{i,j-1}}{\Delta y} = 0 \text{ for all } i, j. \tag{4.34}$$

Although the error will be small, after transformation, the velocity field will not be exactly divergence free in this sense. Since condition (4.34) is of paramount importance for conservation of mass, a pressure projection is applied to restore zero divergence.

Now, the solver can run for time T. The resulting velocity field is transformed back onto the reference domain, and the divergence error is removed. This velocity field, together with the current interface configuration, is stored as $\boldsymbol{x}_{k+} = (\boldsymbol{u}_0 + \epsilon \boldsymbol{u}_k(T), h_0 + \epsilon h_j(T))$. In the same way, $\boldsymbol{x}_{k-}$ is determined, and $\boldsymbol{B}\boldsymbol{\zeta}_k$ can be computed by (4.8).

Calculation of the initial perturbation

The random initial perturbation is calculated by first computing a random velocity field, consisting of uniformly distributed random numbers. Then, boundary conditions for the velocity are enforced, and pressure correction is applied, to obtain a solenoidal velocity field $\tilde{\boldsymbol{u}}_1$.

To determine the random initial perturbation of the interface, we start by computing a vector $\tilde{h}_1$ of n_i uniformly distributed random numbers, with zero mean and variance Δx. Here, n_i is the number of grid points in x-direction, and Δx the grid width. Now, a random walk is determined by computing the cumulative sum of these numbers. In the case of inflow/outflow boundary, we are done.

For periodic boundary conditions, it is not sufficient that the interfacial perturbation starts at 0. In order to ensure periodicity, it also has to end in 0. A random function with this property is called a Brownian bridge, and is computed via

$$\tilde{h}_1(i) = \tilde{h}_1(i) - \frac{i}{n_i}\tilde{h}_1(n_i), 1 \leq i \leq n_i. \tag{4.35}$$

Since conservation of mass is another requirement in the periodic case, we finish by subtracting the mean value.

In both cases, the random initial perturbation can be defined by

$$\boldsymbol{\zeta}_1 = (\boldsymbol{u}_1, h_1) := \frac{(\tilde{\boldsymbol{u}}_1, \tilde{h}_1)}{\|(\tilde{\boldsymbol{u}}_1, \tilde{h}_1)\|}. \tag{4.36}$$

Since perturbations always satisfy homogeneous boundary conditions, $\boldsymbol{\zeta}_1$ is still an admissible perturbation.

4.4. Computational setup

4.4.1. Material parameters and resolution

All the simulations but the grid independence study in Section 4.5.3 were performed with quadratic computational cells of size $h_0/16 \times h_0/16$. For all simulations, the height of the computational domain was $2h_0$. The parameters for the iteration procedure were set to $\epsilon = {}^{\|\boldsymbol{x}_0\|}/_{4000}$, where $\|\boldsymbol{x}_0\|$ denotes the norm of the steady state, and $T = {}^{h_0}/_{\bar{u}} = {}^{3\eta_L}/_{\rho_L g h_0}$.

In Pierson and Whitaker (1977), calculations were performed for a fluid with

$$\mathrm{Ka} = 3397. \tag{4.37}$$

In order to compare to their results, the following material parameters were used: $g = 981\,\mathrm{cm\,s^{-2}}$, $\rho_L = 1.0\,\mathrm{g\,cm^{-3}}$, $\eta_L = 0.01\,\mathrm{g\,s^{-1}\,cm^{-1}}$, and $\sigma = 72.72\,\mathrm{g\,s^{-2}}$. All of the presented calculations, except those for the neutral stability curve (Section 4.5.1), were performed with these parameters.

The calculations for the neutral stability curve refer to Chang and Demekhin (2002). They present calculations for a fluid with

$$\mathrm{Ka} = 2900, \tag{4.38}$$

which was matched by setting $\sigma = 70\,\mathrm{g\,s^{-2}}$, $g = 1000\,\mathrm{cm\,s^{-2}}$, $\rho_L = 1.0\,\mathrm{g\,cm^{-3}}$, and $\eta_L = 1.09 \times 10^{-2}\,\mathrm{g\,s^{-1}\,cm^{-1}}$. In all calculations, the material parameters for the gas phase were $\rho_G = 1.2 \times 10^{-3}\,\mathrm{g\,cm^{-3}}$ and $\eta_G = 1.8 \times 10^{-4}\,\mathrm{g\,s^{-1}\,cm^{-1}}$.

4.4.2. Boundary conditions for periodic flow

Simulations with inflow/outflow boundary conditions (cf. Section 3.4.2), as well as simulations with periodic flow are performed. The streamwise boundary conditions for periodic flow are

$$\boldsymbol{u}|_{x=0} = \boldsymbol{u}|_{x=\hat{x}}, \tag{4.39}$$

$$(h_0 + h)|_{x=0} = (h_0 + h)|_{x=\hat{x}}. \tag{4.40}$$

4.5. Validation

Results of temporal stability theory relate to flows with enforced periodicity in space. Here, the steady state is parallel to the wall. A numerical solution of the Orr-Sommerfeld equation in its temporal formulation yields the temporal growth behaviour of a sinusoidal perturbation with a certain wave length. In order to reproduce these results, we performed global stability analyses of films on domains with periodic boundary conditions with varying domain length $\hat{x}$. On such a domain, modes of wavelength $\hat{x}, \frac{\hat{x}}{2}, \frac{\hat{x}}{3} \ldots$ can exist, and if their temporal growth rate is large, they will be identified by the algorithm.

4.5.1. Neutral stability curve.

We define a dimensionless wavenumber $\tilde{k}$ as

$$\tilde{k} = \frac{2\pi h_0}{l}, \tag{4.41}$$

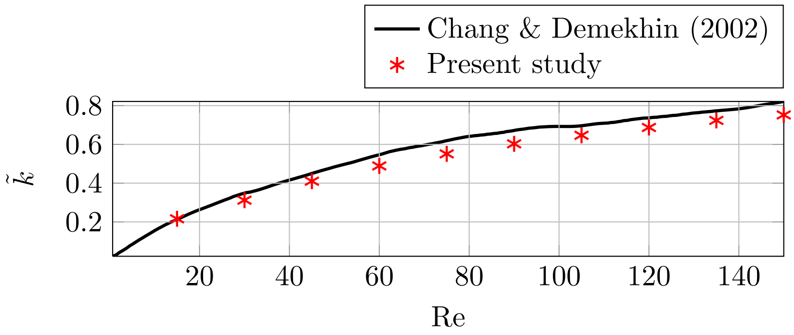

Figure 4.4.: Comparison to the Neutral Stability Curve of Chang and Demekhin (2002).

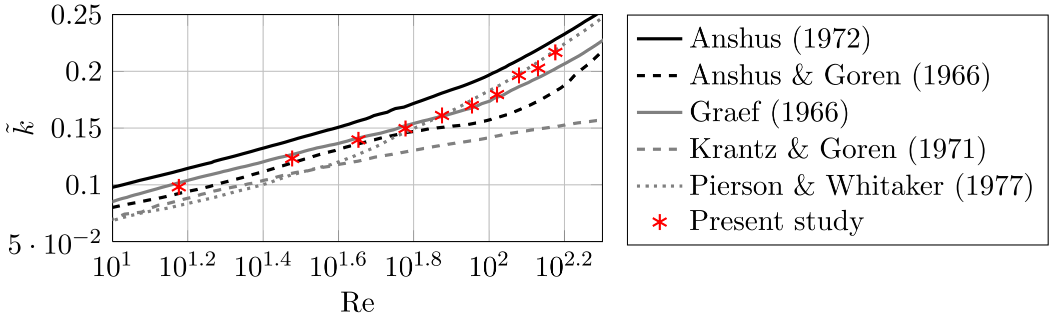

Figure 4.5.: Wavenumber of most amplified mode over Re. Data from Pierson and Whitaker (1977).

where l denotes the wavelength of the perturbation. and we look for the largest wavenumber at which a neutrally stable mode occurs, i.e. one whose eigenvalue fulfills $\mathfrak{Re}\lambda = 0$. To compute our data, we performed a variation of $\hat{x}$ in steps of h_0 around the domain length at which the most amplified mode changes from stable to unstable. We compare to the neutral stability curve published in Chang and Demekhin (2002), see Figure 4.4.

Their analysis was done for flow in a passive atmosphere, cf. Section 1.3.2. It is not easily possible to reproduce that in a VOF solver. Since air has a very low density compared to water, however, the gas atmosphere can be regarded as approximately passive.

4.5.2. Most amplified mode

There exists a wavelength at which a perturbation has the highest growth rate. We search for that by a variation of $\hat{x}$ in steps of h_0 around the domain length at which the eigenvalue with the highest real part occurs. Our results are compared

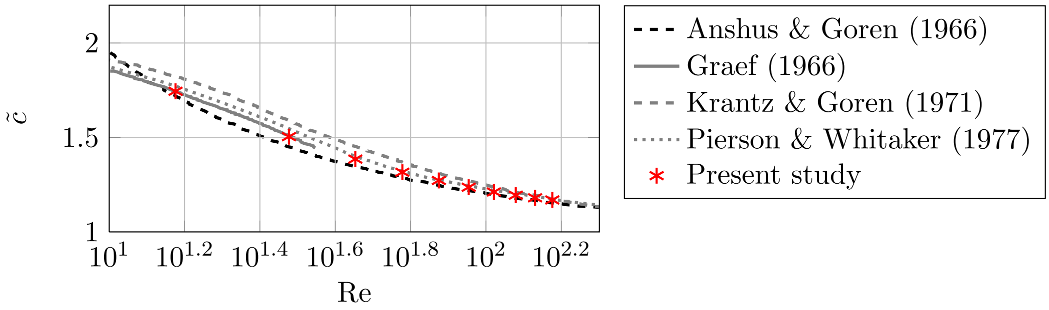

Figure 4.6.: Wave velocity of most amplified mode over Re. Data from Pierson and Whitaker (1977).

to data for the most amplified mode published in Pierson and Whitaker (1977).

In Figure 4.5, we see the dimensionless wavenumber of the most amplified mode. In Figure 4.6, we see its dimensionless wave velocity, defined as

$$\tilde{c} = \frac{\mathfrak{Im} \lambda_1 l}{2\pi u_0}, \tag{4.42}$$

where λ_1 is the eigenvalue of the most amplified mode for the given Re.

Considering that we solve the two-phase problem, whereas in Chang and Demekhin (2002) and Pierson and Whitaker (1977) the one-phase problem is examined, Figures 4.4, 4.5, and 4.6 show favorable agreement with known results, and serve to show that the algorithm can correctly reproduce known results of temporal stability theory.

4.5.3. Influence of mesh size, T and ϵ

In section 3.6.4, it was shown that simulations with a grid size of $h_0/16$ are sufficiently resolved to capture the flow physics of falling films. In order to assess the influence of spatial resolution on the outcome of the presented algorithm, the stability of a periodic film of Re = 90, $\hat{x} = 32h_0$ was analyzed in the periodic setting with three different resolutions: $h_0/8$, $h_0/16$ and $h_0/32$. The eigenvalues with the three largest real parts are given in Table 4.1. It is concluded that a mesh size of $h_0/16$ is sufficient.

In order to perform a stability analysis with the presented method, the parameters T and ϵ have to be chosen. In general, after an increase in T, less iterations have to be performed to obtain converged results, and vice versa. Therefore, the overall simulation time $2MT$ stays virtually constant. When T is chosen large, less summations and scalar products must be carried out, which is advantageous for the numerical stability of the algorithm. However, if T is chosen so large that a perturbation can travel for a distance exceeding its wavelength, the imaginary part of the eigenvalues determined by the algorithm may be wrong.

Δx	T	ϵ	λ_1	λ_2	λ_3
$h_0/8$	$h_0/\bar{u}$	$\|\boldsymbol{x}_0\|/4000$	$32.58 + 317.1i$	$15.94 + 723.4i$	$-3.01 + 1270i$
$h_0/16$	$h_0/\bar{u}$	$\|\boldsymbol{x}_0\|/4000$	$32.81 + 315.5i$	$17.32 + 718.9i$	$-1.68 + 1262i$
$h_0/32$	$h_0/\bar{u}$	$\|\boldsymbol{x}_0\|/4000$	$32.89 + 315.6i$	$17.58 + 719.2i$	$-1.30 + 1262i$
$h_0/16$	$h_0/\bar{u}$	$\|\boldsymbol{x}_0\|/2000$	$32.93 + 315.7i$	$17.54 + 719.1i$	$-1.51 + 1262i$
$h_0/16$	$h_0/\bar{u}$	$\|\boldsymbol{x}_0\|/8000$	$32.78 + 315.4i$	$17.22 + 718.9i$	$-1.77 + 1262i$
$h_0/16$	$2h_0/\bar{u}$	$\|\boldsymbol{x}_0\|/4000$	$32.71 + 315.7i$	$17.25 + 719.7i$	$-1.83 + 1263i$
$h_0/16$	$\frac{1}{2}h_0/\bar{u}$	$\|\boldsymbol{x}_0\|/4000$	$33.22 + 316.4i$	$17.57 + 720.7i$	$-1.56 + 1265i$

Table 4.1.: Eigenvalues with the largest real parts of a periodic film of Re = 90, $\hat{x} = 32h_0$, at three different mesh sizes and a variation of T and ϵ.

The parameter ϵ must be chosen so small that a linear analysis is justified. On the other hand, for very small ϵ, cancellation due to finite floating point precision may occur. After extensive testing, it was found that setting $\epsilon = \|\boldsymbol{x}_0\|/4000$, where $\|\boldsymbol{x}_0\|$ denotes the norm of the steady state, and $T = h_0/\bar{u} = 3\eta_L/\rho_L g h_0$, where $\bar{u}$ is the mean velocity of the Nusselt profile, is a good compromise, c.f. Table 4.1.

4.6. Results with periodic flow

In order to investigate the stability behavior of falling films in the periodic setting, we analyzed 10 water/air films, with Reynolds numbers from 15 to 150, in steps of 15. For each Re, we varied the domain length $\hat{x}$ from $4h_0$ to $84h_0$, in steps of $4h_0$. In Figure 4.7, the largest real part encountered in the spectrum in dependence on Re and $\hat{x}$ is shown. We found two different types of eigenmodes: shear modes and surface modes.

4.6.1. Shear modes

Shear modes are eigenmodes with a purely real eigenvalue; in Figure 4.7, they are marked by a surounding black circle. The interfacial perturbation of shear modes is very small. The basis vectors of the constructed Krylov subspace are linearly independent, which does not imply that the according interfacial perturbations are also linearly independent. Despite of that, the presented algorithm cannot easily represent a truly zero interface perturbation. Nevertheless, the found deflections are very small, and we conclude that the algorithm tries to represent zero interface peturbation. The shear modes we found are basically independent of x, and their v-velocities are negligibly small compared to the u-velocities. Accordingly, the occurence of the shear modes is independent of the length of the computational domain.

Moreover, if we normalize the maximal velocity of the least damped shear mode of every considered Reynolds number to 1, and we plot $u(y)$ in dimensionless

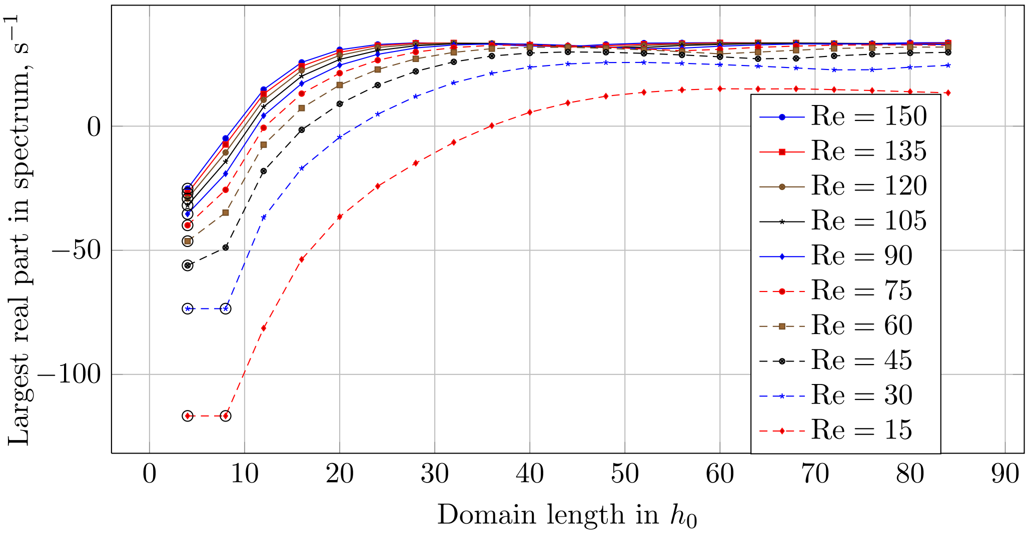

Figure 4.7.: Largest real part in the spectrum in dependence on Re and $\hat{x}$. Purely real eigenvalues are marked by a black circle, corresponding to shear modes. Marks without a surrounding circle are real parts of complex eigenvalues, corresponding to surface modes.

coordinates, the shear modes are independent of the Reynolds number, see Figure 4.8 for that. We see that $\varphi_{Shear,1}$ and $\varphi_{Shear,3}$ are modes that are mainly associated with one phase: $\varphi_{Shear,1}$ with the liquid phase, and $\varphi_{Shear,3}$ with the gas phase. Shear modes $\varphi_{Shear,2}$ and $\varphi_{Shear,4}$, on the other hand, are true two-phase modes.

The eigenvalues of shear modes increase with Re, see Figure 4.9. For the Reynolds numbers considered, the eigenvalues are always negative, and only for very small domain lengths does it happen that a shear mode is the overall least damped eigenmode. In Floryan et al. (1987), however, flow stability on planes with a small angle of inclination was studied, and it was found that in this case, shear modes can dominate stability. The independence of the shear modes on $\hat{x}$ leads to the phenomenon that for very small $\hat{x}$, the asymptotic stability behaviour does not change with increasing domain length, see the curves for Re = 15 and Re = 30 in Figure 4.7.

4.6.2. Surface Modes

Besides shear modes, we find modes that show a significant sinusoidal perturbation of the interface together with a vortex-like perturbation of the velocity fields. Modes of this type have an eigenvalue with a non-zero imaginary part. They are also called Yih modes after Yih (1963). In Figure 4.7, the real parts of their eigenvalues are not marked by a circle.

The growth rate of surface modes is strongly dependent on the wavelength, and

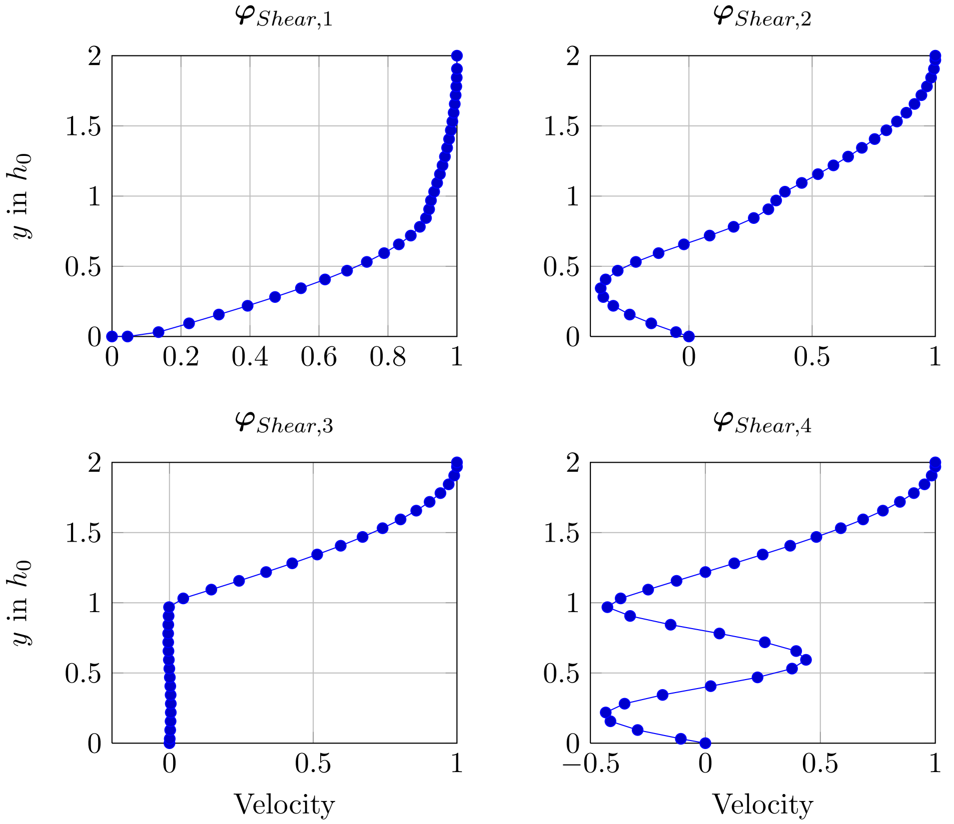

Figure 4.8.: $u(y)$ of the four least damped shear modes.

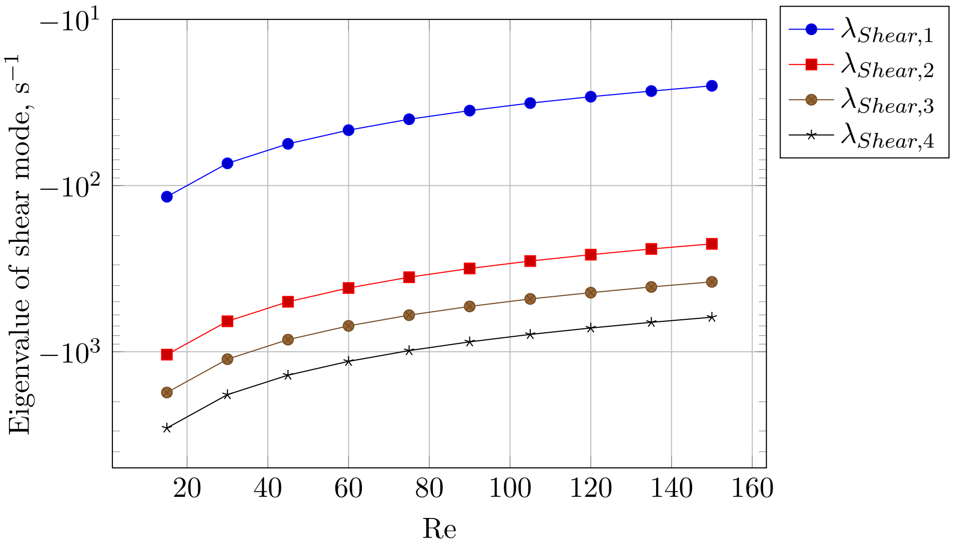

Figure 4.9.: Eigenvalues of the four least damped shear modes.

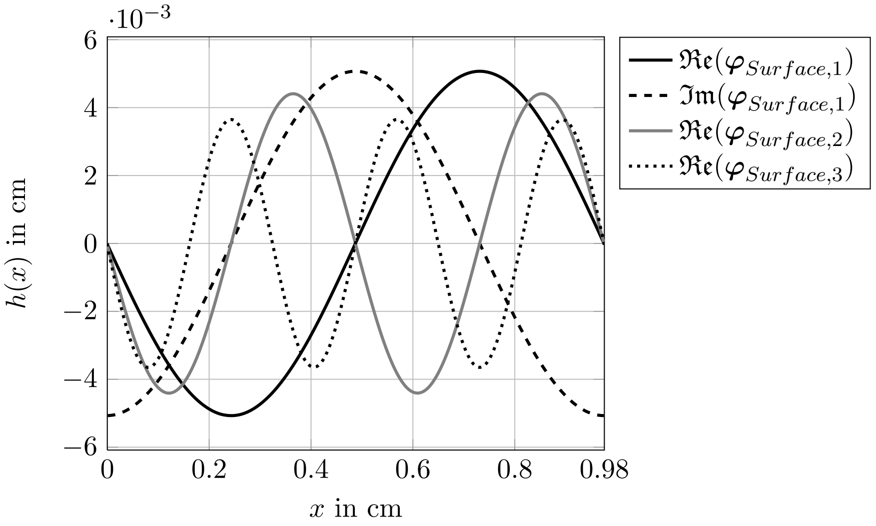

Figure 4.10.: Interfacial perturbation of the three unstable modes at Re = 90. Domain length = $37h_0$.

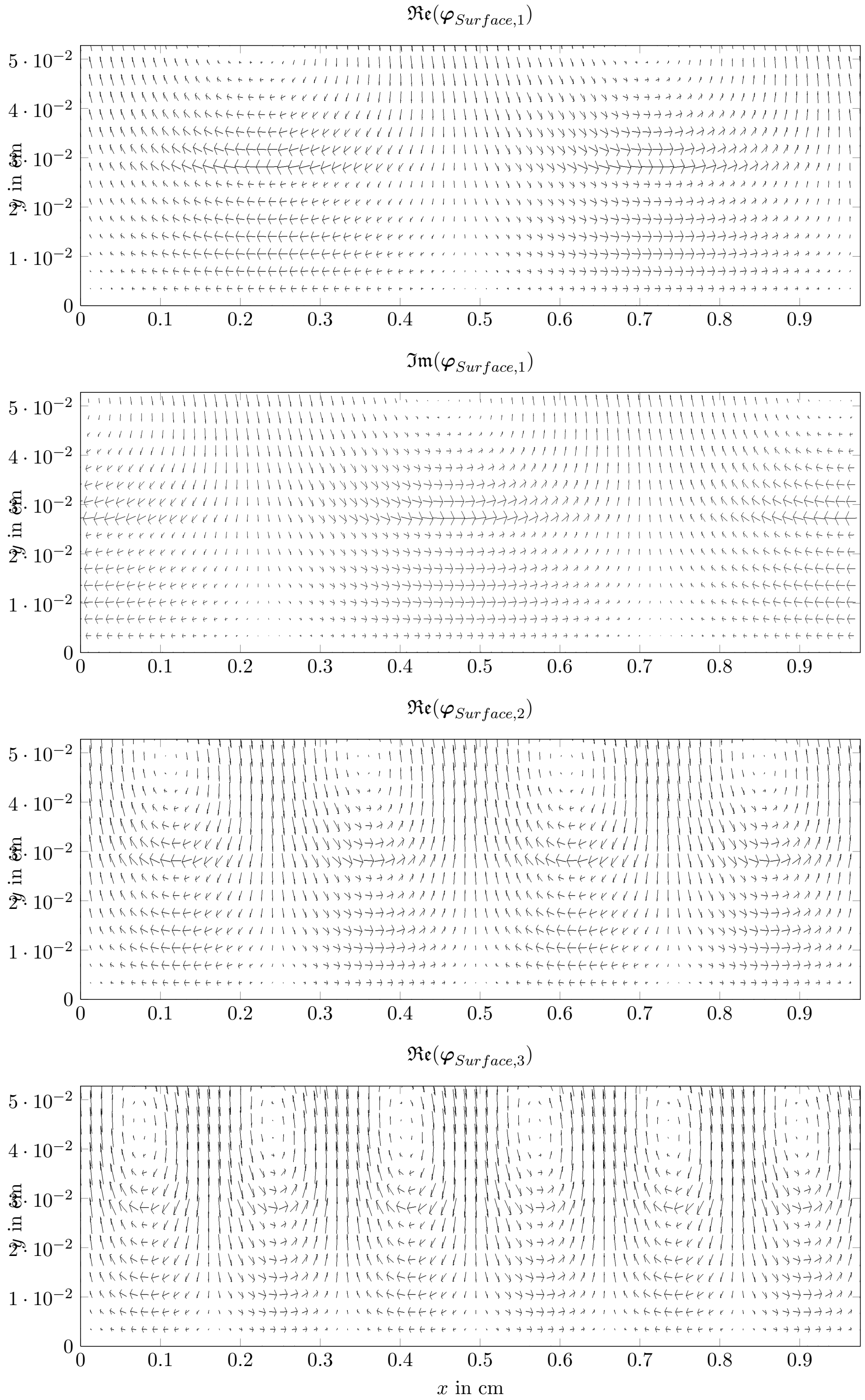

Figure 4.11.: Arrow plot of the velocity perturbation of the three unstable modes at Re = 90. Domain length = $37h_0$.

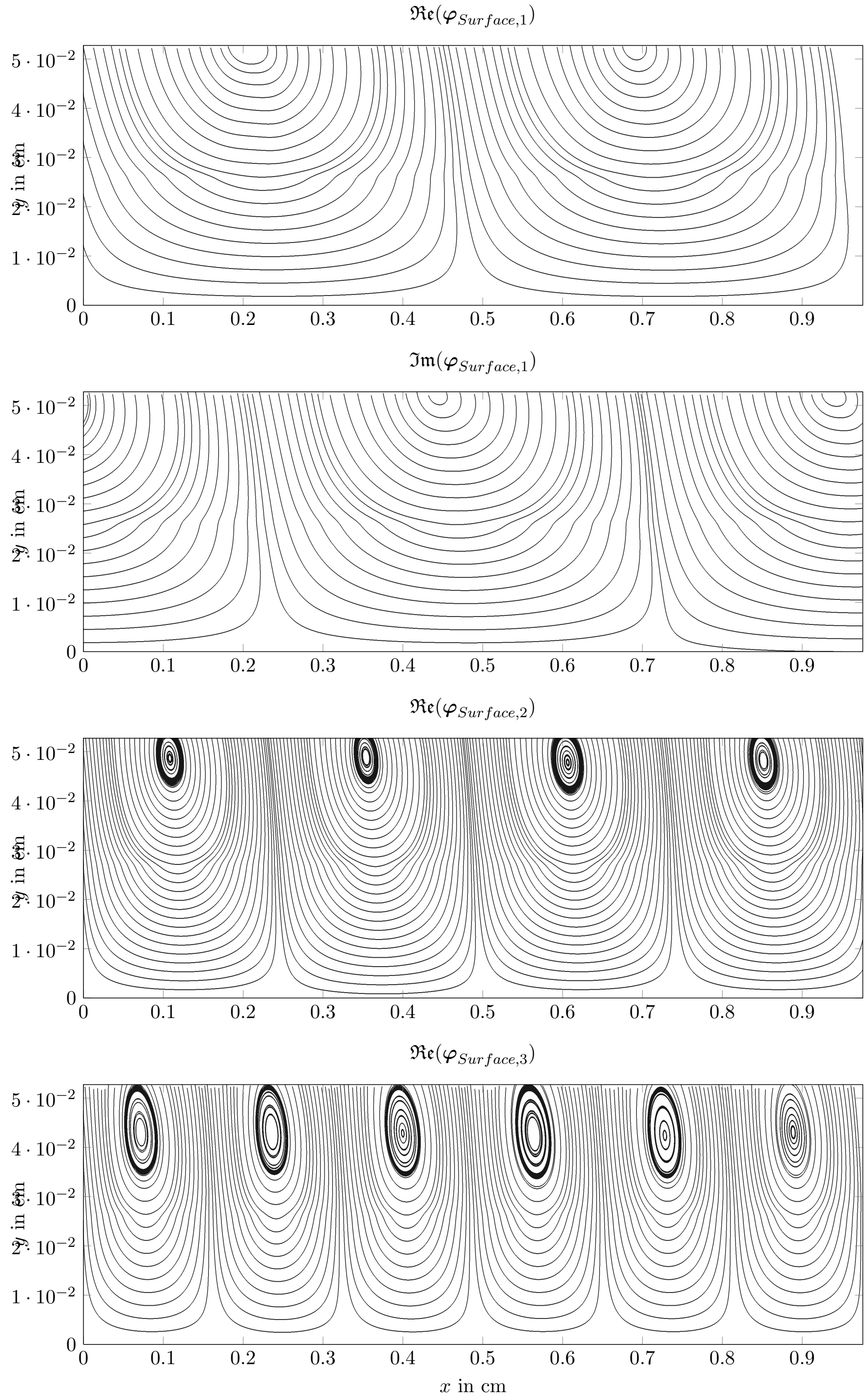

Figure 4.12.: Streamlines of the velocity perturbation of the three unstable modes at Re = 90. Domain length = $37h_0$.

in our simulations, the maximal possible wavelength is constrained by the domain length $\hat{x}$. Starting with short domain lengths, the growth rate of the most amplified surface mode becomes larger with an increase in $\hat{x}$, until it reaches a first local maximum. If we increase $\hat{x}$ further, the growth rates decline somewhat, until a first local minimum is reached. Up to this point, the most amplified surface mode has the maximum possible wavelength. Beyond this point, however, stability is dominated by waves of smaller wavelength. These modes are simply multiples of modes that can be found in shorter domains. For example, the domain at the second local maximum is twice as long as the domain of the first local maximum. The wavelength of the respective most amplified mode, however, is the same.

If more than one unstable surface mode occurs, they have a multiple of the wavenumber of the most unstable mode. Across the considered Reynolds numbers, the eigenmodes were very similar. As an example, we show the real and imaginary part of the most unstable mode at $\mathrm{Re} = 90$, and the real parts of the second and third most amplified mode at the same domain length, see Figures 4.10, 4.11, and 4.12 for modes normalized to an energy of $1 \times 10^{-5}\,\mathrm{J\,m^{-1}}$.

We see that the imaginary part of a surface mode is the same as the real part, with a phase shift of $-\pi/2$. This phaseshift determines the direction in which the wave propagates: Let $\boldsymbol{a} = \mathfrak{Re}\boldsymbol{\varphi}_{Surface,1}$, $\boldsymbol{b} = \mathfrak{Im}\boldsymbol{\varphi}_{Surface,1}$, $\lambda_{Surface,1} = \alpha + i\beta$, and assume that at time $t = 0$ the flat film is perturbed by $\boldsymbol{a}$. The time evolution of the perturbation is then governed by equation (4.6). The perturbation is always given as a linear combination of the real and imaginary parts of the eigenmode. At time $t = \frac{\pi}{2\beta}$, the perturbation is given by $-\exp(\frac{\alpha\pi}{2\beta})\boldsymbol{b}$. Looking at Figure 4.10 with these consideration in mind, we see that the wave hump is traveling in downstream direction. Waves traveling upstream would correspond to a phaseshift of $+\pi/2$. In all calculations presented in this work, only waves traveling downstream are found. It is expected that waves traveling in upstream direction are heavily damped, and that the presented algorithm cannot find them.

4.7. Results with Inlet/Outlet

4.7.1. Real Modes

Also in the inflow/outflow case, there are real modes present. Their character, however, is completely different from those in the periodic setting. They feature a strong interfacial perturbation, combined with a complicated perturbation of the velocity field. As an example, we show the least damped real eigenmode of the film at $\mathrm{Re} = 90, \hat{x} = 32h_0$, which has an eigenvalue of $-115.19\,\mathrm{s^{-1}}$, see Figures 4.13 and 4.14. As is evident, the v-components of the velocity are not 0, and the velocity depends on x. Therefore, it is not appropriate to speak of a shear mode. We could not find modes resembling the shear modes of the periodic case in our computations. This may be due to the fact that a homogeneous Dirichlet boundary condition for the perturbation applies at the inlet.

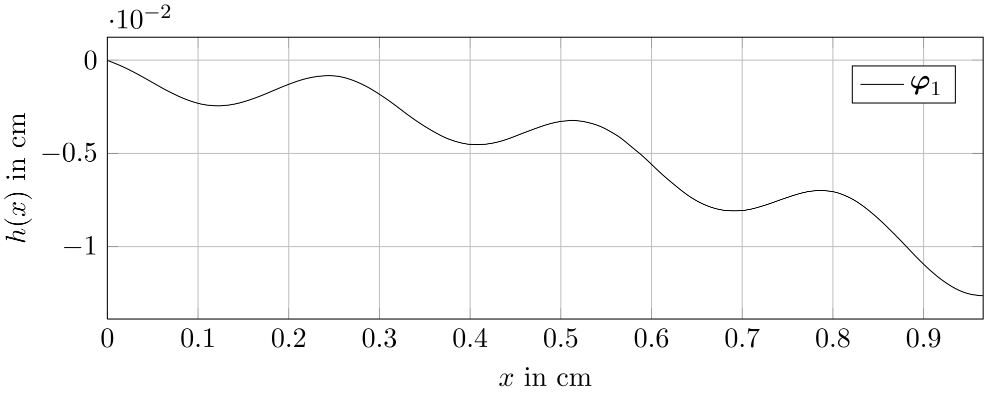

Figure 4.13.: Interfacial perturbation of the least damped real eigenmode, Re = 90, $\hat{x} = 32h_0$, Nusselt profile at the inlet.

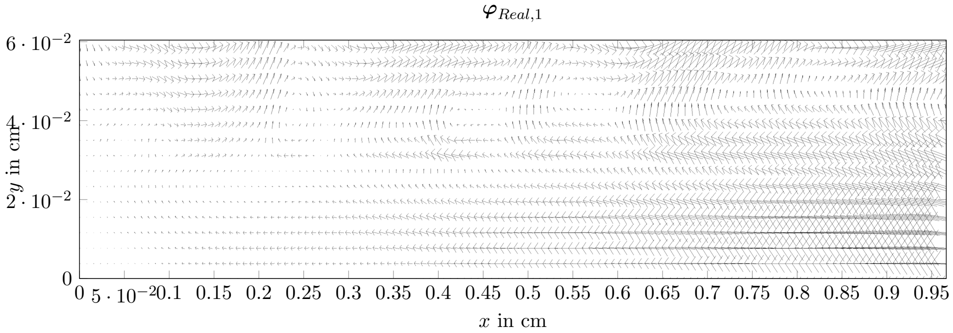

Figure 4.14.: Velocity perturbation of the least damped real eigenmode, Re = 90, $\hat{x} = 32h_0$, Nusselt profile at the inlet.

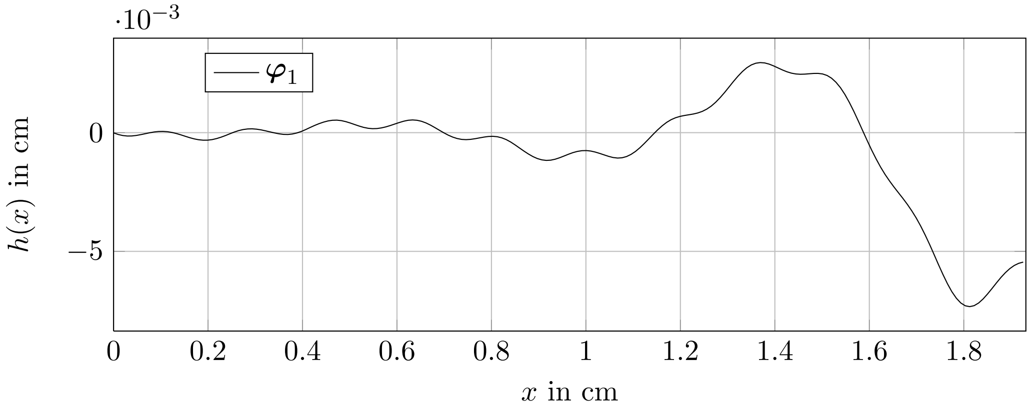

Figure 4.15.: Interfacial perturbation of the least damped complex eigenmode, $\mathrm{Re} = 135$, $\hat{x} = 64h_0$, Nusselt profile at the inlet.

4.7.2. Influence of domain length

Similar to the periodic case, on sufficiently long domains, stability is dominated by complex, wave-like eigenmodes.

On short domains, the influence of the inlet is so strong that wave-like perturbations cannot develop properly. The modes found on such domains look like a complicated superposition of perturbations of different wavelength, see Figure 4.15 for the interfacial perturbation of the least damped mode at $\mathrm{Re} = 135$, $\hat{x} = 64h_0$, which has an eigenvalue of $-106.23 + 142.95i$.

On longer domains, the least damped complex modes are waves, traveling towards the outlet, see Figure 4.16. Their amplitude grows exponentially in x, and at the same time, they grow or decay exponentially in time. The accompanying velocity perturbation is again vortex-like, and its amplitude increases towards the outlet.

Verification

It was verified that the found real modes, and modes on short domains, are truly eigenmodes of the discretized system.

When our algorithm computes an eigenmode $\boldsymbol{\varphi}$ to an eigenvalue λ, there are two ways to compute the time evolution of that perturbation. On one hand, we can initialize the solver with $\boldsymbol{x}_0 + \epsilon\mathfrak{Re}\boldsymbol{\varphi}$, start the simulation, and compute the difference to the steady state after time T. We call the outcome of this $\boldsymbol{B\varphi}_{\mathrm{num}}$. On the other hand, $\boldsymbol{\varphi}$ is supposed to be an eigenmode. Therefore, the time evolution of perturbation $\epsilon\mathfrak{Re}\boldsymbol{\varphi}$ should obey Equation (4.6). We evaluate Equation (4.6) at time T, and call the result $\boldsymbol{B\varphi}_{\mathrm{stab}}$. We define the relative error between both results by

$$d_r = 2\frac{\|\boldsymbol{B\varphi}_{num} - \boldsymbol{B\varphi}_{stab}\|}{\|\boldsymbol{B\varphi}_{num}\| + \|\boldsymbol{B\varphi}_{stab}\|}. \tag{4.43}$$

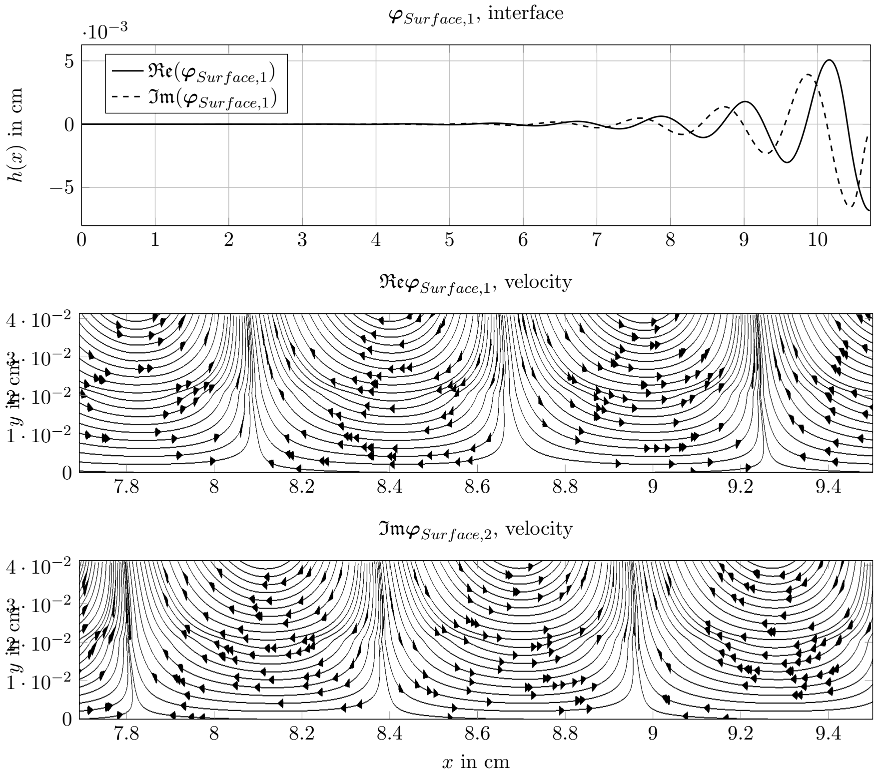

$\varphi_{Surface,1}$, interface

$\mathfrak{Re}\varphi_{Surface,1}$, velocity

$\mathfrak{Im}\varphi_{Surface,2}$, velocity

Figure 4.16.: Eigenmode with the highest spatial growth rate, $\mathrm{Re} = 45, \hat{x} = 512h_0$, Nusselt profile at the inlet.

$\hat{x}$ in h_0	16	32	48	64	128	192	256
d_r	0.027	0.039	0.029	0.031	0.023	0.017	0.032

Table 4.2.: Relative error according to equation (4.43) between the numerical evolution of the most amplified eigenmodes, and the evolution according to equation (4.6). Inflow/outflow-case, Re = 135.

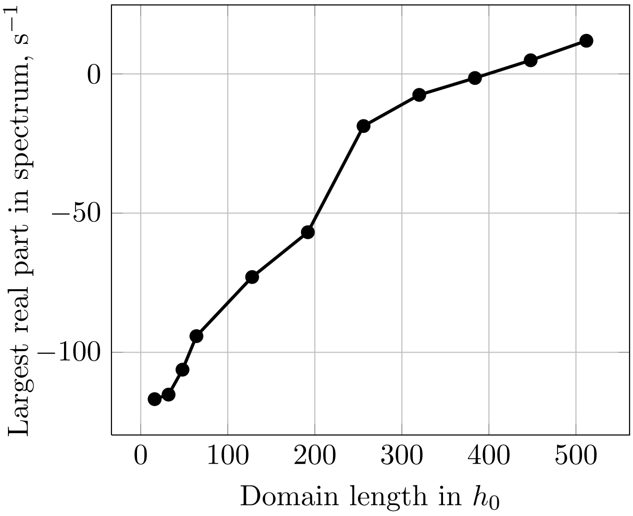

Figure 4.17.: Largest real part in the spectrum in dependence on $\hat{x}$. Nusselt profile at the inlet, Re = 135.

If d_r is small, we say that $\boldsymbol{\varphi}$ actually is an eigenmode to the eigenvalue λ, and that the algorithm worked correctly.

We checked the most amplified modes delivered by our algorithm at Re = 135 for the domain lengths $\hat{x}$ from $16h_0$ to $256h_0$. We set $T = -1/\mathfrak{Re}(\lambda_1)$ for the respective eigenvalue. See Table 4.2 for the results. Compare, however, Section 4.7.4.

Convergence with domain length

In Figure 4.17, the largest real part of the spectrum under a variation of domain length is plotted for films at Re = 135, Nusselt profile at the inlet. It is seen that the temporal growth rate does not converge to a finite value within the considered range of $\hat{x}$. Moreover, we see that modes with a positive real part can occur.

In the inflow/outflow case, the spectrum is continuous, and modes with continuously varying wavelength can exist. In Figure 4.16, a typical mode in the inflow/outflow setting is shown. Besides its eigenvalue, it possesses a clearly defined, homogeneous wavelength. The amplitude grows exponentially: Let x_p be the downstream position of an arbitrary wave peak. Then, the next peak downstream can be found at position $x_p + l$, and the quotient of the respective interface heights, $p := h(x_p + l)/h(x_p)$ is constant throughout the mode. Accordingly, the amplitude of the interfacial amplitude grows like $\exp(\beta x)$, where $\beta = \log(p)/l$. The velocity perturbation is again vortex like, and increases in x with the same growth rate.

The wavelength, as well as the phase velocity

$$c = \frac{\mathfrak{Im}\lambda}{2\pi} l \tag{4.44}$$

are quantities that are easily accessible to measurements. The spatial growth rate β defined above, however, is not directly measurable. Instead, in experiments, a spatial growth rate is determined by measuring the height of wave humps at different downstream positions, and a film is considered unstable if perturbations with a positive spatial growth rate exist, cf. Alekseenko et al. (1985); Liu and Gollub (1994). In order to compare our data to results from experiments or spatial theories, two effects have to be taken into account: On one hand the spatial growth rate β. On the other hand, since it is not possible in the presented algorithm to set $\mathfrak{Re}\lambda$ to 0, a perturbation experiences an additional growth or decay due its temporal growth rate, determined by the real part of its eigenvalue. A wave that travels a downstream distance Δx needs a time $\frac{\Delta x}{c}$ to do so, experiencing a combined growth by a factor of

$$\exp(\beta \Delta x) \exp(\mathfrak{Re}\lambda \frac{\Delta x}{c}) = \exp\left((\beta + \frac{\mathfrak{Re}\lambda}{c})\Delta x\right). \tag{4.45}$$

Accordingly, we define the spatial growth rate $\alpha = \beta + \frac{\mathfrak{Re}\lambda}{c}$. We expect to see the mode with the highest α in the experiment, and refer to it as the most amplified mode.

In order to check if the three physical quantities wavelength, phase velocity and spatial growth rate converge with the domain length, we show these quantities for the calculations made for Figure 4.17 for $\hat{x} \geq 256$, see Table 4.3. For shorter domain length, a wavelength is not clearly identifiable. It is concluded that a convergence takes place, and that a domain length of $512 h_0$ is sufficient.

4.7.3. Comparison to experiments

We expect that the mode with the largest α is the one most likely seen in the experiment. In order to show that the algorithm delivers physically reasonable results in the inflow/outflow setting, we compare results achieved with the homogeneous inlet condition to Alekseenko et al. (1985), where a number of experimental and theoretical results are shown. We compare phase velocity, nondimensionalized by the mean velocity of the developed flow (Figure 4.18), a dimensionless spatial growth rate $\tilde{\alpha} = h_0 \alpha$ (Figure 4.19), and dimensionless wave number (Figure 4.20). In every Figure, the results for the mode with the highest spatial growth rate is plotted.

$\hat{x}$ in h_0	l in cm	c in $\mathrm{cm\,s^{-1}}$	α in $\mathrm{cm^{-1}}$
256	1.41	53.3	0.651
320	1.14	53.0	0.640
384	1.17	52.9	0.638
448	1.19	52.7	0.636
512	1.19	52.6	0.632

Table 4.3.: Wavelength, phase velocity and spatial growth rate of the most amplified mode on a film at Re = 135, Nusselt profile at the inlet, in dependence on domain length.

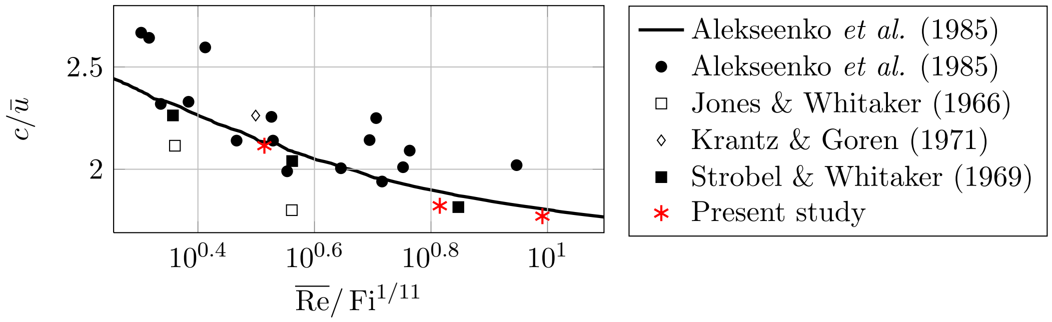

Figure 4.18.: Comparison of phase velocity to data from Alekseenko et al. (1985). Experimental results are marked by symbols, theoretical results by lines.

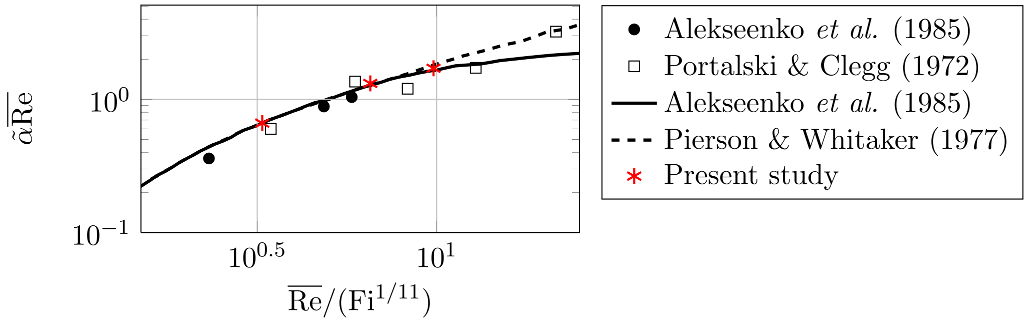

Figure 4.19.: Comparison of spatial growth rate to data from Alekseenko et al. (1985). Experimental results are marked by symbols, theoretical results by lines.

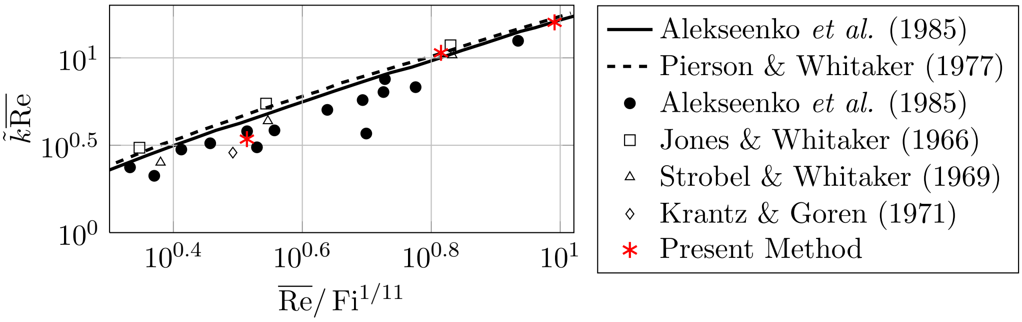

Figure 4.20.: Comparison of wave number to data from Alekseenko et al. (1985). Experimental results are marked by symbols, theoretical results by lines.

4.7.4. The convective character of the instability

In hydrodynamical stability theory, a distinction is made between *absolutely* and *convectively* unstable flows. If a localized perturbation spreads and grows in upstream and downstream direction, and is able to eventually pollute the whole flow field, the instability is considered absolute. If, on the other hand, a perturbation is predominantly transported away from its source, it is called convective. A perturbation of a convectively unstable flow can only grow in a reference frame that is moved with the velocity of the perturbation. For a detailed introduction, see Huerre and Monkewitz (1990); Huerre (2000). The primary instability of a falling film is convective, as was convincingly shown experimentally in Liu et al. (1993), and on more theoretical grounds in Brevdo et al. (1999). The presented method can only partially capture this convective behaviour.

In Figure 4.21, the time evolution of the most amplified mode at $\mathrm{Re} = 135$, homogeneous inlet, is computed with both methods described in section 4.7.2. Until a time of about $100 \times 10^{-3}\,\mathrm{s}$, the evolution by DNS is in good agreement with the theoretical one. As predicted by the positive real part of the mode, the perturbation seems to grow over the whole length of the computational domain, with a growth rate that is correctly predicted by the eigenvalue. Note that $100 \times 10^{-3}\,\mathrm{s}$ is about a hundred times larger than the characteristic convective time of the film, which is also the time T used in the computations. After about $150 \times 10^{-3}\,\mathrm{s}$, the curves start to diverge, and it becomes evident that the perturbation is eventually advected out of the computational domain.

4.7.5. Influence of the outlet boundary condition

Since the outlet boundary is artificial, we investigate the influence of this boundary condition on the stability results. In a numerical simulation, the computational domain has to be truncated at some point, creating an artificial outlet boundary.

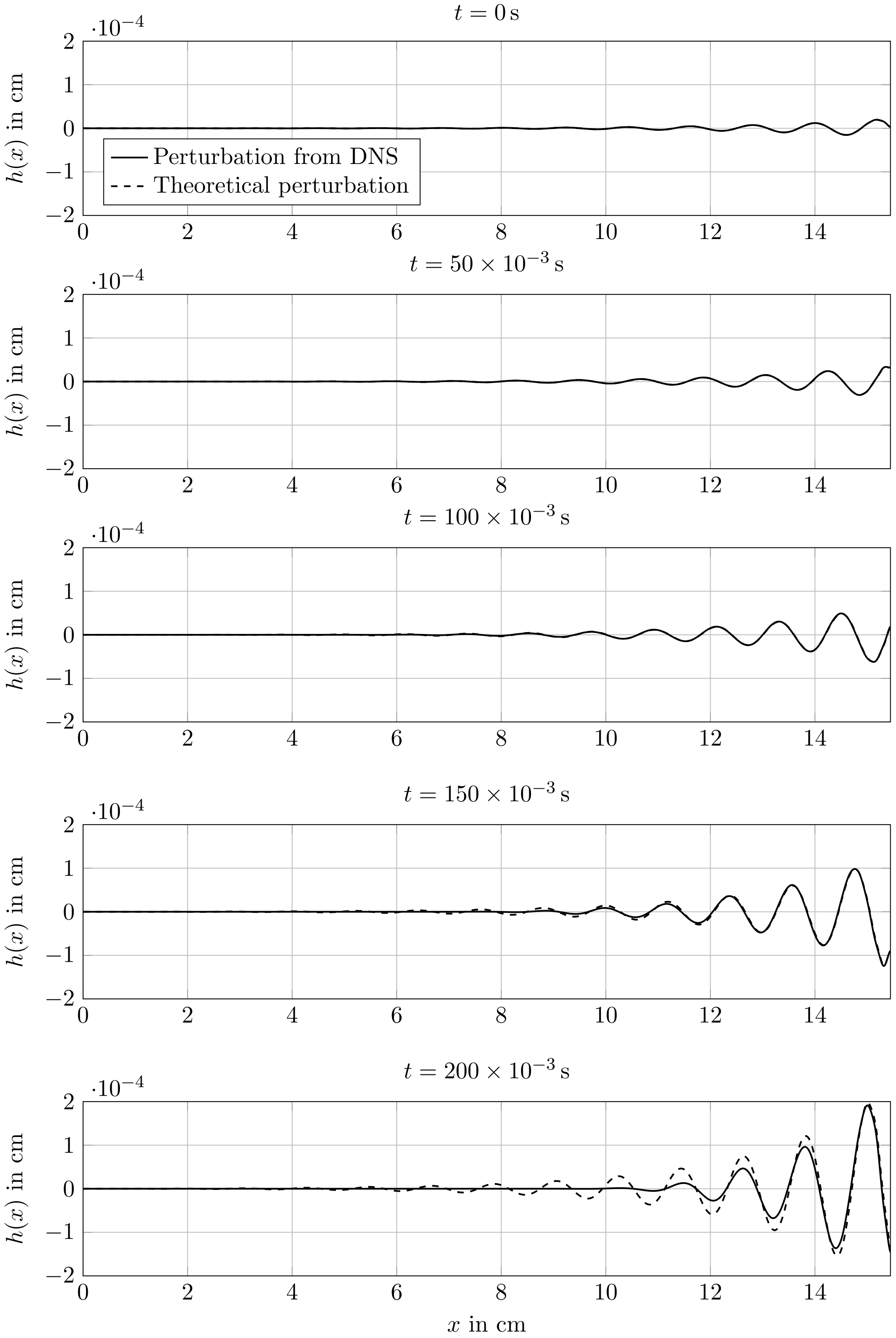

Figure 4.21.: Comparison between the theoretical and computational time evolution of the most amplified mode at Re = 135, Nusselt profile at the inlet.

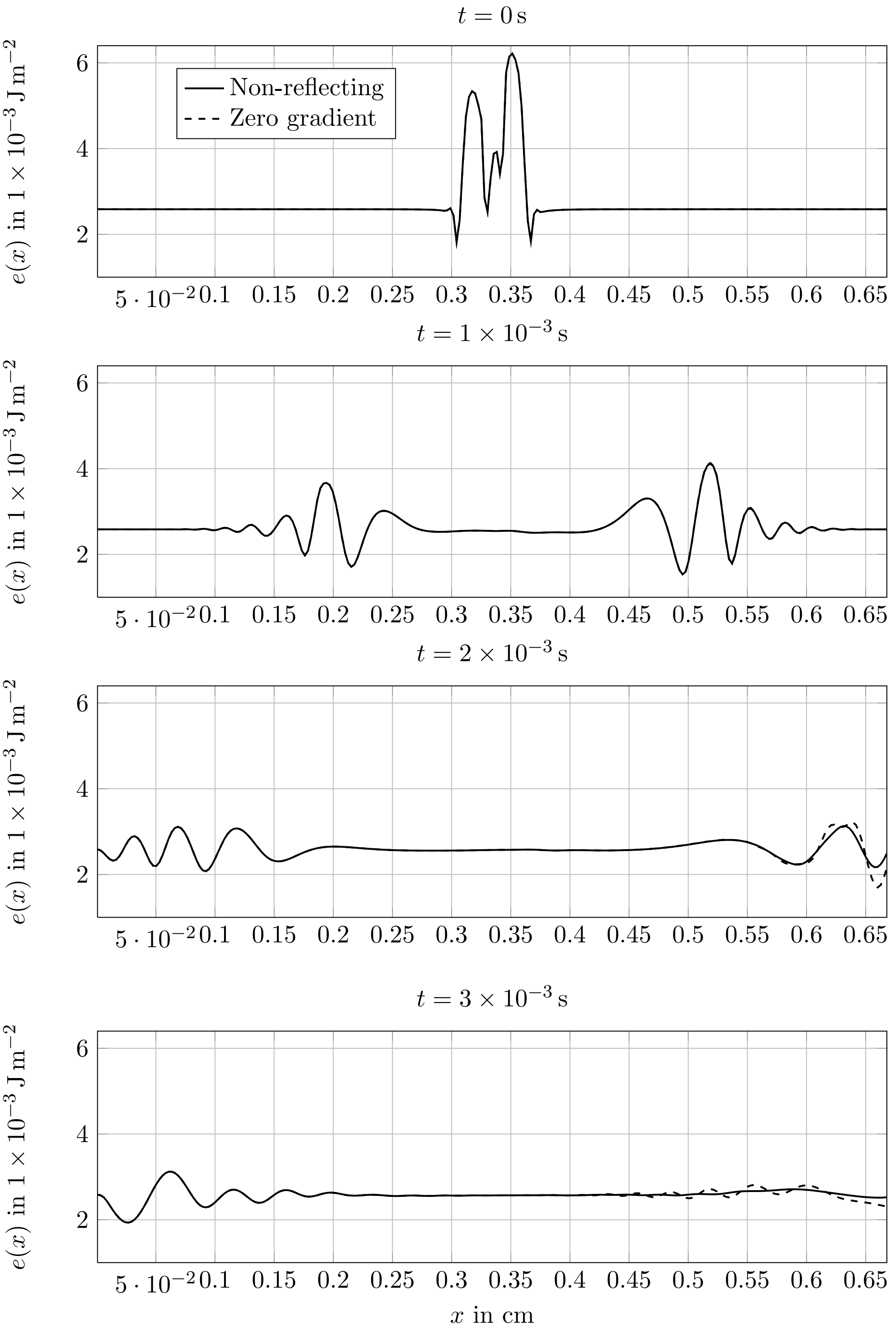
$t = 0\,\mathrm{s}$

$t = 1 \times 10^{-3}\,\mathrm{s}$

$t = 2 \times 10^{-3}\,\mathrm{s}$

$t = 3 \times 10^{-3}\,\mathrm{s}$

Figure 4.22.: Response of different outflow boundary conditions to an impulse.

The most common outlet condition for simulations of falling films is the zero gradient condition (3.37). In a variety of publications (Gao et al. (2003); Dietze et al. (2008); Albert et al. (2012)), it was shown that this condition yields very good agreement with experimental results for simulations of large, nonlinear waves. The same condition is also routinely employed in global stability analyses of other flows, like the flow over a backward facing step (Barkley et al. (2002); Lanzerstorfer and Kuhlmann (2012)).

This boundary condition, however, has the disadvantage that a developed flow is assumed, and that perturbations cannot freely leave the computational domain. Instead, a part of the perturbation is reflected back into the domain and travels in upstream direction, possibly disturbing the results of the presented stability analysis.

In Figure 4.22, this behaviour is demonstrated. The steady state of a water/air film, $\mathrm{Re} = 135$ with the developed flow inlet condition is computed on a domain of length $32h_0$. At $t = 0\,\mathrm{s}$, a sinusoidal perturbation of wavelength $2h_0$ and amplitude $h_0/8$ is superimposed onto the film thickness in the center of the domain. The local energy of the film, defined by

$$e(x) = \frac{1}{2}\int_0^{\hat{y}} \rho \left|\boldsymbol{u}(x,y)\right|^2 \mathrm{d}y + \frac{1}{2}\sigma\partial_x h(x), \tag{4.46}$$

is shown. On the unperturbed film, this quantity is constant. Note that the local energy in the case of the zero gradient condition is marked by a dashed line.

In the second panel of Figure 4.22, the perturbation is seen traveling away from its source in both directions. At $t = 2 \times 10^{-3}\,\mathrm{s}$, it hits the boundary, and undergoes some unphysical deformations at the outlet boundary. Reflection occurs, and the ripples near the outlet, seen at $t = 3 \times 10^{-3}\,\mathrm{s}$ travel in upstream direction, whereas those near the inlet travel downstream.

A variety of non-reflecting or absorbing boundary conditions for different purposes have been proposed. The theory is well developed for hyperbolic problems. In Engquist and Majda (1977), a completely absorbing boundary condition for the wave equation, which is nonlocal in space and time, and therefore unsuitable for numerical calculations, is derived. An implementable version is given by a Padé-approximation to the completely absorbing condition, which is local and still highly absorbing.

This approach was employed by Jin and Braza (1993) to derive the following absorbing boundary condition for Navier-Stokes:

$$u_t + uu_x - \nu u_{yy} = 0, \tag{4.47}$$

$$v_t + uv_x - \nu v_{yy} = 0. \tag{4.48}$$

This condition retains the nonlinear character of the convection term. We implement the following version of this:

$$u_t + u_N u_x - \nu\partial_{yy}(u - u_N) = 0, \tag{4.49}$$

$$v_t + u_N v_x - \nu v_{yy} = 0. \tag{4.50}$$

This linear version is more suitable for a linear stability analysis, and accounts for the presence of the wall. In order to enable an unperturbed outflow of interfacial perturbations, the condition

$$h_t + (2u_N|_{y=h_0})h = 0. \tag{4.51}$$

is implemented. This is similar to the Sommerfeld radiation condition in Orlanski (1976). The optimal factor in front of h would be the phase velocity of surface waves. We approximate this by twice the free surface velocity.

Like in Clément (1996), the dynamic boundary condition stated above is coupled with a damping zone that exponentially damps perturbations to the steady state in the vicinity of the outlet, cf. Rieber et al. (2000). The combination of both approaches yields good absorption behavior, as can be seen in the solid line plots of Figure 4.22. Perturbations are not significantly distorted when they hit the outlet, as can be observed at $t = 2 \times 10^{-3}\,\mathrm{s}$, and no share of the perturbation is reflected back into the domain, see $t = 3 \times 10^{-3}\,\mathrm{s}$.

We analyzed a film with a Nusselt profile at the inlet at $\mathrm{Re} = 135$, $\hat{x} = 512$. The length of the damping zone was set to 1 cm, which is approximately the wavelength of the amplified modes. No qualitative influence of the outlet boundary condition was found. Eigenvalues with a positive real part still occur. The physical parameters of the most amplified mode are $l = 1.15\,\mathrm{cm}, c = 52.7\,\mathrm{cm}$, and $\alpha = 0.638\,\mathrm{cm}^{-1}$; cf. Table 4.3.

It should be noted that another type of boundary conditions has recently been employed in the global analysis of the transient growth behaviour of perturbations (Blackburn et al. (2008); Sharma et al. (2011)). Here, the steady state is computed with a zero gradient condition at the outlet, and a homogeneous Dirichlet condition is employed for the perturbation at the inlet and outlet boundary. Calculations with this set of boundary conditions failed to accurately depict the physical situation on falling films. They consistently delivered a least damped mode with a real eigenvalue, which can only be interpreted as a standing wave, decaying in time.

4.7.6. Influence of the inlet condition

The presented method was applied to analyze the stability of falling films with different inlet conditions. If a velocity profile different from the developed flow is prescribed at the inlet, the flow experiences a spatial development. According to Pierson and Whitaker (1977), the area near the inlet, in which the flow field differs from the Nusselt profile, is expected to have a length of about

$$L_e = (\frac{2\eta_L^2}{\rho_L^2 g})^{1/3}\,\mathrm{Re}^{4/3}\,. \tag{4.52}$$

We expect the effect of the non-homogeneity to become stronger with a higher Reynolds number, which is why we restrict the investigation to films at $\mathrm{Re} = 135$. Films with a plug flow at the inlet (3.34), and with a two-dimensional pipe flow at

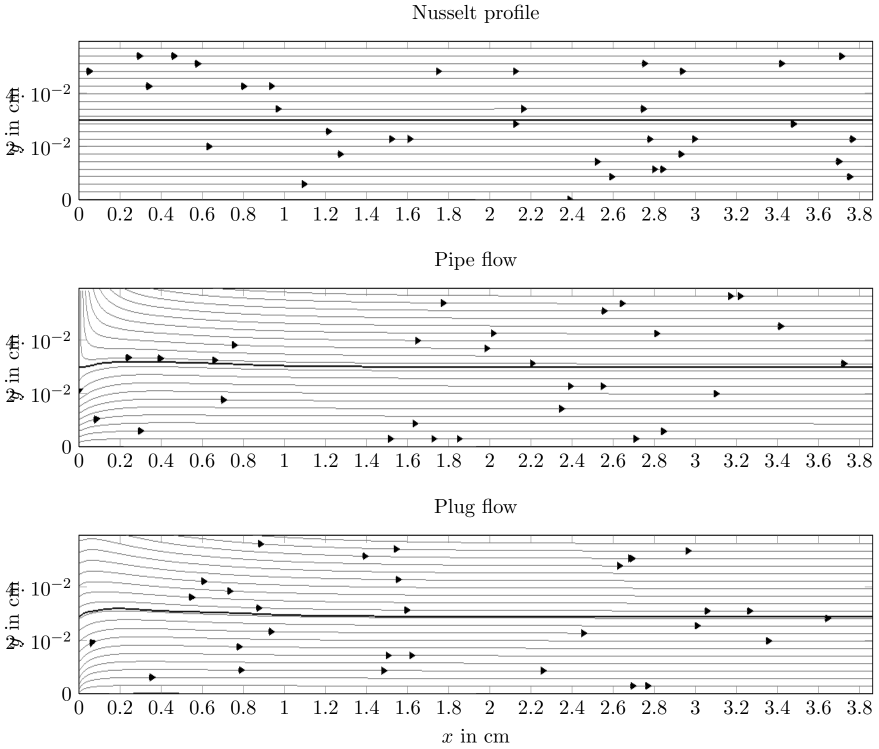

Figure 4.23.: Developing flow fields at the inlet with different velocity profiles at the inlet. Re = 135, inlet height h_0. Thick line marks interface height.

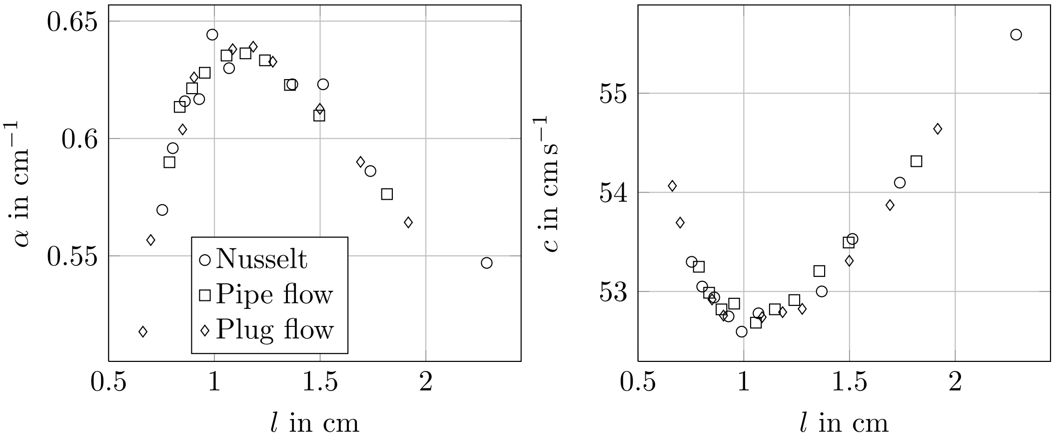

Figure 4.24.: Spatial growth rate α and phase velocity c in dependence of wavelength l of the ten most amplified modes of a film at Re = 135 with different inlet conditions, inlet height=h_0.

the inlet (3.33) were considered, and the results were compared to those achieved with a Nusselt inlet condition (3.31). In Figure 4.23, the developing flow fields near the inlet for the different conditions are shown. In these cases, water entered the domain over a height of h_0.

In Figure 4.24, spatial growth rate and phase velocity of the ten most amplified modes for the different inlet conditions are shown in dependence the wave length. No significant influence of the inlet condition on the results is apparent.

In order to provoke a stronger inlet effect, the height over which water enters the domain was varied. In addition to the computation above, films were considered in which water enters the computational domain from pipes of height $\frac{1}{2}h_0$ and $\frac{3}{2}h_0$, see Figure 4.25 for the flow fields. Spatial growth rates and phase velocites are shown in Figure 4.26. There is still no noticeable effect on the spatial growth rates. Phase velocities in the case of a small inlet, however, are a little faster than in the other cases. This might be explained by the fact that, in order to maintain a constant flow rate, higher velocities must be prescribed in the case of a small inlet height.

4.8. Conclusion

Based on the well-validated numerical method of Chapter 3, a new numerical algorithm for the global linear stability analysis of free surface flows was presented. The algorithm is based on an application of Arnoldi's method to the evolution operator. To do so, linear algebra must be performed on the set of all admissible perturbations, which is difficult due to the free boundary. It was shown how this problem can be overcome by a suitable transformation to a time-independent

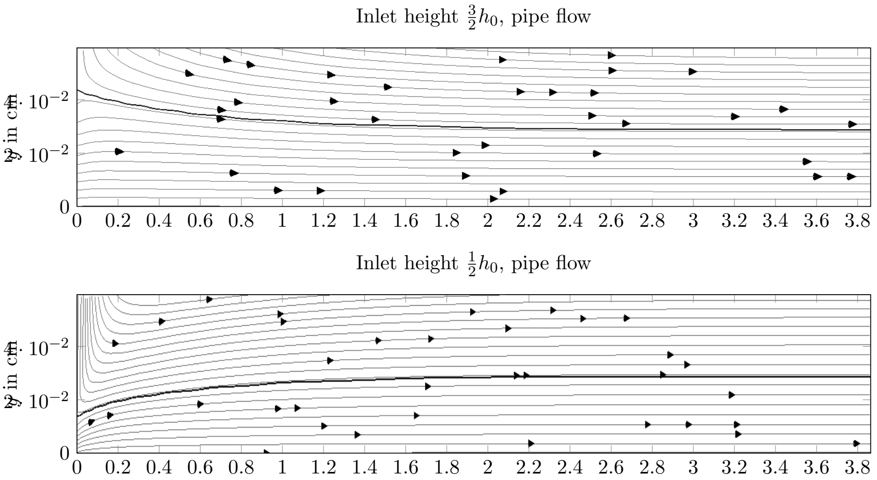

Figure 4.25.: Developing flow fields at the inlet with a parabolic velocity profile at the inlet, but different inlet heights, Re = 135. The flow rate at the inlet is kept constant. Thick line marks interface height.

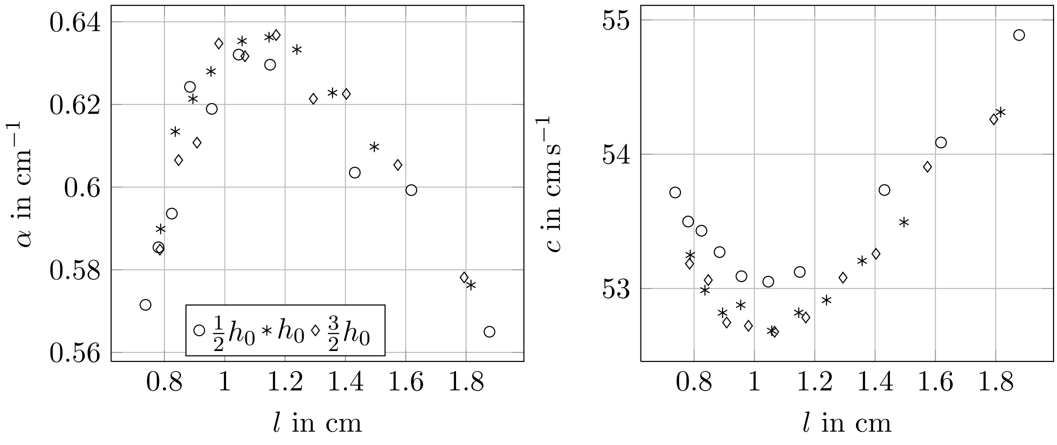

Figure 4.26.: Spatial growth rate α and phase velocity c in dependence of wavelength l of the ten most amplified modes of a film at Re = 135 with pipe flow at the inlet and different inlet heights.

reference domain.

The method was thoroughly validated by comparison to results achieved with the temporal formulation of the Orr-Sommerfeld equation, corresponding to flow that is periodic in space. The flow field of shear modes and surface modes was described.

Results of stability analyses on films with inlet and outlet were compared to the spatial formulation of Orr-Sommerfeld and to experiments. Convincing agreement was found. The influence of the domain length was studied, and a physically sound interpretation of the modes was given. The results of the algorithm were viewed under consideration of the fact that a falling film is only convectively unstable in the inlet/outlet-setting. Finally, a non-homogeneity was introduced at the inlet, leading to a spatially developing flow field. A weak inhomogeneity as introduced by a change in the velocity field at the inlet is not found to have a marked impact on the results. A stronger non-parallelity of the flow was enforced by a variation of the inlet height. It was found that the high velocities introduced by a small inlet result in higher phase velocities.

5. Vortices and species transfer

5.1. Introduction

In Chapters 2 and 4, conditions were found under which perturbations to the flat film grow while they are transported downstream. As we have seen, the onset of waves is a linear process, which means that initially, perturbations grow exponentially. Naturally, this growth rate can not be kept up indefinitely. Instead, for sufficiently large perturbations, nonlinear effects start to play a role, which inhibit further growth of perturbations. The amplitude of surface waves saturates, and nonlinear waves become visible that travel for a considerable distance in downstream direction without changing their form, see Figure 1.2, region II.

Falling films are used in a variety of industrial applications where large rates of heat or mass transfer are desired. Examples are cooling devices (Kulankara and Herold, 2000), gas absorbers (Yih and Kuo, 1988; Dam et al., 1999), desalination units (Zhang et al., 2003; Raach and Mitrovic, 2007) and falling film microreactors (Jähnisch et al., 2000; Yeong et al., 2003). In these devices, surface waves are known to play a central role for the enhancement of heat and mass transfer rates. Experiments show that the presence of surface waves has an intensifying effect on the observed heat transfer rates from the wall into the film (Frisk and Davis, 1972). For the transport of a chemical species from the gas into the liquid, this effect is even larger (Alekseenko et al., 1996).

Since surface waves change the overall interface area only marginally, this increase in mass transfer rates must be explained by the fact that the flow in nonlinear waves shows large deviations from the wall parallel steady state solution. This flow structure, in turn, depends on the wavelength of the perturbation from which it develops. Using the numerical method of Bothe and Fleckenstein (2013), this chapter is devoted to the study of flow processes inside these waves. As a particular system, we will investigate the flow of a water film in a surrounding atmosphere of pure oxygen, and will examine the influence of vortices in the waves on local species transfer rates.

The first numerical simulations of mass transfer into falling films were performed by Wasden and Dukler (1990). They used experimentally measured film thicknesses to compute the local flow fields, and solved a stationary species transport equation for a single wave. Boundary conditions in streamwise direction for the species concentration were computed by a solution of the concentration profile for a flat film. More recent simulations have been performed in Sisoev et al. (2005) and Rastaturin et al. (2006), where the hydrodynamics was not modeled by the full Navier-Stokes equations, but by a simpler model derived by Shkadov (1967), where the velocity profile is considered semi-parabolic at each streamwise direction. If this model is able to correctly predict the onset of vortices in the liquid, however, remains unclear. In Bo et al. (2011) the hydrodynamics of the falling film was computed by Direct Numerical Simulation (DNS), while the species concentration was solved for stationary conditions, employing the method of Wasden and Dukler (1990). Here, the effect of the choice of artificial boundary conditions is unclear. Mass transfer simulations into falling films were also performed in Xu et al. (2008). The transient species transport equation was solved over the whole length of the film. Unfortunately, the range of investigated hydrodynamical parameters was quite small, and local mass transfer rates were only provided for a single simulation.

Direct numerical simulations of falling films are still very expensive, and engineers must rely on the solution of simpler model equations in order to appropriately dimension falling film apparatus. By direct numerical simulations, light is shed upon the influence of distinct flow regions on local species transfer characteristics. This is expected to furnish valuable input for the derivation of simpler, cheaply solvable model equations, that are still able to correctly predict the mass transfer characteristics of a falling film device.

In Section 5.2, the system of equations governing the transport of a chemical species from the gas into the liquid is presented. It is assumed that the species is dilute, and that the species concentration has no relevant feedback on the hydrodynamics. The employed numerical method, which is due to Bothe and Fleckenstein (2013), is briefly summarized. The material parameters used in this chapter are shown in Section 5.3. Validation data is presented in Section 5.4. Finally, the wave effect on species transfer rates is discussed in Section 5.5.

It is found that a local maximum of the transfer rates occurs in the wave troughs. At these points, where the film is especially thin, the combination of a large wall influence and a rapid increase of pressure in downstream direction can lead to localized backflow: water that flows against the direction of gravity in the reference frame of the wall. The occurrence of this phenomenon, however, is not found to have a qualitative effect on species transfer rates.

Depending on the size of the waves, a vortex can occur in the large wave humps in the reference frame of the moving wave. If this vortex is absent, the water is everywhere slower than the wave, and a local minimum in species transfer coincides with the wave peak. If this vortex is present, the parts of the liquid that are furthest away from the wall move faster than the wave, leading to the creation of two stagnation points at the interface, where the water moves with the wave velocity. One of these points is downstream from the wave peak, and the local minimum moves from the peak to that stagnation point. The other one is upstream of the wave peak, and a new local minimum can occur at that position. This Chapter is based on Albert et al. (2013a).

5.2. Governing equations

We are interested in the transport of oxygen from the gas into the film. Simulations of this are numerically quite challenging, since oxygen is only weakly soluble in water. Therefore, a boundary layer of high oxygen concentration develops near the interface, which is significantly thinner than the film. The thickness of a concentration boundary layer depends on the diffusivity of the considered chemical species. The lower the diffusivity, the thinner the boundary layer. In order to accurately capture the physical processes inside the flow, it is necessary to have sufficiently small grid cells, such that the boundary layer is resolved. The diffusivity of oxygen in water is so low, that sufficiently resolved simulations are not feasible at the moment. This problem is addressed by working with a chemical species that has the material properties of oxygen, but an artificially increased diffusivity. In order to find out how much the diffusivity must be increased, simulations with different diffusion parameters were conducted. The different diffusivities are indexed by i.

As for the mathematical modeling of interfacial species transfer, let us consider a two-phase system containing the transfer species i being transferred from the gaseous into the liquid phase. We assume that species i is dilute and physico-chemically inert. Furthermore, we presume local chemical equilibrium at the interface such that Henry's law holds for the interfacial distribution relation. Together, these assumptions imply that the species concentration has no feedback on the hydrodynamics; inside the bulk phases, the species is transported as a passive scalar, which is subject to an advection-diffusion equation:

$$\partial_t c_i + \nabla \cdot (c_i \boldsymbol{u} + \mathbf{j}_i) = 0, \qquad (x, y) \in \Omega. \tag{5.1}$$

Species flux and concentration obey the following interfacial jump conditions:

$$[\![\mathbf{j}_i]\!] \cdot \boldsymbol{n}_\Sigma = 0, \qquad \boldsymbol{x} \in \Sigma(t), \tag{5.2}$$

$$c_{i,L}|_\Sigma = H c_{i,G}|_\Sigma, \qquad \boldsymbol{x} \in \Sigma(t). \tag{5.3}$$

where we have assumed an ideally mixed gaseous phase for the latter condition. Herein, H denotes the Henry constant and $c_{i,L}|_\Sigma$ is the liquid-sided interfacial limit of the species concentration. Given an ideally diluted system (as considered here), the Fickian law of diffusion with constant diffusivities $D_i > 0$ is suitable to model the molar flux density $\mathbf{j}_i$, i.e.,

$$\mathbf{j}_i = -D_i \nabla c_i. \tag{5.4}$$

This advection-diffusion equation is solved by an unsplit two-scalar approach, where a subgrid scale-model of interfacial species transfer increases the numerical accuracy. For a detailed discussion of the above equations, and for an in-depth description of the numerical method, see Bothe and Fleckenstein (2013).

Interfacial species transfer in falling films is commonly described by means of two dimensionless groups, namely by the Schmidt and Sherwood number,

$$\mathrm{Sc} := \frac{\nu}{D_i}, \tag{5.5}$$

$$\mathrm{Sh} := \frac{k h_0}{D_i}, \tag{5.6}$$

with $k = k_{\text{glob}}$ representing the overall species transfer coefficient, which is determined by integration over the whole interfacial area as

$$k_{\text{glob}} = \frac{\int_0^{\hat{x}} k_{\text{loc}} \sqrt{1 + (\partial_x h(x))^2} \mathrm{d}x}{\int_0^{\hat{x}} \sqrt{1 + (\partial_x h(x))^2} \mathrm{d}x}, \tag{5.7}$$

with the local species transfer coefficient being defined as

$$k_{\text{loc}} := \left. \frac{\partial c}{\partial \boldsymbol{n}_\Sigma} \right|_\Sigma \left(\frac{c_\Sigma - c_\infty}{D_i} \right)^{-1}. \tag{5.8}$$

We will investigate species transfer on films that are perturbed with different frequencies at the inlet. A dimensionless measure of the frequency of disturbance is given be the Strouhal number, defined as

$$\mathrm{Sr} := \frac{\omega h_0}{u_0}. \tag{5.9}$$

5.3. Material parameters and resolution

We consider a water film at 18 °C, surrounded by an atmosphere of pure oxygen of the same temperature. The diffusivity of oxygen in water is small, such that $\mathrm{Sc}_L \approx 400$. As was mentioned above, species with different diffusivities in water are considered. The diffusivities were set in such a way that Schmidt numbers of 15, 30, 50, and 100 were obtained. In Table 5.1 a list of all used material parameters is given. As the concentration in the gas phase is much higher, almost no depletion of oxygen in the atmosphere takes place. Accordingly, in the following, we will only consider the concentration of oxygen inside the liquid.

The usual numerical parameters apply: The simulations were performed on a domain of $\hat{x} = 512h_0$ and $\hat{y} = 4h_0$. A Nusselt profile was prescribed at the inlet. If not mentioned otherwise, quadratic computational cells of edge length $h_0/16$ were used. The simulated time was 1.5 s. For a list of simulated Reynolds numbers and excitation frequencies, see Table 5.2. The amplitude of the excitation at the inlet was set to $A = 0.05$.

As for the boundary conditions at the inlet, fixed concentrations are prescribed as

$$\begin{aligned} c_i &= c_{i|\text{in},L}, \quad x = 0, \quad y < h_0, \\ c_i &= c_{i|\text{in},G}, \quad x = 0, \quad y > h_0. \end{aligned} \tag{5.10}$$

Parameter	Symbol	Value	Unit
Density liquid	ρ_L	$9.987\,44 \times 10^{-1}$	$\mathrm{g\,cm^{-3}}$
Viscosity liquid	η_L	1.068×10^{-2}	$\mathrm{g\,s^{-1}\,cm^{-1}}$
Density gas	ρ_G	1.3138×10^{-3}	$\mathrm{g\,cm^{-3}}$
Viscosity gas	η_G	2.0274×10^{-4}	$\mathrm{g\,s^{-1}\,cm^{-1}}$
Surface tension	σ	7.3638×10^{1}	$\mathrm{g\,s^{-2}}$
Gravitational acceleration	g	9.81×10^{2}	$\mathrm{cm\,s^{-2}}$
Inlet concentration of O_2, liquid	$c_{i\|\mathrm{in},L}$	2.37×10^{-7}	$\mathrm{mol\,cm^{-3}}$
Inlet concentration of O_2, gas	$c_{i\|\mathrm{in},G}$	4.186×10^{-5}	$\mathrm{mol\,cm^{-3}}$
Henry constant	H	2.70×10^{-2}	
Diffusivity of O_2, gas	D_G	2.0173×10^{-1}	$\mathrm{cm^2\,s^{-1}}$
Diffusivity of O_2, liquid, $\mathrm{Sc} = 15$	$D_{L,15}$	7.1290×10^{-4}	$\mathrm{cm^2\,s^{-1}}$
Diffusivity of O_2, liquid, $\mathrm{Sc} = 30$	$D_{L,30}$	3.5645×10^{-4}	$\mathrm{cm^2\,s^{-1}}$
Diffusivity of O_2, liquid, $\mathrm{Sc} = 50$	$D_{L,50}$	2.1387×10^{-4}	$\mathrm{cm^2\,s^{-1}}$
Diffusivity of O_2, liquid, $\mathrm{Sc} = 100$	$D_{L,100}$	1.0693×10^{-4}	$\mathrm{cm^2\,s^{-1}}$
Diffusivity of O_2, liquid, $\mathrm{Sc} = 200$	$D_{L,200}$	5.3467×10^{-5}	$\mathrm{cm^2\,s^{-1}}$
Diffusivity of O_2, liquid, $\mathrm{Sc} = 400$	$D_{L,400}$	2.6734×10^{-5}	$\mathrm{cm^2\,s^{-1}}$
Kapitza Number	Ka	3.1497×10^{3}	

Table 5.1.: Material parameters and dimensionless groups used for Direct Numerical Simulations

Re	Ca	Fr	ω in Hz	Sr
22.5	2.01×10^{-2}	3.35	15,20,25,30,35	0.0188, 0.0251, 0.0314, 0.0376, 0.0439
34.5	2.67×10^{-2}	4.15	15,20,25,30,35	0.0163, 0.0217, 0.0272, 0.0327, 0.0381
46.5	3.25×10^{-2}	4.82	20,25,30,35,40,45	0.0197, 0.0246, 0.0295, 0.0345, 0.0394, 0.0443
79.5	4.65×10^{-2}	6.30	0,20,30,40,50,60	0, 0.0164, 0.0247, 0.0329, 0.0412, 0.0494

Table 5.2.: Reynolds, Froude, Capillary numbers and excitation frequencies/Strouhal numbers used for Direct Numerical Simulations

Here, $c_{i|\text{in},L/G}$ is the species concentration at the inlet of liquid and gas, respectively. At the other boundaries, homogeneous Neumann boundary conditions are prescribed.

$$\begin{aligned}\frac{\partial c}{\partial y} &= 0, \quad 0 \le x \le \hat{x}, \quad y = 0,\\ \frac{\partial c}{\partial y} &= 0, \quad 0 \le x \le \hat{x}, \quad y = \hat{y},\\ \frac{\partial c}{\partial x} &= 0, \quad x = \hat{x}, \qquad\quad 0 \le y \le \hat{y}.\end{aligned} \tag{5.11}$$

As initial condition, the concentration of species i was fixed, setting $c_{i|\text{in},G}$ in the gas, and to $c_{i|\text{in},L}$ in the liquid.

5.4. Validation

Setting an excitation frequency of $\omega = 0\,\text{Hz}$, we can compute the flat film solution (1.49)-(1.51) inside FS3D. Since we have an analytic expression for the velocity field, and since the interface is flat, we can numerically solve the resulting advection-diffusion equation for mass transfer inside the liquid phase with high numerical accuracy. A validation against experiments is not possible, since sufficiently resolved measurement data for species transport in falling films is not available.

We consider species concentration, averaged over the film height as the validation quantity, i.e.

$$\overline{c}(t,x) = \frac{1}{h_0 + h(t,x)} \int_0^{h_0+h(t,x)} c(t,x,y)\mathrm{d}y. \tag{5.12}$$

In order to obtain reference solutions for validation at high resolutions, we ignore diffusion in streamwise direction. Since the problem is strongly convection-dominated, the absolute error compared to the full diffusion problem is considered negligible. Accordingly, the system of governing equations simplifies to become

$$\frac{\rho_L g}{2\mu_L}(2h_0 y - y^2)\partial_x c_i = \partial_{yy} c_i, \qquad 0 < x < \hat{x}, 0 < y < h_0, \tag{5.13}$$

$$c_i = c_{i|\text{in},L}, \qquad x = 0, \tag{5.14}$$

$$\frac{\partial c_i}{\partial y} = 0, \qquad y = 0, \tag{5.15}$$

$$c_i = H c_{i|\text{in},G}, \qquad y = h_0. \tag{5.16}$$

This can be viewed as a one-dimensional heat equation, with the diffusivity depending on the y-coordinate (cf. Equation 5.13). In this case, (5.14) provides the initial condition. The system is complemented by a homogeneous Neumann and a non-homogeneous Dirichlet condition – cf. Equations (5.15) and (5.16), respectively. Using second order Finite Difference Method (FDM) for discretization in y-direction, the system can be integrated in x-direction using a standard Ordinary Differential Equation (ODE) solver. Since the ODE-problem is still very stiff, the

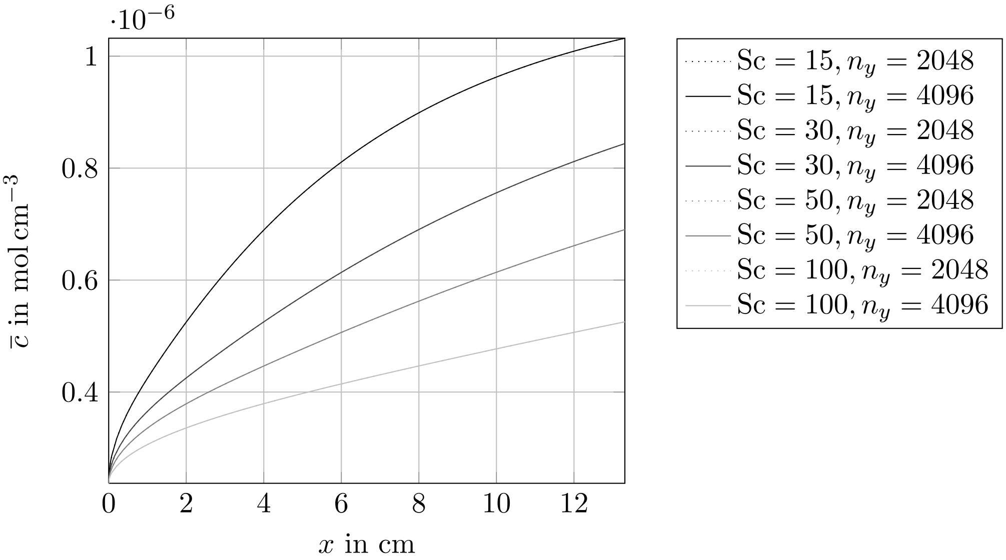

Figure 5.1.: Grid-independence of the reference solution. The validation quantitiy $\bar{c}$ is shown over the film length for all considered Schmidt numbers, and for a mean film height that is resolved with 2048 and 4096 grid points.

`ode15s-solver` of Matlab® (R2011b) was employed to integrate the equation up to $x = \hat{x}$.

The reference solution is calculated with a resolution of 4096 equidistant points in y-direction. This resolution is sufficient to achieve a grid independent reference solution, as shown in Figure 5.1. The step size in x-direction is adaptively adjusted by the ODE-solver.

For validation, we used FS3D to obtain the solution for a flat film at Re = 79.5. The onset of surface waves was avoided by setting $\omega = 0\,\mathrm{Hz}$. As for the required mesh density, this is to be considered the most challenging case, since the size of the computational cells becomes larger with Re.

Simulations at the three resolutions $h_0/8$, $h_0/16$, and $h_0/24$ were performed. In order to prove that stationarity has been reached after 1.5 s, we consider the averaged concentrations $\bar{c}$ for different Schmidt numbers at 1.4 s and 1.5 s for medium resolution, cf. Fig. 5.2. The numerical solutions can be assumed stationary, since the corresponding lines for constant Sc cannot be distinguished anymore. The same holds for other spatial resolutions considered herein.

For validation, the averaged concentration values $\bar{c}$ are compared at different axial positions, cf. Fig. 5.3. Given the number of cases examined, the performed DNS reached the limit of acceptable computational costs at the intermediate resolution $h_0/16$ (taking computation times of up to several weeks). Evidently, the numerical simulations at high Sc numbers show significant deviations from the

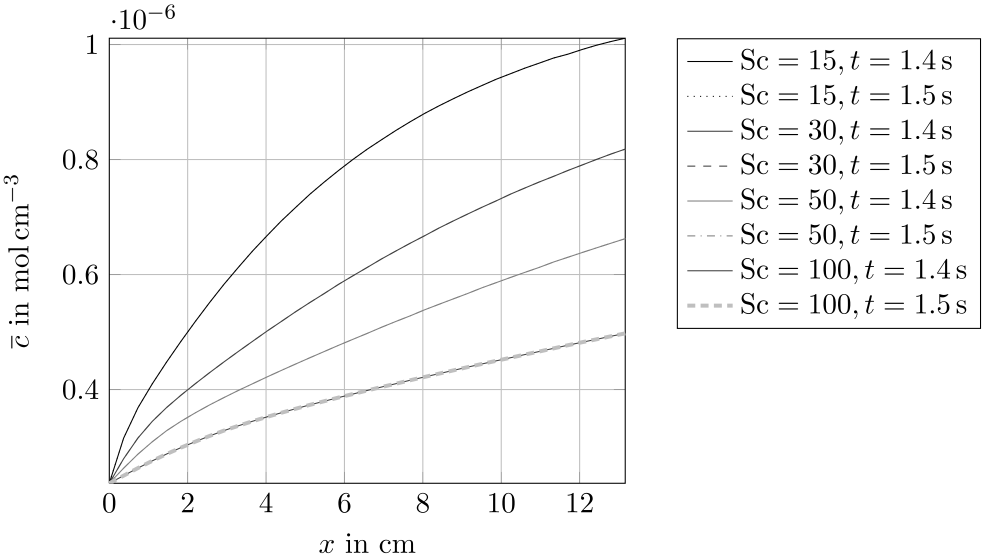

Figure 5.2.: Validation study — Comparison of solutions after 1.4 s and 1.5 s. Stationarity is reached after 1.4 s.

reference solutions. With increasing Schmidt numbers the deviations become more pronounced. For this reason, we shall discuss only simulation results obtained for Sc up to 50 in the remainder, while disregarding results beyond this limit, as they cannot be considered reliable. Notably, however, DNS of interfacial mass transfer into falling films at these moderate Schmidt numbers already shows relevant features of high Schmidt number cases as will be shown in the remainder.

5.5. Species transfer into falling film

5.5.1. Hydrodynamics

This section aims to increase the understanding of how different wave regions facilitate the intensification of interfacial mass transfer. The inner flow fields of nonlinear waves show complex structures which are expected to have a significant influence on the observed species transfer rates. We are especially interested in the effect of two hydrodynamical phenomena — backflow and vortices — that can be observed on falling films within distinct wave regimes, depending on Reynolds number and frequency of excitation.

Therefore, we first discuss the hydrodynamics of falling films on the basis of characteristic wave regimes, vortices and backflow. Then, the influence of these hydrodynamical phenomena on interfacial mass transfer into falling films is revealed. We identify distinct mass transfer enhancement mechanisms taking effect in the considered wave regimes. Our discussion is set out in terms of local Sherwood

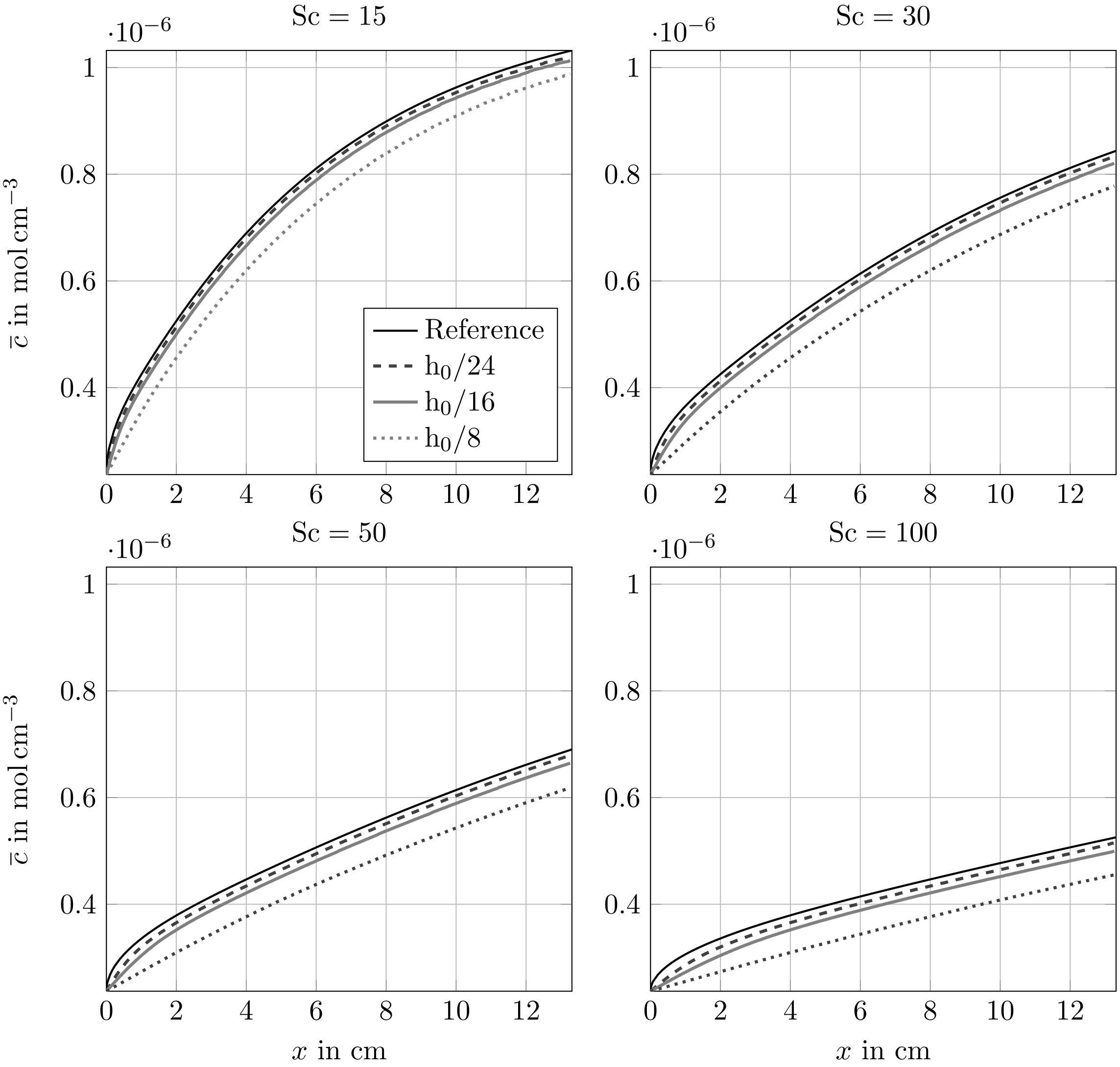

Figure 5.3.: Validation — Species concentration averaged over the film height.

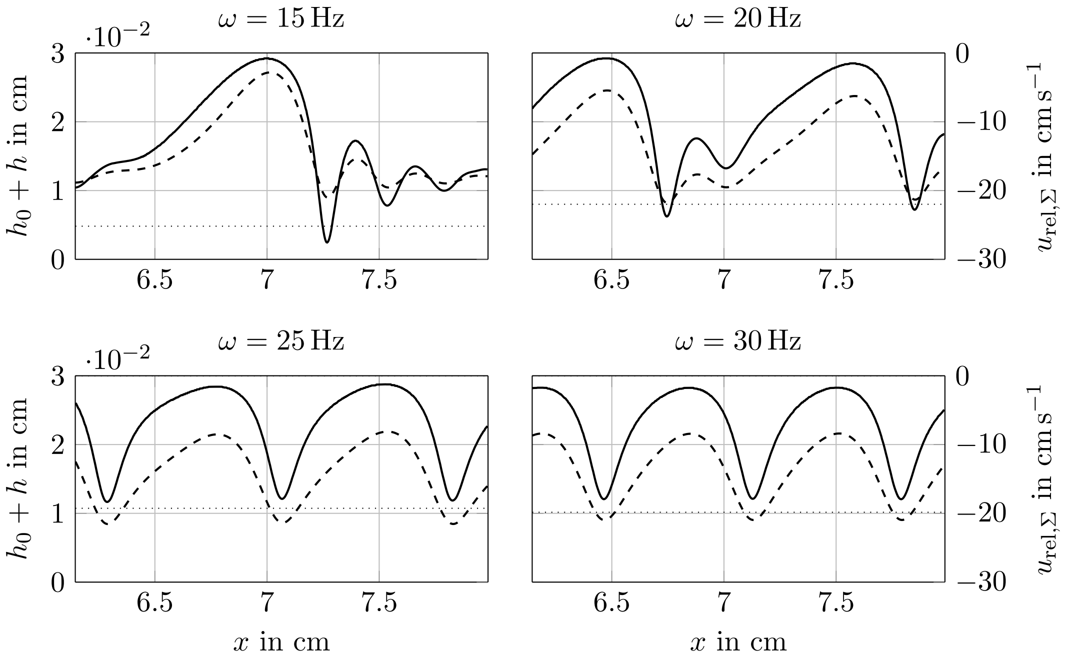

Figure 5.4.: Film height (dashed line) and streamwise velocity, relative to wave velocity, at the interface (solid line); Re = 22.5.

number profiles (i.e. local mass transfer rates) and the typical concentration patterns arising thereof.

Once perturbations have developed into saturated nonlinear waves, they keep their shape for a significant downstream distance, cf. Figure 1.2, region II. In the experiment or in three-dimensional simulations, these time periodic waves are susceptible to spanwise perturbations and disintegrate into horseshoe-shaped solitary waves sufficiently far downstream, see Park and Nosoko (2003). The flow inside the two-dimensional waves can be regarded as stationary, if it is considered in the reference frame of the moving wave. This observation allows simulations as they were performed in Bo et al. (2011), where a stationary advection-diffusion problem was solved on a flow field that was determined in advance. Also in the present section, this quasi-stationarity is exploited: With the notable exception of Section 5.5.2, flow physics and species concentration patterns are discussed on the basis of the simulation results at a single time ($t = 1.5\,\mathrm{s}$).

Observed wave regimes

In Figures 5.4 – 5.7, dashed lines show the local film thickness on a representative part of the domain for different Reynolds numbers and excitation frequencies. As depicted in Fig. 5.6 for $\omega = 20\,\mathrm{Hz}$, low excitation frequencies are known to lead to

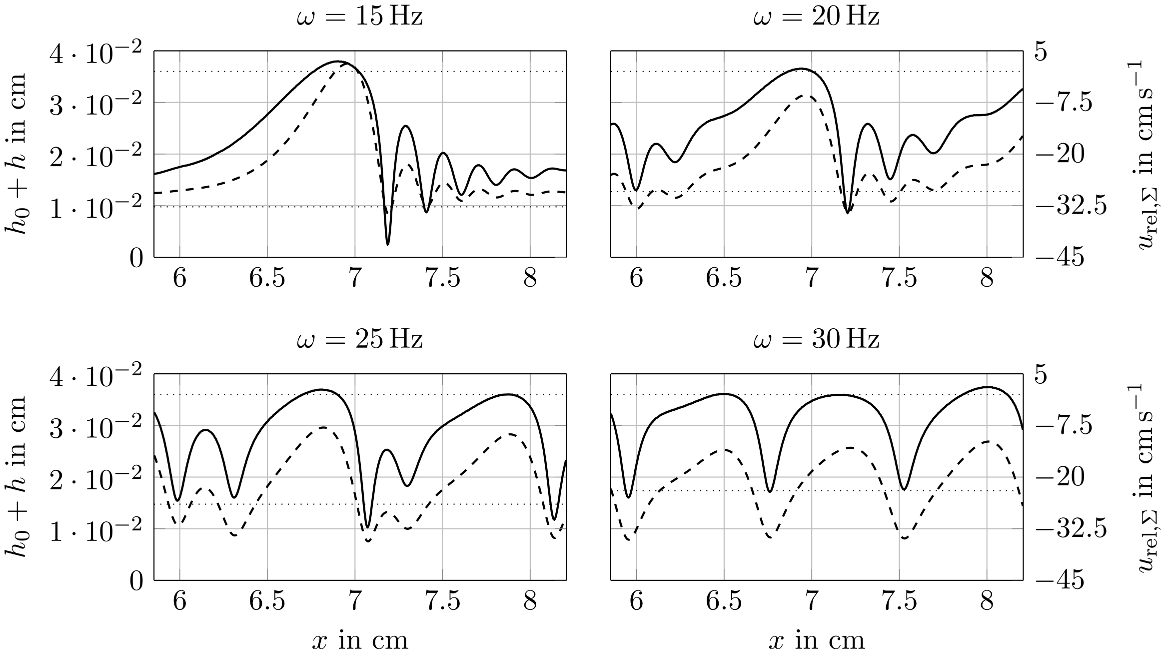

Figure 5.5.: Film height (dashed line) and streamwise velocity, relative to wave velocity, at the interface (solid line); Re = 31.5.

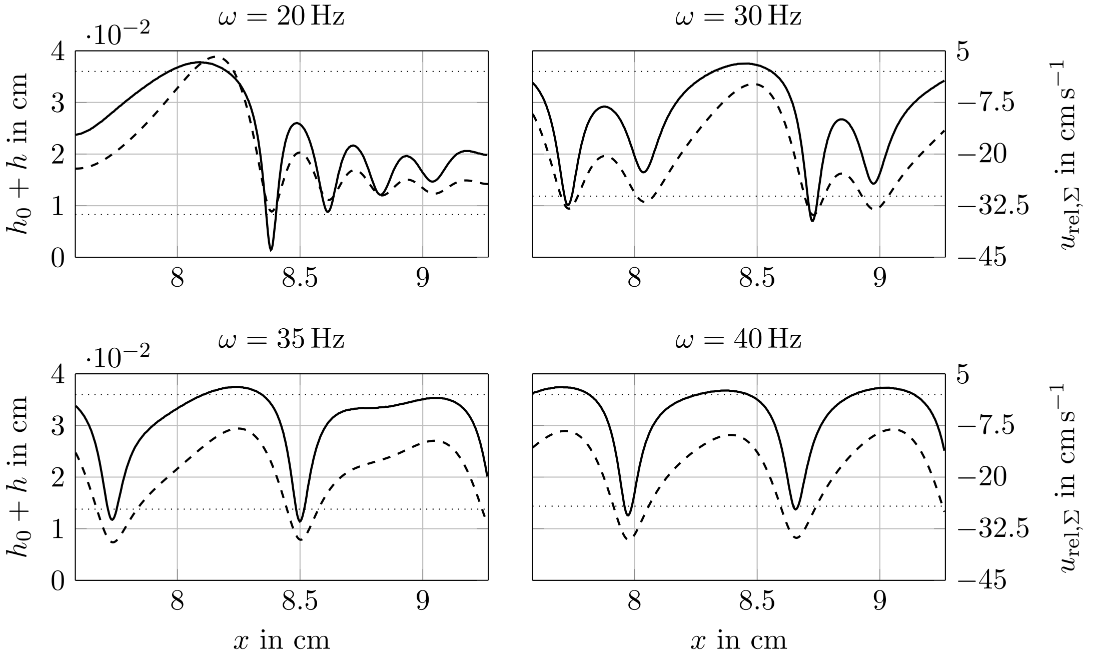

Figure 5.6.: Film height (dashed line) and streamwise velocity, relative to wave velocity, at the interface (solid line); Re = 46.5.

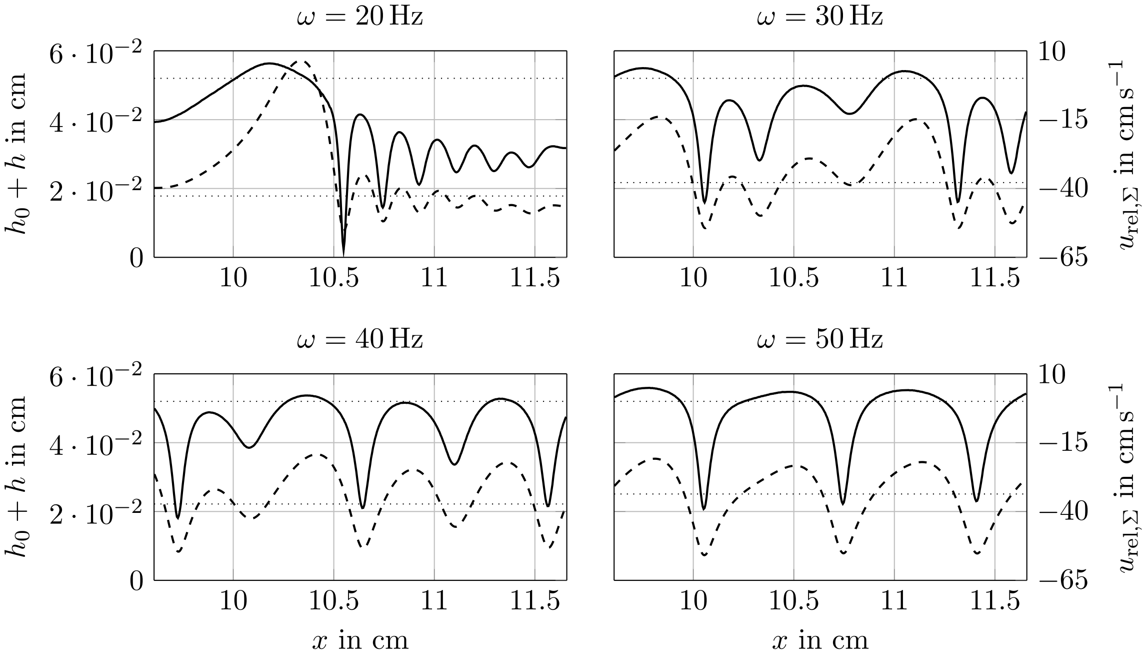

Figure 5.7.: Film height (dashed line) and streamwise velocity, relative to wave velocity, at the interface (solid line); Re = 79.5.

waves with long wavelength, exhibiting a characteristic roll wave/capillary wave structure. In this wave regime, large wave humps (roll waves) are preceded by several smaller wave humps (capillary waves). An increase in excitation frequency first leads to a decrease of the number of capillary waves as shown in Fig. 5.6 for $\omega = 30\,\text{Hz}$, and finally their disappearance ($\omega = 40\,\text{Hz}$). This means that for sufficiently high excitation frequencies only large wave humps with an approximately sinusoidal form remain. Furthermore, there exists an intermediate wave regime, where genuine time-periodic waves do not appear (Fig. 5.6 for $\omega = 35\,\text{Hz}$). In general, both wave amplitude and wave length decrease with excitation frequency. The notion of "low" and "high" frequencies depends on the Reynolds number. The higher the Reynolds number, the higher the necessary frequency for a certain wave regime. This can be seen by rewriting the Strouhal number (5.9) in terms of the Reynolds number:

$$\mathrm{Sr} = \omega \left(\frac{3\nu_L}{g} \right)^{\frac{2}{3}} \mathrm{Re}^{-\frac{1}{3}} \,. \tag{5.17}$$

In the performed simulations, capillary waves vanish for Strouhal numbers exceeding a value of about 0.03.

Vortices

It is known that for sufficiently large wave humps a vortex can occur in the coordinate system of the wave. This phenomenon has been studied in detail by Malamataris and Balakotaiah (2008), and direct experimental evidence was presented in Alekseenko et al. (2007), in the slighty different, yet related case of liquid flow down the outside of an inclined tube. In Fig. 5.4 – 5.7, solid lines show the streamwise velocity component at the interface in the coordinate system of the moving wave, $u_{\text{rel},\Sigma} = u_\Sigma - u_{\text{wave}}$. Here, $u_\Sigma = u|_{y=h_0+h}$ and u_{wave} is the phase velocity of the wave. The presence or absence of a vortex is indicated by an auxiliary dotted line drawn at $u_\Sigma - u_{\text{wave}} = 0$. For positive values, the fluid near the interface moves faster than the wave, and a vortex is present in the reference frame of the moving wave. We observe vortices in the large wave humps only for films at sufficiently large Re. Since the ratio between maximal and residual film thickness increases with Re, this is in agreement with Brauner and Moalem Maron (1983) and Moalem Maron et al. (1989), who predict that this vortex occurs when the ratio between the large wave humps and the residual film exceeds a threshold value of about 2.5. Accordingly, vortices cannot be observed in the crests of capillary waves.

Backflow

Backflow denotes a localized region of the flow field where negative streamwise velocities, opposing the direction of gravity, occur at the interface in the (fixed) reference frame of the wall — cf. Fig. 5.8 for velocity arrows in the wave trough at $\mathrm{Re} = 79.5$ and $\omega = 50\,\text{Hz}$. In Fig. 5.4 – 5.7, a line is drawn at $u_{\text{rel},\Sigma} = -u_{\text{wave}}$.

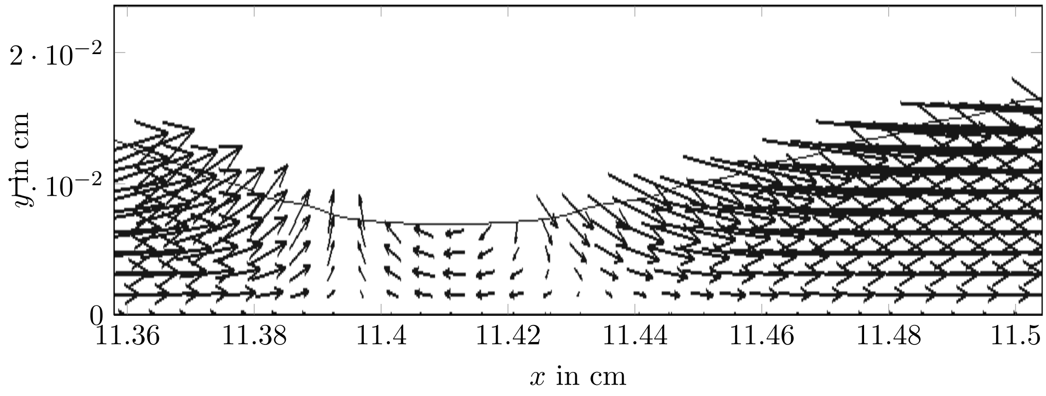

Figure 5.8.: Local backflow in the wave troughs, $\mathrm{Re} = 79.5, \omega = 50\,\mathrm{Hz}$. Velocities are shown in the reference frame of the laboratory.

When interfacial velocities fall below this threshold, it means that u_Σ is negative in the wall-fixed coordinate frame, indicating the occurence of local backflow.

Detailed numerical and experimental studies of the backflow phenomenon were performed in Dietze et al. (2008, 2009). There, the occurence of backflow was linked to the derivative of interfacial curvature in the following way: Due to the small thickness of the film, the bulk pressure in the liquid is almost entirely determined by the law of Young-Laplace,

$$p_L \approx \sigma\kappa + p_G,$$

where the atmospheric pressure p_G is nearly constant. Curvature in the capillary troughs is negative, while curvature in the wave humps is positive. This sharp increase of pressure leads to a pressure gradient that exerts a force in negative x-direction, leading to an deceleration of the liquid. For low Re, backflow is only observed for waves of a low frequency, associated with the presence of capillary waves. This is in accordance with Dietze et al. (2008), where flows of low Reynolds numbers were investigated, and backflow was only found in the presence of capillary waves, where the steepest pressure gradients occur. For large Re, however, backflow is also observed in the high frequency regime, where no capillary waves are present. Here, the gradient of interfacial curvature between two large wave humps is large enough to induce backflow.

5.5.2. Species transfer

Local Sherwood number profiles (local transfer rates)

We define the local Sherwood number as

$$\mathrm{Sh}_{\mathrm{loc}}(x) = -\frac{h_0}{c_\Sigma - c_{L,0}} \frac{\partial c}{\partial \boldsymbol{n}_\Sigma}(x), \tag{5.18}$$

Re	Sc	$\omega = 0\,\mathrm{Hz}$	$\omega = 15\,\mathrm{Hz}$	$\omega = 20\,\mathrm{Hz}$	$\omega = 25\,\mathrm{Hz}$	$\omega = 30\,\mathrm{Hz}$	$\omega = 35\,\mathrm{Hz}$	$\omega = 40\,\mathrm{Hz}$	$\omega = 45\,\mathrm{Hz}$	$\omega = 50\,\mathrm{Hz}$	$\omega = 60\,\mathrm{Hz}$
22.5	15		0.11341	0.11408	0.11398	0.11413	0.11386				
22.5	30		0.16022	0.16054	0.16083	0.16045	0.15996				
22.5	50		0.20006	0.19952	0.20017	0.19892	0.19657				
34.5	15		0.18997	0.18910	0.19101	0.19087	0.1897				
34.5	30		0.26046	0.26074	0.26203	0.26183	0.26118				
34.5	50		0.31087	0.31105	0.31215	0.31098	0.31065				
46.5	15			0.25511	0.25680	0.25668	0.25773	0.25783	0.25749		
46.5	30			0.34408	0.34508	0.34555	0.34614	0.34606	0.34402		
46.5	50			0.39921	0.40005	0.40075	0.40138	0.40035	0.39514		
79.5	15	0.38829		0.39639		0.40144		0.40430		0.40597	0.40698
79.5	30	0.43363		0.49920		0.50855		0.51211		0.51574	0.51455
79.5	50	0.43761		0.54140		0.55430		0.55763		0.56088	0.55758

Table 5.3.: Variation of $\mathrm{Sh}_{\mathrm{glob}}/\sqrt{Sc}$ (absorption rate) with frequency, Reynolds and Schmidt number

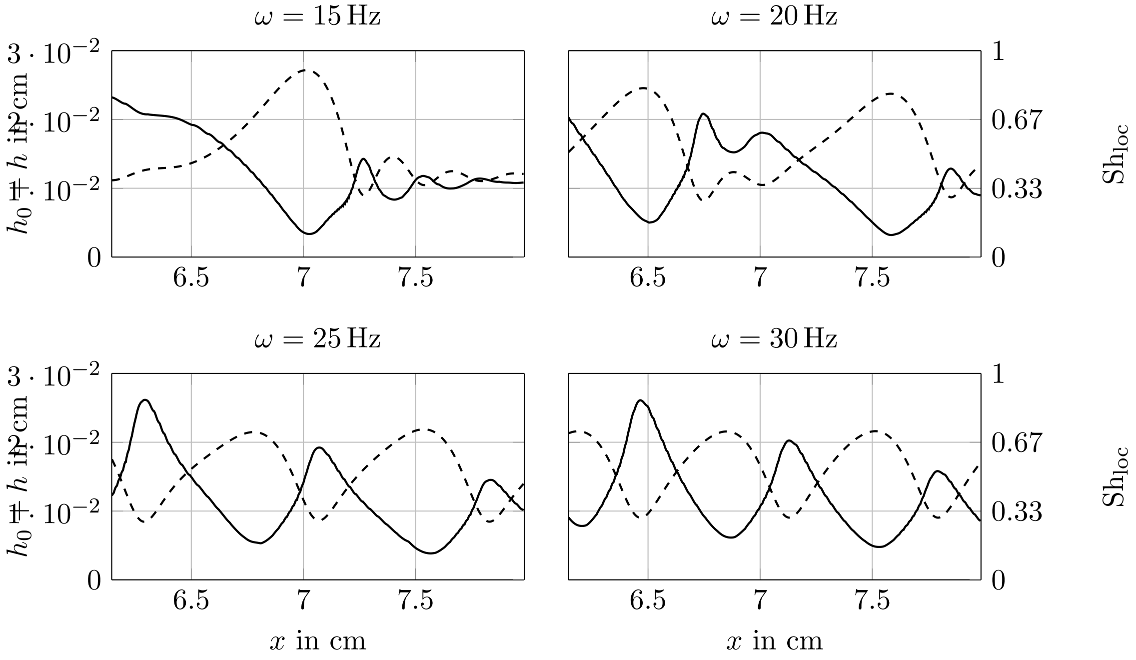

Figure 5.9.: Film height (dashed line) and local Sherwood number (solid line) at Re = 22.5.

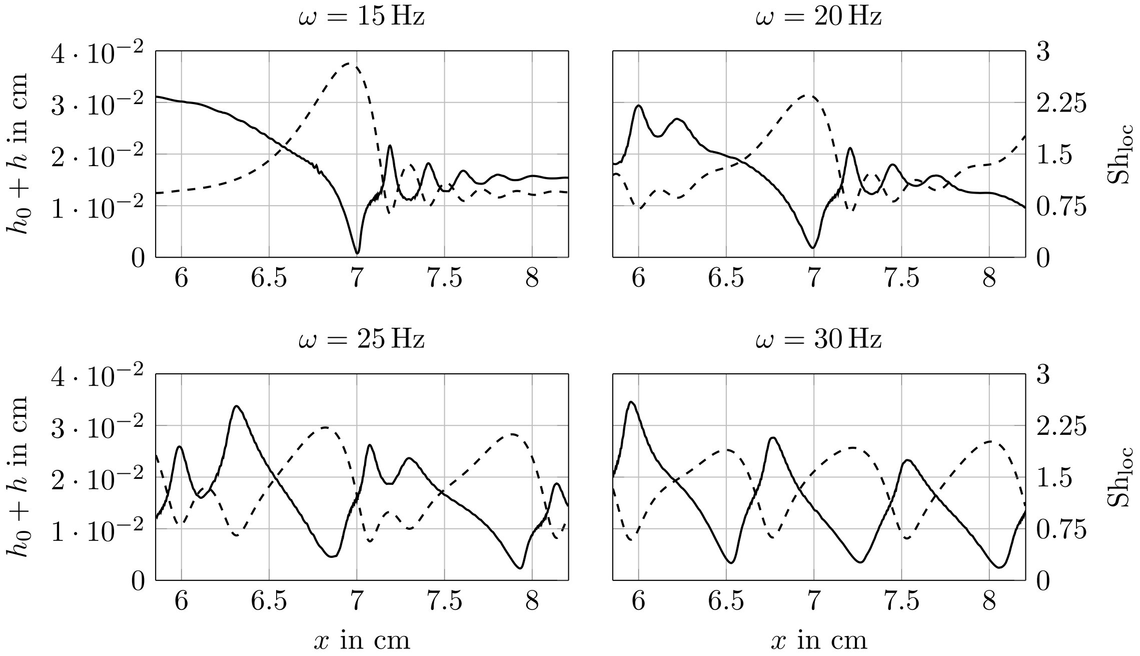

Figure 5.10.: Film height (dashed line) and local Sherwood number (solid line) at $\mathrm{Re} = 34.5$.

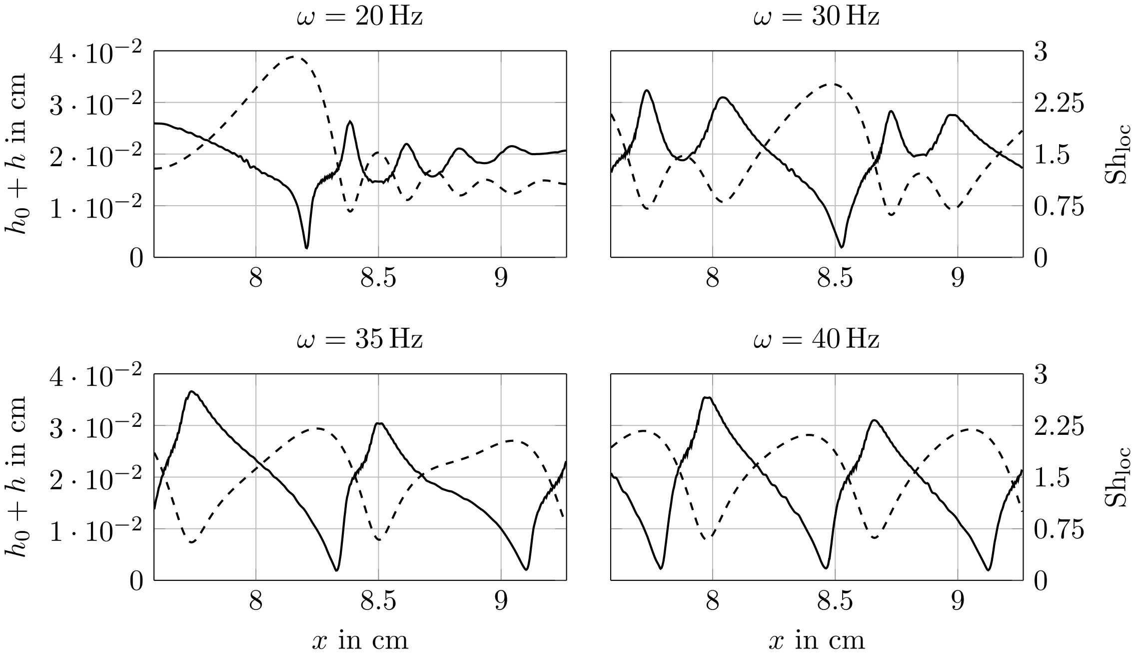

Figure 5.11.: Film height (dashed line) and local Sherwood number (solid line) at Re = 46.5.

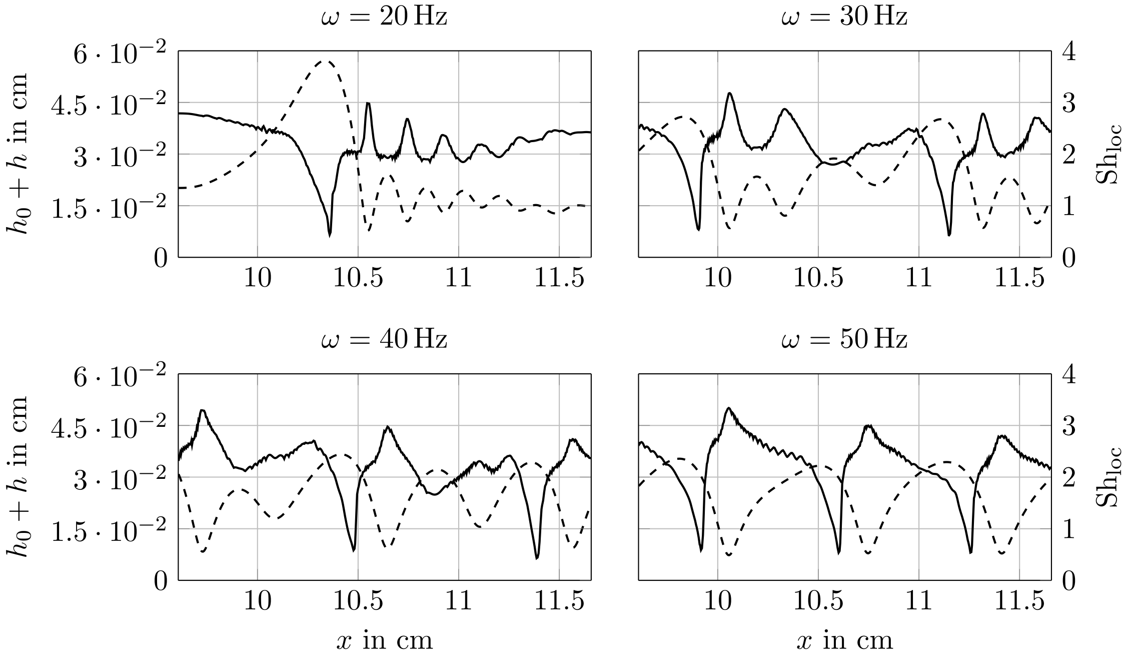

Figure 5.12.: Film height (dashed line) and local Sherwood number (solid line) at Re = 79.5.

i.e., as an appropriately normalized derivative in normal direction, where c_Σ is the species concentration at the interface. The global Sherwood number is defined as the line integral of the local Sherwood number over the free surface, averaged over the interface length, i.e.,

$$\mathrm{Sh}_{\mathrm{glob}} = \frac{\int_0^{\hat{x}} \mathrm{Sh}_{\mathrm{loc}}(x)\sqrt{1+(\partial_x h(x))^2}\mathrm{d}x}{\int_0^{\hat{x}} \sqrt{1+(\partial_x h(x))^2}\mathrm{d}x}. \tag{5.19}$$

In Fig. 5.9 to 5.12, local species transfer rates are shown over a representative part of the film, and are indicated by solid lines. For ease of comparison, film thickness is shown by a dashed line. Global Sherwood numbers for all simulated cases are given in Table 5.3.

For all Reynolds numbers and excitation frequencies considered, a local maximum occurs in the wave troughs, irrespective of the type of adjacent wave humps. This observation is affirmed by measurements reported in (Schagen et al., 2006; Schagen and Modigell, 2007) for heat transfer coefficients. The occurrence of a local maximum in the wave troughs is, in particular, independent of the presence of backflow. This behaviour can be explained by the fact that $u_{\mathrm{rel},\Sigma}$ exhibits a local minimum that coincides with the local minimum of film height. The quantity $u_{\mathrm{rel},\Sigma}$ can be interpreted as a surface renewal rate. In the wave troughs, water at the surface, that bears a high concentration of oxygen, is advected into the bulk with a high velocity.

For roll waves without vortex as well as in capillary waves, a local minimum of species transfer rate coincides with the wave crest. These local minima are met by local maxima of $u_{\mathrm{rel},\Sigma}$, meaning that the velocity of fluid at that point is close to wave velocity, resulting in a smaller surface renewal rate.

In larger wave humps – either due to a higher Reynolds number, or due to a smaller excitation frequency – the maximum of $u_{\mathrm{rel},\Sigma}$ gradually approaches 0, until a vortex occurs. In this case two critical points appear – saddle points, such as stagnation or separation points. These points are denoted as A for the critical point upstream of the wave crest and B for the critical point at the downstream position (cf. streamline plots provided in Fig. 5.14). The local minimum of species transfer rate migrates from the wave crest to the downstream critical point B, where an afflux of species occurs from two positions: from the capillary wave region downstream, and from the part of the interface between both critical points.

The upstream point A, on the other hand, experiences an efflux of liquid. If the local maximum in the nearest wave trough is sufficiently strong, this leads to the development of a plateau, as can be seen in Fig. 5.12 for $\omega = 50\,\mathrm{Hz}$. However, if capillary waves are sufficiently close to this point, another local maximum can occur on this position; cf. Fig. 5.12 for $\omega = 30/40\,\mathrm{Hz}$.

Concentration patterns

In Fig. 5.13 and 5.14, species concentration fields and local flow fields in the moving reference frame are shown for four representative wave regimes: small and large

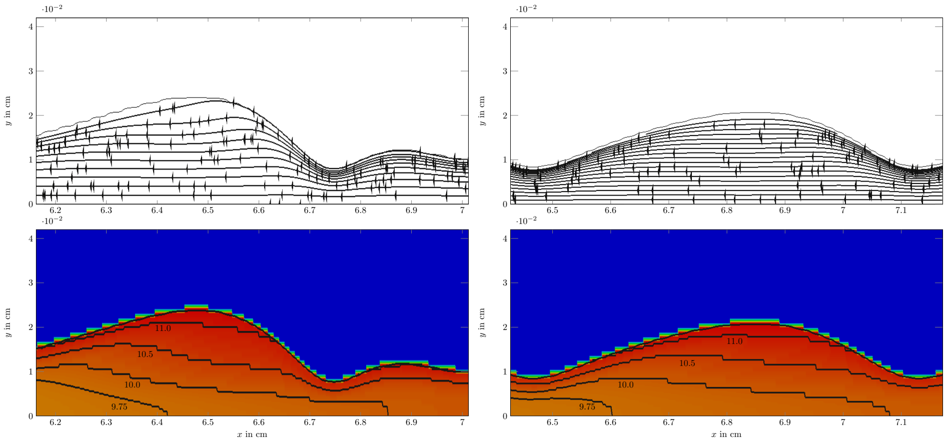

(a) 20 Hz. **(b)** 30 Hz.

Figure 5.13.: Velocity and concentration fields for Re = 22.5

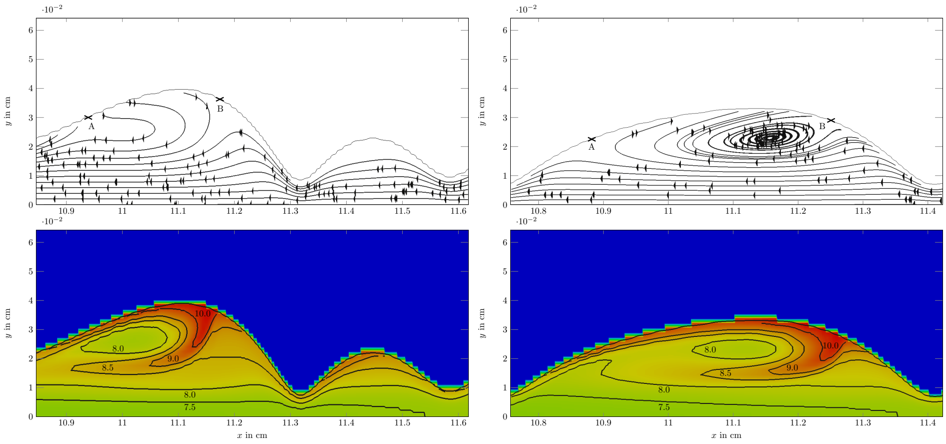

(a) 20 Hz. **(b)** 30 Hz.

Figure 5.14.: Velocity and concentration fields for Re = 79.5.

Reynolds numbers, each with and without capillary waves.

In Fig. 5.13, we see continuous concentration boundary layers; the concentration pattern is mainly determined by diffusive transport from the interface. No roll up of species concentration can be observed in the roll waves, and species concentration decreases monotonously with distance from the interface. In the wave trough, the deceleration of liquid due to the adverse pressure gradient leads to a concentration boundary layer that is significantly thinner than the one in the large wave hump. In Fig. 5.13b we see a wave in the sinusoidal regime at a low Reynolds number, where no backflow occurs. The species distribution is very similar to Fig. 5.13a.

In Fig. 5.14, waves with a vortex are considered. Species concentration is highly influenced by the presence of the vortex. A finger of high concentration starts at the downstream critical point and is rolled up, following the streamlines. In this regime, species concentration does not monotonously decrease with distance from the interface. In Malamataris and Balakotaiah (2008) it was pointed out that the vortex is not seen in the stationary frame of reference. This is true for the velocity field. In the presence of an advected scalar like species concentration, however, the vortex becomes clearly visible.

Time periodic behaviour inside the large wave humps

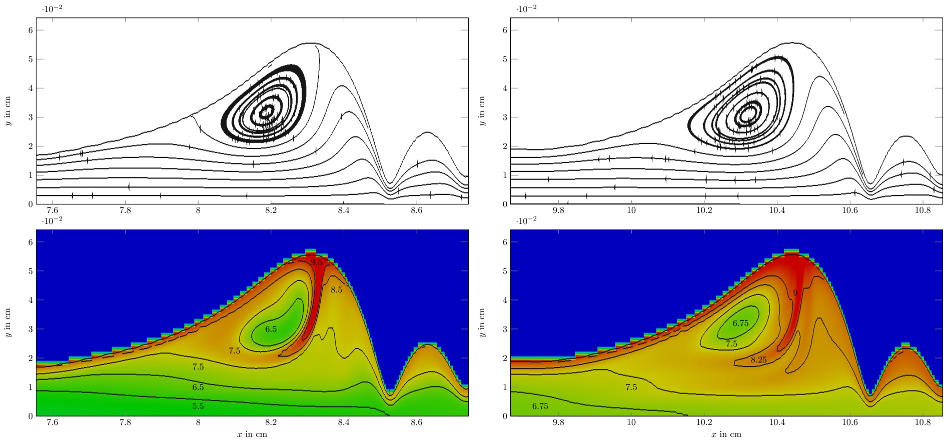

(a) Single finger.

(b) Double finger.

Figure 5.15.: Velocity and concentration fields for $\mathrm{Re} = 53, \omega = 20\,\mathrm{Hz}$.

We find that the assumption of stationarity inside the large wave humps is not valid anymore for large Reynolds numbers. The wave hump at $\mathrm{Re} = 79.5$ and $\omega = 20\,\mathrm{Hz}$ is the largest one considered in this work. A new hydrodynamical bifurcation is observed, where the vortex starts to show slight oscillations. In Fig. 5.15a, the large vortex and the associated species concentration field are shown at $x = 8.3\,\mathrm{cm}$. In Fig. 5.15b, the same wave hump is shown further downstream, with a time difference of $0.05\,\mathrm{s} = \frac{1}{\omega}$. The oscillation of the vortex leads to the formation of a second finger of high concentration. This second finger vanishes again after another $0.05\,\mathrm{s}$, meaning that it oscillates with $10\,\mathrm{Hz}$. In order to make sure that this is not an effect of insufficient resolution, the simulation was repeated with a higher resolution of $\frac{h_0}{24}$, with the same result. In none of the other simulations, a similar behaviour was observed.

5.6. Conclusion

In this chapter, simulations of the species transfer from a gas atmosphere into a falling film were performed. The numerical approach was validated by comparison to a highly resolved reference solution that was computed on the basis of the steady state. It was found that simulations with Schmidt numbers up to 50 can be considered reliable.

The influence of the flow field in fully saturated, nonlinear waves on local species transfer rates was investigated. Special attention was turned to two hydrodynamic phenomena: Vortices in the large wave humps, and backflow in the capillary wave region. Large rates of species transfer are observed in the wave troughs, whether backflow occurs or not. Over all considered Reynolds numbers and wave regimes, a local maximum of species transfer rate coincides with a local minimum of film height. For small Re, no vortex is present in the large wave humps. In this case, a local minimum of species transfer coincides with the wave peak, where the surface renewal rate is highest. In waves without a vortex, species distribution is mainly determined by diffusion from the interface, and no roll-up of concentration isolines is observed. On sufficiently large waves, a vortex occurs, and the local minimum migrates from the wave peak to a stagnation point downstream of the wave peak. Another stagnation point is positioned upstream of the wave peak; at this point, a local maximum can occur. When a vortex is present, concentration isolines roll up and follow the streamlines in the reference frame of the moving wave.

It is noted that for very large wave humps, the often assumed stationarity of the flow field in the moving reference frame is not valid anymore. The onset of a small oscillation of the vortex is observed, which leads to the periodic appearance and disappearance of a second finger of high concentration.

A. Transformation to the fixed domain

In order to solve the system of equations, a transformation from the physical, time-dependent domain

$$\Omega_P = \{(x,y) \in \mathbb{R}^2 : 0 < y < 1 + h(t,x)\} \tag{A.1}$$

to a fixed domain

$$\Omega_F = \{(x,y) \in \mathbb{R}^2 : 0 < y < 1\} \tag{A.2}$$

is employed. The set of coordinates on the fixed domain is x', y', t'. We define a regularizing extension of the height function into the flow domain:

$$h'(x',y',t') = \sum_{k \in \mathbb{Z}\setminus\{0\}} \frac{h^{(k)}(t')}{1 + |kl|^2 (y'-1)^2} e^{iklx'}. \tag{A.3}$$

This regularization is necessary since, after transformation, third derivatives of the height function appear. Using this, we define a diffeomorphism $\boldsymbol{t} : \Omega_F \to \Omega_P$ by

$$\boldsymbol{t}(x',y',t') = \begin{pmatrix} x' \\ y' + y'h'(x',y',t') \\ t' \end{pmatrix} = \begin{pmatrix} x \\ y \\ t \end{pmatrix}. \tag{A.4}$$

The Jacobian $D\boldsymbol{t}$ of $\boldsymbol{t}$ is

$$\begin{aligned} D\boldsymbol{t}(x',y',t') &= \begin{pmatrix} \frac{\partial x}{\partial x'} & \frac{\partial x}{\partial y'} & \frac{\partial x}{\partial t'} \\ \frac{\partial y}{\partial x'} & \frac{\partial y}{\partial y'} & \frac{\partial y}{\partial t'} \\ \frac{\partial t}{\partial x'} & \frac{\partial t}{\partial y'} & \frac{\partial t}{\partial t'} \end{pmatrix} (x',y',t') \\ &= \begin{pmatrix} 1 & 0 & 0 \\ y'\partial_{x'}h' & 1 + h' + y'\partial_{y'}h' & y'\partial_{t'}h' \\ 0 & 0 & 1 \end{pmatrix} (x',y',t') \\ &= \begin{pmatrix} 1 & 0 & 0 \\ T_{21} & T_{22} & T_{23} \\ 0 & 0 & 1 \end{pmatrix} (x',y',t'). \end{aligned} \tag{A.5}$$

Therefore,

$$J(x',y',t') = \det D\boldsymbol{t}(x',y',t') = (1 + h' + y'\partial_{y'}h')(x',y',t'). \tag{A.6}$$

We employ a divergence free transformation for the velocity field, which was introduced for the solution of the Navier-Stokes equations with a free boundary in

Bock (1977), and was popularized in Beale (1981, 1984):

$$\begin{aligned}\begin{pmatrix} u \\ v \end{pmatrix}(x,y,t) &= \left.\left(\frac{1}{J} D\boldsymbol{t} \begin{pmatrix} u' \\ v' \end{pmatrix}\right)\right|_{\boldsymbol{t}^{-1}(x,y,t)} \\ &= \frac{1}{T_{22}} \begin{pmatrix} u' \\ T_{21}u' + T_{22}v'. \end{pmatrix}\end{aligned} \tag{A.7}$$

where DT is the Jacobian of T.

The inverse function theorem gives

$$\begin{aligned} D\boldsymbol{t}^{-1}(x,y,t) &= \begin{pmatrix} \frac{\partial x'}{\partial x} & \frac{\partial x'}{\partial y} & \frac{\partial x'}{\partial t} \\ \frac{\partial y'}{\partial x} & \frac{\partial y'}{\partial y} & \frac{\partial y'}{\partial t} \\ \frac{\partial t'}{\partial x} & \frac{\partial t'}{\partial y} & \frac{\partial t'}{\partial t} \end{pmatrix}(x,y,t) \\ &= \begin{pmatrix} 1 & 0 & 0 \\ \frac{-y'\partial_{x'}h'}{J} & \frac{1}{J} & \frac{-y'\partial_{t'}h'}{J} \\ 0 & 0 & 1 \end{pmatrix}(\boldsymbol{t}^{-1}(x,y,t)) \\ &= \begin{pmatrix} 1 & 0 & 0 \\ S_{21} & S_{22} & S_{23} \\ 0 & 0 & 1 \end{pmatrix}(\boldsymbol{t}^{-1}(x,y,t)). \end{aligned} \tag{A.8}$$

A.0.1. Transformation of the differential operators

Under the stated mapping, the differential operators transform in the following way:

$$\begin{aligned} \partial_t f(x',y',t') &= \frac{\partial f}{\partial x'}\frac{\partial x'}{\partial t} + \frac{\partial f}{\partial y'}\frac{\partial y'}{\partial t} + \frac{\partial f}{\partial t'}\frac{\partial t'}{\partial t} \\ &= S_{23}\partial_{y'} f + \partial_{t'} f, \end{aligned} \tag{A.9}$$

$$\begin{aligned} \partial_x f(x',y',t') &= \frac{\partial f}{\partial x'}\frac{\partial x'}{\partial x} + \frac{\partial f}{\partial y'}\frac{\partial y'}{\partial x} + \frac{\partial f}{\partial t'}\frac{\partial t'}{\partial x} \\ &= \partial_{x'} f + S_{21}\partial_{y'} f, \end{aligned} \tag{A.10}$$

$$\begin{aligned} \partial_y f(x',y',t') &= \frac{\partial f}{\partial x'}\frac{\partial x'}{\partial y} + \frac{\partial f}{\partial y'}\frac{\partial y'}{\partial y} + \frac{\partial f}{\partial t'}\frac{\partial t'}{\partial y} \\ &= S_{22}\partial_{y'} f, \end{aligned} \tag{A.11}$$

$$\partial_{xx} f = \left(\partial^2_{x'x'} + S_{21}^2\partial^2_{y'y'} + 2S_{21}\partial^2_{x'y'} + (\partial_{x'}S_{21} + S_{21}\partial_{y'}S_{21})\partial_{y'}\right) f, \tag{A.12}$$

$$\partial_{yy} f = \left(S_{22}\partial_{y'}S_{22}\partial_{y'} + S_{22}^2\partial^2_{y'y'}\right) f. \tag{A.13}$$

A.0.2. Derivatives of components of the Jacobian

We need the following derivatives of components of $D\boldsymbol{t}$ and $D\boldsymbol{t}^{-1}$ where, for ease of notation, all the primes on the right hand side are dropped:

$$\partial_{t'}T_{21} = yh_{xt}, \tag{A.14}$$

$$\partial_{x'}T_{21} = yh_{xx}, \tag{A.15}$$

$$\partial_{y'}T_{21} = h_x + yh_{xy}, \tag{A.16}$$

$$\partial_{x'x'}T_{21} = yh_{xxx}, \tag{A.17}$$

$$\partial_{y'y'}T_{21} = 2h_{xy} + yh_{xyy}, \tag{A.18}$$

$$\partial_{x'y'}T_{21} = h_{xx} + yh_{xxy}, \tag{A.19}$$

$$\partial_{t'}T_{22} = h_t + yh_{ty}, \tag{A.20}$$

$$\partial_{x'}T_{22} = h_x + yh_{xy}, \tag{A.21}$$

$$\partial_{y'}T_{22} = 2h_y + yh_{yy}, \tag{A.22}$$

$$\partial_{x'x'}T_{22} = h_{xx} + yh_{xxy}, \tag{A.23}$$

$$\partial_{y'y'}T_{22} = 3h_{yy} + yh_{yyy}, \tag{A.24}$$

$$\partial_{x'y'}T_{22} = 2h_{xy} + yh_{xyy}, \tag{A.25}$$

$$\partial_{x'}S_{21} = \frac{yh_x(h_x + yh_{xy}) - yh_{xx}J}{J^2}, \tag{A.26}$$

$$\partial_{y'}S_{21} = \frac{yh_x(2h_y + yh_{yy}) - (h_x + yh_{xy})J}{J^2}, \tag{A.27}$$

$$\partial_{y'}S_{22} = -\frac{2h_y + yh_{yy}}{J^2}. \tag{A.28}$$

A.0.3. Transformation of the velocity components

In order to apply the transformed differential operators (A.9)-(A.13) to the velocities, we need the following formulas. Again, on the right hand side, all quantities are to be understood with a prime, which is dropped.

$$\begin{aligned}\partial_{x'}u &= \partial_{x'}(\frac{u'}{T_{22}}) \\ &= \frac{u_x}{J} - \frac{h_x + yh_{xy}}{J^2}u,\end{aligned} \tag{A.29}$$

$$\begin{aligned}\partial_{y'}u &= \partial_{y'}(\frac{u'}{T_{22}}) \\ &= \frac{u_y}{J} - \frac{2h_y + yh_{yy}}{J^2}u,\end{aligned} \tag{A.30}$$

$$\begin{aligned}\partial_{x'x'}u =& \frac{u_{xx}}{J} - 2\frac{h_x + yh_{xy}}{J^2}u_x - \frac{h_{xx} + yh_{xxy}}{J^2}u \\ &+ 2\frac{(h_x + yh_{xy})^2}{J^3}u,\end{aligned} \tag{A.31}$$

$$\begin{aligned}\partial_{x'y'}u =&\frac{u_{xy}}{J}-\frac{2h_y+yh_{yy}}{J^2}u_x-\frac{h_x+yh_{xy}}{J^2}u_y\\&-\frac{2h_{xy}+yh_{xyy}}{J^2}u+2\frac{(h_x+yh_{xy})(1h_y+yh_{yy})}{J^3}u,\end{aligned}\tag{A.32}$$

$$\begin{aligned}\partial_{y'y'}u =&\frac{u_{yy}}{J}-\frac{2h_y+yh_{yy}}{J^2}u_y-\frac{3h_{yy}+yh_{yyy}}{J^2}u\\&+\frac{4h_y+2yh_{yy}}{J^3}u-\frac{2h_y+yh_{yy}}{J^2}u_y,\end{aligned}\tag{A.33}$$

$$\begin{aligned}\partial_{x'}v &= \partial_{x'}(\frac{T_{21}}{T_{22}}u'+v')\\&=\frac{yh_{xx}}{J}u-\frac{yh_{xx}(h_x+yh_{xy})}{J^2}u+\frac{yh_x}{J}u_x+v_x,\end{aligned}\tag{A.34}$$

$$\begin{aligned}\partial_{y'}v &= \partial_{y'}(\frac{T_{21}}{T_{22}}u'+v')\\&=\frac{h_x+yh_{xy}}{J}u-\frac{yh_x(2h_y+yh_{yy})}{J^2}u+\frac{yh_x}{J}u_y+v_y,\end{aligned}\tag{A.35}$$

$$\begin{aligned}\partial_{x'x'}v =&\frac{yh_{xxx}}{J}u-2\frac{yh_{xx}(h_x+yh_{xy})}{J^2}u+\frac{yh_{xx}}{J}u_x\\&-\frac{yh_x(h_{xx}+yh_{xxy})}{J^2}u+2\frac{yh_x(h_x+yh_{xy})^2}{J^3}u-\frac{yh_x(h_x+yh_{xy})}{J^2}u_x\\&+\frac{yh_{xx}}{J}u_x-\frac{yh_x(h_x+yh_{xy})}{J^2}u_x+\frac{yh_x}{J}u_{xx}+v_{xx},\end{aligned}\tag{A.36}$$

$$\begin{aligned}\partial_{y'y'}v =&\frac{2h_{xy}+yh_{xyy}}{J}u-\frac{(h_x+yh_{xy})(2h_y+yh_{yy})}{J^2}u+\frac{h_x+yh_{xy}}{J}u_y\\&-\frac{(h_x+yh_{xy})(2h_y+yh_{yy})}{J^2}u-\frac{yh_x(2h_{xy}+yh_{xyy})}{J^2}u+2\frac{yh_x(2h_y+yh_{yy})^2}{J^3}u\\&-\frac{yh_x(2h_y+yh_{yy})}{J^2}u_y+\frac{h_x+yh_{xy}}{J}u_y-\frac{yh_x(2h_y+yh_{yy})}{J^2}u_y\\&+\frac{yh_x}{J}u_{yy}+v_{yy},\end{aligned}\tag{A.37}$$

$$\begin{aligned}\partial_{x'y'}v =&\frac{h_{xx}+yh_{xxy}}{J}u-\frac{(h_x+yh_{xy})^2}{J^2}u+\frac{h_x+yh_{xy}}{J}u_x\\&-\frac{yh_{xx}(2h_y+yh_{yy})}{J^2}u-\frac{yh_x(2h_{xy}+yh_{xyy})}{J^2}u+2\frac{yh_x(2h_y+yh_{yy})(h_x+yh_{xy})}{J^3}u\\&-\frac{yh_x(2h_y+yh_{yy})}{J^2}u_x+\frac{yh_{xx}}{J}u_y-\frac{yh_x(h_x+yh_{xy})}{J^2}u_y+\frac{yh_x}{J}u_{xy}+v_{xy}.\end{aligned}\tag{A.38}$$

With these, we can finally calculate the transformation of the velocity components and pressure (all quantities on the right hand side with apostrophs:

$$\partial_t u=\frac{-yh_t}{J^2}u_y+\frac{2yh_th_y+y^2h_th_{yy}}{J^3}u+\frac{u_t}{J}-\frac{h_t+yh_{ty}}{J^2}u,\tag{A.39}$$

$$
\begin{aligned}
\partial_x u =& \frac{u_x}{J} - \frac{h_x + y h_{xy}}{J^2} u \\
& - \frac{y h_x}{J} \left(\frac{u_y}{J} - \frac{2h_y + y h_{yy}}{J^2} u \right),
\end{aligned} \tag{A.40}
$$

$$
\partial_y u = \frac{u_y}{J^2} - \frac{2h_y + y h_{yy}}{J^3} u, \tag{A.41}
$$

$$
\begin{aligned}
\partial_{xx} u =& \frac{u_{xx}}{J} - 2 \frac{h_x + y h_{xy}}{J^2} u_x - \frac{h_{xx} + y h_{xxy}}{J^2} u \\
& + 2 \frac{(h_x + y h_{xy})^2}{J^3} u \\
& + \frac{(y h_x)^2}{J^3} \left(\frac{u_{yy}}{J} - \frac{2h_y + y h_{yy}}{J^2} u_y - \frac{3h_{yy} + y h_{yyy}}{J^2} u \right. \\
& \left. + \frac{4h_y + 2y h_{yy}}{J^3} u - \frac{2h_y + y h_{yy}}{J^2} u_y \right) \\
& - \frac{2 y h_x}{J^2} \left(\frac{u_{xy}}{J} - \frac{2h_y + y h_{yy}}{J^2} u_x - \frac{h_x + y h_{xy}}{J^2} u_y \right. \\
& \left. - \frac{2h_{xy} + y h_{xyy}}{J^2} u + 2 \frac{(h_x + y h_{xy})(1h_y + y h_{yy})}{J^3} u \right) \\
& + \left(\frac{y h_x (h_x + y h_{xy}) - y h_{xx} J}{J^2} - y h_x \frac{y h_x (2h_y + y h_{yy}) - J(h_x + y h_{xy})}{J^3} \right) \cdot \\
& \left(\frac{u_y}{J} - \frac{2h_y + y h_{yy}}{J^2} u \right),
\end{aligned} \tag{A.42}
$$

$$
\begin{aligned}
\partial_{yy} u = & -\frac{2h_y + y h_{yy}}{J^3} \left(\frac{u_y}{J} - \frac{2h_y + y h_{yy}}{J^2} u \right) \\
& + \frac{1}{J^3} \left(u_{yy} - \frac{2h_y + y h_{yy}}{J} u_y - \frac{3h_{yy} + y h_{yyy}}{J} u \right. \\
& \left. + \frac{4h_y + 2y h_{yy}}{J^2} u - \frac{2h_y + y h_{yy}}{J} u_y \right),
\end{aligned} \tag{A.43}
$$

$$
\begin{aligned}
\partial_t v = & -\frac{y h_t (h_x + y h_{xy})}{J^2} u + \frac{y^2 h_t h_x (2h_y + y h_{yy})}{J^2} u - \frac{y^2 h_t h_x}{J^2} u_y \\
& - \frac{y h_t}{J} v_y + \frac{y h_{xt}}{J} u - \frac{y h_x (h_t + y h_{ty})}{J^2} u + \frac{y h_x}{J} u_t + v_t,
\end{aligned} \tag{A.44}
$$

$$
\begin{aligned}
\partial_x v = & \frac{y h_{xx}}{J} u - \frac{y h_{xx} (h_x + y h_{xy})}{J^2} u + \frac{y h_x}{J} u_x + v_x \\
& - \frac{y h_x}{J} \left(\frac{h_x + y h_{xy}}{J} u - \frac{y h_x (2h_y + y h_{yy})}{J^2} u + \frac{y h_x}{J} u_y + v_y \right),
\end{aligned} \tag{A.45}
$$

$$
\partial_y v = \frac{1}{J} \left(\frac{h_x + y h_{xy}}{J} u - \frac{y h_x (2h_y + y h_{yy})}{J^2} u + \frac{y h_x}{J} u_y + v_y \right), \tag{A.46}
$$

$$
\begin{aligned}
\partial_{xx} v = {} & \frac{y h_{xxx}}{J} u - 2 \frac{y h_{xx}(h_x + y h_{xy})}{J^2} u + \frac{y h_{xx}}{J} u_x \\
& - \frac{y h_x (h_{xx} + y h_{xxy})}{J^2} u + 2 \frac{y h_x (h_x + y h_{xy})^2}{J^3} u - \frac{y h_x (h_x + y h_{xy})}{J^2} u_x \\
& + \frac{y h_{xx}}{J} u_x - \frac{y h_x (h_x + y h_{xy})}{J^2} u_x + \frac{y h_x}{J} u_{xx} + v_{xx} \\
& + \frac{(y h_x)^2}{J^2} \Bigg(\frac{2 h_{xy} + y h_{xyy}}{J} u - \frac{(h_x + y h_{xy})(2 h_y + y h_{yy})}{J^2} u + \frac{h_x + y h_{xy}}{J} u_y \\
& - \frac{(h_x + y h_{xy})(2 h_y + y h_{yy})}{J^2} u - \frac{y h_x (2 h_{xy} + y h_{xyy})}{J^2} u + 2 \frac{y h_x (2 h_y + y h_{yy})^2}{J^3} u \\
& - \frac{y h_x (2 h_y + y h_{yy})}{J^2} u_y + \frac{h_x + y h_{xy}}{J} u_y - \frac{y h_x (2 h_y + y h_{yy})}{J^2} u_y \\
& + \frac{y h_x}{J} u_{yy} + v_{yy} \Bigg) \\
& - \frac{2 y h_x}{J} \Bigg(\frac{h_{xx} + y h_{xxy}}{J} u - \frac{(h_x + y h_{xy})^2}{J^2} u + \frac{h_x + y h_{xy}}{J} u_x \\
& - \frac{y h_{xx} (2 h_y + y h_{yy})}{J^2} u - \frac{y h_x (2 h_{xy} + y h_{xyy})}{J^2} u + 2 \frac{y h_x (2 h_y + y h_{yy})(h_x + y h_{xy})}{J^3} u \\
& - \frac{y h_x (2 h_y + y h_{yy})}{J^2} u_x + \frac{y h_{xx}}{J} u_y - \frac{y h_x (h_x + y h_{xy})}{J^2} u_y + \frac{y h_x}{J} u_{xy} + v_{xy} \Bigg) \\
& + \Bigg(\frac{y h_x (h_x + y h_{xy}) - y h_{xx} J}{J^2} - y h_x \frac{y h_x (2 h_y + y h_{yy}) - J (h_x + y h_{xy})}{J^3} \Bigg) \cdot \\
& \Bigg(\frac{h_x + y h_{xy}}{J} u - \frac{y h_x (2 h_y + y h_{yy})}{J^2} u + \frac{y h_x}{J} u_y + v_y \Bigg),
\end{aligned}
\tag{A.47}
$$

$$
\begin{aligned}
\partial_{yy} v = {} & - \frac{2 h_y + y h_{yy}}{J^3} \Bigg(\frac{h_x + y h_{xy}}{J} u - \frac{y h_x (2 h_y + y h_{yy})}{J^2} u + \frac{y h_x}{J} u_y + v_y \Bigg) \\
& + \frac{1}{J^2} \Bigg(\frac{2 h_{xy} + y h_{xyy}}{J} u - \frac{(h_x + y h_{xy})(2 h_y + y h_{yy})}{J^2} u + \frac{h_x + y h_{xy}}{J} u_y \\
& - \frac{(h_x + y h_{xy})(2 h_y + y h_{yy})}{J^2} u - \frac{y h_x (2 h_{xy} + y h_{xyy})}{J^2} u + 2 \frac{y h_x (2 h_y + y h_{yy})^2}{J^3} u \\
& - \frac{y h_x (2 h_y + y h_{yy})}{J^2} u_y + \frac{h_x + y h_{xy}}{J} u_y - \frac{y h_x (2 h_y + y h_{yy})}{J^2} u_y \\
& + \frac{y h_x}{J} u_{yy} + v_{yy} \Bigg),
\end{aligned}
\tag{A.48}
$$

$$
\partial_x p = p_x - \frac{y h_x}{J} p_y, \tag{A.49}
$$

$$
\partial_y p = \frac{p_y}{J}. \tag{A.50}
$$

B. Derivation of the Orr-Sommerfeld equation

For reference, we give a derivation of the (temporal) Orr-Sommerfeld equation for free surface flow down an inclined plane. We follow Nishida et al. (1994). We start with the eigenfunction equation for flows without surfactant, cf. Section 2.4.2:

$$
\begin{aligned}
u_t + (2y-y^2)u_x + (2-2y)v - \frac{1}{\mathrm{Re}}u_{xx} - \frac{1}{\mathrm{Re}}u_{yy} + \frac{1}{\mathrm{Re}}p_x &= 0, \quad \boldsymbol{x} \in \Omega, && \text{(B.1)}\\
v_t + (2y-y^2)v_x - \frac{1}{\mathrm{Re}}v_{xx} - \frac{1}{\mathrm{Re}}v_{yy} + \frac{1}{\mathrm{Re}}p_y &= 0, \quad \boldsymbol{x} \in \Omega, && \text{(B.2)}\\
u_x + v_y &= 0, \quad \boldsymbol{x} \in \Omega, && \text{(B.3)}\\
u = v &= 0, \quad \boldsymbol{x} \in W && \text{(B.4)}\\
\lambda h + h_x - v &= 0, \quad \boldsymbol{x} \in \Sigma, && \text{(B.5)}\\
p - 2\cot\vartheta h - 2v_y + \frac{1}{\mathrm{Ca}}h_{xx} &= 0, \quad \boldsymbol{x} \in \Sigma, && \text{(B.6)}\\
u_y + v_x - 2h &= 0, \quad \boldsymbol{x} \in \Sigma. && \text{(B.7)}
\end{aligned}
$$

We introduce a streamfunction ψ such that $u = \psi_y$ and $v = -\psi_x$. By this, (B.3) is automatically fulfilled. Pressure is eliminated and a single ordinary differential equation of fourth order is derived by taking the derivative of (B.1) in y-direction, and subtracting the derivative of (B.2) in x-direction:

$$
\psi_{txx} + \psi_{tyy} + (2y-y^2)(\psi_{xxx} + \psi_{xyy}) + 2\psi_x - \frac{1}{\mathrm{Re}}(\psi_{xxxx} + 2\psi_{xxyy} + \psi_{yyyy}) = 0. \quad \text{(B.8)}
$$

Pressure is eliminated from (B.6) by taking its derivative in x-direction, and inserting equation (B.1) at $y = 1$:

$$
u_{xx} + u_{yy} - \mathrm{Re}\big(u_t + (2y-y^2)u_x + (2-2y)v\big) - 2h_x\cot\vartheta - 2v_{xy} + \frac{1}{\mathrm{Ca}}h_{xx} = 0. \quad \text{(B.9)}
$$

Modal solutions are assumed:

$$
\begin{aligned}
\psi(x,y) &= \phi(y)\exp(i\xi x - \lambda t), && \text{(B.10)}\\
h(x) &= h\exp(i\xi x - \lambda t), && \text{(B.11)}
\end{aligned}
$$

where $\xi = \frac{2\pi k}{L}$. Equation (B.5) becomes

$$
-\lambda h + i\xi h - i\xi\phi(1) = 0. \quad \text{(B.12)}
$$

With this equation, h is eliminated from (B.6) and (B.7), leaving us with the following ODE eigenvalue problem:

$$\begin{aligned} &\phi'''' - 2\xi^2\phi'' + \xi^4\phi \\ &-i\xi\,\mathrm{Re}(2y - y^2 - \frac{\lambda}{i\xi})\phi'' + i\xi\,\mathrm{Re}\left(\xi^2(2y - y^2 - \frac{\lambda}{i\xi}) - 2\right)\phi = 0, \quad 0 < y < 1, \end{aligned} \tag{B.13}$$

$$\phi = 0, \qquad y = 0, \tag{B.14}$$

$$\phi' = 0, \qquad y = 0, \tag{B.15}$$

$$\phi'' + \xi^2\phi + \frac{2i\xi}{i\xi - \lambda}\phi' = 0, \qquad y = 1, \tag{B.16}$$

$$\phi''' - i\xi\,\mathrm{Re}(1 - \frac{\lambda}{i\xi})\phi' - 3\xi^2\phi' + \frac{i\xi}{1 - \frac{\lambda}{i\xi}}(\frac{\xi^2}{\mathrm{Ca}} + 2\cot\vartheta)\phi = 0, \qquad y = 1. \tag{B.17}$$

The spectrum of the linearized stability operator is the set of all $\lambda \in \mathbb{C}$ such that a solution ϕ of these equations exists. The equation must still be solved numerically. In Nishida et al. (1994), a shooting algorithm was employed. Another popular solution method is Chebyshev collocation, cf. Orszag (1971).

Bibliography

R. A. Adams. *Sobolev spaces*, volume 140 of *Pure and Applied Mathematics*. Academic Press, 1975.

C. Albert, H. Raach, and D. Bothe. Influence of surface tension models on the hydrodynamics of wavy laminar falling films in Volume of Fluid-simulations. *International Journal of Multiphase Flow*, 43:66–71, 2012.

C. Albert, H. Marschall, and D. Bothe. Direct numerical simulation of interfacial mass transfer into falling films. *submitted to the International Journal of Heat and Mass Transfer*, 2013a.

C. Albert, A. Tezuka, and D. Bothe. Global Linear Stability Analysis of Falling Films with In- and Outlet. *In revision at the Journal of Fluid Mechanics*, 2013b.

S. Alekseenko, V. Antipin, A. Bobylev, and D. Markovich. Application of PIV to velocity measurements in a liquid film flowing down an inclined cylinder. *Experiments in Fluids*, 43:197–207, 2007.

S. V. Alekseenko, V. Y. Nakoryakov, and B. G. Pokusaev. Wave formation on a vertical falling liquid film. *AIChE Journal*, 31(9):1446–1460, 1985.

S. V. Alekseenko, V. E. Nakoryakov, and B. G. Pokusaev. *Wave flow of liquid films.* Begell House New York, 1994.

S. V. Alekseenko, V. E. Nakoryakov, and B. G. Pokusaev. Wave effect on the transfer processes in liquid films. *Chemical Engineering Communications*, 141-142 (1):359–385, 1996.

B. E. Anshus. On the asymptotic solution to the falling film stability problem. *Industrial & Engineering Chemistry Fundamentals*, 11(4):502–508, 1972.

B. E. Anshus and S. L. Goren. A method of getting approximate solutions to the Orr-Sommerfeld equation for flow on a vertical wall. *AIChE Journal*, 12(5): 1004–1008, 1966.

W. E. Arnoldi. The principle of minimized iterations in the solution of the matrix eigenvalue problem. *Quarterly of Applied Mathematics*, 9:17–29, 1951.

D. Barkley, M. Gomes, M. Gabriela, and R. D. Henderson. Three-dimensional instability in flow over a backward-facing step. *Journal of Fluid Mechanics*, 473: 167–190, 11 2002.

J. Thomas Beale. The initial value problem for the Navier-Stokes equations with a free surface. *Communications on Pure and Applied Mathematics*, 34(3):359–392, 1981.

J Thomas Beale. Large-time regularity of viscous surface waves. *Archive for Rational Mechanics and Analysis*, 84(4):307–352, 1984.

J. Thomas Beale and Takaaki Nishida. Large-time behavior of viscous surface waves. In Kyûya Masuda and Masayasu Mimura, editors, *Recent Topics in Nonlinear PDE II*, volume 128 of *North-Holland Mathematics Studies*, pages 1 – 14. North-Holland, 1985.

J. B. Bell, P. Colella, and H. M. Glaz. A second-order projection method for the incompressible Navier-Stokes equations. *Journal of Computational Physics*, 85 (2):257–283, 1989.

T. B. Benjamin. Wave formation in laminar flow down an inclined plane. *Journal of Fluid Mechanics*, 2(06):554–573, 1957.

H. M. Blackburn, D. Barkley, and S. J. Sherwin. Convective instability and transient growth in flow over a backward-facing step. *Journal of Fluid Mechanics*, 603: 271–304, 4 2008.

J. Blazek. *Computational Fluid Dynamics: Principles and Applications: Principles and Applications*. Elsevier Science, 2001.

S. Bo, X. Ma, H. Chen, and Z. Lan. Numerical simulation on vapor absorption by wavy lithium bromide aqueous solution films. *Heat and Mass Transfer*, 47(12): 1611–1619, 2011. doi: 10.1007/s00231-011-0820-x.

D. N. Bock. On the Navier-Stokes Equations in Noncylindrical Domains. *Journal of Differential Equations*, 25:151–162, 1977.

M. Boger, J. Schlottke, C. D. Munz, and B. Weigand. Reduction of parasitic currents in the DNS VOF code FS3D. In *Ercoftac 12th Workshop on Two-Phase Flow Predictions*, Halle (Saale), Germany, March 22-25 2010.

D. Bothe and S. Fleckenstein. A volume-of-fluid-based method for mass transfer processes at fluid particles. *Chemical Engineering Science*, 101(0):283 – 302, 2013.

D. Bothe, J. Prüss, and G. Simonett. Well-posedness of a two-phase flow with soluble surfactant. In Haim Brezis, Michel Chipot, and Joachim Escher, editors, *Nonlinear Elliptic and Parabolic Problems*, volume 64 of *Progress in Nonlinear Differential Equations and Their Applications*, pages 37–61. Birkhäuser Basel, 2005.

D. Bothe, M. Schmidtke, and H.-J. Warnecke. VOF-Simulation of the Lift Force for Single Bubbles in a Simple Shear Flow. *Chemical Engineering and Technology*, 29(9):1048–1053, 2006.

Dieter Bothe and Jan Prüss. Stability of equilibria for two-phase flows with soluble surfactant. *The Quarterly Journal of Mechanics and Applied Mathematics*, 63 (2):177–199, 2010.

Dieter Bothe, Matthias Köhne, and Jan Prüss. On two-phase flows with soluble surfactant. *arXiv preprint arXiv:1210.8131*, 2012.

J. U. Brackbill, D. B. Kothe, and C. Zemach. A continuum method for modeling surface tension. *Journal of Computational Physics*, 100(2):335–354, 1992.

N. Brauner and D. Moalem Maron. Modeling of wavy flow in inclined thin films. *Chemical Engineering Science*, 38(5):775–788, 1983.

L. Brevdo, P. Laure, F. Dias, and T. J. Bridges. Linear pulse structure and signalling in a film flow on an inclined plane. *Journal of Fluid Mechanics*, 396: 37–71, 9 1999.

H.-C. Chang and E. A. Demekhin. *Complex Wave Dynamics on Thin Films.* Number 14 in Studies in Interface Science. Elsevier, 2002.

S. Chiba. Global stability analysis of incompressible viscous flow (In Japanese). *Journal of the Japanese society for Computational Fluid Dynamics*, 7:20–48, 1998.

A. J. Chorin. Numerical solution of the Navier-Stokes equations. *Mathematics of Computation*, 22(104):745–762, 1968.

K. N. Christodoulou and L. E. Scriven. Finding leading modes of a viscous free surface flow: An asymmetric generalized eigenproblem. *Journal of Scientific Computing*, 3:355–406, 1988.

A. Clément. Coupling of two absorbing boundary conditions for 2d time-domain simulations of free surface gravity waves. *Journal of Computational Physics*, 126 (1):139 – 151, 1996.

M. H. H. Van Dam, J.-P. Corriou, N. Midoux, A.-S. Lamine, and C. Roizard. Modeling and measurement of sulfur dioxide absorption rate in a laminar falling film reactor. *Chemical Engineering Science*, 54(21):5311–5318, 1999.

R. DeBar. Fundamentals of the KRAKEN code. *Lawrence Livermore Laboratory, UCIR-760, Technical Report*, 1974.

U. Dierkes, S. Hildebrandt, and F. Sauvigny. Minimal surfaces. volume 339 of *Grundlehren der mathematischen Wissenschaften.* Springer Berlin Heidelberg, 2010.

G. F. Dietze, A. Leefken, and R. Kneer. Investigation of the backflow phenomenon in falling liquid films. *Journal of Fluid Mechanics*, 595:435–459, 2008.

G. F. Dietze, F. Al-Sibai, and R. Kneer. Experimental study of flow separation in laminar falling liquid films. *Journal of Fluid Mechanics*, 637:73–104, 2009.

P. G. Drazin and W. H. Reid. *Hydrodynamic stability.* Cambridge university press, 2004.

K.-J. Engel and R. Nagel. One-parameter semigroups for linear evolution equations. volume 194 of *Graduate Texts in Mathematics.* Springer, 2000.

B. Engquist and A. Majda. Absorbing boundary conditions for numerical simulation of waves. *Proceedings of the National Academy of Sciences USA*, 74(5):1765–1766, 1977.

L. E. Eriksson and A. Rizzi. Computer-aided analysis of the convergence to steady state of discrete approximations to the Euler equations. *Journal of Computational Physics*, 57(1):90 – 128, 1985.

J. M. Floryan, S. H. Davis, and R. E. Kelly. Instabilities of a liquid film flowing down a slightly inclined plane. *Physics of Fluids*, 30(4):983–989, 1987.

C. Focke and D. Bothe. Direct numerical simulation of binary off-center collisions of shear thinning droplets at high Weber numbers. *Physics of Fluids*, 24(7): 073105, 2012.

M. M. Francois, S. J. Cummins, E. D. Dendy, D. B. Kothe, J. M. Sicilian, and M. W. Williams. A balanced-force algorithm for continuous and sharp interfacial surface tension models within a volume tracking framework. *Journal of Computational Physics*, 213(1):141–173, 2006.

D. P. Frisk and E. J. Davis. The enhancement of heat transfer by waves in stratified gas-liquid flow. *International Journal of Heat and Mass Transfer*, 15(8):1537 – 1552, 1972.

D. Gao, N. B. Morley, and V. Dhir. Numerical simulation of wavy falling film flow using VOF method. *Journal of Computational Physics*, 192(2):624–642, 2003.

M. Graef. Über die Eigenschaften zwei-und dreidimensionaler Störungen in Rieselfilmen an geneigten Wänden. *Selbstverlag Max-Planck-Institut für Strömungsforschung und Aerodynamische Versuchsanstalt, Göttingen*, 26, 1966.

F. H. Harlow and J. E. Welch. Numerical calculation of time-dependent viscous incompressible flow of fluid with free surface. *Physics of Fluids*, 8(12):2182–2189, 1965.

C. W. Hirt and B. D. Nichols. Volume of fluid (VOF) method for the dynamics of free boundaries. *Journal of Computational Physics*, 39(1):201–225, 1981.

K. J. Hollenbeck. A matlab function for numerical inversion of Laplace transforms by the de Hoog algorithm, 1998. URL `http://www.isva.dtu.dk/staff/karl/invlap.htm`.

P. Huerre. *Open shear flow instabilities, in Perspectives in Fluid Dynamics.* Cambridge Univ. Press, 2000.

P. Huerre and P. A. Monkewitz. Local and global instabilities in spatially developing flows. *Annual Review of Fluid Mechanics*, 22:473–537, 1990.

E. Isaacson. *Analysis of numerical methods.* Courier Dover Publications, 1994.

M. Ishii and T. Hibiki. *Thermo-fluid dynamics of two-phase flow.* Springer, 2011.

G. Jin and M. Braza. A nonreflecting outlet boundary condition for incompressible unsteady Navier-Stokes calculations. *Journal of Computational Physics*, 107(2): 239 – 253, 1993.

L. O. Jones and S. Whitaker. An experimental study of falling liquid films. *AIChE Journal*, 12(3):525–529, 1966.

K. Jähnisch, M. Baerns, V. Hessel, W. Ehrfeld, V. Haverkamp, H. Löwe, C. Wille, and A. Guber. Direct fluorination of toluene using elemental fluorine in gas/liquid microreactors. *Journal of Fluorine Chemistry*, 105(1):117–128, 2000.

W. Kahan. Pracniques: further remarks on reducing truncation errors. *Communications of the ACM*, 8(1):40–41, January 1965.

S. Kalliadasis, C. Ruyer-Quil, B. Scheid, and M. G. Velarde. *Falling liquid films.* Springer London, 2012.

P.L. Kapitza and S.P. Kapitza. Wave flow of thin layers of a viscous fluid: III. Experimental study of undulatory flow conditions. *Journal of Experimental and Theoretical Physics*, 19, 1949.

M. Koebe, D. Bothe, and H.-J. Warnecke. Direct numerical simulation of air bubbles in water/glycerol mixtures: Shapes and velocity fields. *Proceedings of the 2003 ASME Joint U.S.-European Fluids Engineering Conference*, 2003.

W. B. Krantz and S. L. Goren. Stability of thin liquid films flowing down a plane. *Industrial & Engineering Chemistry Fundamentals*, 10(1):91–101, 1971.

W. B. Krantz and W. B. Owens. Spatial formulation of the Orr-Sommerfeld equation for thin liquid films flowing down a plane. *AIChE Journal*, 19(6): 1163–1169, 1973.

S. Kulankara and K. E. Herold. Theory of heat/mass transfer additives in absorption chillers. *HVAC&R Research*, 6(4):369–380, 2000.

B. Lafaurie, C. Nardone, R. Scardovelli, S. Zaleski, and G. Zanetti. Modelling Merging and Fragmentation in Multiphase Flows with SURFER. *Journal of Computational Physics*, 113(1):134 – 147, 1994.

D. Lanzerstorfer and H. C. Kuhlmann. Global stability of the two-dimensional flow over a backward-facing step. *Journal of Fluid Mechanics*, 693:1–27, 1 2012.

R. J. LeVeque. *Finite volume methods for hyperbolic problems*, volume 31 of *Cambridge Texts in Applied Mathematics.* Cambridge university press, 2002.

J. Liu and J. P. Gollub. Solitary wave dynamics of film flows. *Physics of Fluids*, 6: 1702 – 1712, 1994.

J. Liu, J. D. Paul, and J. P. Gollub. Measurements of the primary instabilities of film flows. *Journal of Fluid Mechanics*, 250:69–101, 4 1993.

C. Ma and D. Bothe. Direct numerical simulation of thermocapillary flow based on the volume of fluid method. *International Journal of Multiphase Flow*, 37(9): 1045 – 1058, 2011.

N. A. Malamataris and V. Balakotaiah. Flow structure underneath the large amplitude waves of a vertically falling film. *AIChE Journal*, 54(7):1725–1740, 2008.

D. Moalem Maron, N. Brauner, and G. F. Hewitt. Flow patterns in wavy thin films: numerical simulation. *International communications in heat and mass transfer*, 16(5):655–666, 1989.

T. Nishida, Y. Teramoto, and H. A. Win. Navier-stokes flow down an inclined plane: Downward periodic motion. *Kyoto Journal of Mathematics*, 33(3):787–801, 1993.

T. Nishida, Y. Teramoto, and H. Yoshihara. Eigenvalue problems of the parameter dependent system of ordinary differential equations and computer aided proof. *RIMS Kokyuroku*, 865:57–64, 1994.

T. Nishida, Y. Teramoto, and H. Yoshihara. Hopf bifurcation in viscous incompressible flow down an inclined plane. *Journal of Mathematical Fluid Mechanics*, 7(1):29–71, 2005.

T. Nishida, Y. Teramoto, and K. Tomoeda. On the equations for motion of viscous incompressible flow down a vertical plane. *Preprint*, 2013.

T. Nosoko, P. N. Yoshimura, T. Nagata, and K. Oyakawa. Characteristics of two-dimensional waves on a falling liquid film. *Chemical Engineering Science*, 51 (5):725–732, 1996.

W. Nusselt. Der Wärmeaustausch am Berieselungskühler. *VDI-Zeitschrift*, 67: 206–210, 1923.

Wilhelm Nusselt. Die Oberflächenkondensation des Wasserdampfes. *VDI-Zeitschrift*, 60:541–546, 1916.

I. Orlanski. A simple boundary condition for unbounded hyperbolic flows. *Journal of Computational Physics*, 21(3):251 – 269, 1976.

S. A. Orszag. Accurate solution of the Orr-Sommerfeld stability equation. *Journal of Fluid Mechanics*, 50(4):689–703, 1971.

M. Padula. Nonlinear stability of liquid flow down an inclined plane. *Preprint, Università degli Studi di Ferrara*, 2012.

M. Padula and V. A. Solonnikov. On Rayleigh-Taylor stability. *Annali dell'Università di Ferrara*, 46(1):307–336, 2000.

C. D. Park and T. Nosoko. Three-dimensional wave dynamics on a falling film and associated mass transfer. *AIChE Journal*, 49(11):2715–2727, 2003.

A. Pazy. *Semigroups of linear operators and applications to partial differential equations.* Springer-Verlag, New York, 1983.

F. W. Pierson and S. Whitaker. Some theoretical and experimental observations of the wave structure of falling liquid films. *Industrial & Engineering Chemistry Fundamentals*, 16(4):401–408, 1977.

S. Popinet. An accurate adaptive solver for surface-tension-driven interfacial flows. *Journal of Computational Physics*, 228(16):5838 – 5866, 2009.

S. Portalski and A. J. Clegg. An experimental study of wave inception on falling liquid films. *Chemical Engineering Science*, 27(6):1257 – 1265, 1972.

A. Prosperetti. Motion of two superposed viscous fluids. *Physics of Fluids*, 24(7): 1217 – 1223, 1981.

Jan Prüss and Gieri Simonett. On the manifold of closed hypersurfaces in R^n. *arXiv preprint arXiv:1212.6445*, 2012.

H. Raach and J. Mitrovic. Simulation of heat and mass transfer in a multi-effect distillation plant for seawater desalination. *Desalination*, 204(1–3):416–422, 2007.

A. Rastaturin, E. Demekhin, and E. Kalaidin. Optimal regimes of heat-mass transfer in a falling film. *Journal of Non-Equilibrium Thermodynamics*, 31:1–10, 2006.

D. Rempfer. On boundary conditions for incompressible navier-stokes problems. *Applied Mechanics Reviews*, 59:107, 2006.

Y. Renardy and M. Renardy. PROST: A Parabolic Reconstruction of Surface Tension for the Volume-of-Fluid Method. *Journal of Computational Physics*, 183(2):400 – 421, 2002.

O. Reynolds. An experimental investigation of the circumstances which determine whether the motion of water shall be direct or sinuous, and of the law of resistance in parallel channels. *Proceedings of the Royal Society of London*, 35(224-226): 84–99, 1883.

O. Reynolds. On the dynamical theory of incompressible viscous fluids and the determination of the criterion. *Philosophical Transactions of the Royal Society of London. A*, 186:123–164, 1895.

W. J. Rider and D. B. Kothe. Reconstructing Volume Tracking. *Journal of Computational Physics*, 141(2):112–152, 1998.

M. Rieber. *Numerische Modellierung der Dynamik freier Grenzflächen in Zweiphasenströmungen.* PhD thesis, University of Stuttgart, 2004.

M. Rieber and A. Frohn. A numerical study on the mechanism of splashing. *International Journal of Heat and Fluid Flow*, 20(5):455 – 461, 1999.

M. Rieber, F. Graf, M. Hase, N. Roth, and B. Weigand. Numerical simulation of moving spherical and strongly deformed droplets. *Proceedings ILASS-Europe, Darmstadt*, 2000.

A. Schagen and M. Modigell. Local film thickness and temperature distribution measurement in wavy liquid films with a laser-induced luminescence technique. *Experiments in Fluids*, 43(2-3):209–221, 2007.

A. Schagen, M. Modigell, G. Dietze, and R. Kneer. Simultaneous measurement of local film thickness and temperature distribution in wavy liquid films using a luminescence technique. *International Journal of Heat and Mass Transfer*, 49 (25–26):5049–5061, 2006.

P. J. Schmid and D. S. Henningson. *Stability and transition in shear flows*, volume 142 of *Applied Mathematical Sciences.* Springer, 2001.

A. S. Sharma, N. Abdessemed, S. J. Sherwin, and V. Theofilis. Transient growth mechanisms of low Reynolds number flow over a low-pressure turbine blade. *Theoretical and Computational Fluid Dynamics*, 25(1-4):19–30, 2011.

V.Ya. Shkadov. Wave flow regimes of a thin layer of viscous fluid subject to gravity. *Fluid Dynamics*, 2(1):29–34, 1967.

G. M. Sisoev, O. K. Matar, and C. J. Lawrence. Absorption of gas into a wavy falling film. *Chemical Engineering Science*, 60(3):827–838, 2005.

J. C. Slattery. *Advanced Transport Phenomena.* Cambridge University Press, 1999.

V. A. Solonnikov. Estimates of solutions of an initial-and boundary-value problem for the linear nonstationary navier-stokes system. *Zapiski Nauchnykh Seminarov POMI*, 59:178–254, 1976.

V. A. Solonnikov. On an initial-boundary value problem for the Stokes systems arising in the study of a problem with a free boundary. *Proceedings of the Steklov Institute of Mathematics*, 3:191–239, 1991.

H. B. Squire. On the stability for three-dimensional disturbances of viscous fluid flow between parallel walls. *Proceedings of the Royal Society of London. Series A*, 142(847):621–628, 1933.

W. J. Strobel and S. Whitaker. The effect of surfactants on the flow characteristics of falling liquid films. *AIChE Journal*, 15(4):527–532, 1969.

R Temam. Remark on the pressure boundary condition for the projection method. *Theoretical and Computational Fluid Dynamics*, 3(3):181–184, 1991.

Y. Teramoto. On the Navier-Stokes flow down an inclined plane. *Kyoto Journal of Mathematics*, 32(3):593–619, 1992. ISSN 0023-608X.

Yoshiaki Teramoto. The initial value problem for viscous incompressible flow down an inclined plane. *Hiroshima Mathematical Journal*, 15(3):619–643, 1985.

Yoshiaki Teramoto and Kyoko Tomoeda. Optimal Korn's inequality for solenoidal vector fields on a periodic slab. *Proceedings of the Japan Academy, Series A, Mathematical Sciences*, 88(10):168–172, 2012.

A. Tezuka and K. Suzuki. Three dimensional global linear stability analysis of flow around a spheroid. *AIAA Journal*, 44(8):1697–1708, 2006.

V. Theofilis. Advances in global linear instability analysis of nonparallel and three-dimensional flows. *Progress in aerospace sciences*, 39(4):249–315, 2003.

V. Theofilis. Global linear instability. *Annual Review of Fluid Mechanics*, 43: 319–352, 2011.

G. Tryggvason, R. Scardovelli, and S. Zaleski. *Direct numerical simulations of gas-liquid multiphase flows.* Cambridge University Press, 2011.

H. K. Versteeg and W. Malalasekera. *An Introduction to Computational Fluid Dynamics: The Finite Volume Method.* Prentice Hall, 2007.

F. K. Wasden and A. E. Dukler. A numerical study of mass transfer in free falling wavy films. *AIChE Journal*, 36(9):1379–1390, 1990.

J. V. Wehausen and E. V. Laitone. *Surface waves.* Springer, 1960.

Z.F. Xu, B.C. Khoo, and N.E. Wijeysundera. Mass transfer across the falling film: Simulations and experiments. *Chem. Eng. Sci.*, 63(9):2559–2575, 2008.

K. K. Yeong, A. Gavriilidis, R. Zapf, and V. Hessel. Catalyst preparation and deactivation issues for nitrobenzene hydrogenation in a microstructured falling film reactor. *Catalysis Today*, 81(4):641–651, 2003.

C. S. Yih. Stability of two-dimensional parallel flows for three-dimensional disturbances. *The Quarterly of Applied Mathematics*, 12(4), 1955.

C. S. Yih. Stability of liquid flow down an inclined plane. *Physics of Fluids*, 6(3): 321–334, 1963.

S.-M. Yih and C.-C. Kuo. Design and testing of a new type of falling film gas-liquid contacting device. *AIChE Journal*, 34(3):499–501, 1988.

L. Zhang, H. Zheng, and Y. Wu. Experimental study on a horizontal tube falling film evaporation and closed circulation solar desalination system. *Renewable Energy*, 28(8):1187–1199, 2003.

Curriculum Vitae

Persönliche Daten

Name: Christoph Hermann Albert
Geburtsdatum: 16. März 1982
Geburtsort: Aschaffenburg

Bildungsweg

08.2010 – 08.2013: **Promotionsstudium**
am Fachbereich Mathematik der TU Darmstadt
Titel: *On Stability of Falling Films: Numerical and Analytical Investigations*
Gutachter: Prof. Dr. Dieter Bothe, Prof. Dr. Jürgen Saal, Prof. Dr. Takaaki Nishida

10.2004 – 07.2010 **Studium der Mathematik**
mit Nebenfach Informatik an der TU Darmstadt
Diplomarbeit: *Nichtlineare Stabilität von Ekman- und Ekman-Hartmann-Grenzschichten*
Betreuer: Prof. Dr. Matthias Hieber

09.1999 – 07.2002 **Ausbildung zum IT-Systemelektroniker**
bei m+s Elektronik AG, Niedernberg